



HAL
open science

Microstructure optimization of ferrite-martensite steels with 3.5wt% Mn: from phase transformation to micromechanics

Qingquan Lai

► **To cite this version:**

Qingquan Lai. Microstructure optimization of ferrite-martensite steels with 3.5wt% Mn: from phase transformation to micromechanics. Chemical and Process Engineering. Université de Grenoble, 2014. English. NNT: 2014GRENI086 . tel-01310288

HAL Id: tel-01310288

<https://theses.hal.science/tel-01310288>

Submitted on 2 May 2016

HAL is a multi-disciplinary open access archive for the deposit and dissemination of scientific research documents, whether they are published or not. The documents may come from teaching and research institutions in France or abroad, or from public or private research centers.

L'archive ouverte pluridisciplinaire **HAL**, est destinée au dépôt et à la diffusion de documents scientifiques de niveau recherche, publiés ou non, émanant des établissements d'enseignement et de recherche français ou étrangers, des laboratoires publics ou privés.

THÈSE

Pour obtenir le grade de

DOCTEUR DE L'UNIVERSITÉ DE GRENOBLE

Spécialité : **Matériaux Mécanique Génie Civil Electrochimie**

Arrêté ministériel : 7 août 2006

Présentée par

Qingquan LAI

Thèse dirigée par **Yves BRECHET** et

Co-dirigée par **Olivier BOUAZIZ**

préparée au sein du **Laboratoire SIMaP**
dans **l'École Doctorale I-MEP2**

Optimisation de la microstructure d'aciers ferrito-martensitiques à 3.5%pds Mn: des transformations de phase à la micro-mécanique

Thèse soutenue publiquement le **3 novembre 2014**,
devant le jury composé de :

M. Ke LU

Professeur, Institute of Metal Research, Président

M. Javier GIL SEVILLANO

Professeur, University of Navarra, Rapporteur

Mme. Anne-Françoise GOURGUES-LORENZON

Professeur, Ecole des Mines de Paris, Rapporteur

M. Thierry IUNG

Ingénieur de recherche, ArcelorMittal R&D, Examineur

M. Thomas PARDOEN

Professeur, Université catholique de Louvain, Examineur

M. Yves BRECHET

Professeur, Grenoble-INP, Directeur de thèse

M. Olivier BOUAZIZ

Professeur, Université de Lorraine, Co-Directeur de thèse

M. David EMBURY

Professeur, McMaster University, Invité

M. Mohamed GOUNE

Professeur, ICMCB, Invité

Mme. Astrid PERLADE

Ingénieur de recherche, ArcelorMittal R&D, Invité



Acknowledgements

First of all, I would like to express my sincere gratitude to Prof. Yves Breché. Yves discovered me during his visit in China, and brought me to Grenoble for PhD thesis. During these 3 years, I found it most enjoyable to work with him. The discussions were always stimulating, giving birth to a lot of new ideas. Yves always encouraged me and gave me large freedom for research. I was always impressed by his capability of making decision, guiding my thesis in the right direction. The supervising style of Yves has deeply influenced my PhD research, and will influence my future career.

I would also like to greatly thank Prof. Olivier Bouaziz, my co-director in Metz. He offered me the PhD position together with Yves. Olivier is very experienced in steel research, and the co-operation with him made it easy to enter the field of steel metallurgy. He shared with me a lot of original ideas. But he respected the efforts of the student and encouraged me to carry out my own ideas.

I greatly appreciate the financial support from ArcelorMittal. Thanks go to Dr. Astrid Perlade for her help in experiment and for the useful discussions. I should also thank Dr. Thierry Jung, Dr. David Barbier and Dr. Jean-Philippe Masse for the interesting discussions and hospitality during my trips to Metz.

During my thesis, I have the opportunity to closely collaborate with excellent scientists of different expertise. During the early stage of my PhD, I worked a lot with Prof. Mohamed Gouné on microstructure development. I appreciate Mohamed for sharing his broad and deep knowledge of phase transformation. His suggestions are important in the achievement of microstructures. For my work on mechanical properties, the help from the UCL group was essential. Prof. Thomas Pardoën is probably the best people to discuss with about mechanical behavior, because of his mixed background of materials science and solid mechanics. I am very grateful to Thomas for his invaluable advices, his strong support, and his efficiency in correcting my manuscripts and slides. I have to thank Prof. Pascal Jacques for his generous help in experiment and for his helpful comments about my results. The help of Dr. Laurence Brassart on micromechanical modeling is also highly appreciated!

I would like to express my gratitude to Prof. Ke Lu (IMR), Prof. Javier Gil Sevillano (University of Navarra), Prof. Anne-Françoise Gourgues-Lorenzon (Ecole des Mines de

Acknowledgements

Paris) and Prof. David Embury (McMaster University) for serving in the PhD committee. It is special for me that Prof. Lu can come to my PhD defense, because my research career was nucleated in IMR. The deep and thoughtful reports of Javier and Anne-Françoise will be a guide to my future approach to research. I should also thank David for the various fruitful discussions and for his support.

I have to express my appreciation to the SIMaP colleagues. The help from Dr. Guillaume Parry is very important to the micromechanical modeling work. Prof. Alexis Deschamps, Prof. Marc Verdier, Prof. Muriel Veron, Prof. Frédéric Livet, Prof. Patricia Donnadieu and other permanent researchers have kindly helped me in managing a lot of things. Prof. Nicolas Eustathopoulos is always very supportive to me! Thanks also go to Fanny Mas, Nicolas Sallez, Laurent Couturier, Olivier Jay, Dan Liu, Eva Gumbmann, Thomas Dorin, Maxime Dupraz, Hasan Naser, Audrey Lechartier, Mahmoud Saied, Simon Langlais, Rosen Ivanov, Kitty Ratter and Oleksii Liashenko for their helps in my work and my life in France.

Acknowledgements also go to the colleagues in CMTC, including Joelle Clalbro, Frédéric Charlot and Florence Robaut, for helping me in the SEM, EPMA and EBSD analysis. I have also to thank Nathalie Valle (Gabriel Lippmann, Luxembourg) for the NanoSIMS measurement.

I should thank my family for their love and understanding during these years, especially concerning the limited time of staying together with them. I have to specially thank my wife Qianyu for her love, support and patience, without which I couldn't have fully devoted to my thesis!

Abstract

Ferrite-martensite dual-phase (DP) steels have been widely used in automotive industry due to their excellent mechanical properties, such as high work-hardening rate and a good compromise between strength and ductility allowing high energy absorbing performance. In order to fully exploit the potential of DP steels and extend the application, the dual-phase microstructure has to be optimized for better combination of strength and formability that is characterized by uniform strain and/or fracture strain. As a starting point, detailed literature review is made on the microstructure development and mechanical properties of DP steels, and the key factors controlling microstructural features and determining mechanical properties are identified. Through experimental investigation, microstructures are developed in order to decouple the effects of various microstructural features, and the microstructure—mechanical properties relationship is systematically studied. Micromechanical modeling is used to further understand the experimental results within a quantitative framework, and to provide a support for microstructure refinement of DP steels by parametric study. Strategies of designing DP steels to fulfill specific forming operation have been proposed, and the concept of DP steels with graded martensite islands has been discussed with FEM analysis as a possibility of improving strength—formability trade-off.

Key words: dual-phase steels; phase transformation; formability; modeling; alloy design

Abstract

Résumé

Les aciers Dual-Phase sont largement utilisés dans le secteur de l'automobile en raison de leurs propriétés mécaniques remarquables et du bon compromis résistance ductilité qui lui donne d'intéressantes potentialités comme absorbeur d'énergie mécanique. Cependant, la recherche de bons compromis entre les propriétés mécaniques en traction et celles de formabilité nécessite une optimisation des paramètres microstructuraux. Ce travail de thèse s'inscrit dans cet optique. Dans une première partie, l'étude bibliographique proposée permet de mieux cerner les paramètres influençant la formation des microstructures ainsi que les propriétés des aciers DP. Dans une seconde partie, nous proposons un travail expérimental original permettant de mieux comprendre la formation des microstructures des aciers DP et de découpler l'effet de certains paramètres microstructuraux sur les propriétés de ces aciers. Enfin, la modélisation micromécanique proposée permet de compléter et d'interpréter les données expérimentales acquises. Ce travail ouvre des voies intéressantes de « design » des microstructures des aciers DP en vue de développer des aciers de nouvelles générations possédant des propriétés optimisées.

Mots clés: aciers dual-Phase; Transformation de phases; formabilité; modélisation; la conception d'alliages

Table of contents

Acknowledgements.....	I
Abstract.....	III
Résumé.....	V
Table of contents.....	1
List of symbols.....	5
Introduction.....	9
Chapter 1 Literature review of ferrite-martensite dual-phase steels: microstructure and mechanical properties.....	13
1.1 Dual-Phase microstructure formation during intercritical annealing.....	14
1.1.1 Reaustenitization from ferrite + carbide mixture.....	14
1.1.2 Reaustenitization from as-quenched martensite and cold-rolled martensite.....	18
1.1.3 Phase transformations during cooling.....	19
1.2 Mechanical properties of dual-phase steels.....	20
1.2.1 Mechanical characteristics of ferrite and martensite phases.....	20
1.2.2 Plastic properties of dual-phase steels.....	23
1.2.3 Damage and fracture of dual-phase steels.....	30
1.3 Summary.....	41
Chapter 2 Phase transformation and microstructure development: experiments and modeling.....	43
2.1 Materials and methodology.....	44
2.1.1 Materials processing.....	44
2.1.2 Microstructure characterization.....	44
2.1.3 Simulation of phase transformation.....	46
2.2 Investigation of the mechanisms of austenite formation.....	46
2.2.1 Re-austenitization from spheroidized microstructure.....	47
2.2.2 Re-austenitization from cold-rolled martensite.....	64
2.3 Microstructure development.....	68
2.3.1 On the influences of the volume fraction and composition of martensite.....	69
2.3.2 On the influence of microstructure refinement.....	73
2.4 Summary.....	79

Table of contents

Chapter 3 Plastic properties of dual phase steels: experimental investigation and qualitative discussion.....	81
3.1 Experimental procedures.....	82
3.2 Influence of martensite volume fraction on strength and ductility of dual-phase steels	82
3.2.1 Microstructures for comparison	82
3.2.2 Tensile behavior and work-hardening rate	84
3.2.3 Yield strength, tensile strength and uniform elongation	86
3.2.4 Brief discussion	88
3.3 Influence of martensite composition on strength and ductility of dual-phase steels	92
3.3.1 Yield strength, tensile strength, uniform elongation and strength-ductility product	92
3.3.2 Comparison between QT-700-37% and QT-740-35%: case of similar martensite volume fraction	95
3.3.3 Comparison between QT-700-28% and QT-740-35%: case of different martensite volume fractions but similar tensile strength	97
3.3.4 Brief discussion	98
3.4 Influence of microstructure refinement on strength and ductility of dual-phase steels	104
3.4.1 Tensile behavior of coarse-grained dual-phase steels (CG-DP) and ultrafine-grained dual-phase steels (UFG-DP)	105
3.4.2 Comparison between CG-DP-36% and UFG-DP-37%	106
3.4.3 Bonus of TRIP effect.....	107
3.4.4 Comparison of mechanical properties between CG- and UFG-DP	109
3.4.5 Brief discussion	112
3.5 Summary	117
Chapter 4 Damage and fracture of dual-phase steels: experimental investigation and qualitative discussion.....	119
4.1 Experimental procedure	120
4.1.1 Analysis of fracture surface.....	120
4.1.2 Damage observation and quantification of damage accumulation	120
4.1.3 Microhardness test	121
4.2 Influence of martensite volume fraction on damage and fracture	121

Table of contents

4.2.1	Effect of martensite volume fraction on damage accumulation.....	121
4.2.2	Effect of martensite volume fraction on fracture resistance	129
4.2.3	Brief discussion	132
4.3	Influence of martensite composition on damage and fracture.....	136
4.3.1	Effect of martensite composition on fracture strain	136
4.3.2	Effect of martensite composition on damage accumulation.....	137
4.3.3	Brief discussion	141
4.4	Influence of microstructure refinement on damage and fracture	143
4.4.1	Effect of microstructure refinement on fracture strain.....	143
4.4.2	Effect of microstructure refinement on damage and fracture: CG-DP-36% VS UFG-DP-37%	145
4.4.3	Effect of microstructure refinement on damage and fracture: UFG-DP-27% VS CG-DP-21%	153
4.4.4	Discussion	158
4.5	Summary	163
Chapter 5 Micromechanical modeling of plasticity and fracture of DP steels		165
5.1	Micromechanical model	166
5.1.1	Constitutive laws of the phases	166
5.1.2	Finite element unit cell model.....	167
5.2	Plastic properties of DP steels.....	169
5.2.1	Effect of martensite volume fraction on strength and ductility of DP steels	170
5.2.2	Effect of the martensite composition on the strength and ductility of DP steels: a parametric study	180
5.2.3	Effect of microstructure refinement on strength and ductility of DP steels	187
5.3	Fracture of DP steels	194
5.3.1	Description of fracture modeling.....	194
5.3.2	Effect of martensite volume fraction on fracture strain	197
5.3.3	Effect of martensite composition on fracture strain: a parametric study	201
5.3.4	Effect of microstructure refinement on fracture strain.....	204
5.4	Summary	208
Chapter 6 Microstructure optimization		211
6.1	Microstructure optimization for the balance between strength and	

Table of contents

formability.....	212
6.1.1 Predictions of mechanical properties	212
6.1.2 Microstructure optimization of DP steels	215
6.2 On the concept of graded martensite islands.....	218
6.3 Summary	221
Conclusions and perspectives	223
References.....	229
Appendix A: Pre-existing defects of cold-rolled martensite	241
Résumé étendu	243

List of symbols

Symbol	Description
AHSS	Advanced high strength steels
HSLA	High-strength low-alloy steels
DP	Dual-phase
TRIP	Transformation-induced-plasticity
TWIP	Twinning-induced-plasticity
Q&P	Quench-and-partitioning
STEM	Scanning transmission electron microscope
BCC	Body-centered cubic
FCC	Face-centered cubic
BCT	Body-centered tetragonal
α	Ferrite
γ	Austenite
α'	Martensite
V_m	Volume fraction of martensite
HV	Vickers' hardness
ECAP	Equal channel angular press
FEM	Finite Element Method
RVE	Representative volume element
DIC	Digital image correlation
SEM	Scanning electron microscope
SE	Secondary electron
BSE	Back scattered electron
TEM	Transmission electron microscope
EBSD	Electron back scatter diffraction

List of symbols

IPF	Inverse pole figure
IQ	Image quality
XRD	X-ray diffraction
EDX	Energy-dispersive X-ray spectroscopy
SIMS	Secondary ion mass spectrometry
APT	Atom probe tomography
\overline{L}_α	Mean free path of ferrite
\overline{L}_α'	Mean linear size of martensite
P_L	Intersections density between scanning line and interface
CSM	Continuous stiffness measurement
LE	Local equilibrium
LEP	Local equilibrium with partitioning
LENP	Local equilibrium with negligible partitioning
f_θ	Cementite volume fraction
f_γ	Austenite volume fraction
C_θ	Mean carbon content in cementite
C_γ	Mean carbon content in austenite
UFG-DP	Ultrafine-grained dual-phase steels
CG-DP	Coarse-grained dual-phase steels
QT	Spheroidized microstructure
QT-700	Annealing spheroidized microstructure at 700°C
GND	Geometrically necessary dislocation
μ	Shear modulus
M_s	Martensite-start temperature
ε_f	Fracture strain
A_0	Initial area
A_f	Area of the fracture surface
$\varepsilon_{thickness}$	Thickness strain

List of symbols

h_0	Initial thickness
h_f	Thickness after deformation
d_d	Mean distance between dimples
d_m	Mean distance between martensite islands
$\sigma_{y_0,\alpha'}$	Yield strength of martensite
$\sigma_{y,\alpha'}$	Flow stress of martensite
ε_p	Accumulated plastic strain
$k_{\alpha'}$	Hardening modulus of martensite
$n_{\alpha'}$	Hardening exponent of martensite
$C_{\alpha'}$	Carbon content in martensite
$\sigma_{y_0,\alpha}$	Yield strength of ferrite
$\sigma_{y,\alpha}$	Flow stress of ferrite
θ_{α}	Initial work hardening rate of ferrite
β	Dynamic recovery coefficient
σ_y^{tr}	The stress of transition from stage-III to stage-IV hardening
ε_p^{tr}	The strain of transition from stage-III to stage-IV hardening
θ_{IV}	Stage-IV hardening rate
SHA	Stacked hexagonal array
d	Radius of inclusion in the unit cell
L	Dimension of the unit cell
PEEQ	Equivalent plastic strain
$\sigma_{f,UFG}$	Flow stress of ultrafine-grained ferrite
$\sigma_{f,CG}$	Flow stress of coarse-grained ferrite
MPS	Maximum principal stress
R_x	Radial radius of void
R_{x0}	Initial radial radius of void
R_z	Void radius in the tensile (z) direction
β_H	A constant in the Rice-Tracey model

List of symbols

ε_{α}	Plastic strain in ferrite
T_{α}	Stress triaxiality in ferrite
σ_{macro}	Macroscopic stress of the unit cell
ε_{macro}	Macroscopic strain of the unit cell
$\sigma_{c,\alpha'}$	Fracture stress of martensite
$\varepsilon_{c,\alpha}$	Critical strain of ferrite related to martensite fracture
σ_n	The stress normal to the ligament between voids
σ_{α}	Yield stress of ferrite
δ	A parameter of strain hardening
n	Strain hardening exponent in a power law
W	Aspect ratio of voids
λ_0	Initial particle distribution parameter
χ	Relative void spacing
L_x	Half the distance between the voids
ε_n	Strain at necking
$R_{\alpha'}$	Average radius of martensite islands
$L_{\alpha'}$	Half spacing between martensite islands

Introduction

1 Industrial motivations

The developments of advanced high strength steels (AHSS) were essentially achieved due to the strong demands of automotive industry [1, 2]. Weight reduction and passenger safety improvement have become the main targets of the car manufacturers over the past decades. As analyzed in [2], the safety (or crash worthiness) and weight saving are both partly determined by the strength of the material, and thus AHSS can have better performance than low-strength steels. However, the main constraint is the formability that requires the steels to be formed into complex parts before finding applications, but the formability usually deteriorates with increasing strength.

Tremendous research efforts have been put into fulfilling various material requirements, resulting in the development of dual-phase (DP) steels [3-7], transformation-induced-plasticity (TRIP) steels [8, 9], twinning-induced-plasticity (TWIP) steels [10], quench-and-partitioning (Q&P) steels [11] and, most recently, medium-Mn steels [12-14]. Among these steel grades, DP steels are the most developed and widely used in the automotive industry. Their industrial production began in the 1990s [2]. An example of the application is shown in Figure 1 [15], highlighting the energy absorbing performance of DP steels.

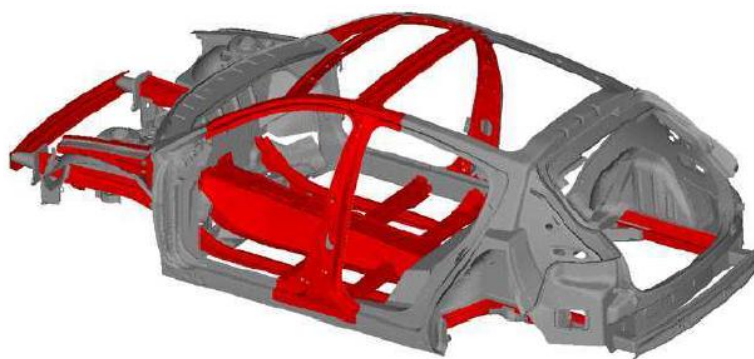


Figure 1. Parts of the automotive BIW (Body-in-white) made of DP steel grades [15].

2 Ferrite-martensite dual-phase steels

A ferrite-martensite DP steel is composed of two phases, namely a hard martensite phase embedded in a soft ferrite matrix phase. Other phases, such as retained austenite and bainite, are often present in smaller amount, depending on the alloy

Introduction

composition and processing routes. A typical DP microstructure is shown in Figure 2 [2]. This kind of microstructure is usually obtained by an intercritical annealing in the austenite-ferrite zone followed by a fast quenching.

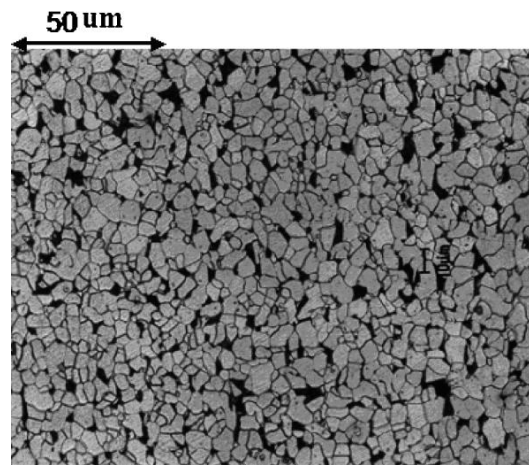


Figure 2. Typical microstructure of a dual-phase microstructure. Ferrite appears gray and martensite appears black. [2]

The DP steels are characterized by a low yield/tensile strength ratio of less than 0.5, high strain hardening, and good bake-hardening properties [1, 3]. The comparison with the mechanical properties of other steel grades is shown in Figure 3 [16]. DP steels exhibit better strength/total elongation balance than traditional HS steels. TRIP steels have higher performance than DP steels; but their cost is higher due to increased alloying element contents, and also the processing routes are less robust than for DP steels. In this sense, DP steels are still clearly competitive in automotive application.

Improving the balance between strength and formability is an important issue in extending the application of DP steels. The formability is characterized either by the uniform strain or fracture strain, depending on whether the forming operation is controlled by strain localization or fracture [2]. Both these properties are decreased with increasing strength, leading to a problem of finding the right trade-off as a function of the requirements of each specific component. For the optimization of DP steels, it is of primary importance to clarify the relationship between microstructure and strength, uniform elongation and fracture strain by well-designed experiments and micromechanical modeling. Only from there, it is possible to build a scientific-based design approach of DP microstructures with improved mechanical properties and fulfilling requirements for specific applications, which is the main target of this thesis.

Introduction

On the road to the well-nested microstructure-properties relationship of DP steels, several questions have to be answered, which remains the scientific challenges in steel metallurgy. Examples of such questions are:

- How does the strong but deformable martensite phase influence the plastic behavior of DP steels? Subsequently, how does the volume fraction of martensite determine the balance between strength and ductility?
- Does the martensite composition have an effect on the plastic properties of DP steels?
- Does the martensite composition affect the void nucleation and determine the fracture strain of DP steels?
- How does microstructure refinement influence the trade-off between strength and uniform elongation or fracture strain?

In this thesis, efforts are made to address these questions by revisiting literature and then by systematic experimental and modeling investigation.

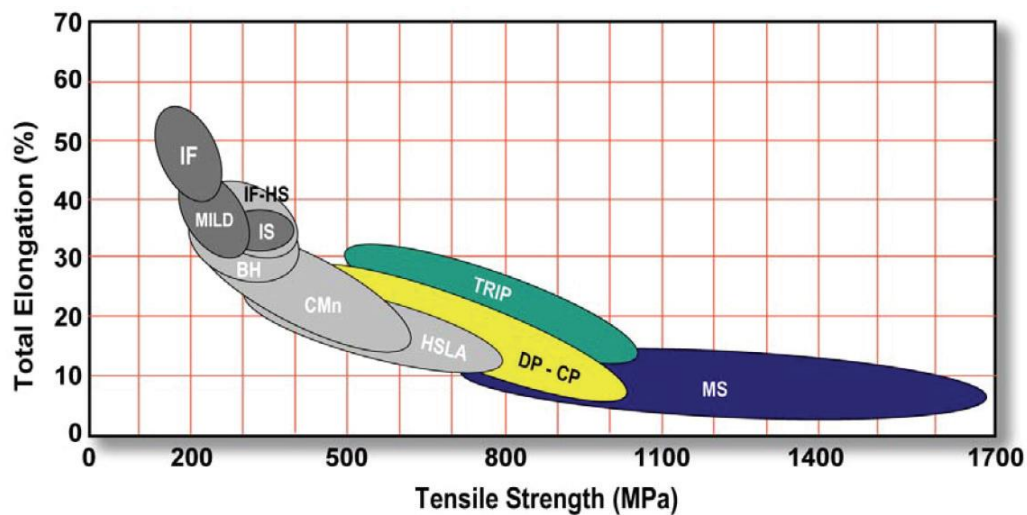


Figure 3. Schematic picture comparing the mechanical properties of AHSS with low-strength steels (dark grey) and traditional HS steels (grey) [16].

3 Outline of the thesis

The purpose of this work is to clarify the effects of microstructural features on plastic and fracture properties of DP steels and then to achieve microstructure optimization.

Introduction

In **chapter 1**, the key factors of microstructure control and mechanical properties of DP steels are identified by a detailed literature review, and the state-of-the-art understanding of the deformation and damage mechanisms is summarized. Based on these, the mechanism and kinetics of austenite formation in a model steel are studied, and the microstructures are developed to decouple the influences of various microstructural features in **chapter 2**. The effects of microstructural features on plastic and fracture properties are investigated experimentally in **chapter 3** and **chapter 4**, associated with qualitative discussion. Systematic micromechanical modeling is performed in **chapter 5** to rationalize the mechanical properties and experimental observations. Using the framework provided by micromechanical modeling, a parametric study is performed in **chapter 6**, proposing the guideline of optimizing the microstructure of DP steels for better balance between strength and formability. Figure 4 gives a summary of the approach followed throughout this work.

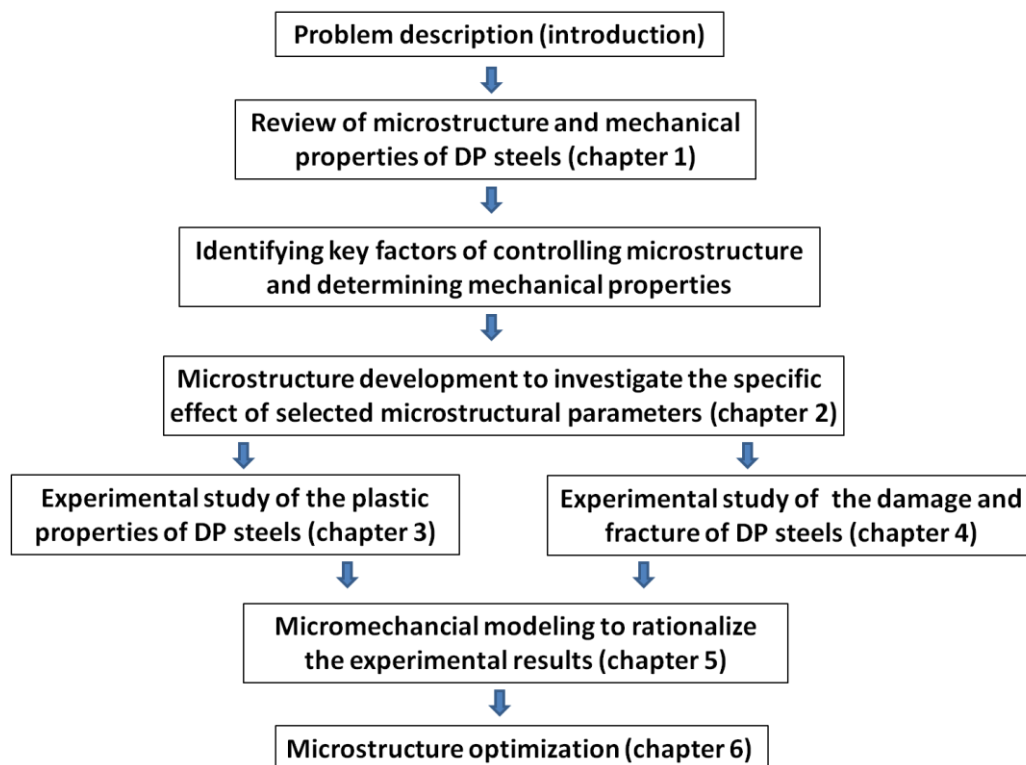


Figure 4. Outline of the thesis.

Chapter 1 Literature review of ferrite-martensite dual-phase steels: microstructure and mechanical properties

Improving the mechanical properties of ferrite-martensite dual-phase (DP) steels relies on the knowledge of the microstructure—properties relationship and the ability to control microstructure. The first part of this chapter aims at revealing the generation of DP microstructure during heat treatment and figuring out the important considerations in microstructure control. The second part is to thoroughly describe the microstructure—properties relationship and the mechanisms of plastic deformation and ductile fracture. Detailed survey is made on the key factors influencing the mechanical properties of DP steels.

1.1 Dual-Phase microstructure formation during intercritical annealing

Ferrite-martensite dual-phase microstructure can be developed by intercritical annealing and subsequent cooling. The typical heat treatment route is shown in Figure 1.1. During intercritical annealing, carbide spheroidization, austenite formation, recrystallization and grain growth of ferrite will occur and probably overlap with each other. Therefore, microstructure features such as ferrite grain size and martensite islands distribution, and also the element distribution are determined by processing parameters. In order to control the microstructure of DP steels and to optimize the mechanical properties, the fundamental understanding of microstructure evolution during intercritical annealing and of the effects of processing parameters becomes of importance. Large amount of knowledge has been accumulated and the main publications in this field are summarized as follows. This summary aims at offering the guideline to experiment design in this thesis.

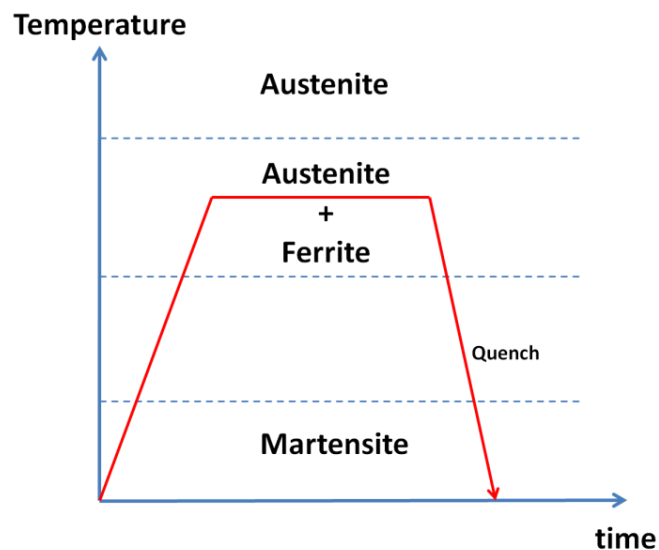


Figure 1.1. The processing route of intercritical annealing.

1.1.1 Reaustenitization from ferrite + carbide mixture

- **Austenite nucleation**

For the initial microstructure of ferrite + carbide mixture, austenite forms following carbide dissolution. It nucleates at ferrite/carbide interface [17], and the distribution

Chapter 1 Literature review

of carbides determines the distribution of martensite. Thermodynamically, the stability of carbide is determined by the enrichment of substitutional elements such as manganese [18], which influences the transformation starting temperature and kinetics of the transformation. It is also argued that austenite can form at ferrite grain boundaries without carbide but nucleate by carbon rejection from ferrite during heating [19].

Although the ferrite/carbide interface provides the favorable site for nucleation, it is only a necessary condition and the nucleation event is also influenced by other factors. In the pearlite— austenite transformation, nucleation of austenite occurred mainly at the pearlite colony boundaries and secondarily at ferrite/carbide boundaries within a pearlite colony [20, 21]. For the spheroidized microstructure, austenite preferentially forms at the carbides along the ferrite grain boundaries but not at the carbide particles within the ferrite grains [21-24]. The main difference between intergranular and intragranular carbides lies in the junctions between carbides and ferrite grain boundaries, and it is argued that the existence of such triple junctions can lower the energy barrier for austenite nucleation and promote austenite formation [17, 25]. This was observed in cold-rolled ferrite-pearlite steels during intercritical annealing [25]. For the intragranular carbides, it was observed that they were dissolved without austenite formation but served to supply the carbon to the austenite formed at ferrite grain boundaries [24]. However, it may not be true at higher annealing temperature because the nucleation barrier can be low enough that austenite may nucleate at the intragranular carbides.

● Growth of austenite

The austenite growth is controlled by the diffusion of carbon and/or substitutional elements. The tie-line for austenite growth depends on both the carbide dissolution and the austenite growth process.

For Fe-C-Mn steels, the driving force for cementite dissolution and the growth of austenite have been investigated and the role of Mn is essential [18]. Mn enrichment in cementite retards the austenite transformation. Based on thermodynamic and kinetic considerations, a criterion for the change between fast and slow regime of cementite dissolution has been proposed in ref [18], which outlines the effect of Mn enrichment and annealing temperature on austenite growth.

Chapter 1 Literature review

For ferrite + pearlite initial microstructure [17, 26], austenite growth can be separated into three stages: (1) very rapid growth of austenite into pearlite until pearlite dissolution is complete; (2) slower growth of austenite into ferrite at a rate that is controlled by carbon diffusion in austenite at high temperatures and by Mn diffusion in ferrite at low temperatures; and (3) very slow final equilibration of ferrite and austenite at a rate controlled by Mn diffusion in austenite. The step in which the austenite growth is controlled by the carbon diffusion is of the order of a few seconds and the subsequent growth of austenite is determined by the partitioning of the alloying elements [27]. The partitioning of Mn was observed experimentally by STEM (scanning transmission electron microscopy) (see Figure 1.2) [27].

For cold-rolled steels, the carbide dissolution and austenite formation would be more complicated, because phase transformations can overlap with ferrite recrystallization [21, 22].

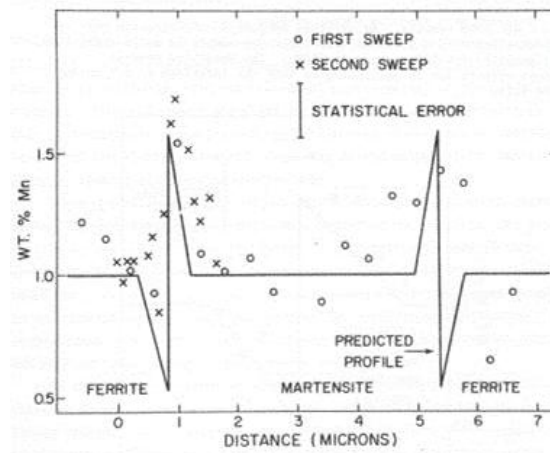


Figure 1.2. An observed manganese concentration profile is shown along with a predicted profile. The sample is an Fe-0.08%C-1%Mn steel annealed for 500 seconds at 750°C. The predicted profile neglects the effects due to sectioning so that the interface is not normal to the foil. [27]

● Interaction between ferrite recrystallization and austenite formation in cold-rolled ferrite + pearlite steels

Cold-rolled ferrite + pearlite mixture is a common initial structure for DP steels. In continuous annealing, several processes, including pearlite spheroidization, ferrite recrystallization, and austenite formation, will occur concurrently. The interaction between them varies with the processing parameters and can result in various microstructures. Several publications [17, 21, 22, 28-34] have been devoted to this

Chapter 1 Literature review

topic, which constitutes the framework of interpretation.

The interaction between ferrite recrystallization and austenite formation is rather complicated. The rationalization requires a good modeling of ferrite recrystallization and the fundamental understanding of nucleation and growth of austenite. Austenite prefers to nucleate at the carbides on ferrite grain boundaries, and the recrystallization of ferrite modifies the position of carbides and thus manipulates the nucleation site, which is one of the origins of the interaction [28]. Secondly, the austenite growth depends on the diffusion in ferrite matrix, both in the aspects of diffusivity and diffusion length, which are also related to the ferrite recrystallization [28, 33]. Additionally, the effect of heating rate has to be taken into account. It influences both the tie-line for phase transformation [28, 32], the occurrence of ferrite recrystallization [21, 28-30] and pearlite spheroidization [21]. Increasing the heating rate can delay the occurrence of ferrite recrystallization, enhancing the interaction with austenite formation [25]. Also, the austenite growth shows very different behavior at high heating rate ($>100^{\circ}\text{C/s}$) [21, 28], which cannot be well interpreted yet.

The overlapping between ferrite recrystallization and austenite formation depends on the A_{c1} temperature, cold reduction and heating rate. The possible microstructures are summarized in Figure 1.3 [28]. With low heating rate, ferrite will recrystallize before austenite formation, leading to random distribution of austenite and more equiaxed microstructure; while with high heating rate, the ferrite recrystallization is delayed, and the austenite will inherit the position and shape of the elongated pearlite, resulting in the banded microstructure. Such microstructure generation processes have been well simulated with a cellular automaton model [33].

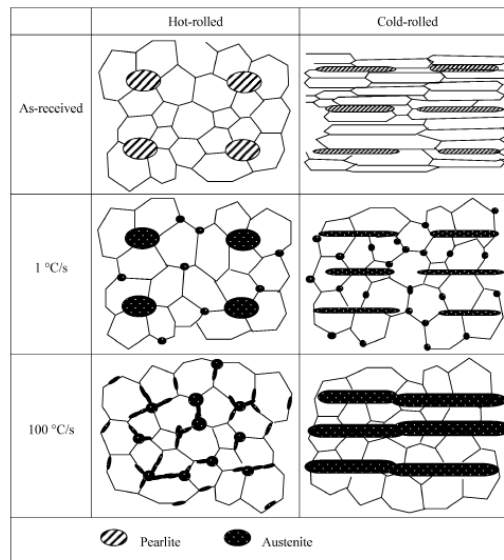


Figure 1.3. Schematic illustration of the microstructure evolution of cold-rolled Fe-C-Mn-Mo steel annealed with different heating rates to holding temperature [28].

1.1.2 Reaustenitization from as-quenched martensite and cold-rolled martensite

During intercritical annealing, the as-quenched martensite experiences carbide precipitation, recovery of martensitic ferrite and austenite formation. Usually, recrystallization should not occur in low-carbon martensitic steels [35]. The as-formed dual-phase microstructure has the acicular morphology (see in Figure 1.4) [17]. Considering the strong driving force for carbide precipitation during heating, the initial microstructure of as-quenched martensite normally should be treated as the ferrite + carbide mixture in the study of reaustenitization.

As to the cold-rolled martensite, ferrite recrystallization will occur during intercritical annealing, depending on the heating rate and cold reduction [36], and the kinetics is faster than cold-rolled ferrite + pearlite mixture [25]. Thus, the DP microstructure is determined by the competition between ferrite recrystallization and austenite formation [25], but the influence of carbide precipitation is still not clear yet. Figure 1.5 shows the effect of cold reduction and heating rate on the resulting DP microstructure [29]. Large cold reduction and high heating rate favor the microstructure refinement of DP steels.

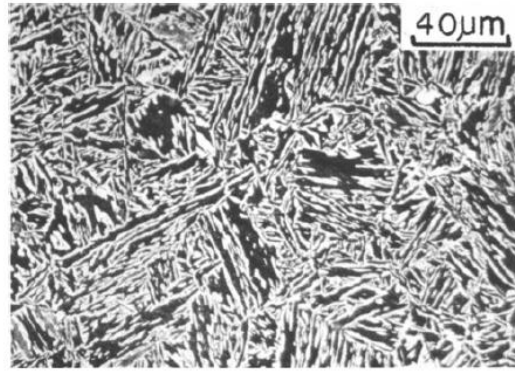


Figure 1.4. DP microstructure developed from the as-quenched martensite [17].

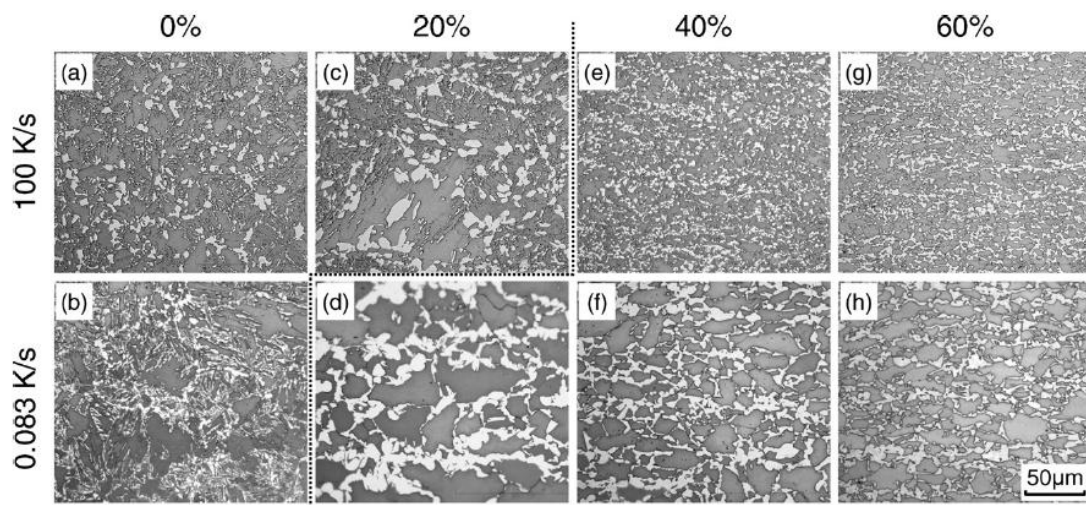


Figure 1.5. Optical micrographs of DP structures formed by partial reversion of cold-rolled martensite under different conditions of rolling reduction and heating rates [29].

1.1.3 Phase transformations during cooling

The microstructure of DP steels is not solely determined by austenite formation during intercritical annealing but also by the phase transformations during cooling. Several possible transformations can occur during cooling, including epitaxial ferrite growth, bainite and martensite transformations.

Austenite—ferrite transformation can occur at the temperature below intercritical range. Because the ferrite already pre-exists, the transformation can proceed by epitaxial growth of this “old” ferrite into austenite with no nucleation step required

[4, 37].

As the temperature decreases to intermediate range, bainite can form in austenite phase by temper aging or slow cooling. The austenite transforms to martensite when the temperature is below M_s , resulting in the plastic deformation and residual stresses in the surrounding ferrite [4]. The martensitic transformation is not complete and retained austenite is generally present in the DP steels in amounts varying from 2 to 9 percents [4].

The occurrence of these transformations depends on the cooling rate and the hardenability of austenite. With a high cooling rate, for instance by water-quenching, epitaxial ferrite and bainite formations can be suppressed and the DP microstructure is only controlled by martensitic transformation. Hardenability of austenite has the equivalent effect of heating rate, which can delay ferrite and bainite formation during cooling. The hardenability of austenite can be enhanced by high carbon content and Mn enrichment [4]. Additionally, the average Mn content of steel alloys can be essential to the mobility of austenite/ferrite interface and thus to the microstructure evolution during cooling. In a medium-Mn steel [38], the austenite—ferrite transformation is so slow that there is little ferrite formation even after a lengthy annealing time.

1.2 Mechanical properties of dual-phase steels

1.2.1 Mechanical characteristics of ferrite and martensite phases

1.2.1.1 Ferrite

BCC ferrite (α) is an allotrope of iron that is stable at low temperature. At room temperature, ferrite has very low solubility of interstitial elements (see Table 1.1 [35]). Thus, interstitial solid solution is not an important strengthening mechanism for ferrite in commercial steels. However, a minute amount of carbon can induce the strain aging in ferrite, resulting in the yield point phenomenon and discontinuous yielding [35]. Typical tensile curve of ferrite presenting yield point phenomenon can be seen in Figure 1.6 [35]. The operating strengthening mechanisms in ferrite include

Chapter 1 Literature review

work hardening, substitutional solid solution, grain size and precipitation strengthening.

	Temperature (°C)	Solubility	
		wt%	at%
C in γ -iron	1150	2.04	8.8
	723	0.80	3.6
C in α -iron	723	0.02	0.095
	20	<0.00005	<0.00012
N in γ -iron	650	2.8	10.3
	590	2.35	8.75
N in α -iron	590	0.10	0.40
	20	<0.0001	<0.0004

Table 1.1. Solubilities of carbon and nitrogen in FCC (γ) and BCC (α) iron [35].

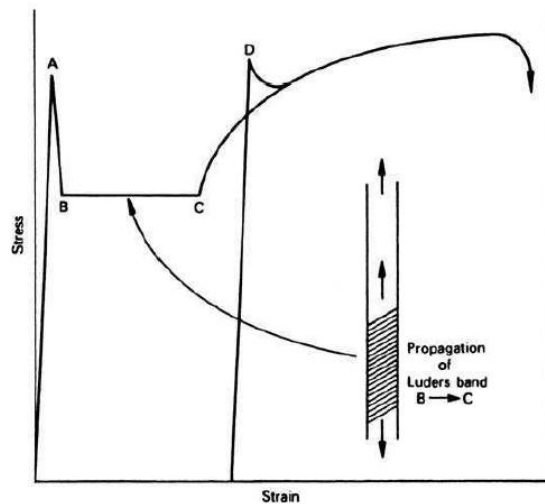


Figure 1.6. Typical tensile curve of ferrite presenting yield point phenomenon [35].

1.2.1.2 Martensite

The quenching of austenite to room temperature leads to the formation of martensite through a diffusionless, shear mechanism [35]. The martensite is supersaturated with carbon due to the diffusionless transformation. This supersaturation can change the structure of martensite from Body-Centred Cubic (BCC) to Body-Centred Tetragonal (BCT) when the carbon content is high [35].

Chapter 1 Literature review

The microstructure of martensite is determined by the composition [35, 39]. For plain carbon and low-alloyed steels with up to about 0.5wt% carbon, the morphology is lath-like, and the laths are grouped together with low angle boundaries between each lath. As the carbon content is increased, plate martensite is found, which is heavily twinned.

There are several possible strengthening mechanisms for martensite due to the complex structure, including solid solution, dislocation strengthening and grain size. The initial work-hardening rate of martensite is too high for a single-phase material and should be attributed to a composite behavior [40]. The strengthening mechanism depends on the alloy system and testing condition. For the martensitic steels (Fe-Ni-C alloys) with M_s far below room temperature, carbon atom aging is prevented and the martensite is strengthened by interstitial solid-solution [39]. In the steels with above-room-temperature M_s temperatures, carbon atoms are probed to segregate in the dislocations and lath boundaries even under as-quenched condition, as shown in Figure 1.7 [41]. Strengthening of martensite becomes dependent on static and dynamic strain aging and the strength of martensite can be significantly increased by increasing carbon content [40].

Substitutional solid solution is reported to be a negligible contribution in the hardness of as-quenched martensite [42]. But the recent results in [43] show that manganese increases strength and strain hardening of martensite in synergy with carbon and this effect is observed in the medium-Mn steels.

Martensite is a hard phase and it is much less ductile than ferrite. The brittleness of martensite is enhanced with increased carbon content. As reported in [44], a martensitic steel with 0.4wt% carbon even breaks before necking in tensile test. For commercial martensitic steels, tempering is important to adjust the balance between strength and ductility. A good strength/ductility balance can also be achieved by other methods, and a recent investigation shows that moderate decarburization of the martensitic steels can improve the ductility without sacrificing strength [44].

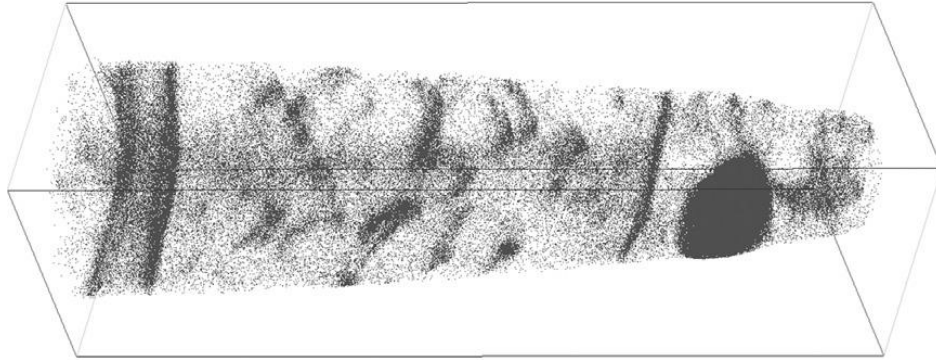


Figure 1.7. APT mapping of C atoms in the as-quenched steel with 0.23wt% of C [41].

1.2.2 Plastic properties of dual-phase steels

1.2.2.1 Initial plastic deformation

- **Continuous yielding**

Conventional high-strength low-alloy (HSLA) steels present discontinuous yielding, which leads to Lüders bands during forming. This discontinuous yielding is due to strain aging, and the origin is the segregation of interstitial atoms at dislocations and the formation of Cottrell atmospheres [35]. In this aspect, it should be the intrinsic characteristics of interstitial-containing alloys.

However, ferrite-martensite dual-phase steels show very interesting behavior in the initial deformation (see in Fig1.8 [3]): low yield stress, continuous yielding and high work-hardening rate. These three points are inter-related.

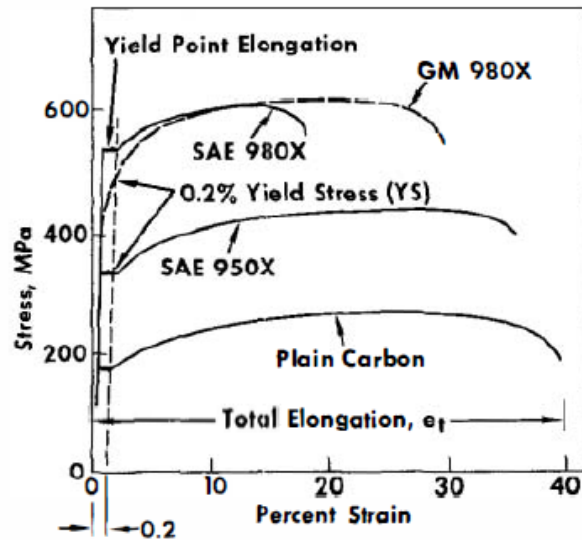


Figure 1.8. Schematic stress-strain curves for plain carbon, HSLA, and dual-phase steels. SAE 950X and 980X are Society of Automotive Engineers designations for HSLA steels of different strength levels. GM 980X is a General Motors developed dual-phase steel. GM 980X is more ductile than SAE 980X although both steels have similar tensile strength. [3]

There are several explanations to the low yield stress and continuous yielding. One is based on the large density of mobile dislocations in ferrite around the martensite islands (see in Figure 1.9 [45]). These dislocations are produced for accommodating the strain of martensitic transformation, and can move at low applied stress.

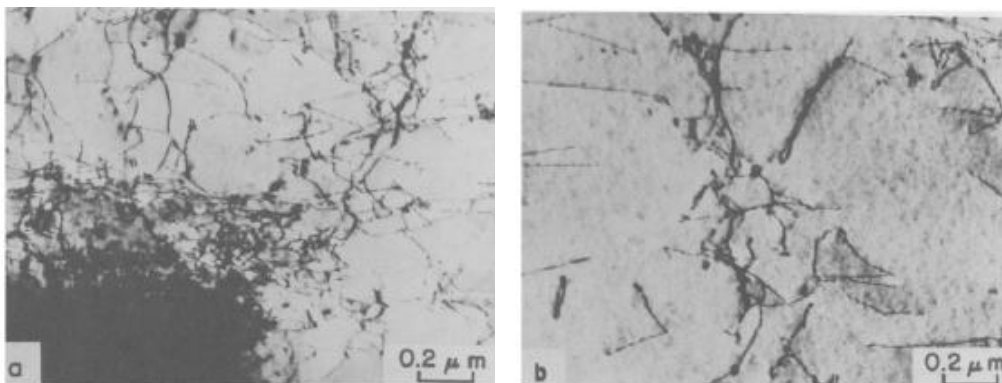


Figure 1.9. Typical dislocation structures observed in a single ferrite grain of the as-produced C-Mn-Si dual-phase steel; (a) high dislocation density adjacent to martensite and (b) lower dislocation density away from martensite. [45]

Another explanation is that the continuous yielding and low yield stress arise from the internal stress set up in the ferrite phase owing to the martensite transformation.

Chapter 1 Literature review

A distribution of this internal stress can build up preferentially yielding zones around the martensite islands [47]. Thus the initial yielding begins simultaneously from these zones under a low applied stress compared to the normal yield strength of ferrite. As the applied stress increases, the yield zones spread until the ferrite yields all over, which is a continuous process.

- **High initial work-hardening rate**

Within a small plastic strain, the work hardening in DP steels is exceptionally large (see Figure 1.10 [6]). An early investigation [48] attributed this to the back stress resulted from the plastic compatibility between ferritic and non-ferritic regions. However, Sarosiek and Owen [49] proposed that it is due to the heterogeneous nature of the plastic flow in ferrite, leading to large Bauschinger stress. The dislocation density in ferrite is not homogeneous due to the transformation-induced strain, and deformation onsets from ferrite regions with less dislocations. They also proposed that the mean long-range stress in the ferrite only makes a significant contribution to hardening at large strain.

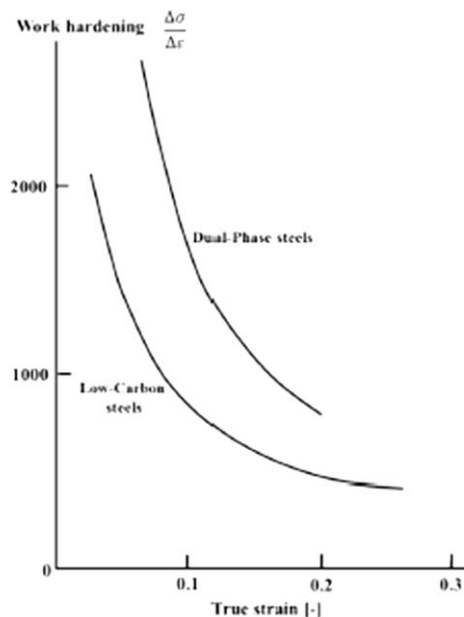


Figure 1.10. Strain hardening as a function of strain for both dual-phase steels and low-carbon steels [6].

1.2.2.2 Strength and ductility of dual-phase steels

The strength and ductility of DP steels are usually investigated by uniaxial tensile test, which is the simplest case and is the starting point for complex loading condition. The information of work-hardening that integrates the kinematic and isotropic contributions, onset of necking and tensile strength can be extracted from the tensile curve.

During plastic flow, ferrite yields first at some preferential zones, and the strain spreads to the over-all matrix. The martensite yields after ferrite; or it might crack without plastic deformation, considering the brittleness. Significant deformation incompatibility can be built up between ferrite and martensite, which is the key for load transfer and the generation of back stress. The back stress is essential to the work-hardening of composite microstructure [50], determining tensile strength and uniform elongation. In summary, the strength and ductility of DP steels are influenced by the properties of constituent phases, the phase fraction, the morphology and the interaction between phases. The roles of these key factors are surveyed as follows.

- **Effect of volume fraction of martensite**

Martensite phase acts as the reinforcement in DP microstructure. The martensitic transformation during quenching introduces accommodation dislocations in the surrounding ferrite matrix. Thus, the volume fraction of martensite (V_m) is essential to understand the plastic behavior of DP steels [5, 49, 51-57]. With the increasing V_m , the discontinuous yielding disappears, and the tensile curve is modified dramatically [52]. It is reported [5, 49, 53, 54, 57, 58] that the tensile strength and yield strength have linear relationship with V_m , which can be described by the rule of mixture. Strength is increased with increasing V_m but the martensite volume fraction has larger influence on the tensile strength than the yield strength (see Figure 1.11 [53]) except when the carbon content in martensite is low [57]. On the contrary to the trend of strength, the uniform elongation is decreased with increasing V_m . However, in some studies [51, 55], obvious deviation of the linear relationship between strength and V_m can be observed, and the uniform strain is not decreased with V_m monotonically.

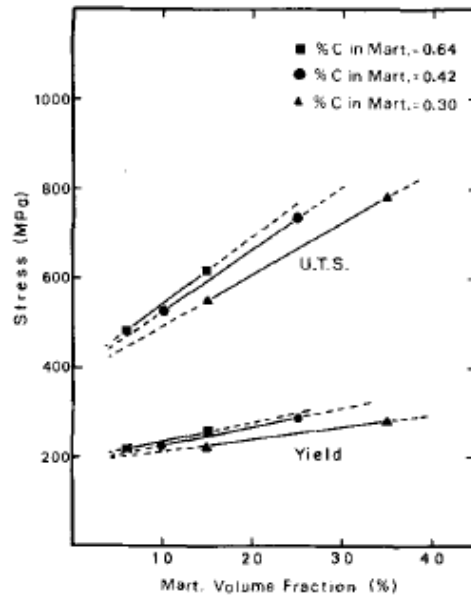


Figure 1.11. Yield and tensile strengths as a function of martensite volume fraction for Fe-C-Mn-Si steels with different martensite carbon contents [53].

● Effect of martensite composition

The effect of martensite composition has received less attention than the effect of martensite volume fraction, and the interpretation is still controversial [5, 52, 53, 59]. Davis [5] has drawn the conclusion from the statistical data that the strength of dual-phase steels is dependent on the ferrite grain size and the volume fraction of martensite but is independent on the composition and strength of the martensite. Ramos [53] and Speich [52] have used similar experiment design and the results show that the tensile strength is increased with increasing carbon content in martensite but the uniform elongation exhibits an opposite trend (Figure 1.12 [53]). In the systematic work of Piermen [59], where the fibrous dual-phase microstructures have been investigated, tensile strength is increased with carbon content in martensite. But the conclusion on uniform elongation depends on the martensite volume fraction. For 60% of martensite, a decrease in martensite carbon content leads to an improvement of uniform strain, which is different with the martensite volume fraction of 15% and 30%.

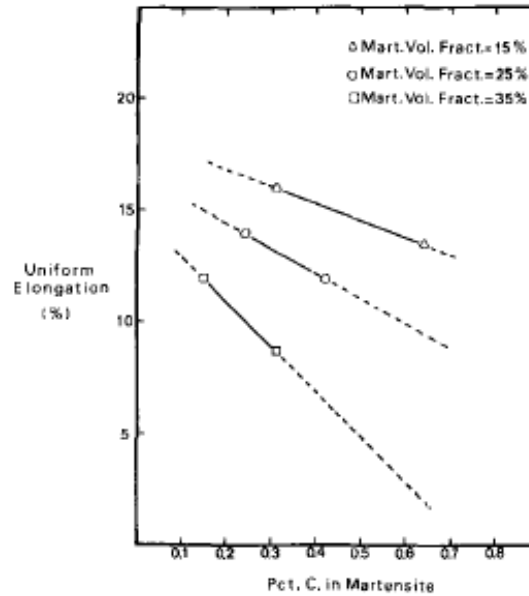


Figure 1.12. Uniform elongation as a function of carbon content in martensite for Fe-C-Mn-Si steels with various martensite volume fractions [53].

● **Effect of ferrite grain size**

In commercial DP steels, the ferrite matrix occupied the volume fraction of 65~75 percents. Thus the properties of ferrite matrix strongly influence the mechanical behavior of DP microstructure.

By decreasing the ferrite grain size, both the yield strength and tensile strength of DP steels can be increased but the yield ratio is decreased because of the stronger ferrite grain size dependence of yield strength than tensile strength (see ref [56]).

But it is also reported that refining ferrite grain size only increases the flow stress and raises the strain hardening rate at small strain, but the effect on strain hardening at large strain is limited [60].

Recently, microstructure refinement of DP steels has raised broad attentions [61-66]. One of the interesting points is to overcome the lack of work-hardenability of ultrafine-grained single-phase metals with a composite structure. Techniques have been developed for fabricating ultrafine-grained DP (UFG-DP) steels, combing severe plastic deformation, such as Equal Channel Angular Pressing (ECAP) [62] and large strain warm rolling [63], and flash heat treatment. The mechanical properties reveal that microstructure refinement of DP steels can result in improved strength without

sacrificing the ductility. In some cases, the refined DP steels even have simultaneously enhanced tensile strength and uniform elongation [63]. The synergic effect of microstructure refinement and martensite strengthening is to be clarified.

- **Effect of morphology of dual-phase microstructure**

Morphology is a complex factor, including the influences of grain size, connectivity and so on. The effect of morphology on strength and ductility of DP steels reported in the literature is somehow contradictory.

It is reported that the strength of DP steels is independent on morphology, but the equiaxed or short-fibrous DP microstructures have superior uniform elongation [7, 57, 67]. The improved ductility was attributed to the lower connectivity of martensite in short-fibrous DP steels [7, 59]. A lower connectivity of martensite results in a less constrained plasticity of ferrite, which acts to increase uniform elongation; also, it can lead to less efficient load transfer, delaying the deformation or failure in martensite [59].

The DP steels with long and well-oriented martensite fibers were reported to have higher strength but lower ductility [68, 69]. These long martensite fibers are parallel to the rolling direction, and have high efficiency of load transfer. The efficient load transfer increases the strength but promotes the fracture of martensite phase.

1.2.2.3 Micromechanical modeling of plastic behavior of DP steels

Various modeling works [46, 57, 70-84] have been devoted to simulating the flow behavior of DP steels, and to understanding the effects of microstructural features. The models, either analytical or numerical, can also work as materials designing tools, accelerating the product development.

Models based on dislocation theory are analytical [73, 74]. They are capturing the microstructure heterogeneity of DP steels and the resulting plastic strain gradient. The increment of work-hardening rate is attributed to the back stress from strong martensite. These models can rationalize the influences of ferrite grain size, and

martensite volume fraction on the plastic properties of DP steels. But the martensite phase is assumed to be undeformable, and thus the influence of martensite composition cannot be studied with these models. Furthermore, these analytical models cannot provide the information of stress/strain state of phases, and cannot be incorporated into the fracture model.

Mean-field homogenization models [57, 76, 77, 80] have been developed to calculate the macroscopic and microscopic response of DP steels. Stress and strain partitioning between the matrix and reinforcement can be computed and the effect of internal stress can be captured. Additionally, the plasticity of martensite phase is taken into account, and the influence of martensite composition can be simulated. The calculated phase response (stress and strain) can be incorporated into the fracture model.

Finite Element Method (FEM) analysis is often carried out to simulate the flow behavior of DP steels, concerning the stress/strain distribution, the interaction between matrix and reinforcement and the influences of microstructural features [46, 70, 71, 78, 79, 81-84]. The predictive capacity of the model is determined by the selection of Representative Volume Element (RVE), the constitutive laws of phases and the boundary conditions. To reduce the computational cost, unit cell with periodic boundary conditions has been used for micromechanical modeling, and it is reported to work reasonably well in simulating the tensile behavior of DP steels [46, 71, 79, 81]. However, the RVE generated from the real microstructure has the advantages in revealing the effect of morphology and the onset of strain localization, which is important to the failure analysis [83, 84].

1.2.3 Damage and fracture of dual-phase steels

1.2.3.1 Damage and fracture mechanisms of DP steels

- **Global map of damage accumulation in dual-phase steels**

A lot of investigations have been devoted to understanding the damage mechanisms of dual-phase steels [54, 57, 85-97] in the aspects of the nucleation, growth and coalescence of voids. A global image of the damaged specimen is shown in Figure 1.13 [90]. Voids have been formed outside the necking zone. With increasing strain,

Chapter 1 Literature review

the number of voids increased and the voids grow longitudinally along the ferrite grain boundaries and parallel to the tensile direction. As approaching to the fracture surface, the stress state became triaxial due to necking and void density was enormous; dramatic strain localization can be observed, accompanying with the void linkage. A 3D representation of the population and distribution of voids inside the deforming sample in its initial stage and just before fracture is shown in Figure 1.14 [95]. The distribution of voids is not homogeneous but is concentrated in the middle of the necking zone.

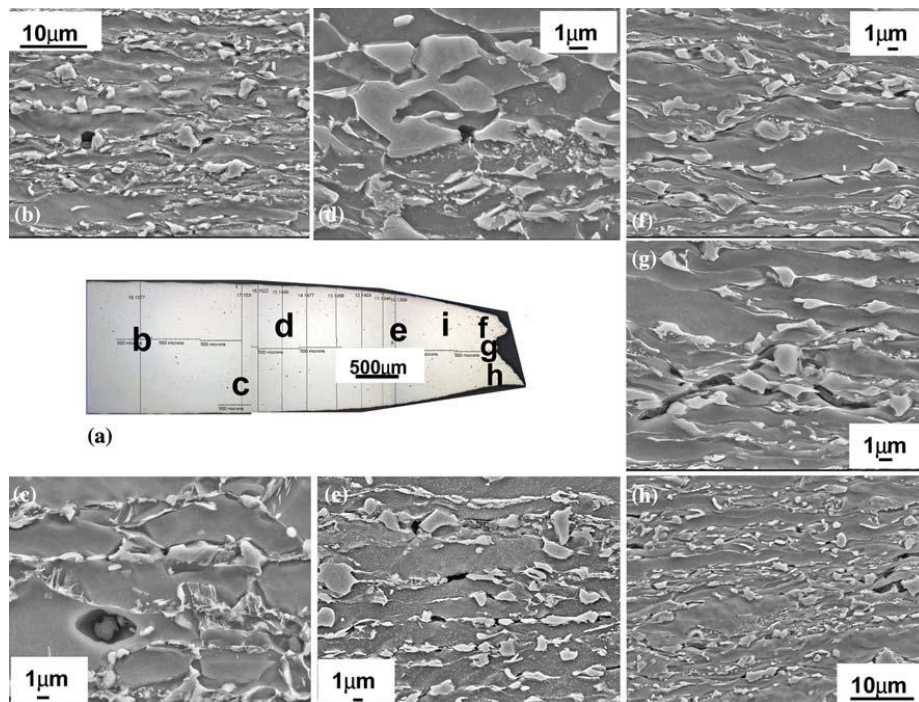


Figure 1.13. SEM micrographs of broken tensile specimen indicating void formation. (a) Central insert shows approximate locations of examined areas. Voids are formed at various thickness strains: (b) 0.13, (c) 0.16, (d) 0.18, (e) 0.52, (f) 0.75, (g) 0.76, and (h) 0.70. [90]

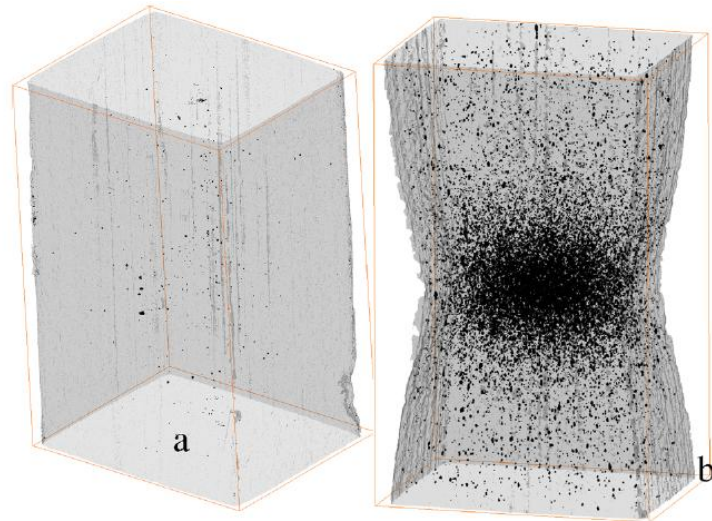


Figure 1.14. Three-dimensional representation of the population of cavities inside the deforming sample in its initial stage (a) and just before fracture (b). The perspective view makes the insertion of a scale bar inappropriate. The dimension of the reconstructed block is $1 \times 1 \times 1.5$ mm. [95]

● Void nucleation

Damage nucleation is the first step of ductile fracture. Several mechanisms have been observed for damage nucleation in dual-phase steels. One important mechanism is the decohesion at ferrite/martensite phase boundary (see Figure 1.15 [93]), which is due to the plastic incompatibility and the resulting high normal stress at the interface.

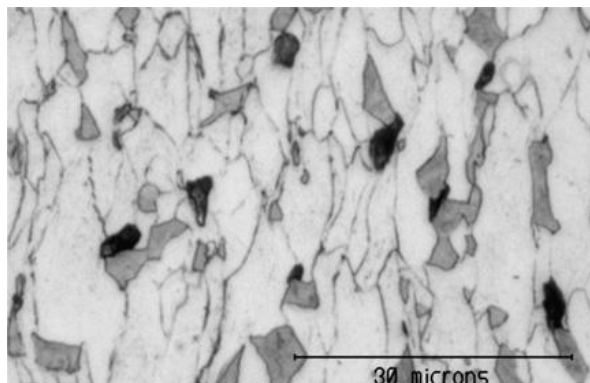


Figure 1.15. A micrograph showing the damage nucleated by interface decohesion [93].

Another important mechanism for damage nucleation is martensite fracture. When the yield stress is reached, plastic deformation of martensite is onset until fracture.

Chapter 1 Literature review

Martensite is reported to fracture either in a brittle or ductile manner [57, 88, 92]. The martensite breaks in a brittle manner when the carbon content is high; but if the carbon content is low, fracture can occur after substantial plastic strain (Figure 1.16 [57]).

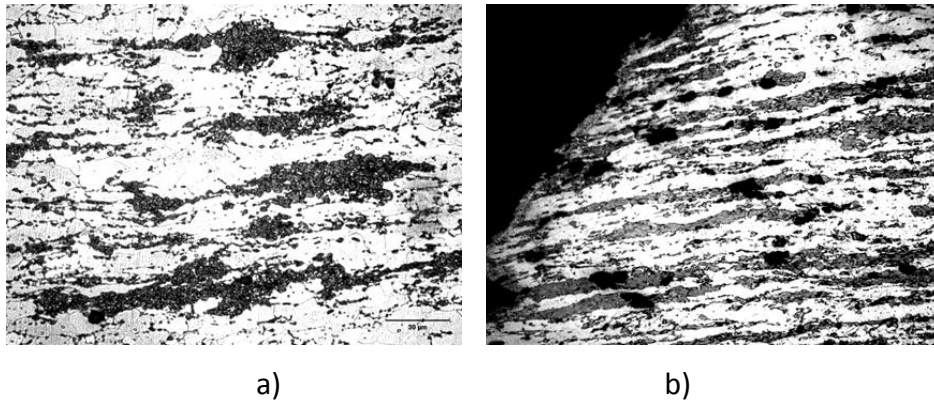


Figure 1.16. Optical micrographs for a dual-phase steel with 41 pct martensite for different levels of far-field deformations: (a) undeformed, and (b) tensile strain of 0.59. Note: both tensile loading and rolling directions are horizontal. [57]

The fracture initiation in martensite also relates to the deformation mode. The martensite islands can deform in tensile, shear or bending mode, according to their configuration with respect to the loading direction, the morphology and deformation state of the surrounding ferrite grains [92]. As shown in Figure 1.17a, the martensite island mainly deforms in a tensile mode. Local necking occurs and micro-crack initiates in the narrow central region. In Figure 1.17b, the bending mode imposed on the martensite phase results in crack initiation from the boundary of the island in a direction perpendicular to the local principal loading direction.

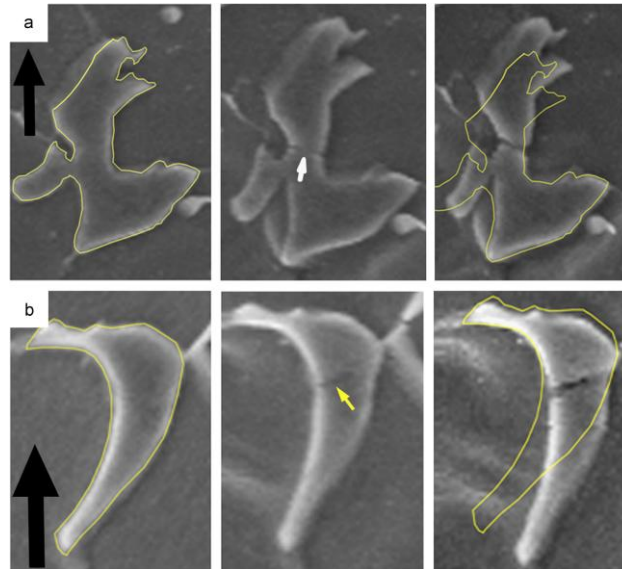


Figure 1.17. Micro-crack initiation within the martensite islands due to (a) tensile deformation and necking and (b) local bending. The vertical arrows show the loading direction. [92]

The damage nucleation is a continuous process, which lasts over most of the deformation [86, 90, 93, 95]. As seen in Figure 1.18 [93], the void density increases with strain first slowly and then dramatically at large strain (above 0.4) due to the triaxial tensile stress at the necking zone.

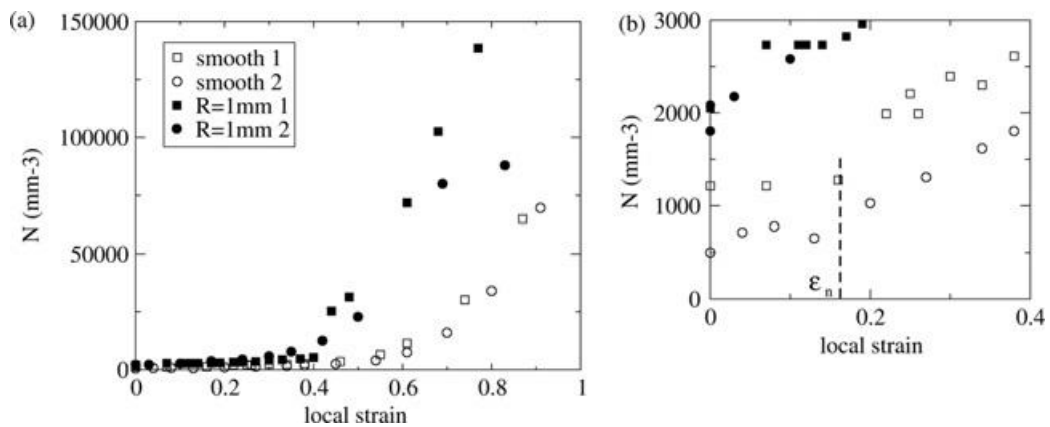


Figure 1.18. Evolution of N , the number of voids per cubic mm, in the four studied samples measured during the in-situ tensile tests. (a) Global view; (b) focus on the low strain region of (a). [93]

- **Void growth**

Due to the difficulties in tracing the growth of individual voids, the damage growth is usually described indirectly by the evolution of void area and density with strain.

Chapter 1 Literature review

Using 2-D metallographic technique, some recent publications [90, 98] reported the evolution of both the void area and average void size with deformation. The void area increased continuously but the average void size kept nearly constant except at small strain. The constant average void size is a result of continuous damage nucleation.

The development of X-ray micro-tomography provides opportunities to revisit the problems of damage growth, due to the capability of tracing the dimension, shape of individual voids with strain. Landron [85] has done very systematic characterization of void growth with this tool. In Figure 1.19, although the average void diameter for the selected individual voids, the 20 largest voids and the 50 largest voids are increasing with strain, the average size of the entire void population remains almost constant because of the nucleation of new porosities. And it is found that the voids are elongated under tensile loading (seen in Figure 1.20). The significant influence of stress triaxiality on void growth has also been checked in the tensile specimens with different notch radii as shown in Figure 1.21.

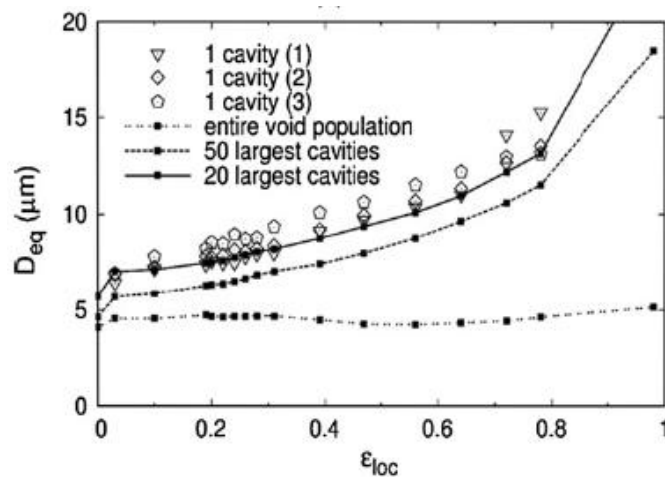


Figure 1.19. Evolution of the average void diameter for different numbers of examined cavities: 1, the 20 largest, the 50 largest and the entire population [85].

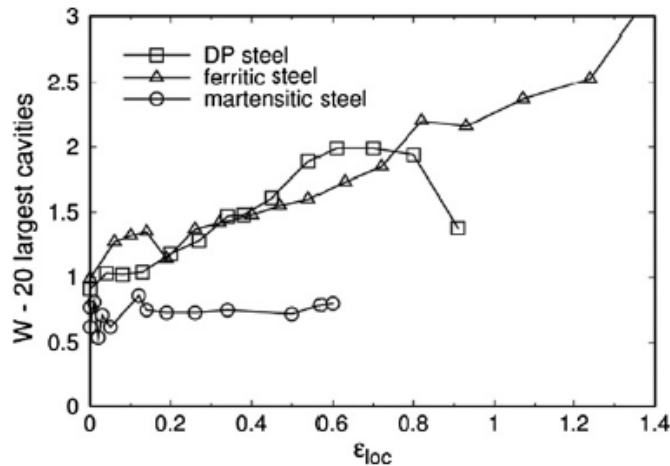


Figure 1.20. Evolution of the aspect ratio of the 20 largest cavities in smooth specimens of DP, ferritic and martensitic steels [85].

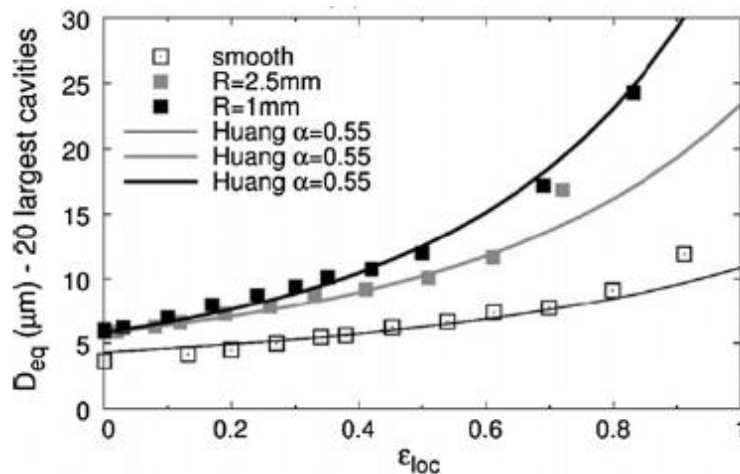


Figure 1.21. Effect of stress triaxiality on growth of voids [85].

● **Void coalescence and fracture**

Void coalescence is the third stage of damage accumulation, leading to the final fracture of ductile materials. The stage of void coalescence only contribute negligibly to the fracture strain, thus the prediction of its onset can be approximated as an estimation of fracture strain [99]. According to the experimental observations, there are three modes of coalescence, depending on the orientation of the coalescing voids [99]: necking of the internal ligaments between voids when the voids are located at 90 degrees to the tensile direction; localization of shear bands when the voids are located at 45 degrees; “necklace” coalescence when the voids are located at 0 degree.

Chapter 1 Literature review

Typical void coalescence due to shear localization (Figure 1.22 [98]) and as a necklace (Figure 1.23 [100]) can be observed in DP steels, and normally they co-exist in damage accumulation. The individual event strongly depends on the size and distribution of martensite, and has been tested by X-ray tomography that the Thomason criterion can be adapted to predict the local coalescence [94].

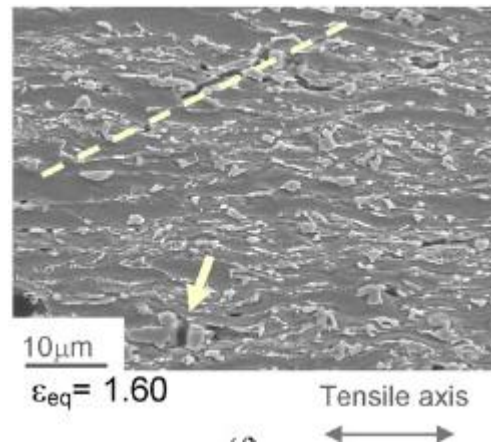


Figure 1.22. Coalescence of voids by shear localization close to fracture surface [98].

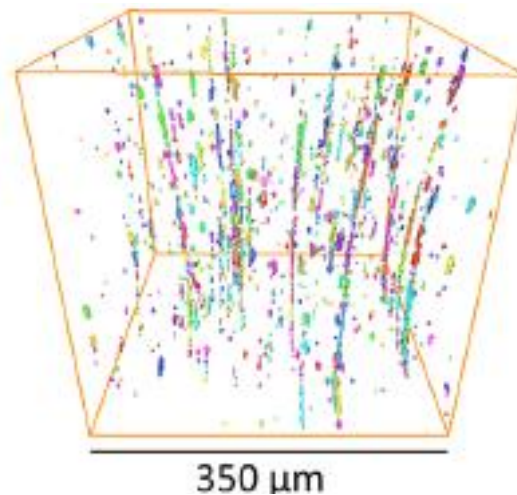


Figure 1.23. Three-Dimensional rendered volume showing the necklace voids present at local strain of 0.6 [100].

It should be mentioned that the damage analysis is mainly made on the DP steels exhibiting ductile fracture. But for the DP steels with coarse microstructure, brittle fracture has been observed [63, 89, 101], which might be an issue in welding. In this case, damage initiates by martensite cracking, then the crack emanates into ferrite matrix by cleavage (see Figure 1.24 [89]).

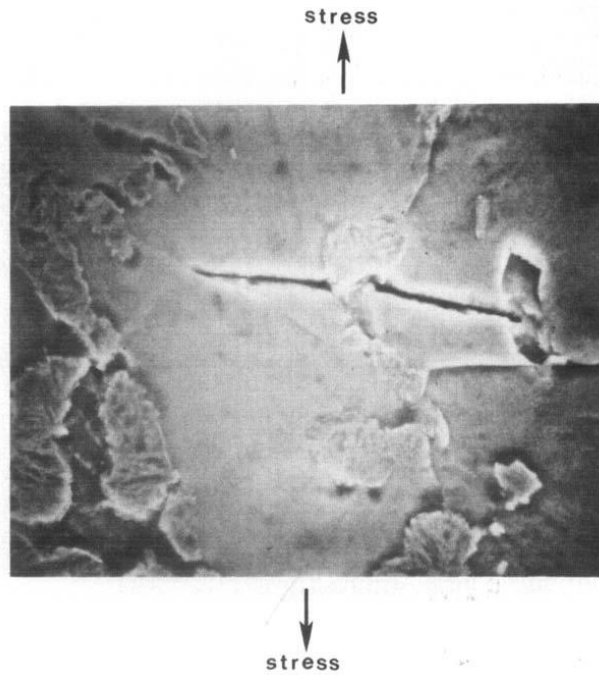


Figure 1.24. Crack emanating from fracture martensite region near fracture surface [89].

1.2.3.2 Damage and fracture resistance of DP steels

The ductile fracture of DP steels includes the stages of damage nucleation, growth and coalescence. Damage nucleation is a continuous process and is interrelated to the growth and coalescence. Therefore, it is difficult to separate their influences on fracture. Instead, the damage and fracture resistance of DP steels is considered based on the effects of various microstructural parameters. The literature review in this section is aimed at figuring out the most important factors in alloy design for fracture strain.

- **Effect of martensite volume fraction**

Many results consistently show that the fracture strain is monotonically decreased with increasing martensite volume fraction and there is a trade-off between strength and fracture strain [52, 59]. However, the interpretation of this effect is not straight forward because several microstructural features, such as morphology and connectivity, are also accounted for by martensite volume fraction. The first-order effect of martensite volume fraction is attributed to the increase of damage

nucleation site and the consequential decrease of intervoid spacing [52, 59]. Additionally, the stress triaxiality in ferrite will also be increased, resulting in a larger void growth rate.

- **Effect of martensite composition**

The composition of martensite is the second factor influencing fracture strain of DP steels. It has been reported that decreasing the carbon content in martensite can improve the fracture strain [52, 57, 59, 102, 103]. The hardness of martensite can be tuned by tempering treatment [102, 103] or changing alloy composition [52, 59]. With a softer martensite phase, the ability to co-deform with ferrite matrix will be enhanced, which can suppress the void nucleation. The plastic deformation of a soft martensite and the delayed martensite fracture have been systematically studied in literature [57].

The martensite composition can also influence the damage nucleation by interface decohesion. The hardness contrast between martensite and ferrite is related to the plastic incompatibility and thus determines the kinematic hardening and stress triaxiality in ferrite. For the case of a hard martensite with high carbon content, back stress from martensite is higher, and the critical interface strength should be reached at lower macroscopic stress [93].

- **Effect of morphology and distribution of martensite**

The fracture strain of DP steels strongly relies on the morphology and/or distribution of martensite phase. The main issues are: 1) whether the martensite islands are interconnected; 2) whether the martensite bands are formed.

The connectivity of martensite can be changed by the heat treatment route. The isolated martensite islands can be achieved by step annealing from austenite region, while the connected martensite can be attained by intercritical annealing [104-106]. The connectivity of martensite can make a considerable difference in fracture strain, even if the martensite volume fraction was kept the same [104-106]. The joint part of martensite islands is the preferential site of damage nucleation [104].

Another issue of martensite distribution is the existence of wide continuous martensite bands due to Mn segregation. The detrimental effect of martensite bands

has been revealed by the careful characterization [98, 107, 108] using Digital Image Correlation (DIC) and in-situ tensile test. Local fracture at the martensite bands can occur very early at the deformation, and big voids can be formed by separating the martensite bands of both sides. The similar results can be observed in DP steels with long and parallel martensite fibers, which act the same role as martensite bands [68, 69]. For cold-rolled DP steels, this effect can be decreased by slow heating and equiaxed morphology can be attained, resulting in improved fracture strain [57].

1.2.3.3 Modeling ductile fracture of DP steels

Modeling and simulation of ductile fracture of DP steels remain a challenging topic in the communities of material science and solid mechanics. The sequential nucleation, growth and coalescence of voids, the competition of damage mechanisms and the stress triaxiality are involved in developing the model, making it a multi-physics, multi-scale problem.

Landron has modeled the void nucleation [93], growth [85] and coalescence [94] in a model DP steel, which are validated with experimental characterization by X-Ray tomography. The Argon criterion of decohesion was modified to include the local stress field and the effect of kinematic hardening present in dual-phase steels, and the model can capture the evolution of void density with local strain, validating the use of local stress triaxiality as the driving force of interface decohesion [93]. The Rice-Tracey model is used to predict void growth evolution, and this model can reproduce the void growth behavior after accounting for the void shape [85]. As to the void coalescence, the Thomason criterion is the best adapted to predict the local coalescence events according to the correlation between actual coalescing couples of voids and local implementation of the criterion [94].

Finite Element Method (FEM) analysis has been proven to be a powerful tool in modeling failure, especially for its ability of using large representative volume elements and of addressing localized deformation problems. Microstructure-based models [84, 109-111] have been developed to analyze the failure of DP steels by plastic strain localization and the properties of martensite have been shown to influence the failure mode [111]. As to the typical ductile fracture initiated by void nucleation, Kadkhodapour [112] has used a crystal plasticity finite element method (CPFEM) to rationalize the experimental observation of void nucleation. Vajragupta [113] used the extended finite element method (XFEM) to study the interaction

Chapter 1 Literature review

between ductile failure of ferrite and brittle failure of martensite, and the propagation of ductile cracks in DP microstructures can be simulated.

Fracture strain can be estimated with the input of void nucleation, growth and coalescence, taking the work of Le Roy [114] with spheroidized carbon steels as an example. A closed-form estimation of fracture strain has been developed by incorporating the simple laws of void nucleation, growth and coalescence, while advanced predictions have also been proposed to discuss the effects of initial void volume fraction, shape, distribution and so on [99].

1.3 Summary

In this chapter, detailed literature review on the microstructure development and mechanical properties of DP steels has been made. The main conclusions are drawn as follows.

For the initial ferrite + carbide mixture, the DP morphology is determined by the distribution of carbide. The kinetics of austenite formation is influenced by the carbide composition and annealing temperature. Additionally, heating rate is an important parameter of processing cold-rolled DP steels.

The volume fraction, composition and distribution of martensite and the grain size of ferrite are the most important factors in determining the plastic and fracture properties of DP steels. The deformation and damage mechanisms are also dependent on these microstructural features. However, the specific effects of each factor are to be clarified by well-designed experiment and modeling.

Finite Element (FE) calculation can provide both macroscopic and microscopic responses of the representative volume element, which is essential in understanding the mechanical properties of DP steels. It is used as the micromechanical modeling tool in this thesis.

Chapter 2 Phase transformation and microstructure development: experiments and modeling

As pointed out in the literature review, the mechanical properties of dual-phase steels strongly depend on the microstructural features (such as volume fraction, size and distribution of martensite and ferrite grain size) and on the chemical composition of phases. From a metallurgical point of view, it is challenging to decouple these factors because usually they are inter-related. For example, for a certain alloy composition, if the volume fraction of martensite is changed, the carbon content in martensite is changed accordingly.

The optimization and tailoring of dual-phase steels require the knowledge of the influence of individual microstructural parameters. Many of them are controlled by both the phase transformation and the recrystallization phenomena.

The aim of this chapter is two-fold. The first is to improve our understanding concerning the mechanisms of austenite formation, so that experiments can be designed to investigate the influence of volume fraction and properties of martensite. The second is to develop robust processing route for ultrafine-grained DP steels in order to study the consequences of microstructure refinement on mechanical properties.

2.1 Materials and methodology

2.1.1 Materials processing

2.1.1.1 As-received material

The steel grade used in this work (0.1wt% C, 3.5wt% Mn) was elaborated in the research center of the ArcelorMittal at Maizières-lès-Metz (France). After the casting, the ingot was held at 1200°C and then hot-rolled at 900°C. It was quenched to attain martensitic microstructure and cold-rolled to 1mm thickness with the reduction of 70%. The actual composition is shown in Table 2.1.

Element	C	Mn	S	P	Si
wt%	0.094	3.4	0.007	0.002	0.003

Table 2.1. Chemical composition (in weight percent) of the steel grade.

2.1.1.2 Heat treatment

Dilatometer DT-1000 was used in the fundamental study of austenite formation because of its capability of controlling heating rate and cooling rate. The atmosphere of He can also be provided to protect the samples from severe oxidation.

Tempering the as-received materials was performed in a tube furnace in order to attain spheroidized microstructure. Intercritical annealing for tensile specimens was performed either in a tube furnace or in a fluidized bath furnace, depending on the requirement of heating rate. The tube furnace can fulfill the required slow heating. The fluidized bath furnace has the advantage of fast heating, and was used for the heat treatments requiring short duration time or high heating rate.

2.1.2 Microstructure characterization

2.1.2.1 Microstructure and micro-chemical analysis

Samples for SEM and EBSD were prepared by standard mechanical grinding and

Chapter 2 Phase transformation

polishing procedures, finishing with 8 min colloidal silica polishing. To reveal the microstructure for SEM observations, the samples were additionally etched with 2% Nital.

Substructures were examined by transmission electron microscope (TEM, JEOL 2010 with 200KV). For TEM observation, thin foils were prepared by a twin-jet polishing technique using a mixture of 20% perchloric acid and 80% methanol at an applied potential of 20V and at -35°C. The ASTAR system [115, 116] in the TEM has also been used for phase mapping on the thin foils.

For micro-chemical analysis, EDX in SEM or TEM was used to measure the distribution of manganese. The mapping of carbon distribution was made by NanoSIMS 50 instrument [117, 118]. The NanoSIMS 50, a scanning ion microscope developed by Onera and Cameca, has been designed for very small area analysis with an optimized lateral resolution (down to 50nm). Recent NanoSIMS [119, 120] investigations demonstrated the high potential for mapping the trace elements such as boron or carbon in steels. The detect limit of carbon in steels is better than 60ppm. The NanoSIMS instrument was operated with a Cs primary ion beam scanning across the selected area and the $^{12}\text{C}_2$ ions are analyzed in this study. The acquisition time is 5 ms/pixel. A pre-sputtering of the surface was performed before any measurement in order to minimize the surface contamination (mainly carbon and oxygen). Since the measurement was not calibrated by standard samples, only qualitative mapping was made. Both EDX and NanoSIMS experiments were performed on the as-polished surfaces.

2.1.2.2 Quantitative metallography

The microstructures were analyzed quantitatively by image analysis. The SEM images were binarized into black-white and the ferrite and martensite phases can be distinguished. The area fraction of martensite, which corresponds to the volume fraction (V_m) in 3-dimensions [121], can be directly measured with ImageJ software [122]. For the average linear size of the phases, several straight lines of unit length were drawn with random orientations, and the number of intercepts with the ferrite/martensite interface was counted. The mean linear size of ferrite ($\overline{L_\alpha}$) and martensite ($\overline{L_{\alpha'}}$) can be respectively calculated by the following equations [121]:

$$\overline{L_{\alpha}} = 2 \frac{1-V_m}{P_L} \quad (2.1)$$

and

$$\overline{L_{\alpha'}} = 2 \frac{V_m}{P_L} \quad (2.2)$$

with P_L the number of intersections (per unit length) between the scanning line and ferrite/martensite phase boundaries. The definition of sizes of ferrite and martensite is seen in Figure 2.21(a).

2.1.2.3 Nanoindentation

Nanoindentation was used to locally probe the hardness of martensite. The samples were mechanically ground and polished, finishing with 8 min colloidal silica polishing in order to eliminate the strained surface layer. A matrix of indents was performed on the microstructures. The hardness of the phases was calculated continuously during the loading thanks to the CSM (continuous Stiffness Measurement) mode which imposes small load oscillation during the indentation.

2.1.3 Simulation of phase transformation

The austenite formation under local equilibrium conditions was simulated by DICTRA (Diffusion-Controlled Transformation) software using the TCFE6 and MOB2 databases [123]. As the input to the DICTRA simulation, the carbide phase has to be identified and the composition should be figured out by experimental measurement. Additionally, the size of the cell has to be fixed according to the initial microstructure. The volume fraction of phases should be balanced by the composition.

2.2 Investigation of the mechanisms of austenite formation

A lot of studies on austenite formation have been made, dedicating to the steels with low Mn content (lower than 2wt%) [17, 18, 21-26, 28-30, 33, 34]. However, the number of studies on the steels with increased Mn content is limited, and there is

still a lack of data and analysis on both experimental and theoretical investigations [38, 124]. The steel grade used in this work has relatively high Mn content (3.5wt%), and the mechanisms of austenite formation in this alloy are to be studied.

The effect of Mn content on austenite formation is complicated. Firstly, it can influence the carbide formation during cooling from hot-rolling processing and then affects the morphology and composition of carbide. Secondly, Manganese is known to decrease the eutectoid temperature and also affect ferrite recrystallization. As a result, a stronger overlap between ferrite recrystallization and austenite formation is expected for cold-rolled steels. Last but not least, Mn enrichment in carbide, as well as temperature, determines the driving force for carbide dissolution and thus the kinetics of austenite formation.

In this part, we propose to clarify the mechanisms of austenite formation in the selected steel grade. Our attention will then be focused on the evolution of both microstructural features and kinetics of the involved phase transformation.

2.2.1 Re-austenitization from spheroidized microstructure

Spheroidized microstructure with cementite particles is selected as a reference state for the study of austenite formation. It is relatively stable during heating. Indeed, carbides are expected to be Mn enriched and consequently any growth and/or coarsening is considerably slowed down. Furthermore, the driving force for ferrite grain growth is expected to be negligible. This stable ferrite grain size during annealing has been observed in a previous study [125].

2.2.1.1 Initial microstructure

The as-received material is cold-rolled martensite. It was then tempered at 550°C for 72 hours (QT). The temperature was chosen according to the decrease of A1 temperature due to the relatively high Mn content.

As shown in Figure 2.1, recrystallization and grain growth of ferrite have occurred. The carbides distribute both along the grain boundaries and within the bulk grains. They are already spheroidized and the size is about 100~300nm. The coarsening is

Chapter 2 Phase transformation

not very significant due to the limited temperature. The phase mapping made by ASTAR in Figure 2.2a reveals that the carbide should be cementite. This identification is supported by the mapping of confidence index in Figure 2.2b. The confidence index represents the matching between the experimental diffraction pattern and the one in data bank. The high brightness in Figure 2.2b means a good match of diffraction patterns and the area of carbide has reasonably high confidence index. According to EDX measurement under TEM (Figure 2.3), Mn content within carbide ranges from 21 to 36wt%, which is much higher than the nominal composition and indicates a Mn enrichment process. But it is still lower than the equilibrium Mn content predicted by ThermoCalc [123] and given in Table 2.2.

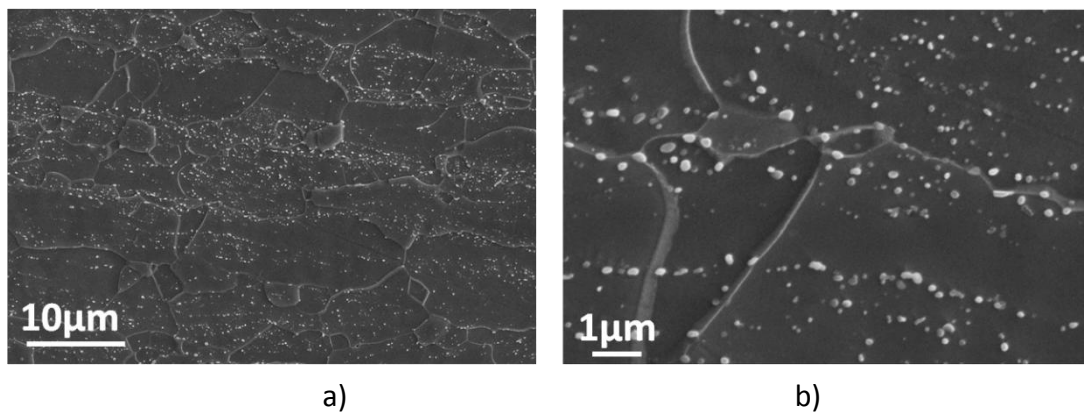


Figure 2.1. Spheroidized microstructure after tempering (at 550°C for 72 hours) observed in SEM with the magnification of 2000 (a) and 10000 (b).

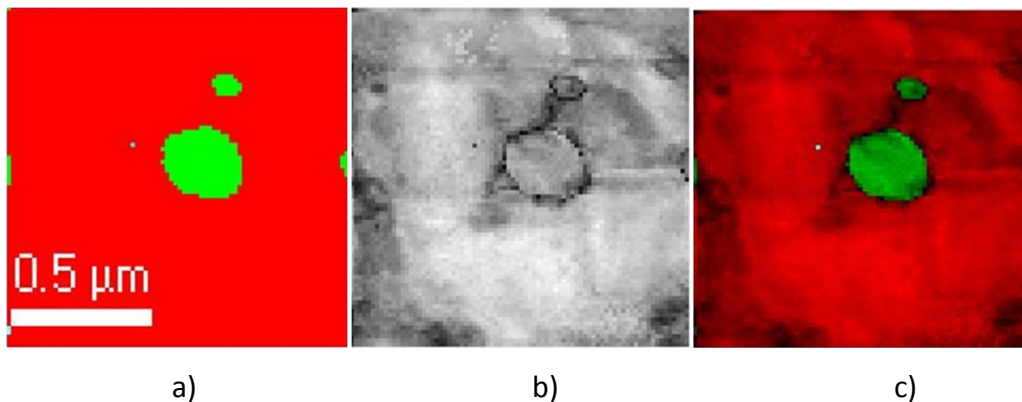


Figure 2.2. Phase mapping (a), confidence index distribution (b), and their superposition (c) of the spheroidized microstructure made by the ASTAR system under TEM. The red area is ferrite, and the green is cementite. The confidence index in cementite shows that the carbide is very probably cementite.

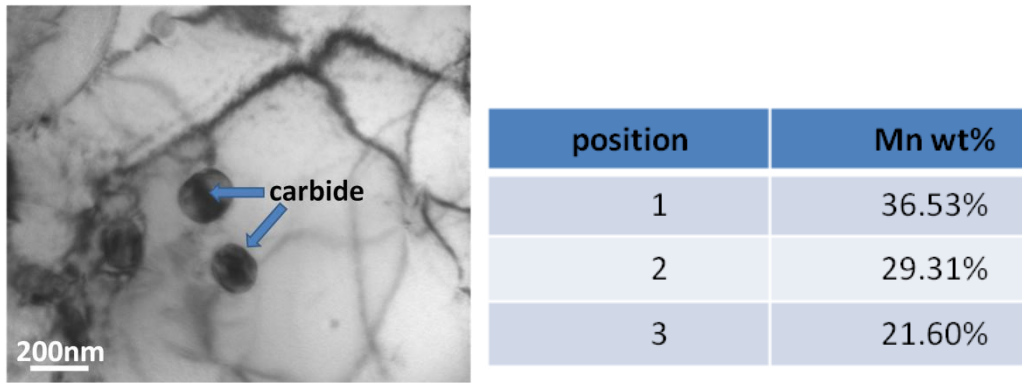


Figure 2.3. TEM observation of carbide and EDX measurements.

Temperature (°C)	Phase	Mn content (wt%)
520	cementite	50
550	cementite	45
570	cementite	42

Table 2.2. Evolution of the equilibrium Mn content in cementite as a function of temperature predicted by Thermocalc.

2.2.1.2 Influence of annealing temperature on microstructure state evolution

The microstructures annealed at 700°C and 740°C with the heating rate of 10°C/sec are compared in Figure 2.4. At both temperatures, carbides at the ferrite grain boundaries are the more favourable sites for austenite nucleation but not those within ferrite grains. This can be due to different nucleation barrier, and the triple junction of carbide and ferrite grain boundary can lower the barrier and facilitate nucleation as calculated in [25]. Once nucleated at the site of dissolving carbides, the austenite islands grow preferentially along grain boundaries due to higher diffusivity, interconnecting with each other and forming a necklace. The preferred growth of austenite also leads to anisometric shape.

Detailed TEM observation in Figure 2.5 shows the hierarchical structure of the austenite islands. Austenite grows simultaneously with carbide dissolution. Before reaching equilibrium, un-dissolved carbide can be retained within austenite. There are often several carbides in a single austenite island, but it is not expected to contribute significantly to dispersion strengthening due to the low volume fraction

Chapter 2 Phase transformation

and density of carbides.

A morphological transition is observed when the annealing temperature is further increased to 780°C (Figure 2.6). Austenite grains at ferrite grain boundaries become more equiaxed. Additionally, the austenite islands grow preferentially into one grain but not equally into both sides of ferrite grain boundary. This suggests an effect of crystal orientation. This observation of morphology transition indicates a limit of annealing temperature for developing microstructures to study mechanical behavior, in addition to the considerations of martensite volume fraction and composition.

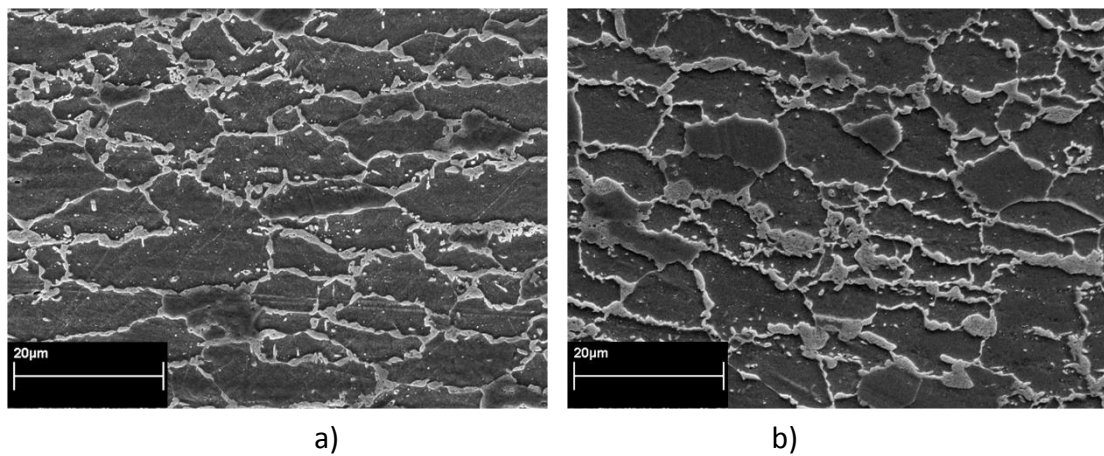


Figure 2.4. Microstructure during re-austenitization at 700 °C for 20 minutes (a) and at 740°C for 15 seconds (b).

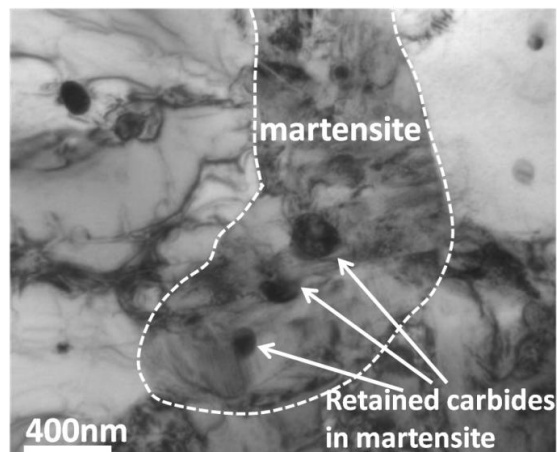


Figure 2.5. Detailed TEM characterization of the martensite with retained carbides after annealing at 700°C for 20 minutes.

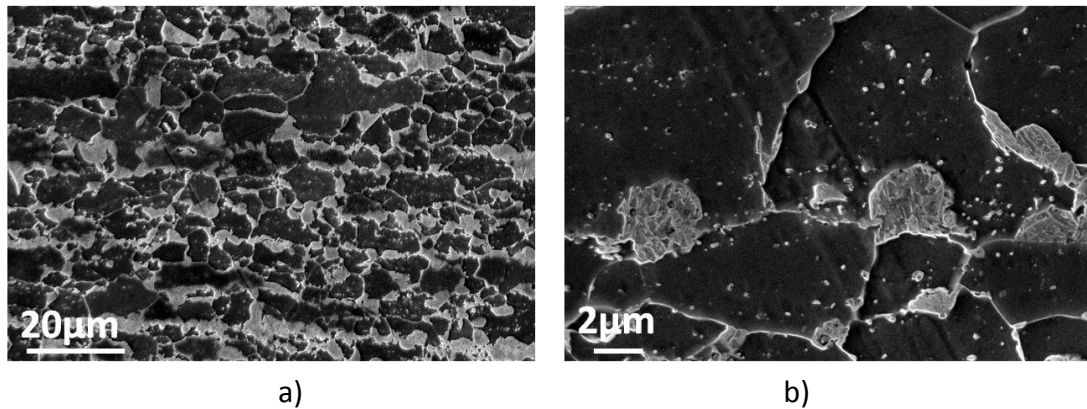


Figure 2.6. Microstructure during re-austenitization at 780°C for 0.5 seconds observed in SEM with the magnification of 1000 (a) and 5000 (b).

2.2.1.3 Influence of annealing temperature on transformation kinetics

The spheroidized microstructure was annealed at different temperatures to study the kinetics of austenite formation. Attention is paid to the sensitivity of phase transformation to temperature, which is the base of microstructure control during processing. Figure 2.7 shows the re-austenitization kinetics at various temperatures from 680°C to 780°C. The transformation kinetics is very sensitive to temperature as reported in [17, 18, 23, 26], and there exists a transition between a slow and a fast regime in this temperature range as reported by [18].

The effects of temperature are two-folds. Firstly, with the increasing temperature, the growth of austenite is accelerated due to enhanced thermodynamic driving force for carbide dissolution and both the Mn and C diffusivities. The transformation at 780°C can finish within 10 seconds while that at 700°C lasts for hours. Secondly, the nucleation of austenite at carbide/ferrite interface occurs earlier at higher temperature. Since the nucleation of austenite is heterogeneous and depends spatially on the location of carbide, only an average behavior can be observed mesoscopically. Thus the apparent incubation time is measured by extrapolating the transformation curves to the moment with zero martensite fraction in a logarithm scale, which is used to compare the nucleation events at different temperatures [126]. The apparent incubation time at 780°C and 740°C are about 0.15 and 3 seconds, but it is increased to 100 seconds at 680°C. Austenite nucleation is initiated by carbide dissolution. As a consequence, the apparent incubation time is also a

marker for the kinetics of carbide dissolution. At higher temperature, there is a stronger driving force for carbide dissolution, and the incubation time for austenite formation will be shorter.

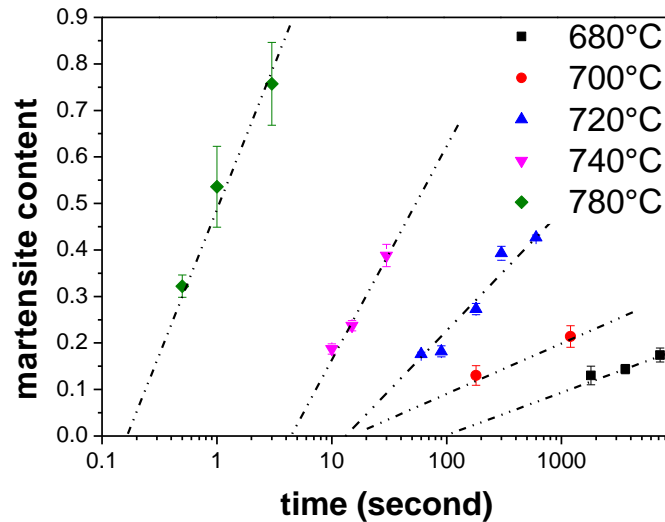


Figure 2.7. Re-austenitization kinetics of spheroidized microstructure at different temperatures. A logarithm time scale is used to highlight the difference in the apparent incubation time.

2.2.1.4 Rationalization by modeling with DICTRA

The experimental results on re-austenitization have provided the phenomenological information for the mechanisms of austenite formation and also for microstructure control. Deeper insight into austenite formation has to be provided by physics-based models. DICTRA was applied to model the austenite formation and to identify the mechanism controlling austenite growth.

The composition profiles within austenite and its evolution with time can also be simulated by DICTRA, providing the strategies of controlling martensite properties for the purpose of optimization. Besides microstructural features, one important factor controlling the mechanical properties of DP steels is the composition of martensite.

● Configuration and assumptions of simulation

The configuration of the simulation of carbide dissolution and austenite growth is

Chapter 2 Phase transformation

given in Figure 2.8. It is a 2-D representation of the spherical geometry. The radius of carbide in Figure 2.8 is 100nm and the width of ferrite is 300nm. The size of carbide is determined by microstructure observation, and the size of ferrite is adjusted according to the volume fraction of phases. The Mn content in carbide is considered to be 25wt%, the mean value measured by TEM-EDX. The Mn and carbon content in ferrite are respectively 3.16wt% and 5×10^{-4} wt%, which are adjusted according to the mass balance. This cell is a closed system, which is equivalent to the periodic condition.

Austenite is set as an inactive phase at ferrite/carbide interface and its nucleation will be initiated when the driving force for precipitation exceeds a pre-defined positive value (0.084J/mol). The interfaces are set to be local equilibrium (LE). It includes partitioning (LEP) or non-partitioning (LENP), depending on both diffusivities and thermodynamic driving force for phase transformation.

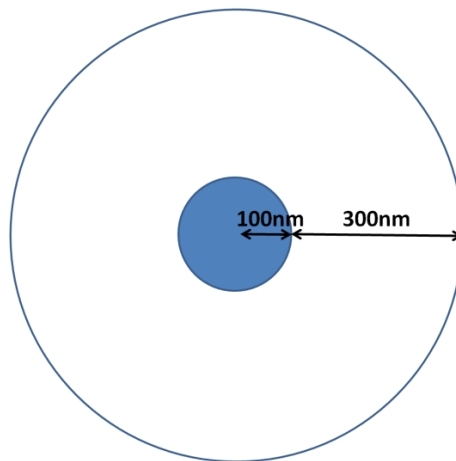


Figure 2.8. Two-dimension representation of the spherical configuration for simulation with DICTRA.

● Simulated kinetics of austenite formation

The comparison between experimental data and calculated kinetics of austenite growth is given in Figure 2.9. The predicted kinetics reproduces the experimental measurements quite well, and the simulation can capture the significant effect of temperature on austenite formation, although the experimental results do not cover the time range for equilibrium. The good agreement allows us to use DICTRA with confidence to analyze the mechanism of austenite growth and the composition profile evolution within austenite.

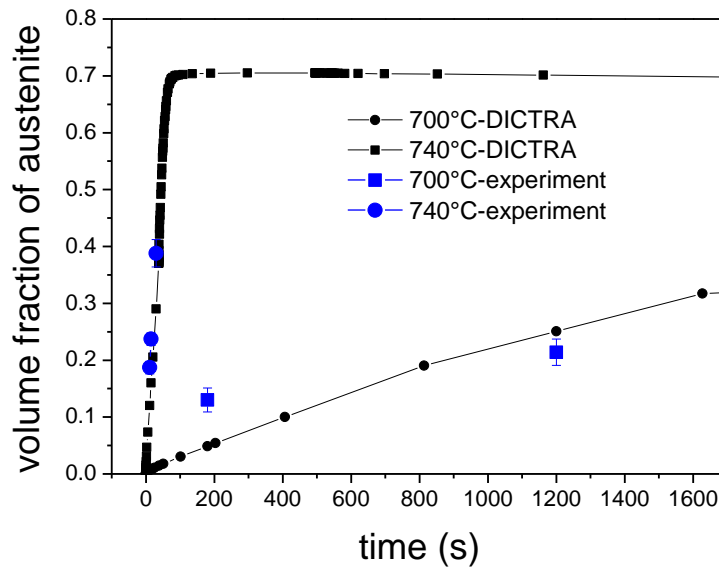


Figure 2.9. Experimental and simulated kinetics of re-austenitization.

● Mechanism of austenite growth

The mechanism of austenite growth is related to the re-distribution of carbon and substitutional elements during the migration of ferrite/austenite interface. Figure 2.10a shows the time evolution of carbon composition profile in the cell at 740°C. There is significant carbon gradient in the austenite very close to carbide or within the former carbide region when the carbide is totally dissolved. In this calculation, the time for total carbide dissolution is about 500 seconds. The carbon gradient extends slowly with time, but the carbon profile in the outer region of austenite is rather flat. Although a carbon composition profile exists in austenite, the austenite growth is not controlled by carbon diffusion in austenite. This can be justified by the evolution of carbon activity profiles shown in Figure 2.10b. There is a significant carbon activity gradient at the very beginning of 0.001 second, but it becomes flat even at the time of 0.1 seconds, indicating that carbon diffusion is essentially not controlling the phase transformation.

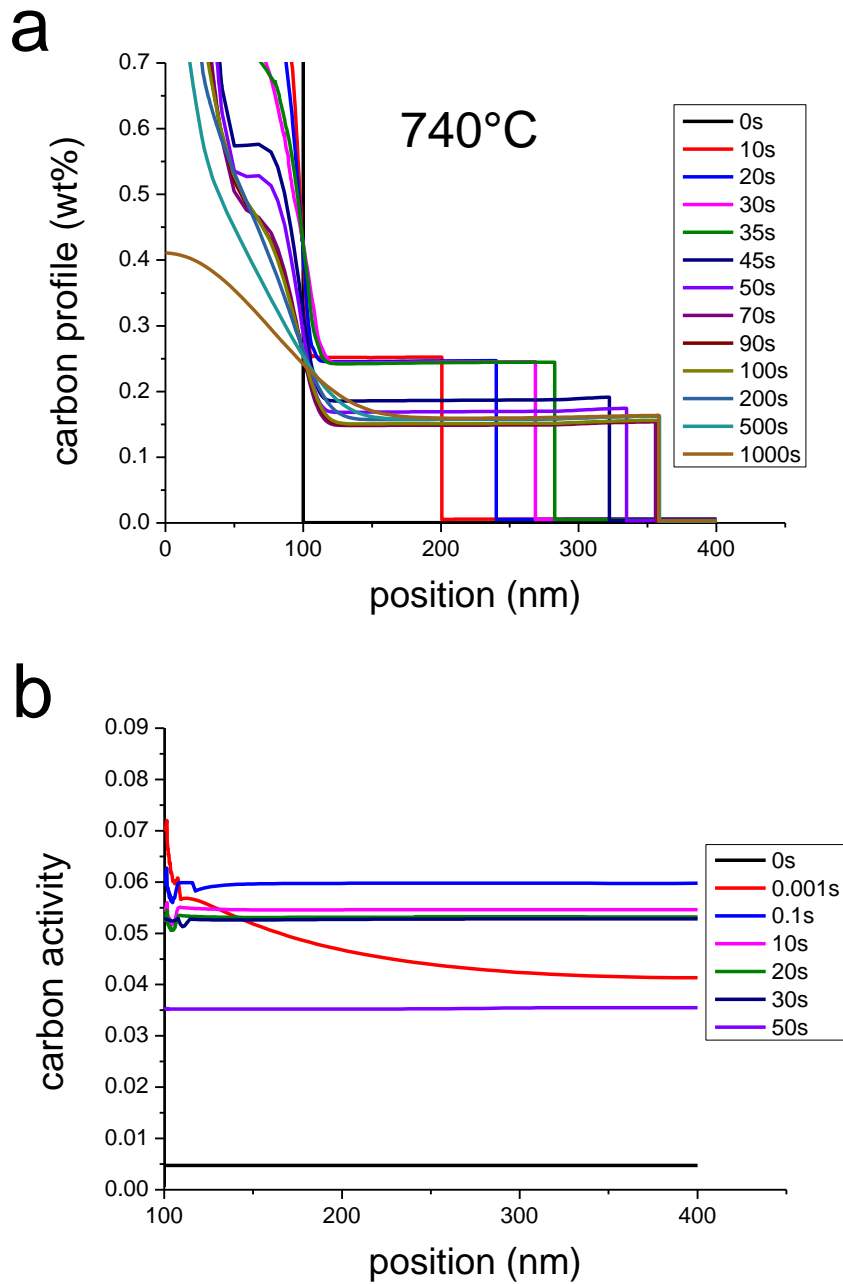


Figure 2.10. Evolution of (a) carbon composition profiles and (b) carbon activity profiles with time at 740°C calculated by DICTRA.

Figure 2.11a shows the evolution of Mn composition profile in the cell with time. There is a significant Mn gradient in the austenite close to carbide or in the former carbide region when the carbide is totally dissolved, which is similar to the carbon gradient. The Mn composition profile in the outer austenite region is rather flat, comparing with that in the core region.

The activity profiles (Figure 2.11b) of Mn give a clear idea about the mechanism of

Chapter 2 Phase transformation

austenite growth. The significant Mn activity gradient in ferrite indicates a diffusion flux from remote ferrite matrix to ferrite/austenite interface. This diffusion flux results from a Mn partitioning process that leads to a Mn enrichment into austenite. In other words, the austenite growth mainly results from Mn partitioning from ferrite but not from Mn diffusion from carbide.

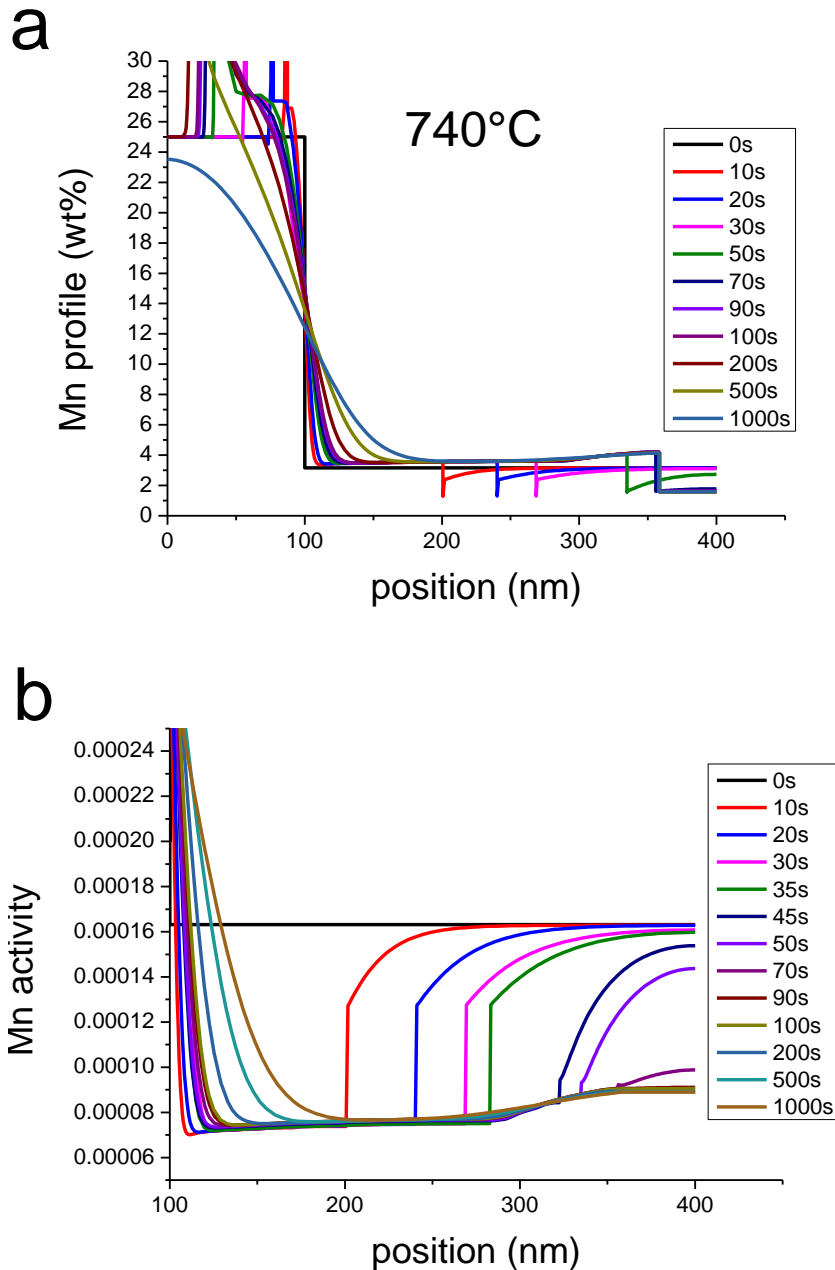


Figure 2.11. Evolution of (a) Mn composition profiles and (b) activity profiles with time at 740°C calculated by DICTRA.

After the growth step limited by Mn partitioning, Mn gradient in ferrite becomes more or less flat. But Mn is still not uniform within austenite and the later stage of

Chapter 2 Phase transformation

austenite transformation is controlled by the Mn diffusion in austenite. As shown in Figure 2.12, this Mn diffusion in austenite will first lead to a slightly shrinkage and later a very slow growth of austenite. The slight shrinkage of austenite volume is a subsequent step of Mn partitioning from ferrite. The final stage of slow austenite growth is driven by the Mn gradient in the core that is shown in Figure 2.11. The kinetics of this stage is very slow because of the low driving force and the low diffusivity of Mn in austenite. Most of the austenite growth is contributed to by the stage of Mn partitioning from ferrite. This observation is different, at some points, with the stages of austenite formation proposed in [26]. Firstly, there is not an observable stage that is controlled by carbon diffusion in austenite as usually considered. Secondly, even if the austenite formation is rather rapid at 740°C, the austenite growth is controlled by Mn diffusion in ferrite but not by carbon diffusion in austenite.

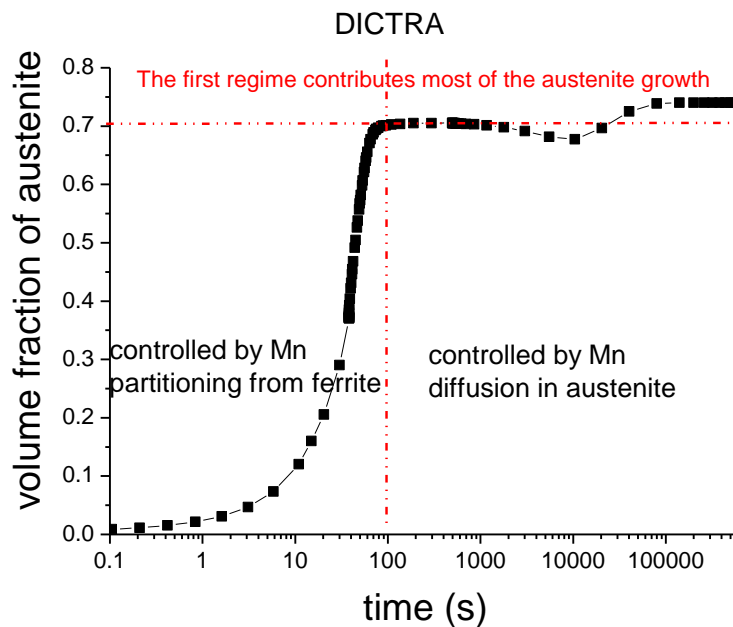


Figure 2.12. Regimes of austenite growth at 740°C. The kinetics of austenite growth is calculated by DICTRA.

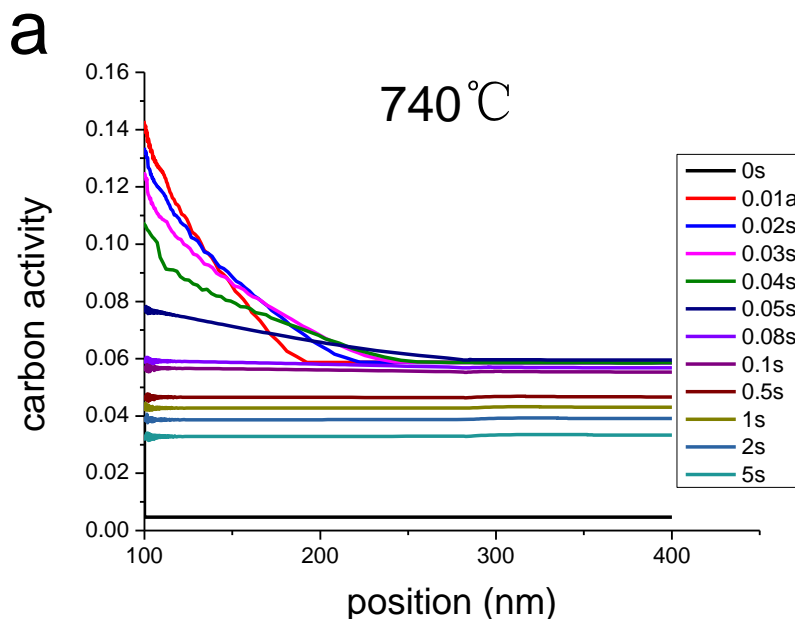
The absence of carbon-diffusion-controlled stage in the previous case can be rationalized by the calculation with 7wt% Mn in cementite, highlighting the effect of cementite composition. The Mn content in ferrite is balanced to be 3.4wt%. The austenite growth mechanisms can be identified by correlating both the activity profiles and the transformation kinetics in Figure 2.13. At the time before 0.05 seconds, the significant carbon activity gradient exists within the growing austenite, but the Mn activity is uniform either in austenite or in ferrite (Figure 2.13a). This stage of austenite growth is controlled by carbon diffusion in austenite and

Chapter 2 Phase transformation

contributes to the austenite fraction of about 40% (Figure 2.13c). After 0.05 seconds, the carbon activity becomes uniform within austenite and ferrite, but there is a significant Mn activity gradient in ferrite, indicating a Mn diffusion process (Figure 2.13b). In this second stage (up to about 12 seconds), the austenite growth is controlled by Mn partitioning from ferrite and contributes to the other 40% of austenite fraction. At the third stage of transformation, the austenite volume fraction remains constant for certain time but is then decreasing during the prolong annealing, which is also observed in [124]. The shrinkage is to increase Mn content in austenite to approach equilibrium composition. Comparing with Figure 2.11b, there is no significant Mn gradient in the core to support the final slow growth of austenite. But this final transformation stage is also controlled by Mn diffusion within austenite.

Therefore, the reduction of Mn content in cementite firstly results in significantly accelerated transformation kinetics (Figure 2.14). Another consequence is the change of austenite growth mechanisms. With less Mn enrichment, the carbon-diffusion-controlled transformation becomes operating. When Mn content in carbide is increased to certain level, Mn diffusion processes are dominating over all the austenite formation.

It is worth mentioning that temperature can have a similar effect as Mn content in carbide. The driving force for carbide dissolution is also determined by the temperature, and increasing annealing temperature can lead to a transition from slow to fast transformation [18].



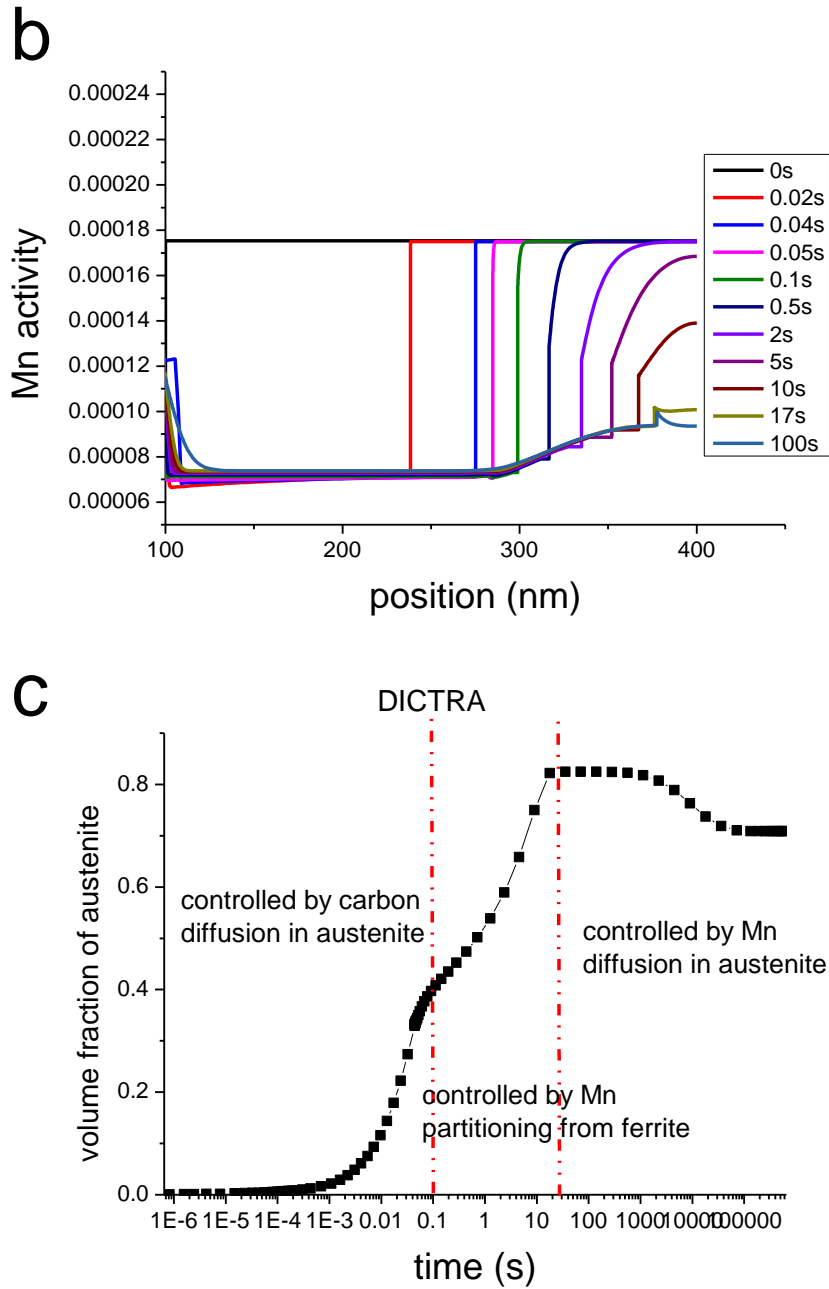


Figure 2.13. Evolution of (a) carbon and (b) Mn activity profiles during austenite formation with 7wt% Mn in cementite at 740°C, and (c) the kinetics of austenite growth calculated by DICTRA. Regimes of austenite growth are identified in (c).

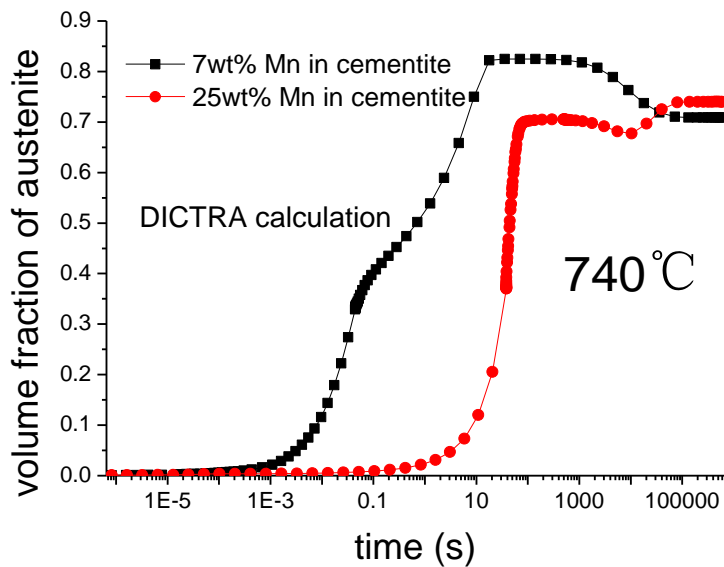


Figure 2.14. The comparison of calculated kinetics of austenite growth in the cases of 7wt% and 25wt% Mn in cementite at 740°C. The kinetics is significantly accelerated with less Mn in cementite.

- **Predicted carbon content in austenite transformed at 700°C and 740°C**

As discussed above, the austenite growth at 740°C is mainly controlled by Mn partitioning from ferrite, resulting in a relatively homogeneous carbon distribution in an austenite island, except in the small volume close to the initial position of carbide. The evolution of carbon and Mn composition profiles at 700°C exhibits the same trend, as shown in Figure 2.15. The qualitative carbon mapping by NanoSIMS is supporting these calculations (Figure 2.16). The martensite and ferrite regions are distinguished due to different signal intensity, revealing the DP microstructure. The distribution of $^{12}\text{C}_2$ is quite uniform within the martensite islands for samples annealed at both 700°C (Figure 2.16a) and 740°C (Figure 2.16b). The brightest particles correspond to cementite, but there is no obvious carbon gradient around the carbides.

The relatively uniform carbon distribution in austenite islands supports the assumption that the average carbon content in austenite can be approximated by the carbon content at the interface. According to this assumption, the evolution of estimated martensite carbon content with martensite volume fraction is shown in Figure 2.17. For the case of annealing at 700°C, the carbon content at first slightly

Chapter 2 Phase transformation

decreases, but generally stays at around 0.3wt% during most of the austenite growth. This constant carbon content can be explained by the mass balance equation. Considering the carbon in austenite coming from carbide dissolution, the composition can be calculated by the following classical equation:

$$C_\gamma = \frac{C_0 - C_\theta f_\theta}{f_\gamma} \quad (2.3)$$

, where f_θ and f_γ are respectively the cementite and austenite volume fraction and C_θ and C_γ are respectively the mean carbon content in cementite and austenite. The necessary condition for constant carbon content in martensite can be arranged from equation (2.3) to the following relationship:

$$\frac{C_\gamma}{C_\theta} = \frac{df_\theta / dt}{df_\gamma / dt}. \quad (2.4)$$

Since the carbon content in cementite is constant, the carbon content in martensite depends on the ratio of austenite growth rate to cementite dissolution rate, as indicated by equation (2.4). Figure 2.18a shows that this ratio increases slightly but later keeps a relatively constant level at 700°C, corresponding to a relatively constant carbon content in martensite. Obviously, if carbides are totally dissolved, the carbon content in austenite decreases as a function of austenite fraction.

The evolution of martensite carbon content at 740°C shows a different behavior (Figure 2.17). The martensite carbon content keeps a rather constant value up to certain martensite volume fraction (about 38%) but drops significantly in the later stage of annealing. Accordingly, the ratio of austenite growth to carbide dissolution rate keeps constant firstly, but it increases dramatically (to several hundreds) during the later austenite growth (Figure 2.18b). Therefore, the significant decrease of martensite carbon content at this stage results from the slower carbide dissolution and from the dilution by austenite growth.

These results are obtained by a mean-field approach. In the real microstructure, carbide dispersion exists in a single martensite island. We have seen previously that several carbides can be retained in some single martensite islands (Figure 2.5 and 2.6). This can have an effect on the element distribution within martensite islands.

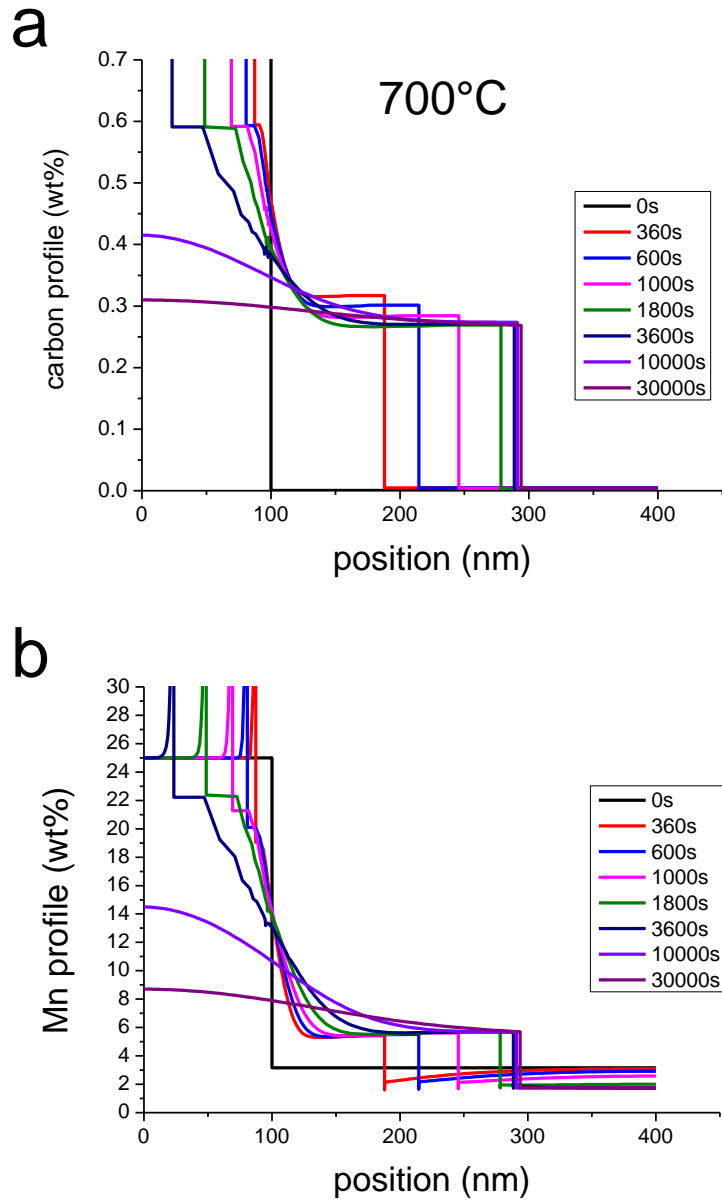


Figure 2.15. Evolution of carbon (a) and Mn (b) composition profiles at 700°C calculated by DICTRA.

Chapter 2 Phase transformation

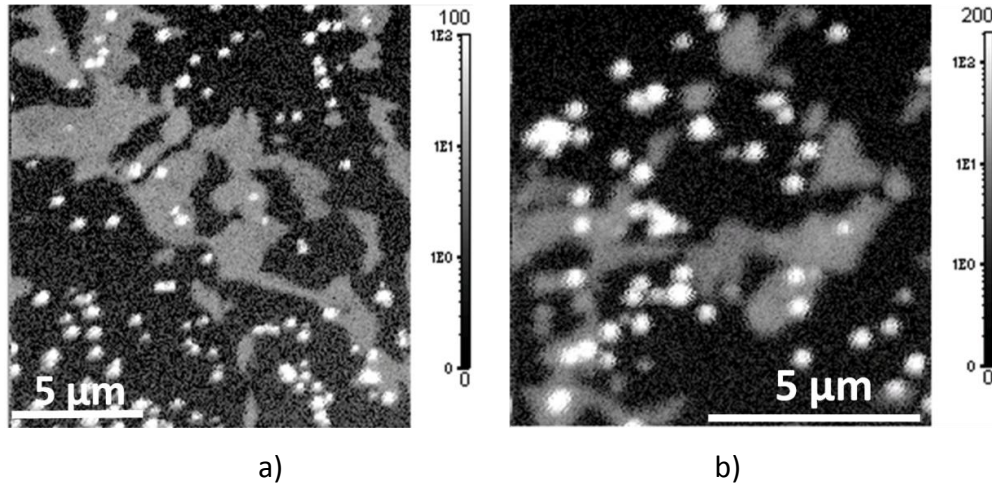


Figure 2.16. Qualitative mapping of carbon distribution in the DP microstructure annealed at 700°C for 2 hours (a) and at 740°C for 35 seconds (b) by NanoSIMS 50. Acquisition time is 5 ms/pixel.

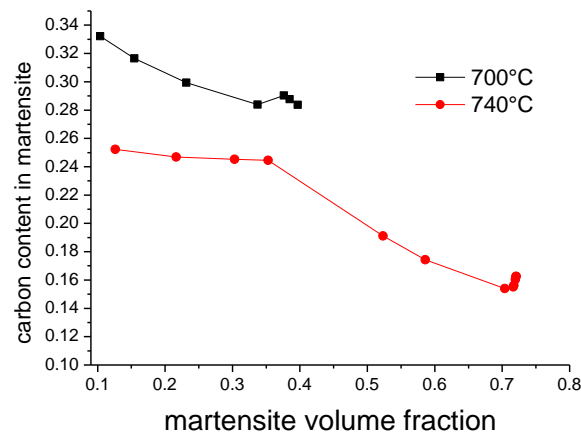


Figure 2.17. Evolution of estimated martensite carbon content with martensite volume fraction calculated by DICTRA.

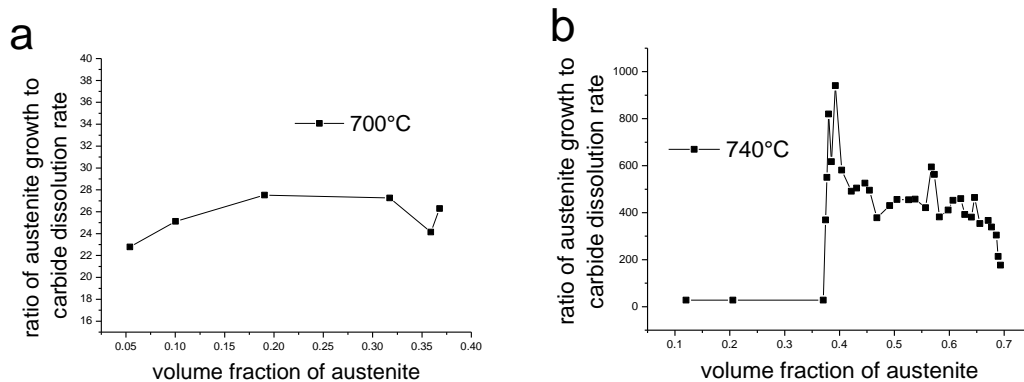


Figure 2.18. Evolution of relative kinetics of austenite growth to carbide dissolution at 700°C (a) and 740°C (b) calculated by DICTRA.

2.2.2 Re-austenitization from cold-rolled martensite

2.2.2.1 Initial microstructure

Martensite has high density of pre-existing dislocations, which are two important points to achieve ultrafine grain size by severe plastic deformation as reported by [127]. The microstructure of cold-rolled martensite (70% rolling reduction) is elongated, as shown in Figure 2.19a. EBSD mapping clearly shows the refined grain size and elongated grain structure (Figure 2.19b). Defining the minimum misorientation to have a grain boundary as 5° , the average grain area is $6.7\mu\text{m}^2$ as measured by EBSD. Large density of dislocations have been generated by martensitic transformation and rolling deformation. Thus there exists a large driving force for recovery and recrystallization during heating and annealing.

As predicted by THERMOCALC, the austenite-forming temperature of this alloy (0.1C3.5Mn) is less than 600°C , at which carbide co-exists. Compared to the common DP steel systems of about 1.5wt% Mn, the A1 temperature is significantly decreased. It is thus expected to have a strong interaction between ferrite recrystallization and austenite formation during intercritical annealing. This interaction provides an opportunity to control microstructure by processing parameters, as reported in [21, 25, 28-30, 33, 36].

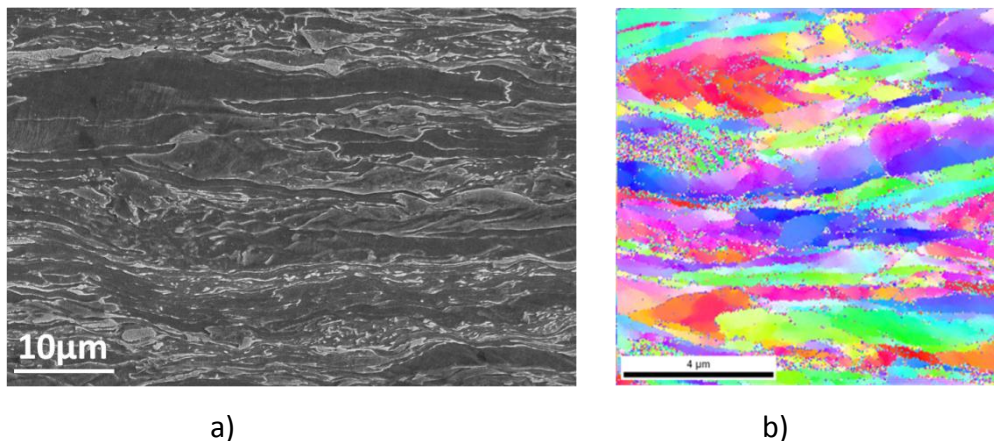


Figure 2.19. Microstructure of cold-rolled martensite (70% rolling reduction) characterized by SEM (a) and EBSD (b). The microstructure is elongated and the grain size is significantly refined. Numerous subgrain boundaries are also observed.

2.2.2.2 Influence of heating rate on dual-phase microstructure

The interaction between ferrite recrystallization and austenite formation is rather complex. For example, the un-recrystallized ferrite matrix is favorable for austenite formation, while the formation of austenite islands can act as pinning points and delay ferrite recrystallization. This interaction provides an opportunity to modify morphology with processing parameters such as heating rate. High heating rate can lead to finer microstructure but the banded features are more significant [25, 28, 34].

Figure 2.20 shows the microstructures annealed at 680°C with different heating rates. As the heating rate increases, the ferrite grains are refined except the case of 100°C/s, and V_m is increased simultaneously. Even with the slow heating rate of 1°C/s, fine-grained DP microstructure (with ferrite grain size of 3.3µm) can be achieved. This indicates an efficient pinning induced by austenite islands if we compare the results at 0.1°C/s and those at 1°C/s. At the heating rate of 10°C/s, which is reasonable for practical manufacturing, ultrafine DP microstructure can already be achieved, where the mean free path of ferrite is decreased to 2 µm and the mean linear size of martensite is about 1µm. The trend can be clearly seen in Figure 2.21.

Heating rate is also influencing the amount of austenite formed. With low heating rate, recrystallization and grain growth of ferrite matrix occur, and some austenite islands are growing inside ferrite grains, as simulated in [33]. The growth of these intragranular islands is slower, comparing with those at grain boundaries due to the difference in diffusivity.

In the achieved ultrafine-grained DP microstructure, there still are banded features, and some ferrite grains are large and elongated along the rolling axis. The banded microstructure is probably a result of Mn segregation and fast heating. Mn tends to segregate and form microbands during solidification and hot-rolling. Since austenite prefers to form in the Mn-rich zone, Mn segregation will lead to banded structure. The effect of fast heating lies in that ferrite grains are elongated by cold-rolling and austenite tends to nucleate at grain boundaries. Fast heating delays ferrite recrystallization and then the austenite islands would inherit the banded distribution.

The microstructure heated at 100°C/s cannot be understood yet. The volume fraction of martensite (49.8%) is larger than other conditions and the value predicted by THERMOCALC under orthoequilibrium conditions (32.3%). The mean free path of

Chapter 2 Phase transformation

ferrite (Figure 21b) is not refined but is larger than the ones at lower heating rate.

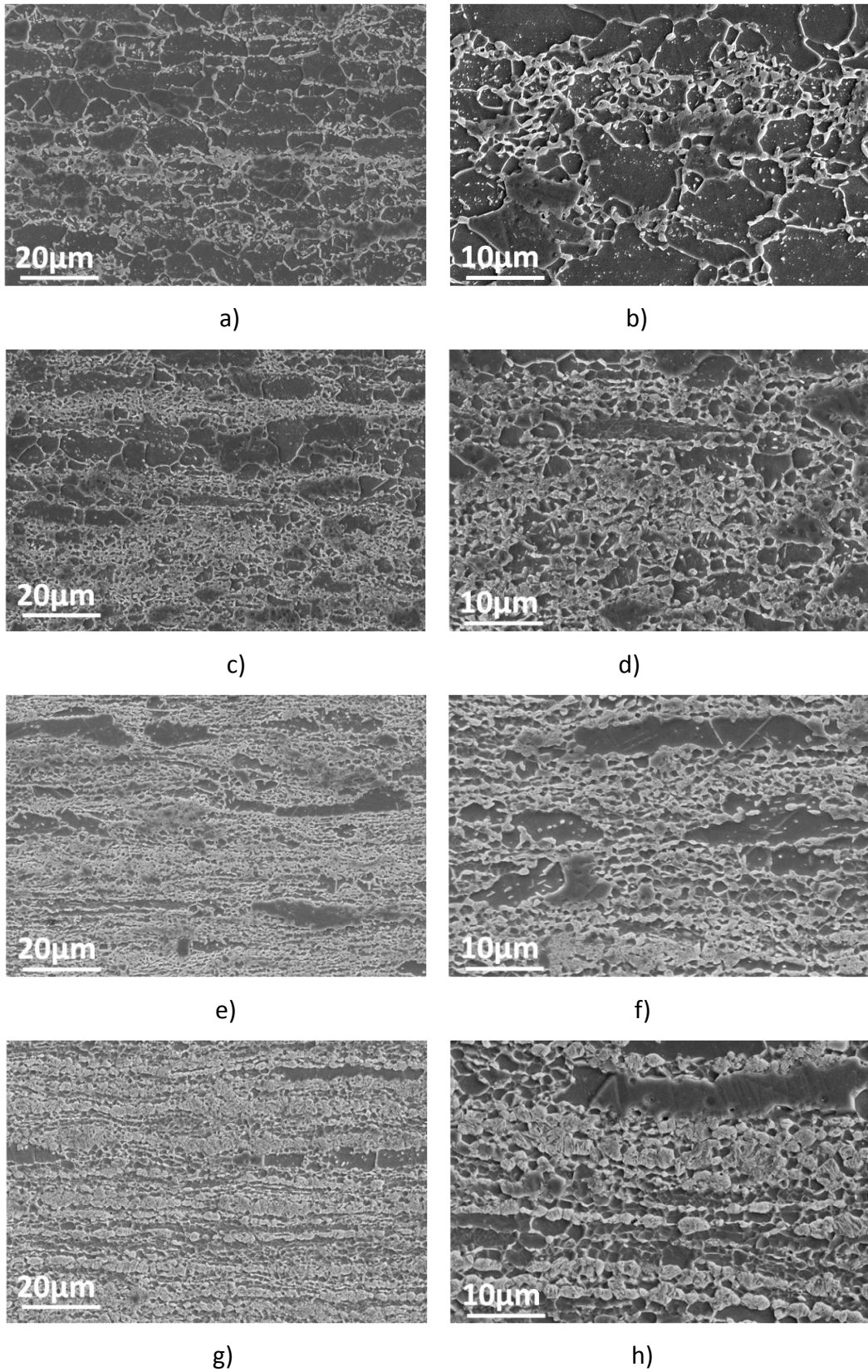


Figure 2.20. Microstructures after annealing at 680°C for 1 hour with the heating rate

Chapter 2 Phase transformation

of 0.1°C/s (a, b), 1°C/s (c, d), 10°C/s (e, f) and 100°C/s (g, h). Comparing (a), (c), (e) and (g) with lower magnification, the effect of heating rate on martensite content and microstructure refinement can be shown. Detailed observations in (b), (d), (f) and (h) show the ferrite grain size, the shape and morphology of martensite islands.

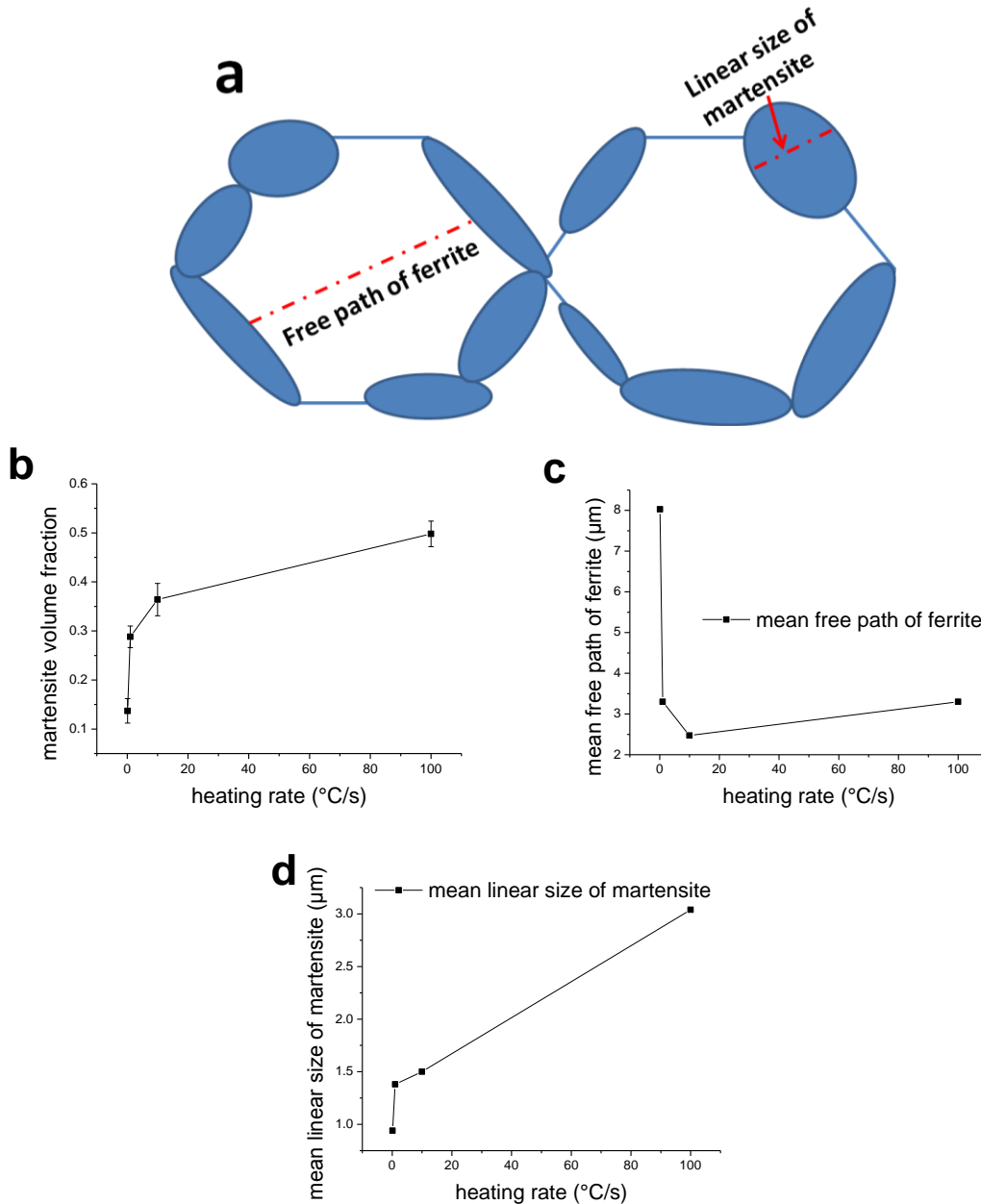


Figure 2.21. Schematic graph of the dual-phase microstructure (a) with the definition of free path of ferrite and linear size of martensite, and the quantification of the microstructures annealed with different heating rates: volume fraction of martensite (b), mean free path of ferrite (c) and mean linear size of martensite (d).

2.2.2.3 Influence of annealing temperature on dual-phase microstructure

The interaction between ferrite recrystallization and austenite formation can also be affected by the annealing temperature, which influences the volume fraction of austenite. It is suspected that a certain volume of austenite is required to obtain a refined microstructure. As shown in Figure 2.22, fine-grained dual-phase microstructure cannot be attained at 650°C with heating rate of both 100°C/s and 10°C/s, although the relatively high Mn content is known to delay recrystallization [128].

One of the possible reasons for this would be that a critical volume fraction or density of austenite islands is necessary to pin the recrystallization and grain growth of ferrite. These results would suggest that austenite volume fraction may play a key role in microstructure refinement.

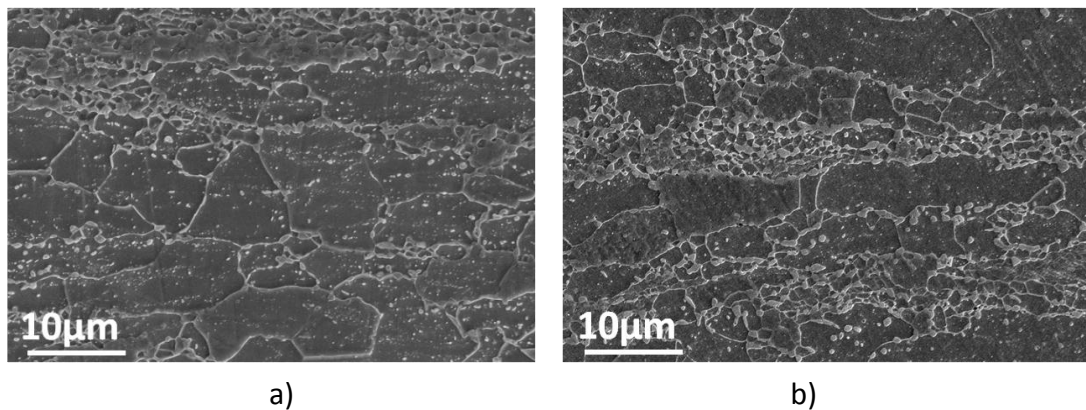


Figure 2.22. Microstructure after annealing at 650°C for 1 hour with the heating rate of 10°C/s (a) and 100°C/s (b).

2.3 Microstructure development

The previous experimental and simulation results have thoroughly explored the austenite formation from spheroidized microstructure and cold-rolled martensite, providing the information of microstructure features and element distribution in phases. These are the important considerations in experiment design for the study of mechanical properties.

2.3.1 On the influences of the volume fraction and composition of martensite

As discussed before, starting from spheroidized microstructure can result in the dual-phase microstructure with the same spatial distribution of martensite islands after annealing at a certain intercritical temperature. Considering the main results of DICTRA calculations that the carbon content in austenite is relatively constant during austenite growth and the average carbon content is decreased at higher annealing temperature, experiments can be designed to investigate the influences of volume fraction and composition of martensite.

On the influence of martensite volume fraction, the spheroidized microstructure should be annealed at 700°C for various duration times, so that dual-phase microstructures with various fractions but the same spatial distribution and properties of martensite can be achieved. In this line of comparison, the differences are martensite volume fraction, the mean free path of ferrite and the mean linear size of martensite. Notice that the plasticity of martensite is mainly determined by composition but not the size.

On the influence of martensite composition, series of annealing should also be performed at 740°C for various duration times. Various volume fractions of martensite can then be attained, but the microstructure features are the same with the samples annealed at 700°C. The main differences are the carbon and Mn contents in martensite.

2.3.1.1 Heat treatment and microstructure features

Tube furnace was used for the annealing at 700°C, while the heat treatments at 740°C were performed in a fluidized bath furnace due to the much shorter duration time. Dual-phase microstructures with various martensite volume fractions have been attained and the microstructure features are quantitatively compared by the mean free path of ferrite and mean linear size of martensite (the definition seen in Figure 2.21a). As the trend shown in Figure 2.23, the mean free path of ferrite is slightly larger at 740°C but they can be considered the same and within the range of measurement scattering. Also, the mean linear size of martensite is the same

between QT-700 and QT-740.

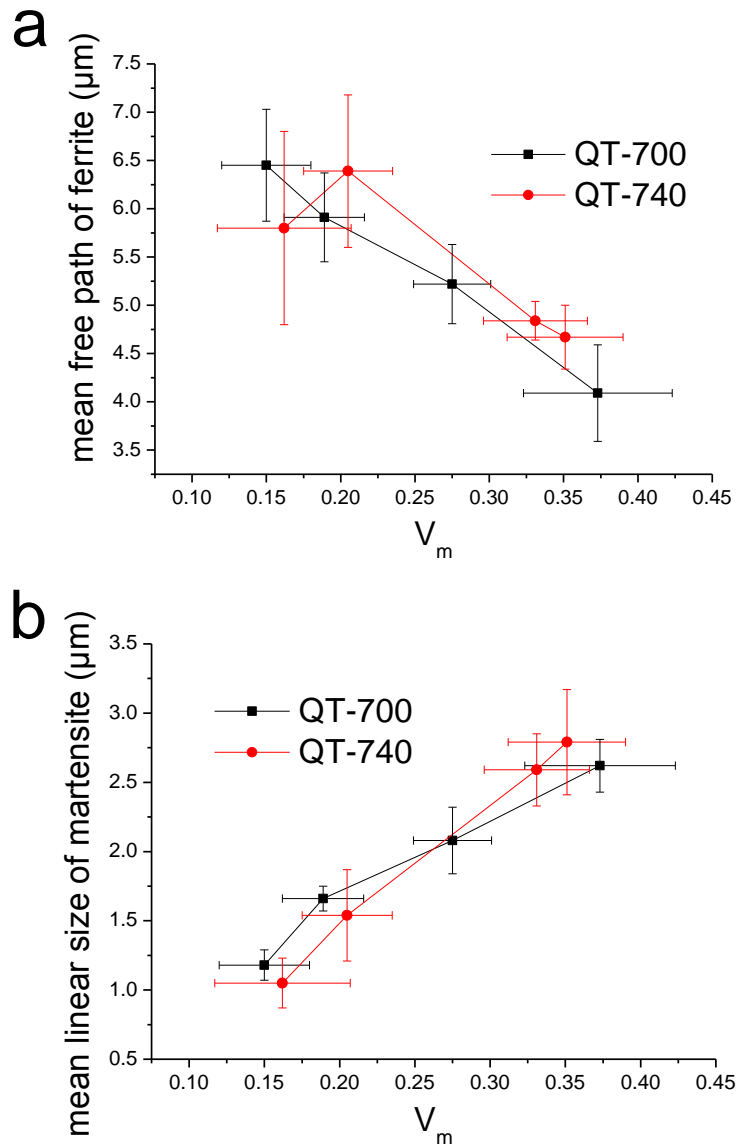


Figure 2.23. Evolution of mean free path of ferrite (a) and mean linear size of martensite (b) with martensite volume fraction of the dual-phase microstructures after annealing at 700°C and 740°C.

2.3.1.2 Nanoindentation for probing phase properties

The research on the influence of martensite properties starts from the estimation of martensite carbon content calculated by DICTRA. According to the calculations, the average carbon content is decreased at higher annealing temperature. This prediction can be experimentally confirmed by probing the hardness of phases by

nanoindentation.

Ferrite and martensite can be distinguished under the Back Scattering Electrons (BSE) mode in SEM, and thus the location of nanoindents can be identified (Figure 2.24a). The evolution of nanohardness with penetration depth is shown in Figure 2.24b, which can be calculated with the CSM (Continuous Stiffness Measurement) mode [129] and the assumption of Oliver-Pharr model [130]. After elasto-plastic transition at small depth, the curves become smooth but the nanohardness keeps decreasing until the penetration depth of 80nm, which might be related to the indentation size effect [131].

Measuring the phase properties in steels have been tried in several previous studies [132-134]. However, it is still challenging to probe accurately the hardness of martensite phase. The first difficulty comes from the small size of martensite islands and the surrounding soft ferrite matrix, which will bring up the composite effect and then influence the measurement [135]. From a 2-D SEM image, it is not enough to judge the actual location of an indent and the interaction volume within the microstructure due to the complicated topology of martensite phase [133, 134]. Additionally, the hierarchical structure of martensite also complicates the hardness measurement of martensite islands [134, 136].

Considering the difficulty to interpret the nanoindentation data on such microstructures, this technique was used as a relative measuring method. To improve the accuracy and reliability of the measurement, only the indents exactly located within the martensite islands were taken into account. The mean hardness value between the depth of 60nm and 90nm was taken for an indent. The hardness value of lower penetration depth was not used to avoid the effect of surface oxide layer, roughness and the tip defect. The nanohardness of martensite in each sample is an average of five to ten indents.

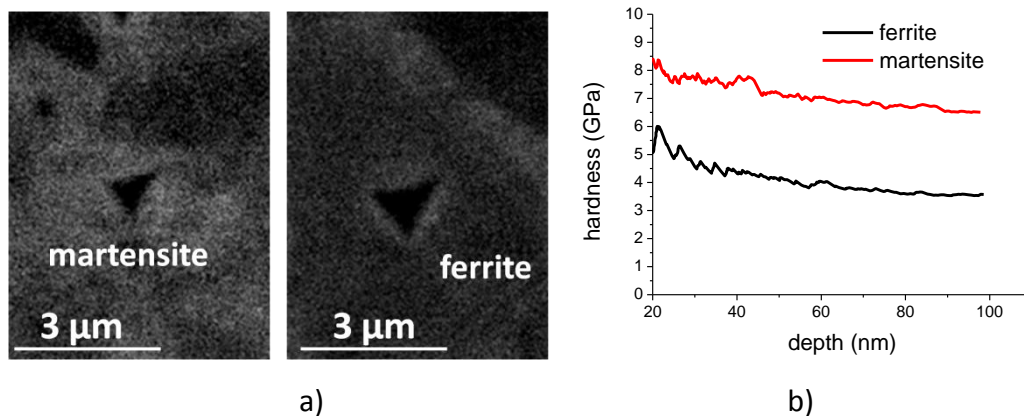


Figure 2.24. Phase contrast and the location of nanoindents under SEM (a) and the hardness evolution of ferrite and martensite with penetration depth (b). The bright area in (a) is martensite and the dark area is ferrite. It should be mentioned that the indent sizes in (a) are corresponding to the final penetration depth of 200nm.

The comparison of nanohardness among the samples annealed at different temperatures is shown in Figure 2.25. Although the scatter is rather large, there is an obvious trend that the hardness of martensite is decreased at higher annealing temperature, which is in agreement with the temperature evolution of carbon content in martensite calculated by DICTRA. For example, the nanohardness of martensite in QT-700-37% is about 8.1GPa, which is 20% higher than that of QT-740-35% (6.7GPa). Furthermore, the nanohardness of martensite should be considered constant at a given temperature if the ranges of scattering are taken into account (Figure 2.25).

The difference in martensite hardness between QT-700 and QT-740 is larger than expected, considering the difference of carbon content (about 0.05wt%, see Figure 2.17). It is suspected that the Mn content influences significantly the properties of martensite. According to the DICTRA calculations, the Mn content in martensite in QT-700 is about 6wt% while that in QT-740 is less than 4wt%. With the EDX in SEM, the Mn content in Martensite in QT-700-37% and QT-700-35% are measured to be about 5.3wt% and 4.1wt%, respectively. The different Mn content, as well as carbon content, in martensite might have a synergic effect on the the plasticity of martensite, as reported in [43].

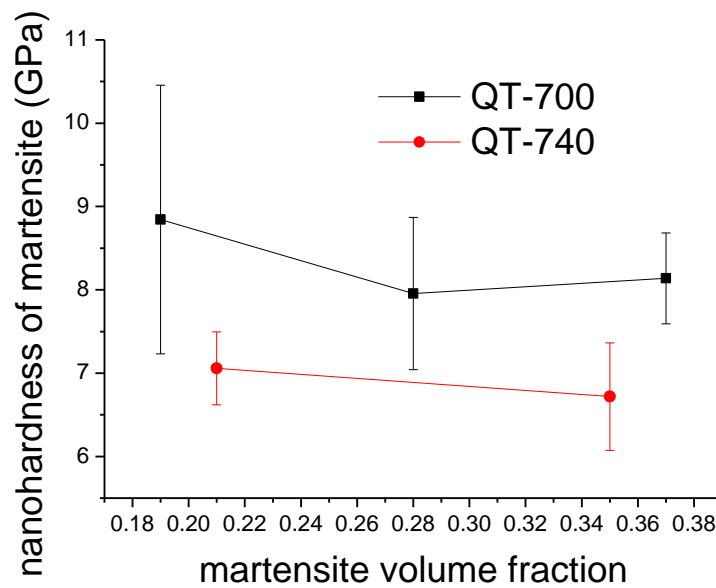


Figure 2.25. Martensite nanohardness of samples annealed at 700°C and 740°C.

2.3.2 On the influence of microstructure refinement

As revealed in section 2.1.2, the cold-rolled reduction and the high manganese content (3.5wt%) promote the achievement of ultrafine-grained DP steels. These microstructures were used to explore the effects of microstructure refinement on both plastic and fracture properties.

2.3.2.1 Heat treatment for ultrafined-grained dual-phase (UFG-DP) steels and microstructure observation

Fluidized bath furnace was used for processing ultrafine-grained DP steels due to its relatively fast heating rate. The samples were inserted into the fluidized bath for 30 minutes and then water-quenched. The martensite volume fraction is controlled by annealing temperature. The UFG-DP annealed at 680°C is shown in Figure 2.26. The martensite islands are small and there are no observable wide and continuous bands. There exist some large ferrite grains, which are elongated along the rolling direction. According to the EBSD analysis (Figure 2.27), the misorientation within the large ferrite grains is low (about 1°), indicating the recrystallized state of this grain.

When the annealing temperature is increased to 700°C, the martensite islands

Chapter 2 Phase transformation

become larger and the connection between martensite islands is more significant due to larger volume fraction (Figure 2.28). In this case, there is still no large and continuous martensite band.

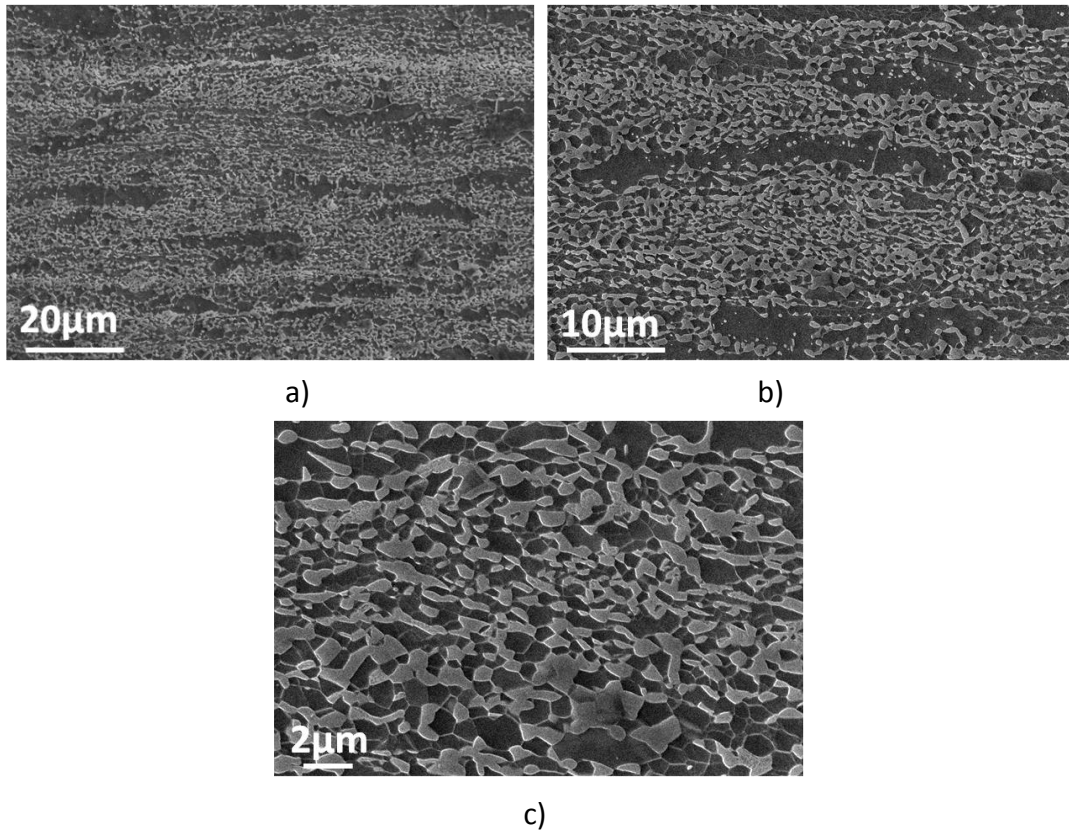
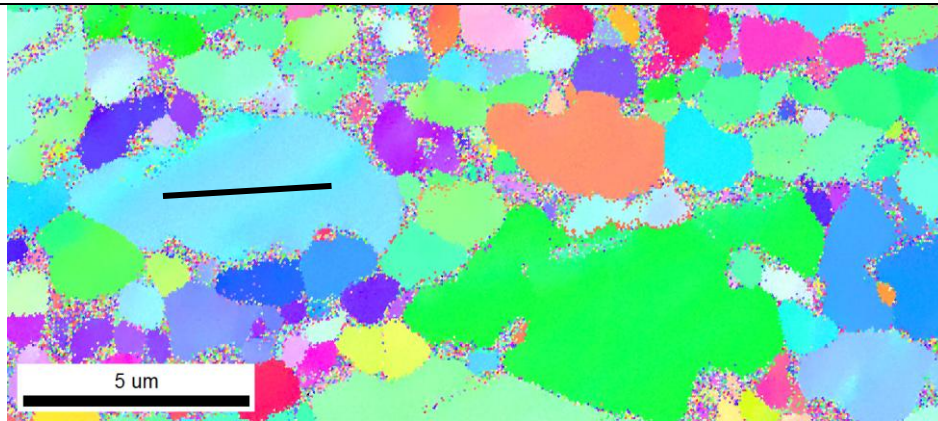
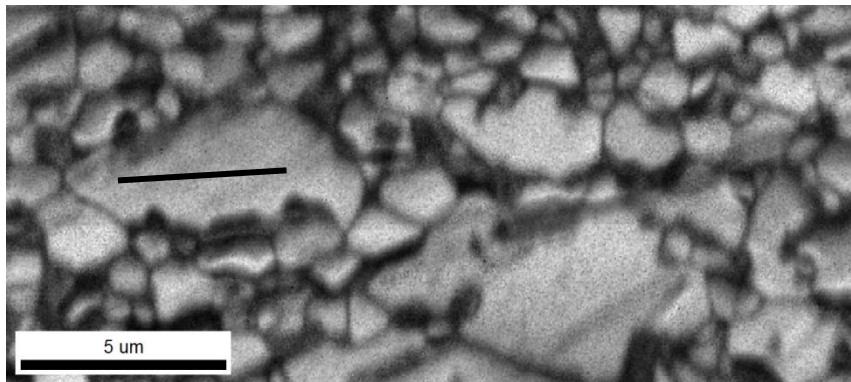


Figure 2.26. Refined dual-phase microstructure after annealing at 680°C with the magnification of 1000 (a), 2000 (b) and 5000 (c). The volume fraction of martensite is about 27%.

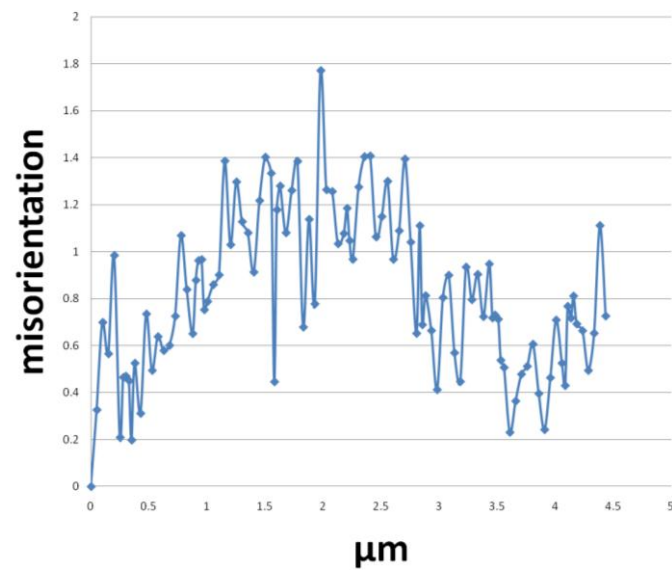
Chapter 2 Phase transformation



a)



b)



c)

Figure 2.27. IPF (Inverse Pole Figure) (a) and IQ (Image Quality) (b) maps of EBSD in a selected area with large ferrite grains. The cumulated misorientation profile within the large ferrite grain is also measured (c).

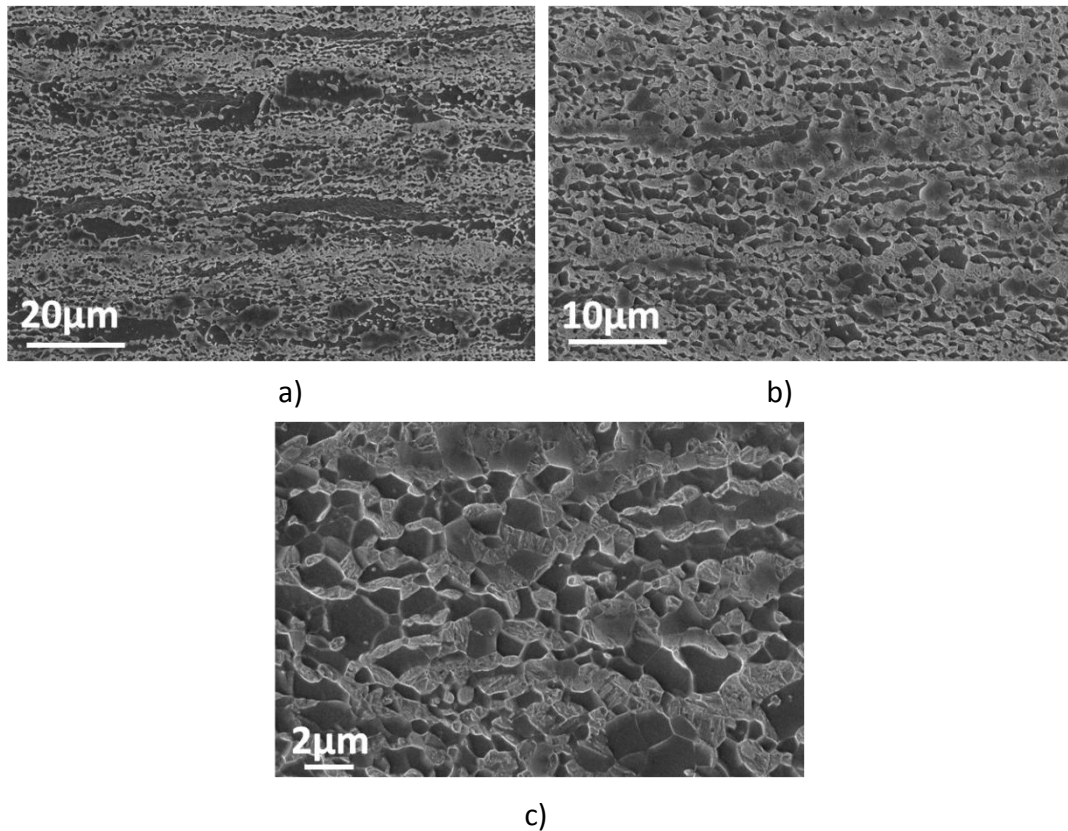


Figure 2.28. Refined DP microstructure after annealing at 700°C with the magnification of 1000 (a), 2000 (b) and 5000 (c). The volume fraction of martensite is about 37%.

2.3.2.2 Heat treatment for coarse-grained dual-phase (CG-DP) steels and microstructure observation

Heat treatments for coarse-grained dual-phase steels were performed in a tube furnace with the slow heating rate of 0.1°C/s, and the volume fraction of martensite is controlled by annealing temperature. As shown in Figure 2.29, for the annealing temperature of 700°C, the ferrite grains are coarse and equiaxed, and the martensite islands are distributed along the grain boundaries. The banding of martensite is obvious.

The martensite bands are more pronounced with higher volume fraction after annealing at 720°C (Figure 2.30). Comparing with the microstructure in Figure 2.28c, wide and continuous martensite bands are observed in CG-DP.

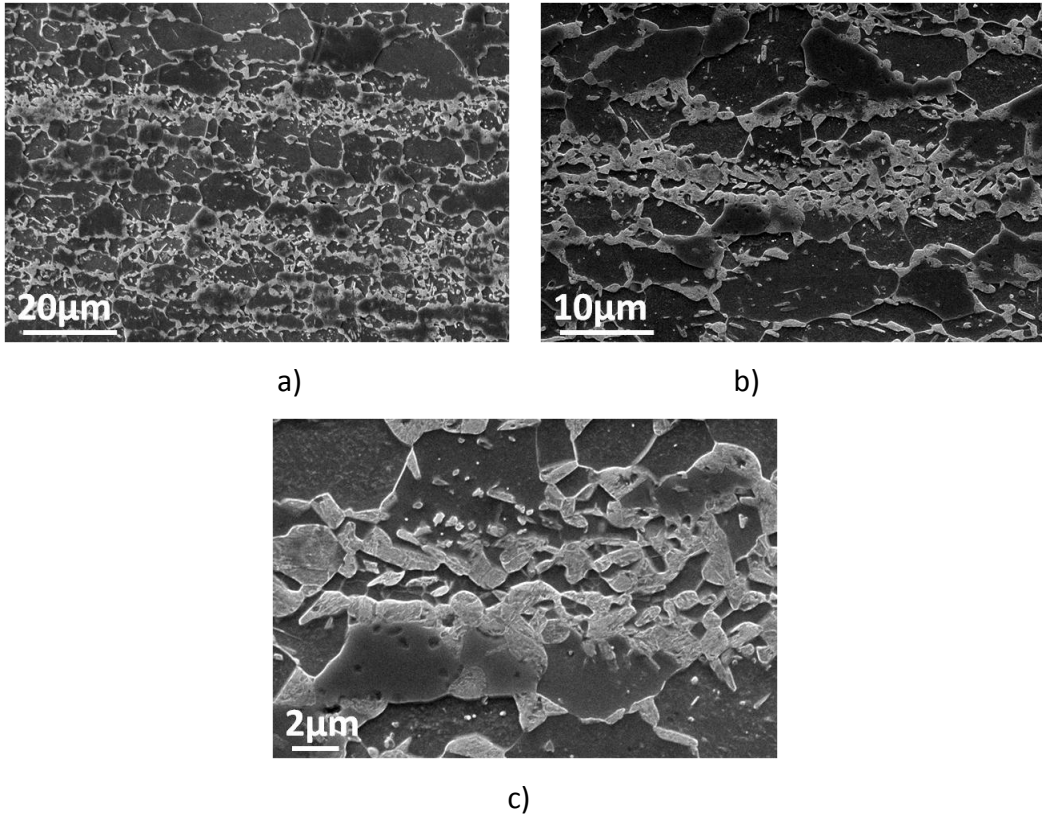


Figure 2.29. Coarse-grained dual-phase microstructure after annealing at 700°C with the magnification of 1000 (a), 2000 (b) and 5000 (c). V_m is about 21%.

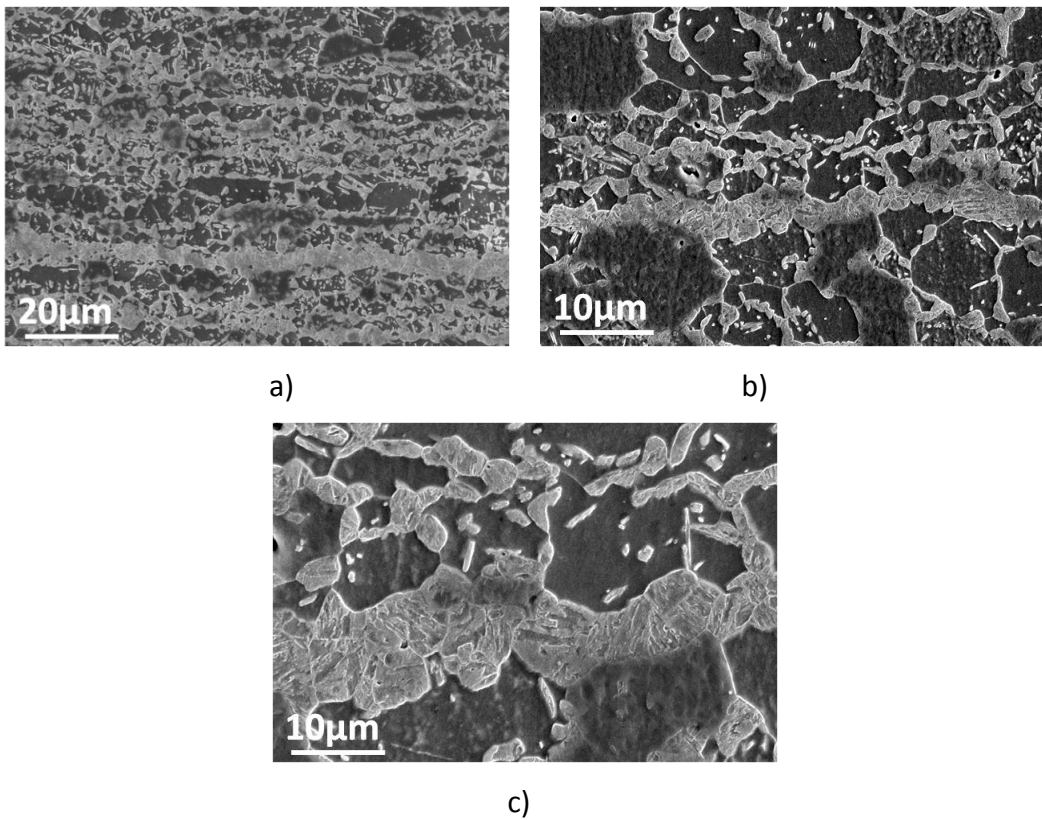


Figure 2.30. Coarse-grained dual-phase microstructure after annealing at 720°C with

the magnification of 1000 (a), 2000 (b) and 5000 (c). V_m is about 36%.

2.3.2.3 Quantitative comparison between the CG- and UFG-DP

The microstructure features of CG- and UFG-DP have been compared quantitatively in Figure 2.31. For both kinds of microstructures, the mean free path of ferrite is decreased with increasing martensite volume fraction, and the mean linear size of martensite is increased. In the case of UFG-DP, both the ferrite and martensite islands are refined. In the UFG-DP with 37% martensite, the mean free path of ferrite and mean linear size of martensite are about $2\mu\text{m}$ and $1.3\mu\text{m}$, respectively; while those of CG-DP with 36% martensite are $4\mu\text{m}$ and $2.5\mu\text{m}$. Notice that the martensite phase in UFG-DP with 27% martensite is smaller than $1\mu\text{m}$ (about $0.7\mu\text{m}$), which might have an impact on austenite stabilization and the hierarchical structure of martensite.

The carbon content in martensite of CG- and UFG-DP is expected to be determined by the phase equilibrium with temperature. As predicted by THERMOCALC, the martensite carbon content at 700°C is about 0.238wt% while that at 720°C is about 0.185wt%. CG-DP is attained by slow heating, during which carbide precipitation and ferrite recrystallization occur. Austenite growth from intragranular carbide is slow (see section 2.2.1.3), and the intragranular carbides in CG-DP-36% are probably not totally dissolved. Therefore, CG-DP-36% (annealed at 720°C) can have similar martensite volume fraction with UFG-DP-37% (annealed at 700°C) but its carbon content in martensite is lower.

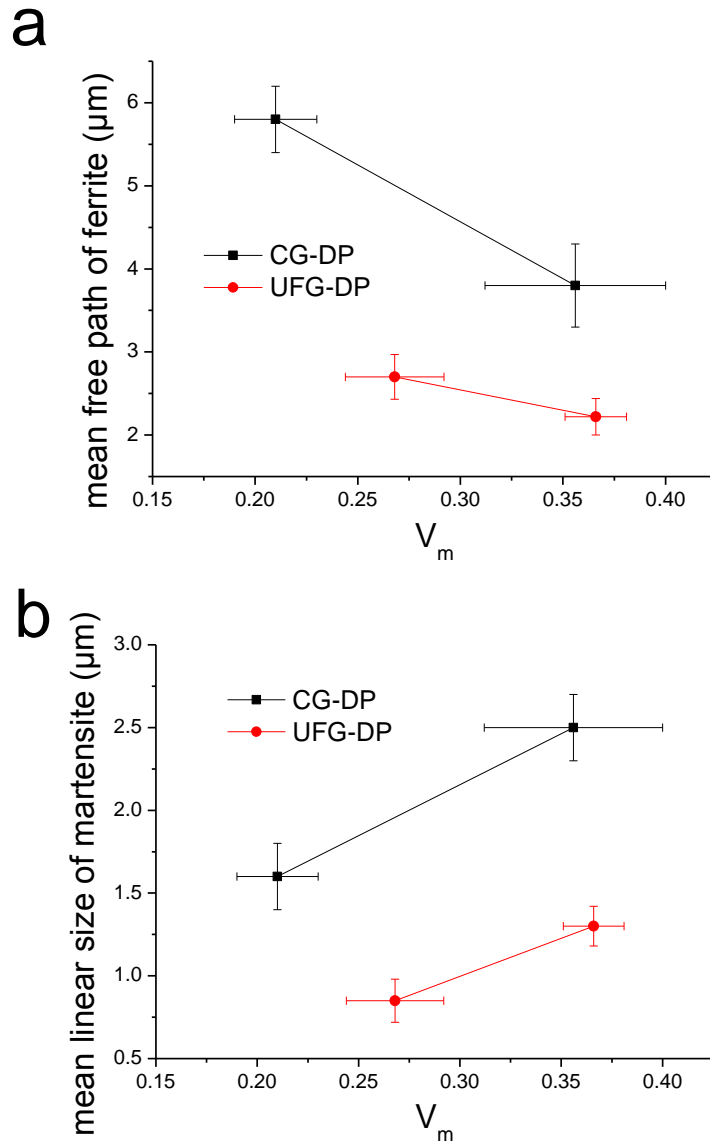


Figure 2.31. Quantification of the mean free path of ferrite (a) and mean linear size of martensite (b) in CG- and UFG-DP microstructures.

2.4 Summary

The re-austenitization from spheroidized microstructure has been studied. The transformation kinetics as a function of temperature has been probed and it is found that the austenite formation is very sensitive to annealing temperature. The observation of microstructure evolution during annealing is made. Austenite islands mainly nucleate at the carbides locating on ferrite grain boundaries. The mechanism of austenite growth is discussed by using DICTRA. It is proposed that the austenite growth is first controlled by Mn partitioning from ferrite and later approaching to

Chapter 2 Phase transformation

final equilibrium by Mn diffusion within austenite. The element distribution in this simple model has been described. Although there are significant carbon and Mn gradients in the small volume of the core, carbon and Mn can be approximated as uniformly distributing within the austenite. The predicted distribution of carbon is supported by the qualitative carbon mapping by NanoSIMS.

The re-austenitization from cold-rolled martensite has also been studied. The refined initial microstructure, high stored energy, and low intercritical temperature due to relatively high Mn content have resulted in significant interaction between ferrite recrystallization and austenite formation. Significantly refined dual-phase microstructure can be attained with conventional heating rate, but there is a lower limit of martensite volume fraction for microstructure refinement.

Based on the results of phase transformation, microstructures have been developed, which will be analyzed for their plastic and fracture properties in the coming chapters. The microstructures developed from spheroidized microstructure are used to investigate the influences of martensite volume fraction and composition, and the proposed effect of annealing temperature on martensite hardness has been confirmed by nanoindentation. Another line of microstructures have also been developed from cold-rolled martensite in order to study the mechanical consequences of microstructure refinement.

Chapter 3 Plastic properties of dual phase steels: experimental investigation and qualitative discussion

Optimization of DP steels requires the knowledge about the specific contributions of various constituents. This has been the subject of extensive investigations [3, 5, 7, 46-49, 52, 53, 55-60, 63, 71-74, 77, 78, 137], but efforts still have to be made to fully exploit the potential of this composite material. The difficulties originate from the complex microstructure of DP steels and the interactions between phases. A variety of parameters, such as the ferrite grain size, and the size, shape, distribution and composition of martensite islands, are necessary to describe the DP microstructure. For a given processing route, these parameters are inter-related so that it is challenging to decouple the various factors for single-variant investigation. Also, the interactions between ferrite and martensite are still un-sufficiently studied, and experiments for probing strain partitioning are still in progress [87, 138-140].

This chapter presents experimental results dedicated to the understanding of the plastic behavior of DP steels. Microstructures have been developed to decouple the influences of martensite volume fraction (V_m) and martensite composition (see chapter 2). In the first two sections, we draw conclusions about the effects of volume fraction and composition of martensite on the plastic properties of DP steels. In the third section, the consequences of microstructure refinement are analyzed. Finally, the highlights are summarized for further rationalization by micromechanical modeling in chapter 5.

3.1 Experimental procedures

- **Tensile test**

The mechanical behavior of the steel grades developed in chapter 2 was measured using uniaxial tensile tests. The sheet steels (with 1mm thickness) were machined into dog-bone specimens with the gauge length of 25mm and the width of 5mm. Tensile tests were performed at room temperature with the displacement rate of 1.5mm/min, which corresponds to an engineering strain rate of 0.001/s. The yield strength is defined as the stress corresponding to 0.2% plastic strain. The uniform elongation is defined by the true strain of necking determined by Considère criterion, which is a measurement of the resistance to strain localization, and the corresponding true stress is defined as tensile strength. Three specimens of each grade were tested.

- **Microstructure characterization**

For the specimens possibly presenting TRIP effect, X-Ray Diffraction (XRD) was used to measure the amount of retained austenite before and after tensile test. EBSD mapping was performed to probe the distribution of retained austenite. The sample preparation procedure for EBSD has been described in chapter 2.

3.2 Influence of martensite volume fraction on strength and ductility of dual-phase steels

3.2.1 Microstructures for comparison

The microstructures were obtained by annealing the spheroidized samples at 700°C (QT-700) with a martensite volume fraction equal to 15%, 17%, 19%, 28% or 37%, as shown in Figure 3.1. The martensite islands mainly nucleate at the ferrite grain boundaries, forming a necklace structure when the martensite islands are fully interconnected. Martensite formation at the intragranular carbides is much delayed and the volume fraction of such intragranular martensite is small. Thus, the mean free path of ferrite defined in Figure 2.21a can be approximated as the ferrite grain size.

The dual-phase microstructure is relatively uniform and equiaxed when V_m is low

Chapter 3 Plastic properties of DP steels

(Figure 3.1a), even though some aggregates of martensite islands can still be observed (Figure 3.1b), which is supposed to be due to Mn segregation [34, 141]. Continuous martensite bands along the rolling direction are becoming obvious when V_m is larger than 19% (Figure 3.1c). The banded structure is most significant when the volume fraction of martensite reaches 37% (Figure 3.1e).

Among these microstructures, the spatial distribution of martensite can be considered the same but the size and connectivity of the second phase are different. Additionally, as predicted by DICTRA and indirectly confirmed by nanoindentation (see chapter 2), the average hardness of martensite phase is relatively constant at 700°C (about 8GPa) even if V_m is increasing.

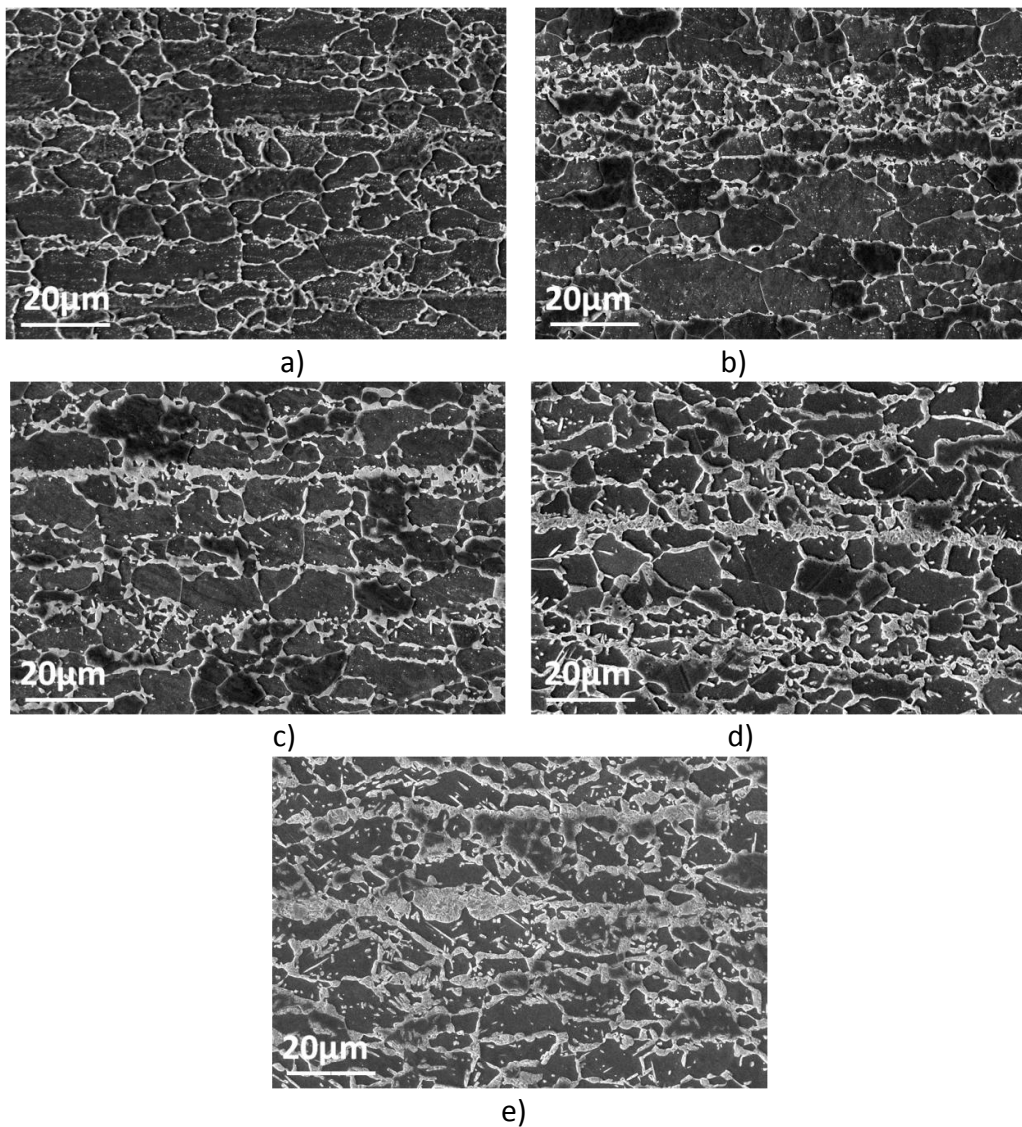


Figure 3.1. QT-700 with martensite volume fractions of 15% (a), 17% (b), 19% (c), 28% (d) and 37% (e) for comparison.

3.2.2 Tensile behavior and work-hardening rate

The tensile behavior of QT-700 is shown in Figure 3.2a for the different martensite volume fractions of 15%, 17%, 19%, 28% and 37%, associated with the tensile response of the spheroidized microstructure (QT). The volume fraction of carbide in QT is about 2%. As V_m is increased, the flow stress is increased accordingly and there is a shape change in the stress-strain curves. When V_m is increased to 28%, the elasto-plastic transition becomes very smooth, and the initial work-hardening rate is high. However, when V_m is smaller than 19%, there is a sharp transition between the elastic and plastic regimes. There seems to be a critical martensite volume fraction, around which the characteristics of the macroscopic response of dual-phase steels are changed, and such critical martensite volume fraction is between 19% and 28% for the present steel grade and processing route.

The yield point is observed in the stress-strain curve of QT, but it is absent for QT-700. QT yields at about 350MPa. But the first yielding of QT-700 initiates at a lower stress, even if the martensite volume fraction is 37%, as shown in Figure 3.2b.

The work-hardening curves of QT-700 (Figure 3.2c) clearly reveal the effect of martensite volume fraction on plastic behavior. For the microstructure with 19% martensite, the initial work-hardening rate is low. After a sharp drop of work-hardening rate during the first initiation of plastic deformation of QT-700-19%, there is a linear relationship between $d\sigma/d\varepsilon$ and σ during most of the flow stress increment. When V_m is increased to 28% and 37%, the initial work-hardening rate is increased significantly, and $d\sigma/d\varepsilon$ does not decrease linearly with stress. The high initial work-hardening rate and its gradual decrease with stress result in a smooth elasto-plastic transition.

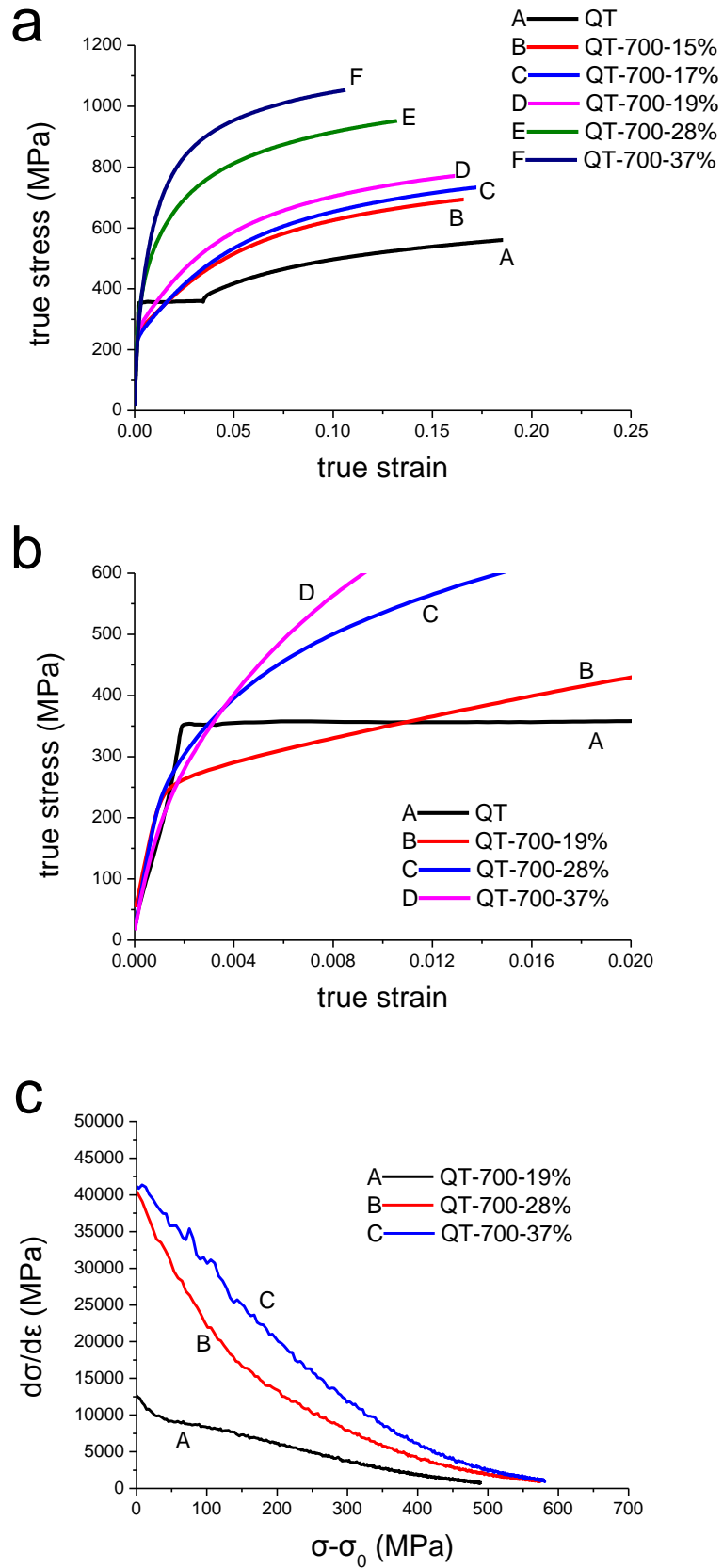


Figure 3.2. True stress-true strain uniaxial tension responses: (a) full curves, (b) zoom of the first percents of deformation, and (c) the Kocks-Mecking plots of

work-hardening of QT-700-19%, 28% and 37%. The tensile curves are shown up to necking.

3.2.3 Yield strength, tensile strength and uniform elongation

The volume fraction of martensite has a very significant influence on the plastic properties. As shown in Figure 3.3a, the yield strength increases linearly with martensite volume fraction. By extrapolating this linearity to zero and 100% martensite, the yield strengths are respectively estimated as 55MPa and 1200MPa, which would correspond to the yield strength of ferrite and martensite, assuming a simple rule of mixture. However, the estimated value for ferrite is much lower than the yield strength of spheroidized microstructure.

The tensile strength also increases linearly with V_m (Figure 3.3b). By extrapolation and assuming a rule of mixture, the tensile strength corresponding to zero and 100% martensite can be estimated as 400MPa and 2300MPa, respectively. The martensite volume fraction has a stronger effect on the tensile strength than on the yield strength. From 15% to 37% martensite, the yield strength increases from 260MPa to 470MPa, with an increment of 210MPa; while the tensile strength increases from 690MPa to 1060MPa and the increment is equal to 370MPa.

Contrary to the yield strength and to the tensile strength, the uniform elongation decreases with increasing martensite volume fraction (Figure 3.3c). QT-700-15% has a uniform elongation of 0.16, but the one of QT-700-37% is 0.11.

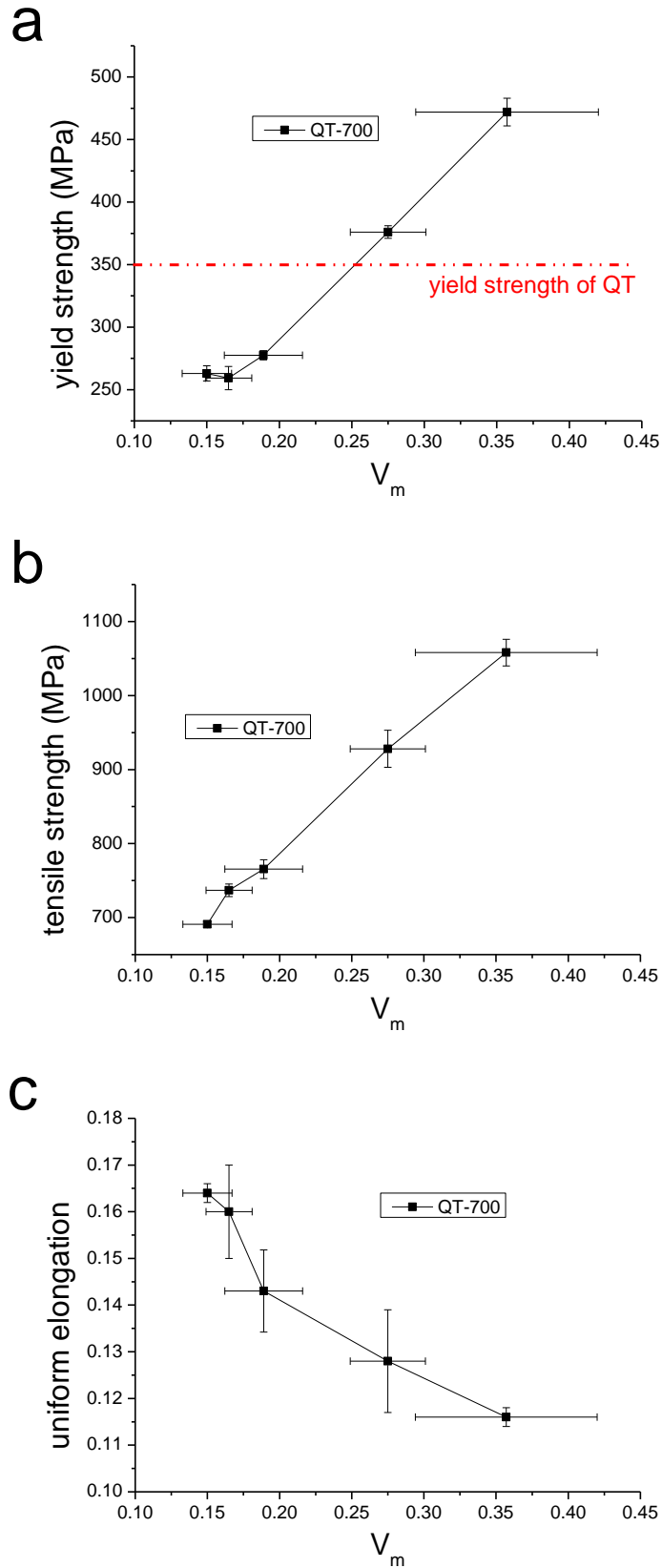


Figure 3.3. Evolution of (a) the yield strength, (b) tensile strength, (c) uniform elongation with the martensite volume fraction. Both yield strength and tensile

strength increase with increasing martensite volume fraction, but the uniform elongation shows an opposite trend.

3.2.4 Brief discussion

3.2.4.1 Influence of the presence of the martensite phase

The ferrite phase alone shows a yield point phenomenon due to static strain aging even when the carbon content is very low [35]. The spheroidized microstructure also shows this behavior (Figure 3.2a). But the presence of martensite can modify the tensile behavior significantly, resulting in the attractive plastic properties of ferrite-martensite dual-phase steels, such as continuous yielding, very high initial work-hardening rate and excellent combination of strength and ductility [3]. The effects of the martensite phase are complex and needs to be clarified.

Firstly, the martensitic transformation brings a shape change and a volume change (of about 2-4% [142]). This transformation results in residual stresses and also introduces geometrically necessary dislocations (GNDs) in the ferrite surrounding martensite so as to accommodate the transformation strain. The residual tensile stresses locate in the ferrite, as reported in [47], and thus the yield stress of DP steels can be lower than in pure ferrite, as shown in Figure 3.2b. The GNDs harden the local ferrite, which has been confirmed by careful nanoindentation [46] and micro-pillar experiments [134], and can be considered as equivalent to a pre-strain effect. The local hardening in the ferrite leads to the heterogeneous spreading of the plasticity in the ferrite matrix [46]. Therefore, if the martensite volume fraction is increased, more dislocations are needed to accommodate the transformation strain, which must influence the macroscopic response.

Secondly and most importantly, the martensite phase exists as a reinforcement of the softer matrix where it is embedded in, and the dual-phase microstructures reveal composite behavior as far as the substantial work-hardening is concerned. The Young's modulus of martensite can be treated the same as ferrite [59], and the dual-phase microstructures can be considered in a first approximation as elastically homogeneous. Load transfer becomes significant when the ferrite matrix deforms plastically while the martensite remains elastic, and the resulting back stress from martensite increases the current flow stress of the material [50] via a kinematic

hardening contribution. As long as the martensite islands remain elastic, the back stress is linear with the volume fraction of second phase [50]. The strength contrast between ferrite and martensite and the resulting plastic incompatibility are the origin of this composite effect. The back stress has been measured to be increasing linearly with strain and results in the high initial work-hardening rate as reported in [48]. The back stress proportional to the martensite volume fraction [50] can explain the results in Figure 3.2a and b that both the flow stress and the work-hardening rate increase significantly with increasing V_m .

The increase of martensite volume fraction can also lead to a decreased ferrite grain size and an increased area of internal boundaries. The associated Hall-Petch effect should strengthen the ferrite matrix and contribute to the strength of the dual-phase microstructure as well. However, according to the measurements in chapter 2, the mean free path of ferrite is only slightly reduced with an increase of martensite volume fraction. For example, the mean free path of ferrite in QT-700-19% is about $5.9\mu\text{m}$, while that of QT-700-28% is about $5.2\mu\text{m}$. It is supposed that the contribution of Hall-Petch effect of ferrite is not significant in this comparison.

3.2.4.2 Effect of martensite volume fraction on yield strength

Ferrite-martensite dual-phase steels are elastically homogeneous and the yield strength of ferrite is much lower than the one of martensite. Therefore, the onset of plastic deformation in ferrite takes place well before than in martensite, and the yield strength of DP steels is primarily controlled by the yield strength of ferrite matrix.

The martensite volume fraction affects the yield strength of ferrite in several ways. Firstly, the residual stress due to martensitic transformation can decrease the yield stress of the surrounding ferrite [47]. This effect is revealed in Figure 3.2b. Additionally, the pre-strain effect has introduced large number of accommodation dislocations and hardened the ferrite close to ferrite/martensite interface, resulting in a high initial hardening rate.

In this study, the yielding of DP steels is characterized by 0.2% yield stress, which involves the initial plastic deformation. Although the DP steels start to yield at a low stress (Figure 3.2b), the high initial work-hardening rate, which is due to the back stress from martensite, can significantly increase the flow stress. The back stress is determined by the amount of martensite. Therefore, as observed in Figure 3.3a, the

yield strength of DP steels increases with an increasing martensite volume fraction.

3.2.4.3 Effect of martensite volume fraction on the tensile strength

During the plastic deformation of the dual-phase microstructure, the martensite phase bears a significant fraction of the load. When the martensite phase remains elastic, the back stress should be proportional to V_m , according to [50]. As a result, the flow stress of dual-phase microstructure is increased with increasing martensite volume fraction, as shown in Figure 3.2a. The strongly increased work-hardening rate with martensite volume fraction (Figure 3.2c) is also a sign of the significant back stress from martensite. The increase of flow stress by increased martensite volume fraction leads to higher tensile strength.

3.2.4.4 Effect of martensite volume fraction on uniform elongation

The back stress due to the plastic incompatibility between ferrite and martensite induces a high work-hardening rate [48]. The magnitude of the back stress has been shown to be proportional to the martensite volume fraction if the martensite remains elastic [50]. Compared with QT-700-19%, the elasto-plastic transition of QT-700-28% becomes smooth, and the work-hardening rate is significantly increased.

An increase of V_m has a negative impact on uniform elongation, as shown in Figure 3.3c. As discussed before, the higher the martensite volume fraction, the higher the work-hardening rate due to back stress, which should act positively on uniform elongation. However, some factors due to higher martensite volume fraction can counteract the effect of martensite strengthening. For instance, when V_m is increased, the connectivity of martensite is enhanced and then the martensite phase is bearing higher stress and plastic deformation can start earlier. The back stress is proportional to the martensite volume fraction if the martensite remains elastic [50]. But once the martensite deforms plastically, the back stress is not increasing linearly with strain but can be kept constant, which is shown in Figure 3.4 [48]. Without the accumulation of back stress, the enhancement of work-hardening will be less

efficient.

This point can be used to rationalize the evolution of work-hardening rate with strain of QT-700-19%, QT-700-28% and QT-700-37%, as shown in Figure 3.5. In the initial stage of deformation (below the true strain of 0.03), the martensite phase in these microstructures remains almost elastic, and the work-hardening rate is higher with increasing V_m . As the deformation proceeds, the stress of martensite reaches the yield stress of this phase and the work-hardening rate decreases dramatically. With higher V_m , the work-hardening rate decreases more significantly due to more plastic strain in martensite. Therefore, the work-hardening rate of QT-700-37% is lower than that of QT-700-19% at large strain, resulting in a lower uniform elongation.

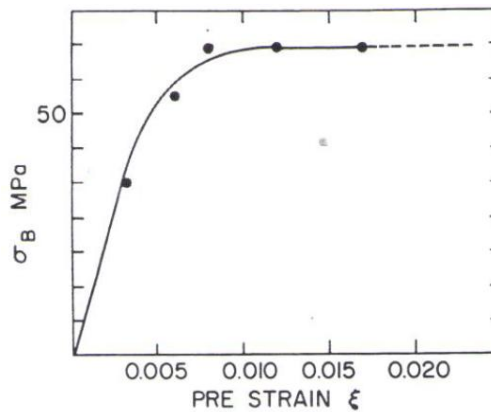


Figure 3.4. Diagram showing the variation of the back stress deduced from the values of the permanent softening as a function of tensile strain [48].

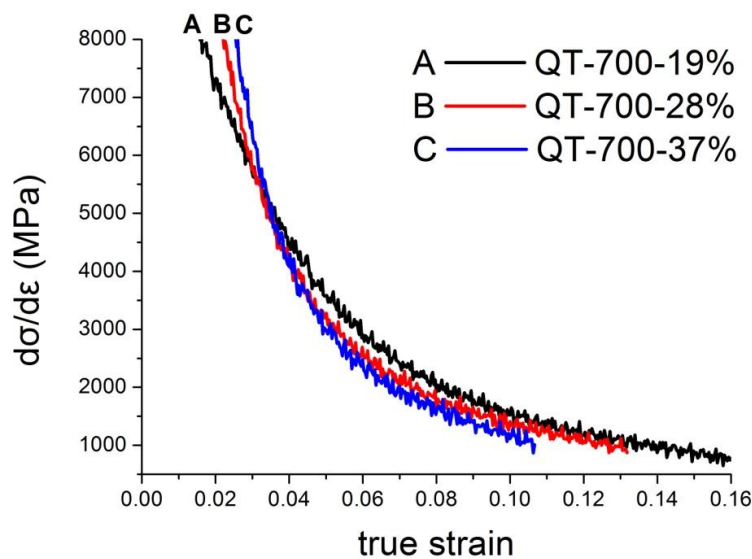


Figure 3.5. Evolution of work-hardening rate with strain of QT-700-19%, QT-700-28% and QT-700-37%.

3.3 Influence of martensite composition on strength and ductility of dual-phase steels

3.3.1 Yield strength, tensile strength, uniform elongation and strength-ductility product

QT-700 and QT-740 have been developed in order to decouple the effects of martensite composition at constant martensite volume fraction (chapter 2). The hardness of martensite in QT-700 is higher than in QT-740 due to higher carbon and manganese contents (Figure 2.25).

The comparison of yield strength and tensile strength between QT-700 and QT-740 are shown in Figure 3.6a and b. The martensite hardness has a limited impact on the yielding of DP steels. There is a linear relationship between the tensile strength and V_m in QT-700. However, the trend in QT-740 is different. When V_m is smaller than 20%, QT-740 has the same tensile strength as QT-700 and a linear relationship with V_m is also observed. But when V_m is higher, the evolution deviates from linear. The strength of QT-740 becomes lower than QT-700 at high V_m : the tensile strength of QT-700-37% is 1060MPa while for QT-740-35% it is equal to 950MPa.

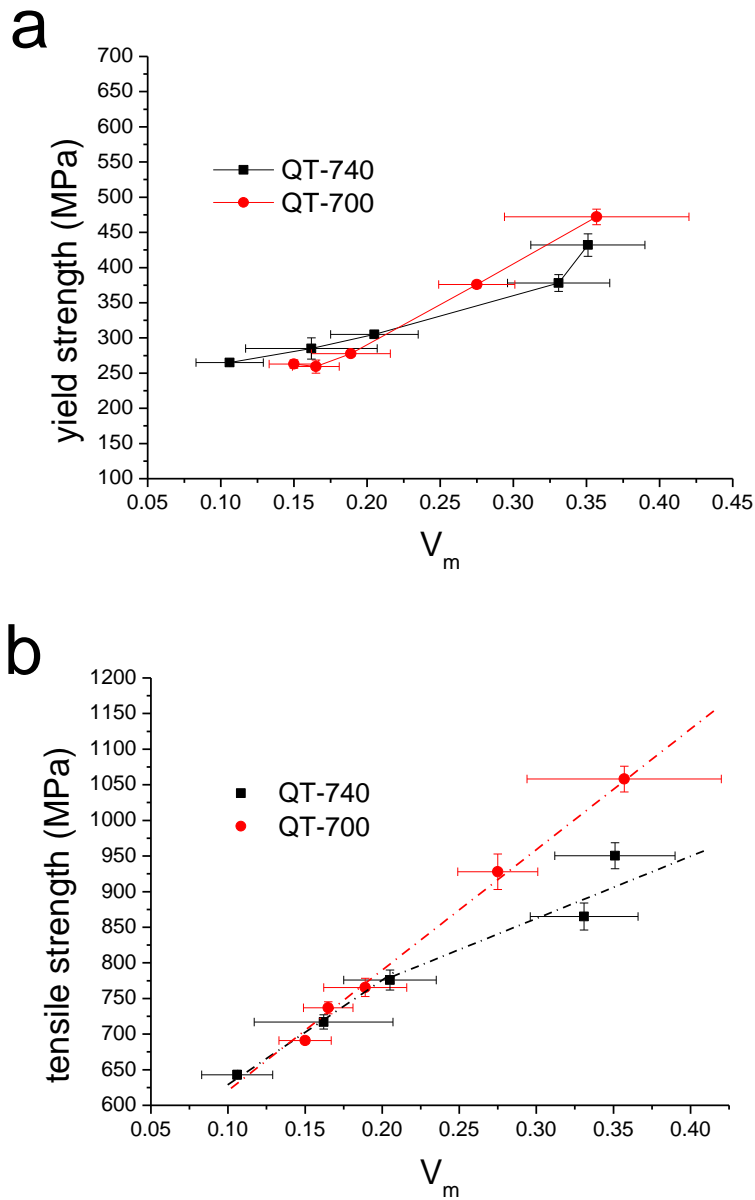
The comparison between the uniform elongations is shown in Figure 3.6c. On average, the uniform elongation is roughly the same for QT-700 and QT-740 except for the case of high volume fraction of martensite. With about 37% of martensite, the difference becomes non-negligible. The uniform elongation of QT-700-37% is equal to 0.11 while it is 0.08 for QT-740-35%.

The comparison of the strength-ductility product shows significant differences between QT-700 and QT-740 (Figure 3.6d). With the increase of V_m , the strength-ductility product, which is related to the energy absorption ability, of QT-740 keeps decreasing, although the tensile strength is increasing. On the contrary, the strength-ductility product of QT-700 remains relatively constant. The difference between QT-700 and QT-740 is enhanced with larger V_m .

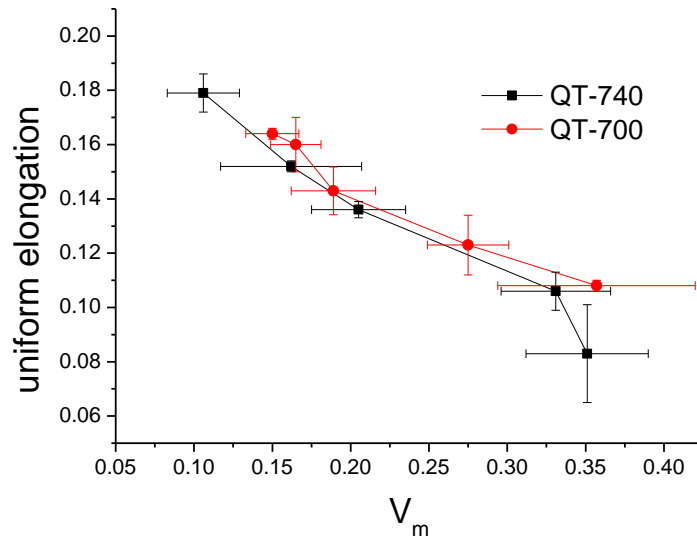
The overall effect of martensite composition on the plastic properties of dual-phase steels and the trade-offs between the properties are shown in Figure 3.6e and f. For both QT-700 and QT-740, the tensile strength decreases when the uniform

Chapter 3 Plastic properties of DP steels

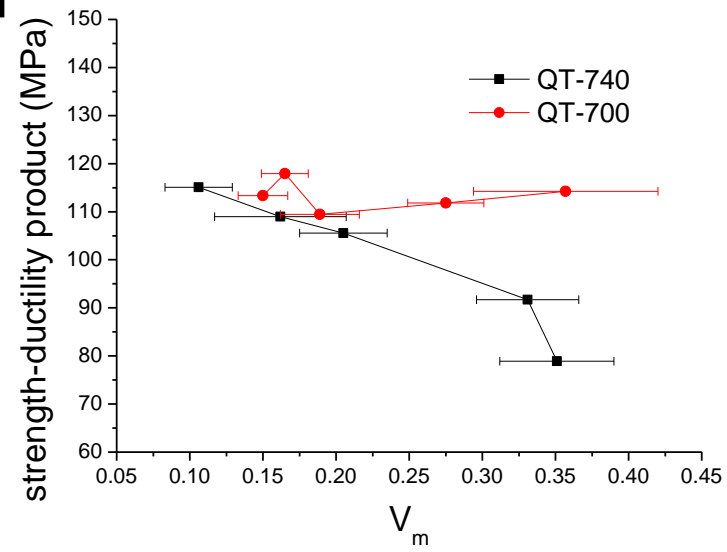
elongation increases (Figure 3.6e). Compared with QT-740, the curve of QT-700 is moved upwards in the space of tensile strength and uniform elongation. Additionally, the strength-ductility product remains constant with changing tensile strength in QT-700, but it shows a decreasing trend for QT-740 (Figure 3.6f). Hence, QT-700 has better plastic properties than QT-740 due to higher martensite hardness.



C



d



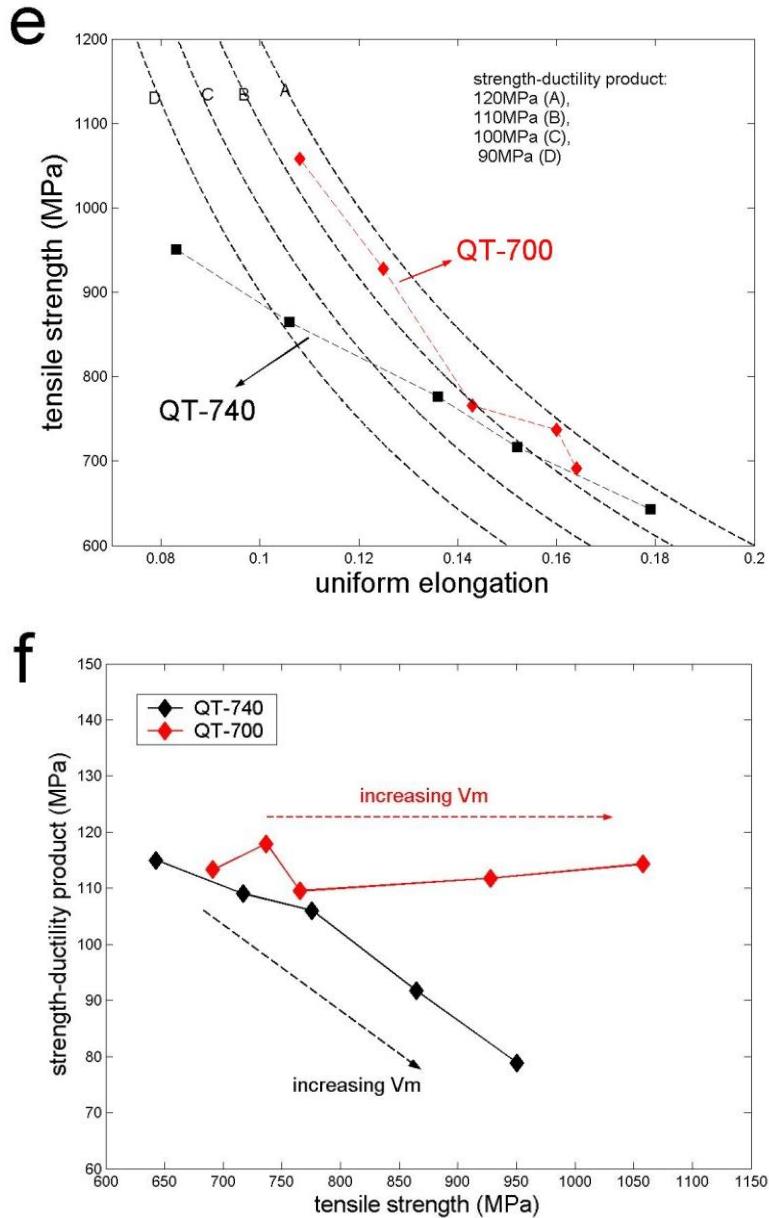


Figure 3.6. Comparison between QT-700 and QT-740 on the evolution of yield strength (a), tensile strength (b), uniform elongation (c), strength-ductility product (d) with V_m , and the tensile strength—uniform elongation relationship (e) and tensile strength—strength-ductility product relationship (f).

3.3.2 Comparison between QT-700-37% and QT-740-35%: case of similar martensite volume fraction

QT-700-37% and QT-740-35% are selected to reveal the effect of martensite composition. The tensile curves are shown in Figure 3.7a. The yield strength of

Chapter 3 Plastic properties of DP steels

QT-740-35% and QT-700-37% are 432 ± 16 MPa and 472 ± 11 MPa, respectively. These results show that the effect of martensite composition on yield strength is relatively weak. However, the flow stress of QT-740-35% is lower than QT-700-37% and the work-hardening rate is also lower except in the initial deformation range (Figure 3.7b). This higher hardening rate of QT-700-37% is essential in improving the balance between tensile strength and uniform elongation by increasing martensite hardness.

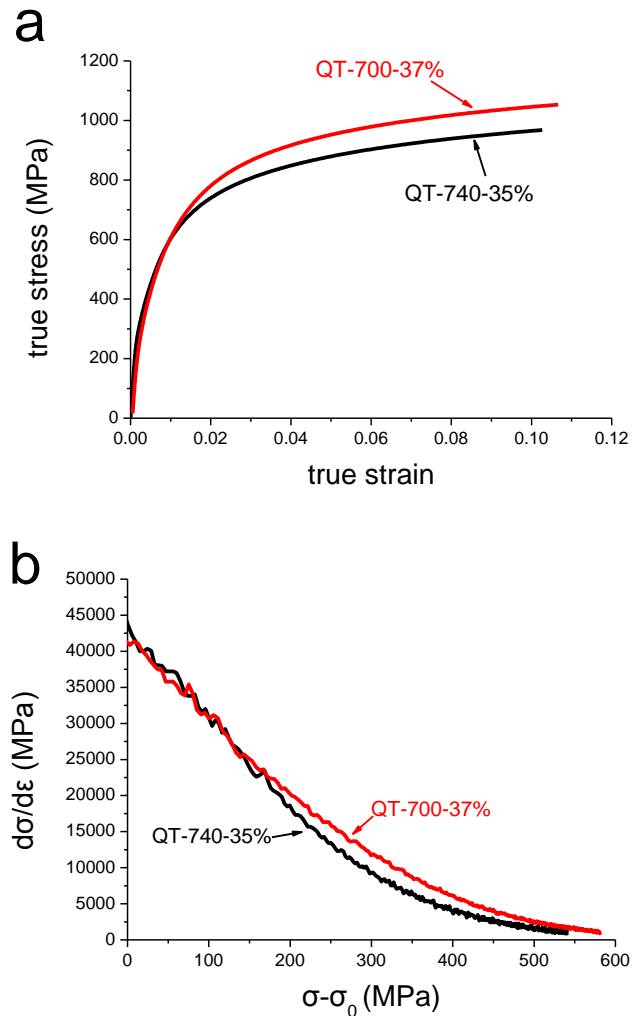


Figure 3.7. Comparison of tensile and work-hardening curves of QT-700-37% and QT-740-35%. The tensile curves are shown upto necking.

3.3.3 Comparison between QT-700-28% and QT-740-35%: case of different martensite volume fractions but similar tensile strength

The impact of martensite composition or hardness is also shown in the comparison between QT-700-28% and QT-740-35%, which have different volume fractions of martensite but similar tensile strength, as shown in Figure 3.6b.

QT-700-28% starts yielding at lower stress (Figure 3.8a), which is in agreement with the result in Figure 3.3a that the yield strength is lower with less martensite. But in the later plastic deformation, it keeps being hardened and reaches the same tensile strength of QT-740-35%.

The differences in macroscopic response are also clearly shown in the work-hardening curves in Figure 3.8b. QT-740-35% has higher martensite volume fraction than QT-700-28%, and there is a higher initial work-hardening rate. In the later deformation, the work-hardening rate of QT-740-35% decreases faster than QT-700-28%, and the work-hardening curves converge at high stress, corresponding to the same strength level of these microstructures. These results reveal that with higher hardness of martensite, the tensile strength can remain the same with lower V_m . Furthermore, lower V_m leads to higher uniform elongation.

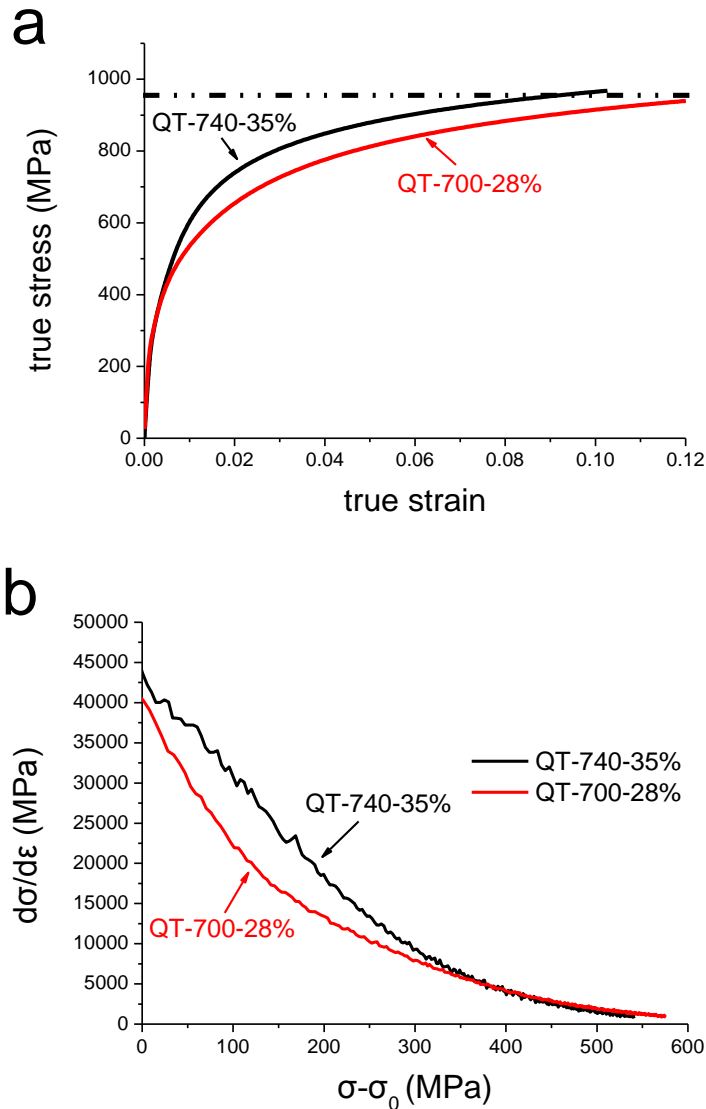


Figure 3.8. Comparison of tensile (a) and work-hardening (b) curves of QT-740-35% and QT-700-28%.

3.3.4 Brief discussion

In earlier literature reports [5, 52, 53, 59], the influences of the microstructure features, such as grain size and morphology, are not sufficiently decoupled from martensite composition, so that the experiments are not examining the effect of hardness of martensite only. For example, the ferrite grain size has important influence on the flow properties of dual-phase steels [56], which might mix with the effect of carbon content in martensite. The experiments in this section aim at examining separately the influence of morphological features and the martensite

composition in order to get a clear interpretation of the effect of martensite hardness. In the comparison between QT-700 and QT-740, the microstructure can be considered the same if V_m is constant. The hardness of martensite is higher in QT-700, which has been confirmed by the nanohardness measurement (Figure 2.25).

The composite behavior is caused by the load transfer to martensite due to the plastic incompatibility between ferrite and martensite. The back stress initially increases linearly with strain but reaches a constant value in the later deformation, which corresponds to the yielding or failure of martensite [48] (see Figure 3.4). Considering the relationship between plastic incompatibility and the composite behavior, the plastic deformation of martensite is essential to the load transfer. Therefore, the martensite hardness, which is controlled by the composition [40, 43], must be the important parameter determining the plastic properties of dual-phase steels.

3.3.4.1 Hardness of martensite and tensile strength

The tensile strength of QT-700 keeps a linear relationship with V_m , but QT-740 shows a different behavior, as shown in Figure 3.6b. When the martensite volume fraction is smaller than 20%, QT-740 keeps the same trend as QT-700 even though the hardness of martensite is lower (see chapter 2). When V_m is further increased, the tensile strength of QT-740 is no longer increasing linearly but keeps a lower level than QT-700.

Two points are raised in this comparison. The first point is that the tensile strength is not sensitive to the martensite composition when V_m is low. In another words, martensite hardness is only influencing the tensile strength with sufficiently high V_m . The second point is that only QT-700 shows a linear tensile strength— V_m relationship. It is predicted by DICTRA that QT-700 should have relatively constant carbon content in martensite, and the nanoindentation measurement in chapter 2 supports this prediction, which supports the assumption of the rule of mixture as well. For the case of QT-740, it has been checked that the martensite nanohardness is similar for 21% and 35% of martensite, but the linear relationship is not followed. Therefore, constant strength of the second phase is not a sufficient condition for generating a linear relationship.

These two points can be rationalized with the deformation state of martensite. Firstly,

Chapter 3 Plastic properties of DP steels

when V_m is low, the flow stress is low and the martensite remains almost elastic even though significant load has been transferred to it. Since the composition cannot change the elastic properties of martensite, the tensile strength in this case is not sensitive to the hardness of martensite. Secondly, when V_m is further increased, the flow stress of DP microstructure is increased. By load transfer, martensite bears a higher stress and plastic deformation starts when it reaches the yield stress, resulting in a relaxation of back stress [48] (Figure 3.4). Therefore, the tensile strength is dependent on the hardness of martensite when V_m is large.

It is proposed that high hardness of martensite is the sufficient condition for the linear strength— V_m relationship. This is supported by the observation in [55]. In [55], the microhardness of the hot-rolled ferrite-martensite dual-phase microstructures shows a linear relationship with up to a martensite volume fraction of 40%, which corresponds to a variation of carbon content in martensite from about 0.4wt% to 0.2wt%, as shown in Figure 3.9. This linear relationship can be explained by the fact that the martensite in these microstructures remains elastic so that the microhardness is only dependent on V_m .

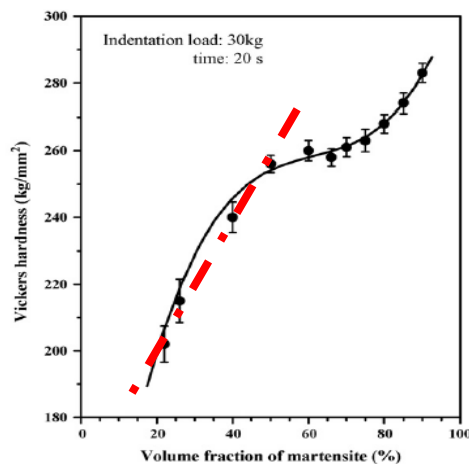


Figure 3.9. Variation of Vickers hardness with percentage volume fraction of martensite [55].

3.3.4.2 Hardness of martensite, work-hardening and uniform elongation

In DP steels, the martensite phase is the load-bearing constituent. The yielding or

Chapter 3 Plastic properties of DP steels

failure of martensite can result in the relaxation of back stress and a less efficient work-hardening [48]. From this point of view, increasing hardness of martensite is beneficial to delay the yielding of martensite. As shown in Figure 3.7b, QT-700-37% has higher hardness of martensite, and it has higher work-hardening rate than QT-740-35% during deformation until necking. The difference in initial work-hardening rate is negligible, indicating that the martensite hardness is not influencing significantly the yielding of dual-phase microstructure. As the deformation continues, the difference in work-hardening rate increases, and QT-740-35% shows a lower work-hardening rate.

Another consequence of higher hardness of martensite is that lower V_m is required to maintain the tensile strength but the uniform elongation can be larger, as shown in the comparison between QT-700-28% and QT-740-35% in Figure 3.8. The flow stress of QT-700-28% keeps below QT-740-35%. But since it has higher uniform elongation, it can reach the same tensile strength as QT-740-35%.

The improved balance between tensile strength and uniform elongation by increasing hardness of martensite has a strong impact on the strength-ductility product. As shown in Figure 3.6d, the strength-ductility product of QT-740 keeps decreasing with increasing V_m , which is dominated by the decrease of uniform elongation. But for QT-700, although the uniform elongation also decreases with increasing V_m , the increased tensile strength results in a relatively constant strength-ductility product.

However, the effect of hardness of martensite on the plastic properties is still not clear [52, 53, 59, 76]. It is concluded in [52, 53] that the uniform elongation decreases when the martensite carbon content is increased. Notice that the carbon content in martensite in [52, 53] can be as high as 0.6wt%, implying a hard but brittle martensite [39, 40]. The fracture of martensite might be influencing the plastic flow of the overall material by inducing a softening effect. The results in [59, 76] show that the ductility of dual-phase steels can increase with the martensite carbon content for a fixed volume fraction of martensite, except for the DP microstructures with a high V_m and a high martensite carbon content.

The premature failure of martensite can explain this discrepancy. For example, in the literature [52], for the microstructures developed from the same initial state but annealed at different temperatures to change both the martensite volume fraction and composition, it is found that the reduction of area is not decreasing but is increasing with increasing V_m (Figure 3.10), indicating that the martensite phase

Chapter 3 Plastic properties of DP steels

annealed at lower temperature is brittle due to the high carbon content. Accordingly, for the case of 30% martensite, the work-hardening rate of the microstructure with 0.4wt% carbon in martensite is initially higher but decreased to below the one with 0.2wt% carbon at large strain. The decrease of work-hardening rate is related to the martensite failure that can result in the release of back stress (Figure 3.11). Therefore, too high carbon content in martensite (0.6wt% for example) will firstly result in a brittle martensite, and the premature failure of martensite will decrease the work-hardening rate at large strain by decreasing the efficiency of the load transfer and then decrease the uniform elongation.

The possible damage-induced softening has been used to rationalize the results in Figure 3.12 [59]. For the case of 15% martensite where the flow stress is low and so is the probability for martensite failure, the uniform elongation is increased with martensite carbon content. For the case of 30% martensite where the flow stress is higher and so is the probability for martensite failure, the uniform elongation is also increased with martensite carbon content but the increment from 0.3wt% to 0.6wt% carbon content is very small due to damage-induced softening. As to the case of 60% martensite, the load transfer leads to high stress level in martensite and the martensite failure becomes significant. This damage-induced softening can be observed by the decrease of incremental work-hardening rate in the case of 0.6wt% of carbon content in 30% and 60% of martensite shown in Figure 3.13 [76].

Therefore, from a theoretical point of view, the prediction of uniform elongation of dual-phase steels with high martensite carbon content and large martensite volume fraction requires the consideration of damage in the model of plasticity.

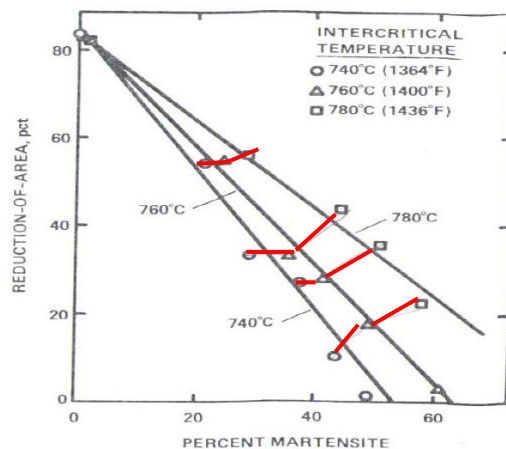


Figure 3.10. Reduction of area of dual-phase steels. The microstructures developed from the same initial states but annealed at different temperatures have been

indicated by red lines [52].

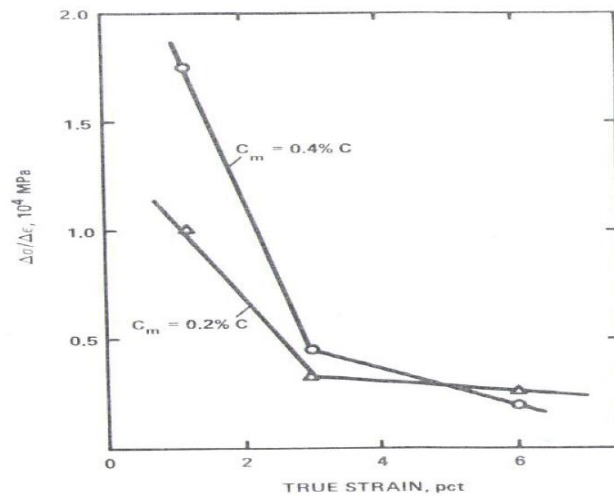


Figure 3.11. Work-hardening rate at 30 percent martensite of ferrite-martensite steels with 0.2wt% and 0.4wt% martensite [52].

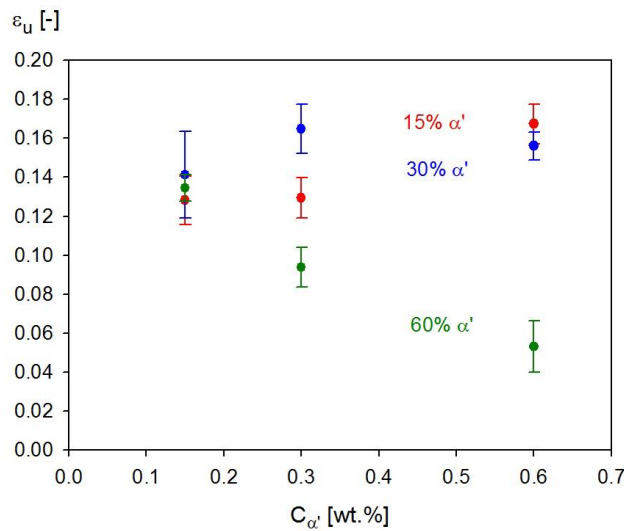


Figure 3.12. Evolution of uniform strain with martensite volume fraction for microstructures with long elongated particles and varying martensite carbon content [59].

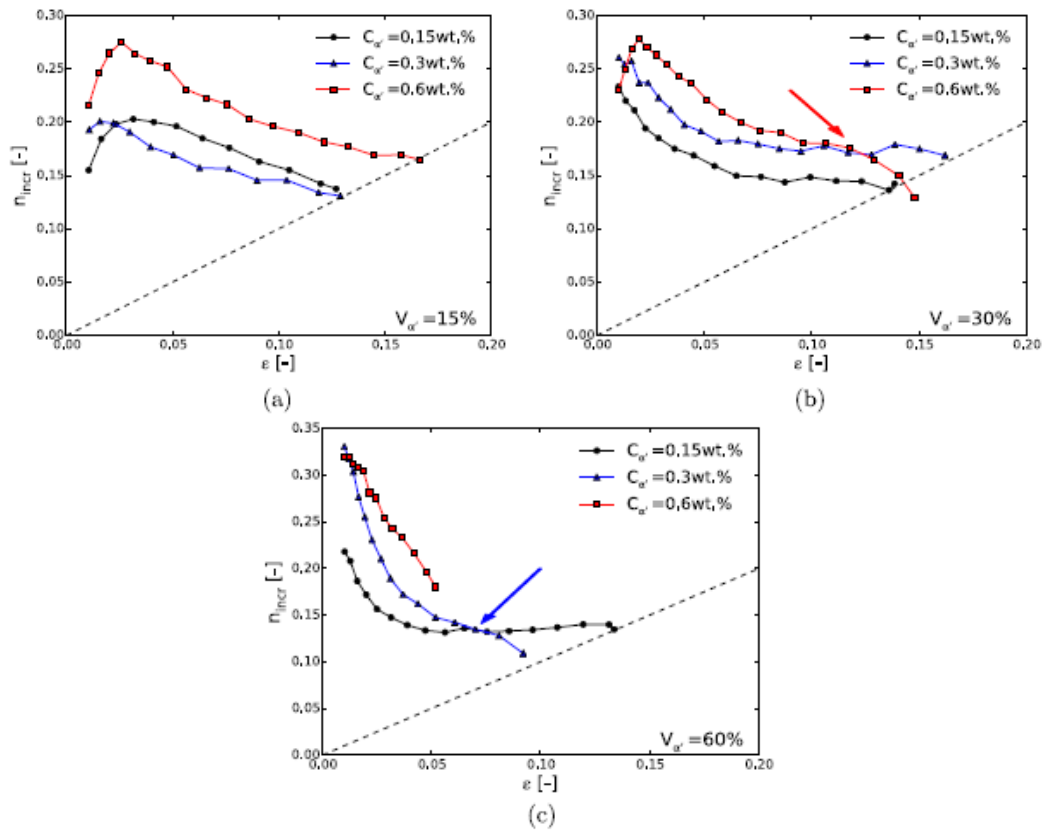


Figure 3.13. (a-c) experimental incremental hardening curves up to the point of maximum load for varying martensite volume fractions and carbon contents (long elongated microstructure). Arrows indicate possible damage-induced softening. [76]

3.4 Influence of microstructure refinement on strength and ductility of dual-phase steels

The strength of dual-phase steels is mainly a consequence of the reinforcement due to martensite. The hardness contrast between ferrite and martensite is the origin of the load transfer and the significant back stress that lead to the remarkable strength/ductility balance of dual-phase steels. In this context, refining the grain size of ferrite will firstly reduce the hardness contrast between ferrite and martensite. Also, refining the dual-phase microstructure actually is modifying the distribution of martensite islands as well.

Specific microstructures, as presented in chapter two, have been developed to examine the mechanical consequences of microstructure refinement.

3.4.1 Tensile behavior of coarse-grained dual-phase steels (CG-DP) and ultrafine-grained dual-phase steels (UFG-DP)

The tensile curves of CG-DP with 21% and 36% of martensite are shown in Figure 3.14a. Higher V_m leads to smoother elasto-plastic transition, high initial work-hardening rate and higher tensile strength, but the uniform elongation is decreased. These are in accordance with the conclusions raised in section 3.2.

The tensile curves of UFG-DP with 27% and 37% martensite are shown in Figure 3.14b. UFG-DP-37% has the same characteristics with CG-DP. But UFG-DP-27% presents different tensile behavior. Although it has a higher V_m than CG-DP-21%, discontinuous yielding is observed, and this lasts for a strain of about 0.01. There is no very high initial work-hardening rate as expected with this amount of second phase. Nevertheless, in the ultrafine-grained microstructures, the tensile strength is increasing with V_m , but the uniform elongation is decreasing.

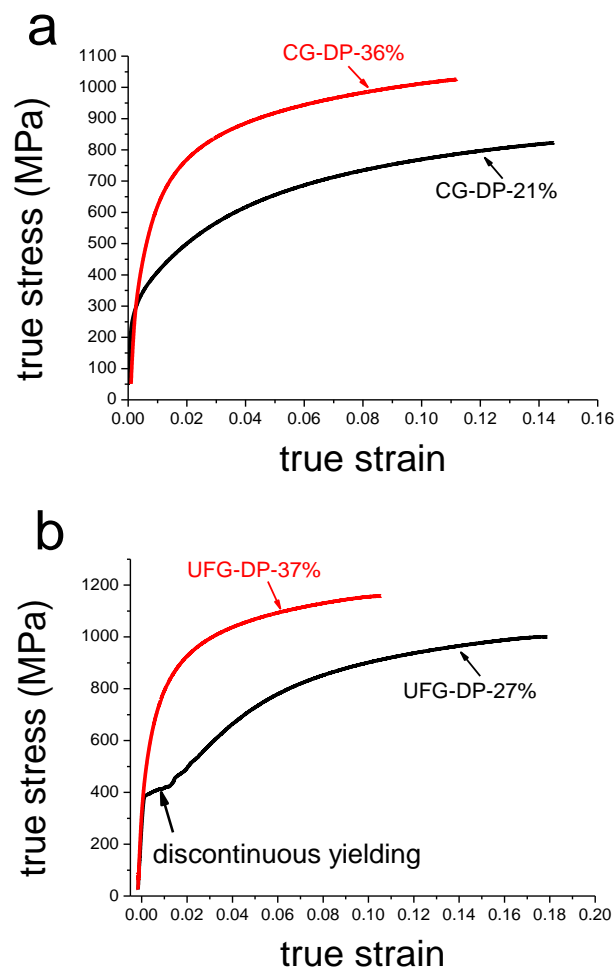


Figure 3.14. Tensile curves of CG-DP (a) and UFG-DP (b). The tensile curves are shown

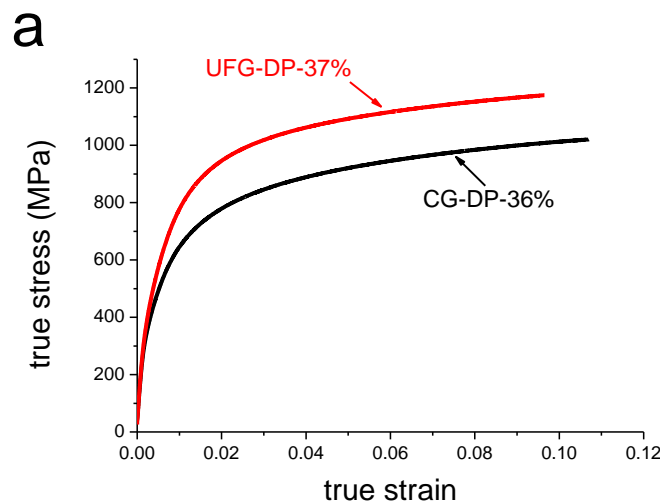
upto necking.

3.4.2 Comparison between CG-DP-36% and UFG-DP-37%

The tensile curves of CG- and UFG-DP with similar V_m are compared in Figure 3.15a. Both curves exhibit a smooth elasto-plastic transition. CG-DP-36% yields at lower stress and the flow stress remains lower than that of UFG-DP-37% during later deformation.

The work-hardening curves in Figure 3.15b clearly show the different mechanical response. UFG-DP-37% has higher initial work-hardening rate. As the stress increases, the work-hardening rate of both samples decreases continuously, and the value of UFG-DP-37% keeps higher than that of CG-DP-36%. The difference in work-hardening rate decreases when the deformation is approaching the onset of necking.

The uniform elongation between these two microstructures is similar. The value of UFG-DP-37% is 0.094 ± 0.005 ; while that of CG-DP-36% is slightly higher as 0.107 ± 0.004 . Therefore, the conclusion in this comparison is that microstructure refinement of DP steels will lead to increased strength at the expense of a slightly lower ductility.



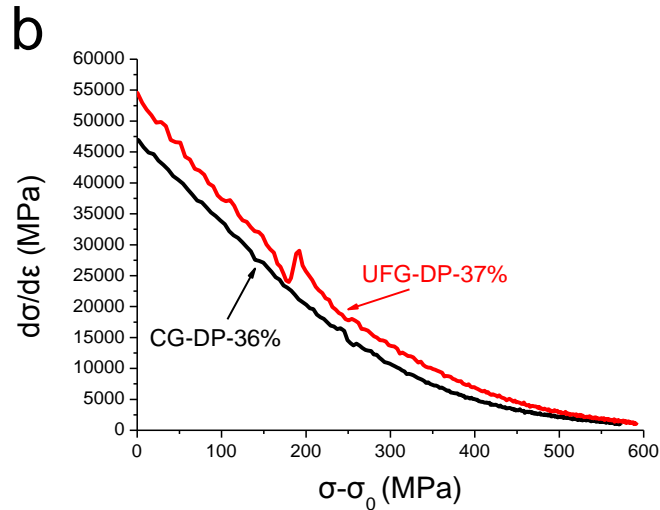


Figure 3.15. Tensile curves (a) and Kock-Mecking plots of work-hardening (b) of UFG-DP-37% and CG-DP-36%. The curves are shown up to necking.

3.4.3 Bonus of TRIP effect

The tensile curve of UFG-DP-27% in Figure 3.14b shows discontinuous yielding, which is not usual for ferrite-martensite dual-phase steels with such martensite volume fraction but is a typical feature of TRIP-assisted multiphase steels [143-145]. Therefore, it is necessary to identify whether or not there is occurrence of a TRIP effect in this microstructure.

3.4.3.1 Distribution of retained austenite

Retained austenite can be identified with EBSD mapping to reveal its distribution. As observed in Figure 3.16, the ferrite grain boundaries can be identified by the darkness due to low confidence index, and the martensite, which has high density of defects, is located in the dark blocks. The retained austenite of size less than $1\mu\text{m}$ is observed at the grain boundaries, neighboring the blocks of martensite. Since the amount of retained austenite is low, no banded features are observed.

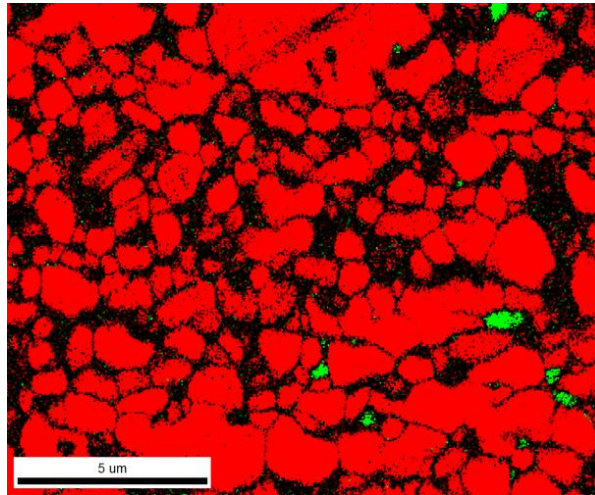


Figure 3.16. EBSD mapping of retained austenite in UFG-DP-27% superimposed with confidential index. The BCC phase is in red and the FCC phase is in green. The dark area is with low confidential index, which should be corresponding to grain boundaries and martensite phase.

3.4.3.2 Proof of TRIP effect

In order to confirm the TRIP effect in this microstructure, XRD measurement has been performed to identify the amount of retained austenite before and after tensile test. As shown in Table 3.1, the volume fraction of retained austenite in UFG-DP-27% before loading is about 16%, but decreases down to zero at the end of the tensile test in the uniform region, which corresponds to the strain of 0.16. The loss of retained austenite during deformation is a proof of TRIP effect. On the contrary, there is no observable retained austenite in UFG-DP-37% by XRD before tensile test, and there is no TRIP effect in this microstructure.

Sample	Volume fraction of retain austenite	
	before tensile test	After tensile test
UFG-DP-27%	16%	0
UFG-DP-37%	0	0

Table 3.1. XRD measurement of retained austenite.

3.4.3.3 Work-hardening of UFG-DP-27%

The work-hardening curve of UFG-DP-27% is shown in Figure 3.17. In the initial stage

of yielding up to the strain of 0.01, the work-hardening rate is very low, and this is due to the discontinuous yielding (see the tensile curve in Figure 3.14b). As the deformation continues, the work hardening rate is increasing dramatically by the interaction with the second phase. The work-hardening rate fluctuates significantly at strains in the range between 0.02 and 0.03 (shown by the arrow). After that, it decreases continuously.

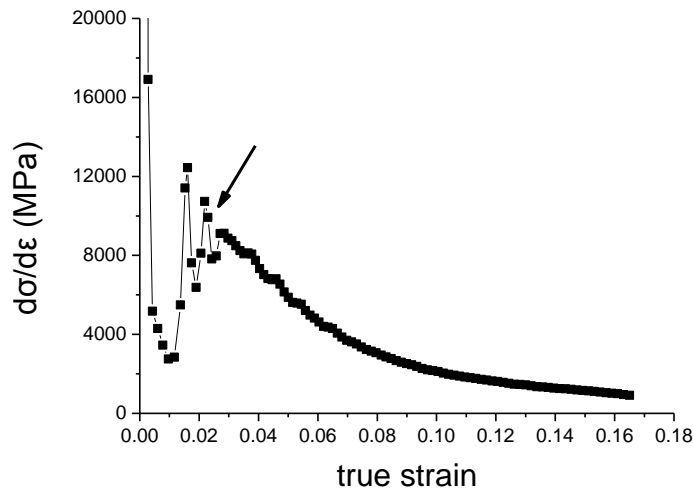


Figure 3.17. Work-hardening curves of UFG-DP-27% annealed at 680°C.

3.4.4 Comparison of mechanical properties between CG- and UFG-DP

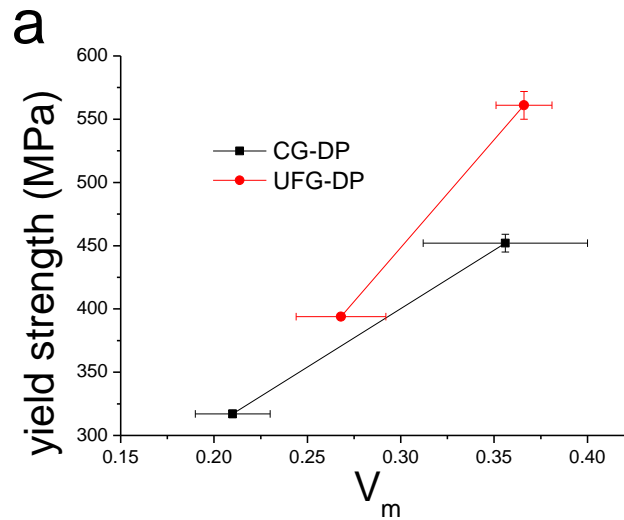
Ferrite grains are refined in the UFG-DP, which first results in the strengthening of the matrix due to Hall-Petch effect. This can be revealed by the comparison of yield stress, although the yield stress of dual-phase steels is difficult to define. As seen in Figure 3.18a, the yield strength of UFG-DP is increased with V_m and generally higher than CG-DP. The yield strength of UFG-DP-37% is about 561MPa, while the one of CG-DP-36% is 452MPa. Notice that the yield strength of UFG-DP-27% is comparable to CG-DP due to the discontinuous yielding and low initial work-hardening rate.

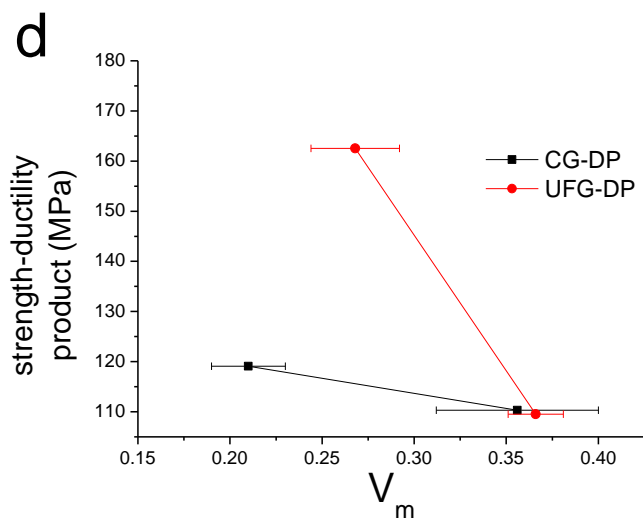
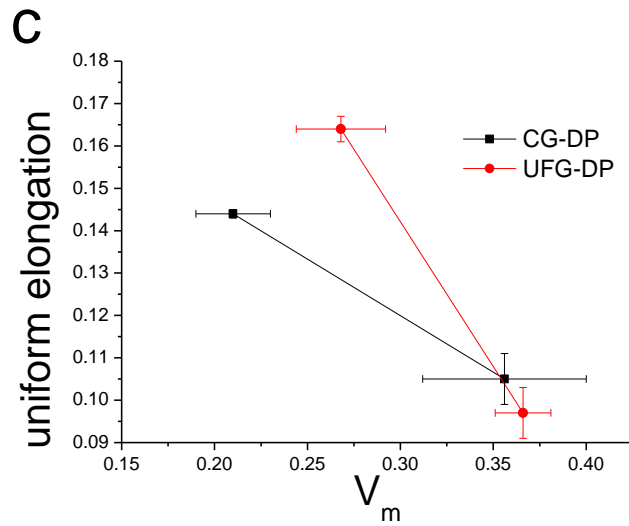
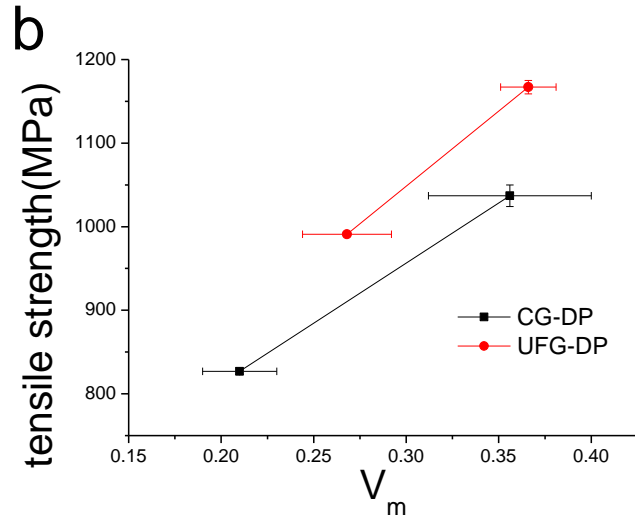
The refined DP microstructures have higher tensile strength than the CG-DP (Figure 3.18b). The tensile strength of UFG-DP-37% is 1165MPa while that of CG-DP-36% is 1031MPa. Until the onset of necking, the flow stress of UFG-DP-37% is increased by 614MPa and that of CG-DP-36% is 579MPa. Microstructure refinement can result in an increase of work-hardenability.

However, the comparison of uniform elongation is more complicated (Figure 3.18c). The comparison between UFG-DP-37% and CG-DP-36% shows that microstructure refinement can lead to slightly reduced ductility. But the uniform elongation of UFG-DP-27% is even higher than CG-DP-21%, considering the effect of martensite volume fraction on ductility shown in Figure 3.3c.

The increase of tensile strength and slightly decreased uniform elongation of UFG-DP-37% results in the same strength-ductility product as CG-DP-36%, as shown in Figure 3.18d. In this aspect, refined DP steels do not show improvement. However, the simultaneously improved tensile strength and uniform elongation of UFG-DP-27% reveal a remarkable strength-ductility product, comparing with other microstructures.

The comparison of strength-ductility relationship has been shown in Figure 3.18e. In the space of tensile strength and uniform elongation, the curve of UFG-DP is locating above of CG-DP, indicating that the microstructures of UFG-DP can have higher strength without reducing ductility or can have improved ductility while keeping the same strength level.





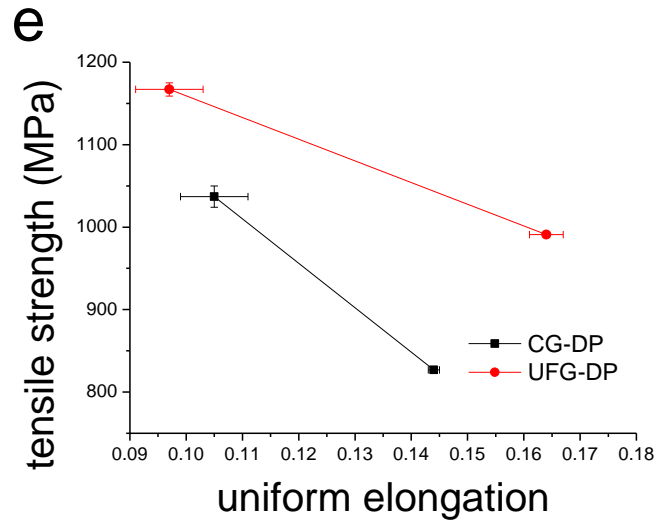


Figure 3.18. Comparison between CG- and UFG-DP on the evolution of yield strength (a), tensile strength (b), uniform elongation (c) and the strength-ductility relationship (d) with V_m , and the trade-off between tensile strength and uniform elongation (e).

3.4.5 Brief discussion

The results above have shown the interesting plastic properties of UFG-DP, such as improved combination of strength and ductility and the involvement of TRIP effect. For the sake of clarity, the contribution of microstructure refinement and TRIP effect will be discussed separately, in order to rationalize the plastic properties of UFG-DP in this study. The aspect of microstructure refinement is focused on the comparison between CG-DP-36% and UFG-DP-37% while the TRIP effect is discussed with UFG-DP-27%.

3.4.5.1 Consequences of microstructure refinement

Microstructure refinement has been investigated extensively in metals. It is consistently found that the yield strength and tensile strength are drastically increased due to grain refinement, whereas the uniform and the total elongation are decreased. For example, UFG ferritic steels with a grain size of around and/or below $1\mu\text{m}$ have been produced [146], and the results shows the poor work-hardenability (Figure 3.19). The uniform elongation is low, although the tensile strength is very high. The decrease of uniform elongation is even more dramatic when the grain size is

reduced to 0.21 μm . This low uniform elongation marks a main limitation to commercial applications.

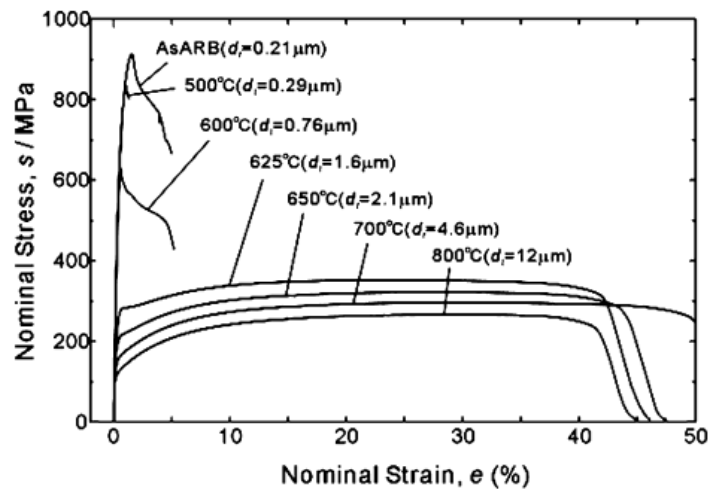


Figure 3.19. Engineering stress-strain curves of the IF steel ARB processed by 7 cycles at room temperature without lubrication and then annealed at various temperatures for 1.8ks. The annealing temperature and mean grain size of each specimen are also indicated. [146]

On the contrary to single-phase UFG metals, the previous studies on microstructure refinement in DP steels reveal that the increase in yield strength and tensile strength is not accompanied by a significant decrease of the uniform elongation and fracture strain (Figure 3.20) [65]. Considering the decreased uniform elongation by grain refinement, the maintenance of uniform elongation of UFG-DP might be due to the typical composite effects.

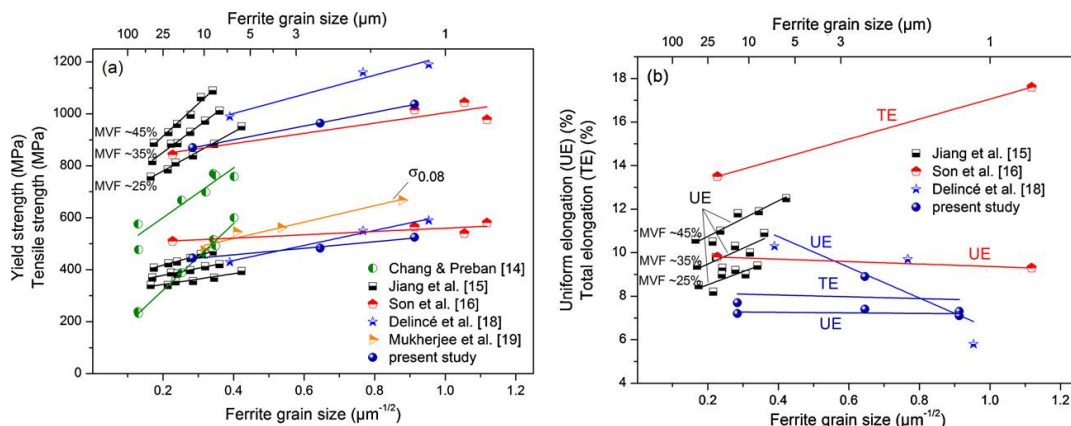


Figure 3.20. Grain size dependence of (a) yield and tensile strength and (b) uniform and total elongation. MVF: martensite volume fraction, $\sigma_{0.08}$: flow stress at 8% strain, UE: uniform elongation, TE: total elongation. [65]

Chapter 3 Plastic properties of DP steels

Firstly, the presence of martensite phase can induce the back stress that is essential to high work-hardening rate, counteracting the decreased hardenability by grain refinement of ferrite. This back stress is increased with martensite volume fraction, and act as a first-order effect.

But compared with the CG-DP, the grain refinement should enhance the plasticity of martensite, which has been experimentally identified in [60, 63]. According to the model in [60], the increase of the yield strength and strain-hardening rate of ferrite due to grain refinement can result in rapid stress transfer to martensite, so that the yielding of martensite is onset at lower strain than in CG-DP. Although the initial work-hardening rate of martensite is very high [40], the flow stress saturates soon after, especially when the carbon content is low. The typical stress-strain curves of martensite are shown in Figure 3.21 [40]. The resulting decreased plastic incompatibility between ferrite and martensite can reduce the back stress and then the work-hardening rate. Thereafter, the combined effect of ferrite grain refinement and martensite strengthening on uniform elongation should also depend on the composition of martensite.

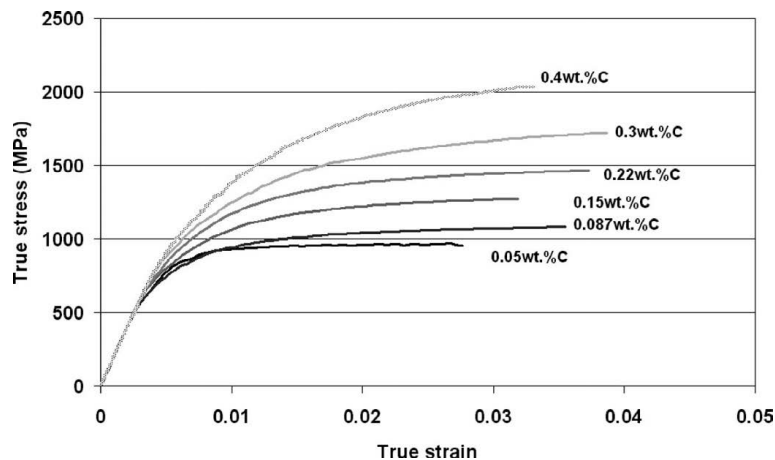


Figure 3.21. Normalized true stress-true strain curves of as-quenched martensite with various carbon contents [40].

Secondly, the microstructure refinement of DP steels leads to a decreased size of martensite islands as well (Figure 2.31). The simultaneous decrease of ferrite grain size and martensite particle size results in the increase of ferrite/martensite phase boundary area. During the macroscopic deformation, the plastic strain incompatibility between ferrite and martensite generates large number of GNDs in ferrite surrounding martensite. The larger ferrite/martensite phase boundary area is, the more GNDs are produced. This large number of GNDs, as well as Hall-Petch effect,

firstly results in the higher yield strength in UFG-DP. The enhanced dislocation multiplication can increase the work-hardening rate according to the dislocation theory [147], counteracting the effect of purely grain refinement of ferrite. As shown in Figure 3.15b, the work-hardening rate of UFG-DP-37% keeps higher than CG-DP-36%, especially in the initial stage of deformation. This enhanced work-hardening partly results from the increased dislocation accumulation, considering the similar martensite volume fraction and hence the back stress from martensite/ferrite plastic incompatibility.

Notice that the martensite carbon content in CG-DP-36% and UFG-DP-37% is not the same since they are annealed at different temperatures. As predicted by THERMOCALC, the martensite carbon content in CG-DP-36% is about 0.185wt% while that in UFG-DP-37% is about 0.238wt%. Comparing the difference in work-hardening between QT-700-37% and QT-740-35% in Figure 3.5b, which reveals that martensite hardness only influences work-hardening rate at large strain, the higher martensite carbon content in UFG-DP-37% should not be the dominating reason of enhanced work-hardening rate as shown in Figure 3.15b.

3.4.5.2 On the TRIP effect in UFG-DP-27%

● Demonstration of the TRIP effect

The XRD measurement on the UFG-DP-27% before and after tensile test shows that martensitic transformation occurs during the deformation, contributing to the transformation-induced plasticity (TRIP) effect. This effect improves the uniform elongation significantly by keeping a high work-hardening rate at large strain [145]. For the UFG-DP-27%, which is supposed to exhibit TRIP effect, the uniform elongation is significantly higher than other microstructures, especially than the CG-DP-21% with less martensite (Figure 3.18c). The high uniform elongation of UFG-DP-27% results in dramatically increased strength-ductility product (Figure 3.18d).

The tensile curve and work-hardening of UFG-DP-27% can also show the features of TRIP effect. Typical DP steels shows continuous yielding and high initial work-hardening rate due to the back stress and accommodation dislocations induced by martensitic transformation during cooling. However, UFG-DP-27% presents discontinuous yielding, indicating the lack of the significant back stress and the accommodation dislocations. The discontinuous yielding is commonly observed in the TRIP-assisted multiphase steels [143-145, 148, 149]. The lack of significant back

stress is due to the less plastic incompatibility between ferrite and austenite. Also, the fluctuation of work-hardening rate shown in Figure 3.17 implies the occurrence of martensitic transformation that can influence the macroscopic response. Notice that, the work-hardening rate of UFG-DP-27% keeps decreasing at medium and large strain, which is different with the case of high austenite stability that the work-hardening rate keeps increasing during deformation [145]. It is supposed that the uniform elongation of UFG-DP-27% can be further enhanced by increasing the austenite stability.

● Origin of austenite stability

In the low-alloyed TRIP-assisted multiphase steels, a bainitic hold treatment is required for stabilizing the austenite by carbon enrichment but simply an intercritical annealing is not enough to bring up TRIP effect [8, 9]. However, the recent investigations of medium-Mn (from 5 to 12wt%) steels show that a TRIP effect can be introduced by an intercritical annealing [12, 150-153]. This is identical to the results in the previous study, although the Mn content here is much lower to the typical medium-Mn steels.

The M_s temperature can be estimated by the following equation [35]:

$$M_s(^{\circ}C) = 539 - 423(\%C) - 30.4(\%Mn) - 7.5(\%Si) + 30(\%Al). \quad (3.1)$$

UFG-DP-27% is annealed at 680°C. As predicted by THERMOCALC, the equilibrium Mn content should be 6.8% and the carbon content should be 0.3wt%. Therefore, the estimated M_s temperature for UFG-DP-27% should be about 205°C and the austenite is expected to transform fully to martensite during cooling to room temperature. According to this equation, the austenite composition alone is not enough for stabilization at room temperature, although this can explain the lower austenite stability in UFG-DP-37% where the M_s temperature is predicted as 258°C.

Other mechanisms of austenite stabilization have been proposed in the literature. One important mechanism is mechanical stabilization by high dislocation density [154]. But according to the TEM observation in [150], the austenite phase formed in intercritical annealing is characterized by a low dislocation density and the frequent presence of stacking faults. Mechanical stabilization is supposed to be negligible in this case.

Another mechanism is austenite stabilization by size effect. It has been reported [155] that the prior austenite grain size contributed substantially to the austenite stability

when the austenite grain size is of submicron size. The size effect is suspected to be important in the austenite stability of UFG-DP-27%. Although the predicted M_s temperature should be much above the room temperature, the mean linear size of intercritical austenite islands in UFG-DP-27% is only about 800nm, and there are a large population of austenite islands much smaller than this average size. Similar conclusion has been drawn in [150] with the fact that when the austenite grain size becomes coarser by very long annealing time, no TRIP effect can be observed.

3.5 Summary

With the microstructures developed in chapter 2, experiments are performed in order to investigate the effects of martensite volume fraction, martensite composition and scale of microstructure on the plastic properties of DP steels. Efforts have been made to decouple the influences of various microstructural features. The main conclusions and highlights are summarized as follows:

- 1) DP steels start to yield at a lower stress than spheroidized microstructure. But the presence of martensite phase eliminates the yield point phenomenon and dramatically increases the work-hardening rate. The work-hardening rate is increased with increasing V_m .
- 2) The yield strength and tensile strength are both increased with increasing V_m , but the uniform elongation shows an opposite trend. This is related to the onset of plastic deformation of martensite, which results in less kinematic hardening. As an indication, the work-hardening rate at large strain is decreased with increasing V_m .
- 3) The martensite composition has limited influence on the yield strength. And its effect on tensile strength is only significant when V_m is large. A DP steel with higher martensite hardness has higher tensile strength.
- 4) The uniform elongation is less affected by martensite composition except with large V_m . QT-700-37% has higher martensite hardness, and its uniform elongation is larger than QT-740-35%.
- 5) With a higher martensite hardness, QT-700 has better plastic properties than QT-740 in the sense of combining strength and ductility.

- 6) Microstructure refinement of DP steels increases the yield strength and tensile strength, but the uniform elongation is slightly decreased. As a consequence, the strength-ductility product is not significantly influenced by microstructure refinement. However, with an additional contribution of TRIP effect, UFG-DP steel can have simultaneous improvement of tensile strength and uniform elongation.

Chapter 4 Damage and fracture of dual-phase steels: experimental investigation and qualitative discussion

Dual-phase (DP) steels have been designed to meet the requirements of high strength and good formability for automotive industry. However, fracture resistance is one of the limitations to application, especially when the components need to undergo substantial deformation during forming.

The damage and fracture of DP steels have been studied for over 30 years, but there is still room for progress to be made to extend the application range of DP steels. One challenge is the complexity of DP microstructure and the influences of various microstructural features that are difficult to decouple. Another challenge is the characterization of damage, and the resolution and accuracy are still the issues of the experimental techniques [97, 156]. This work is dedicated to promote the fundamental understanding of the effects of microstructural parameters on damage and fracture of DP steels. Experiments have been designed, trying to decouple the influence of microstructure features as presented in chapter 2 and 3. Detailed characterizations have been performed to provide the information of damage and fracture mechanisms in order to support the rationalization of fracture properties. The microstructure—fracture behavior relationship is discussed systematically.

4.1 Experimental procedure

4.1.1 Analysis of fracture surface

The fracture surfaces of broken tensile specimens were observed under SEM. Both cleavage- and ductile- type surfaces can be found. For ductile fracture regions, dimple density was characterized by the mean distance between dimple centers. The distances to all the neighboring dimple centers were measured for each selected dimple on a fracture surface. The average value was taken as the mean distance between dimple centers for a fracture surface.

The fracture strain can also be attained from the fracture surface. The fracture strain in this work is defined as the area reduction measured on the sample at the level of the fracture surface. The value of fracture strain ε_f is given by:

$$\varepsilon_f = \ln \frac{A_0}{A_f} \quad (4.1)$$

where A_0 is the initial area before tensile test and A_f is the final area measured from SEM images.

4.1.2 Damage observation and quantification of damage accumulation

Damage accumulation was characterized by void density and area fraction of voids as a function of strain. Sections cut perpendicularly to the ligament at the center location were polished and cleaned. The specimens were observed in SEM using Back Scattering Electrons (BSE) mode, which is more sensitive to porosity at the surface [156]. The images with the magnification of 1000 were adjusted with a proper brightness and contrast, and binarization was applied in order to well differentiate voids from the non-porous surrounding material. The density and area fraction of voids have been analyzed with the software ImageJ [122]. A minimum void size must be defined. In this work, the minimum void sizes have been chosen as $1.23\mu\text{m}^2$, $0.60\mu\text{m}^2$, $0.31\mu\text{m}^2$, $0.20\mu\text{m}^2$ and $0.11\mu\text{m}^2$, which correspond to 100, 49, 25, 16 and 9 pixels of the images, respectively. The reason for selecting several values is to reveal the evolution of void spectrum with strain.

The local strain is taken as the thickness strain $\varepsilon_{thickness}$ given by:

$$\varepsilon_{thickness} = \ln \frac{h_0}{h} \quad (4.2)$$

where h_0 is the initial thickness of the tensile specimen and h is the thickness in the corresponding zone. The measurements are averaged over five micrographs for each deformation level.

After the quantification of damage accumulation, the samples were etched with 2% Nital to reveal the microstructure and observed in SEM with Secondary Electron (SE) mode. The goal of this second observation was to reveal the void nucleation mechanism.

4.1.3 Microhardness test

The post-necking hardening cannot be directly reflected from a uniaxial tensile test. To compare the flow stress at large strain, microhardness tests (Tukon 1202, load of 500g) were performed inside the necking zone of the samples for damage analysis. Four or five measurements were performed for each deformation level, and an evolution of microhardness with deformation is obtained, indirectly revealing the post-necking hardening.

4.2 Influence of martensite volume fraction on damage and fracture

4.2.1 Effect of martensite volume fraction on damage accumulation

4.2.1.1 Comparison of damage accumulation evolutions

Figure 4.1a and b reveal the effect of V_m on damage accumulation, quantified with (a) the void density and (b) the area fraction of voids. Only the voids larger than 110nm^2 are taken into account for these plots.

From the evolution of void density with thickness strain (Figure 4.1a), QT-700 with 15%, 19%, 28% and 37% of martensite all exhibit a continuous damage nucleation process. Indeed, the number of voids increases with increasing macroscopic strain. Two considerations emerge from the comparison shown in Figure 4.1a. Firstly, the damage nucleation strain is only slightly decreased with increasing V_m . Some defects are initially present due to processing cold-rolled martensite (see Appendix A), and there is no significant damage evolution with deformation before necking. The damage nucleation strain here is defined as the thickness strain at which the number of voids starts to increase from the initial value. According to this definition, the strain at which damage starts to nucleate in QT-700-19% is about 0.12, while that of QT-700-37% is about 0.10, which are close to each other. Secondly, the damage nucleation rate is significantly increased by increasing V_m . This can be shown by the comparison of the slope of the curves in Figure 4.1a. As a result, for the same thickness strain, the void density is increased with increasing martensite volume fraction.

The area fraction of voids shown in Figure 4.1b is a characterization of both void density and void size, which is a general representation of damage accumulation. The area fraction of voids in QT-700-19% only starts to increase after a thickness strain of 0.25, while in QT-700-37%, it starts at around 0.1. This difference is much larger than that of damage nucleation strain defined above. However, for the same thickness strain, the area fraction of voids is also increased with increasing V_m .

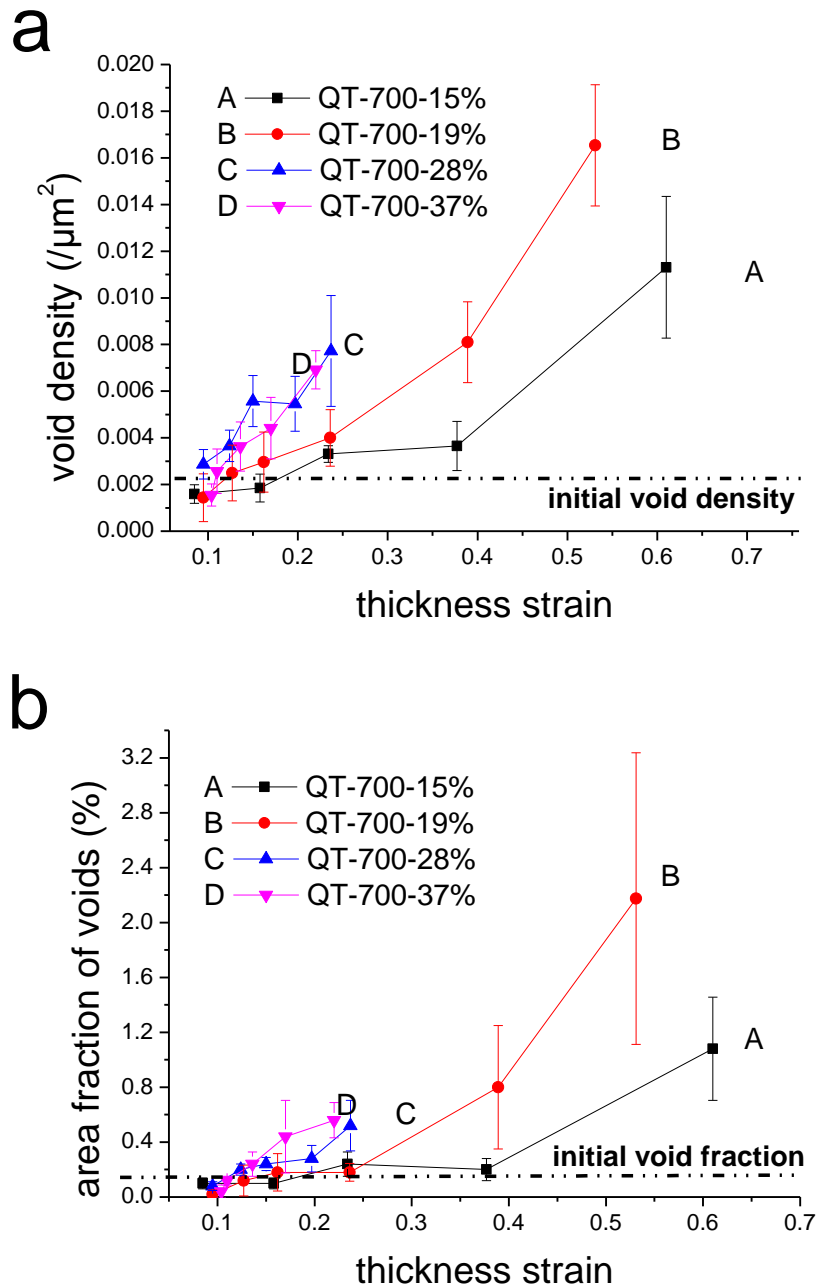
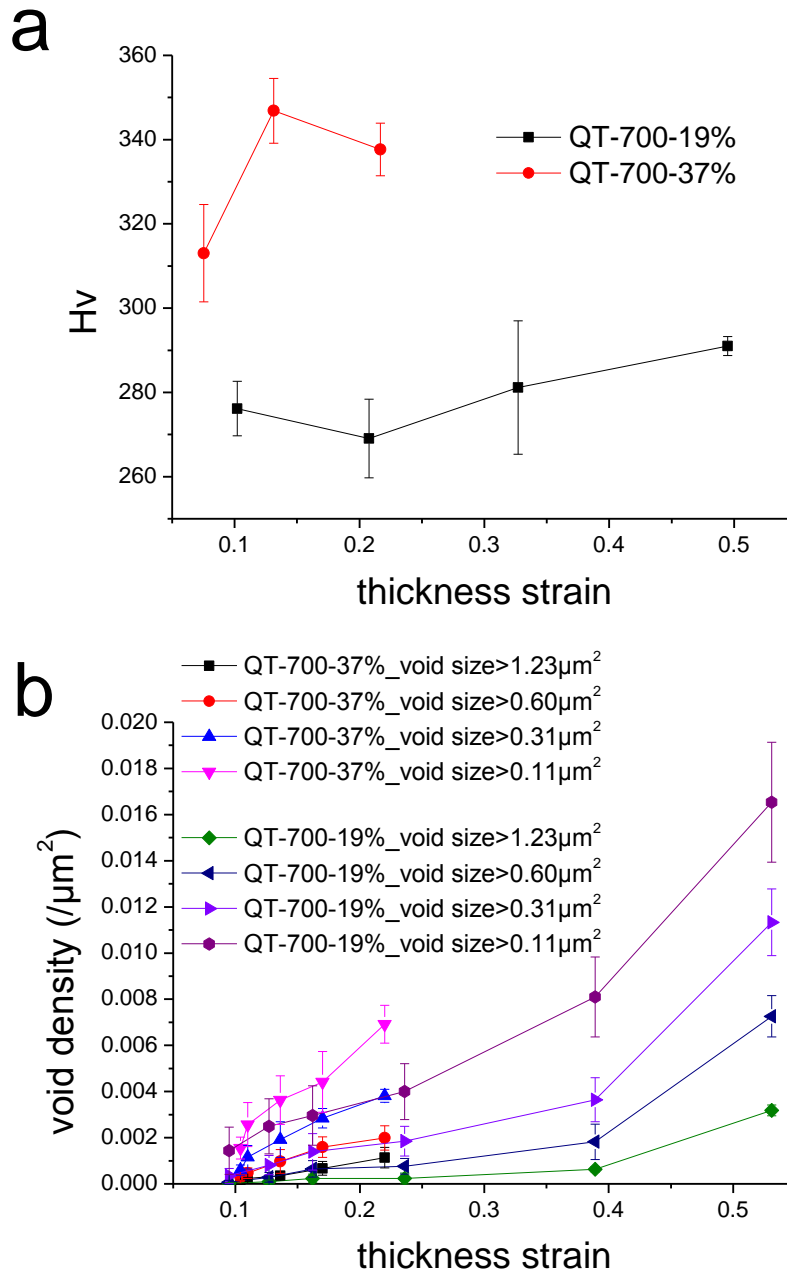


Figure 4.1. The evolution of void density (a) and area fraction of voids (b) with thickness strain. Notice that only voids larger than $0.11\mu\text{m}^2$ are taken into account.

The effect of V_m on damage accumulation in dual-phase steels can also be revealed by the evolution of the void spectrum with strain. QT-700-37% has a higher flow stress than QT-700-19% during necking (Figure 4.2a). Figure 4.2b and c show the evolution of void size distribution in terms of void density and area fraction of voids for QT-700-19% and QT-700-37%. For QT-700-19%, there is a large population of voids smaller than $1.23\mu\text{m}^2$, but about 80% of the void area is contributed to by the voids larger than $1.23\mu\text{m}^2$. For QT-700-37%, there is also a large population of voids

Chapter 4 Damage and fracture of DP steels

smaller than $1.23\mu\text{m}^2$, while about 50% of the void area is contributed by these small voids. That is, small voids are contributing more and more to the damage accumulation when V_m is increased. The void densities with various critical void sizes are all increasing with strain, indicating an on-going void growth process participating to the accumulation of porosity.



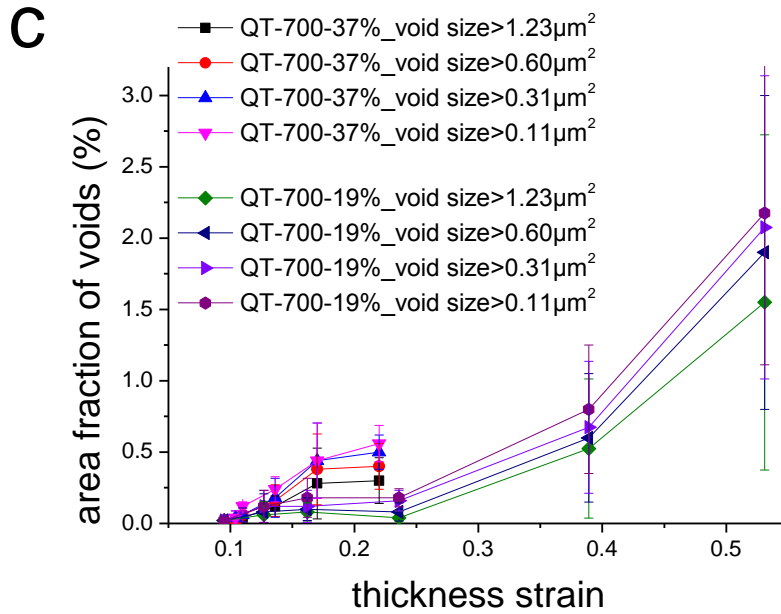


Figure 4.2. Evolution of microhardness (a), void spectrum of QT-700-19% and QT-700-37% with thickness strain in terms of void density (b) and area fraction of voids (c).

4.2.1.2 Martensite volume fraction and damage mechanisms

● Damage mechanisms in QT-700-15%

Figure 4.3a-d are SEM micrographs showing the damage observations in QT-700-15%. The microstructure is significantly elongated and the distribution of martensite is aligned as a result of the large local deformation (Figure 4.3a). Elongated voids are observed and the so-called necklace coalescence [99] occurs in QT-700-15% (Figure 4.3a).

Both martensite fracture (Figure 4.3b) and interface decohesion (Figure 4.3c) operate as damage nucleation mechanisms in QT-700-15%. Notice that several cracks can be observed in a single martensite island (Figure 4.3b). Interface decohesion tends to occur at the triple junction between martensite island and ferrite grain boundary, and grows along the grain boundary as a void (Figure 4.3c) or propagates as a crack (Figure 4.3d). According to the observation, most of the damage occurrences are nucleated by interface decohesion in QT-700-15%.

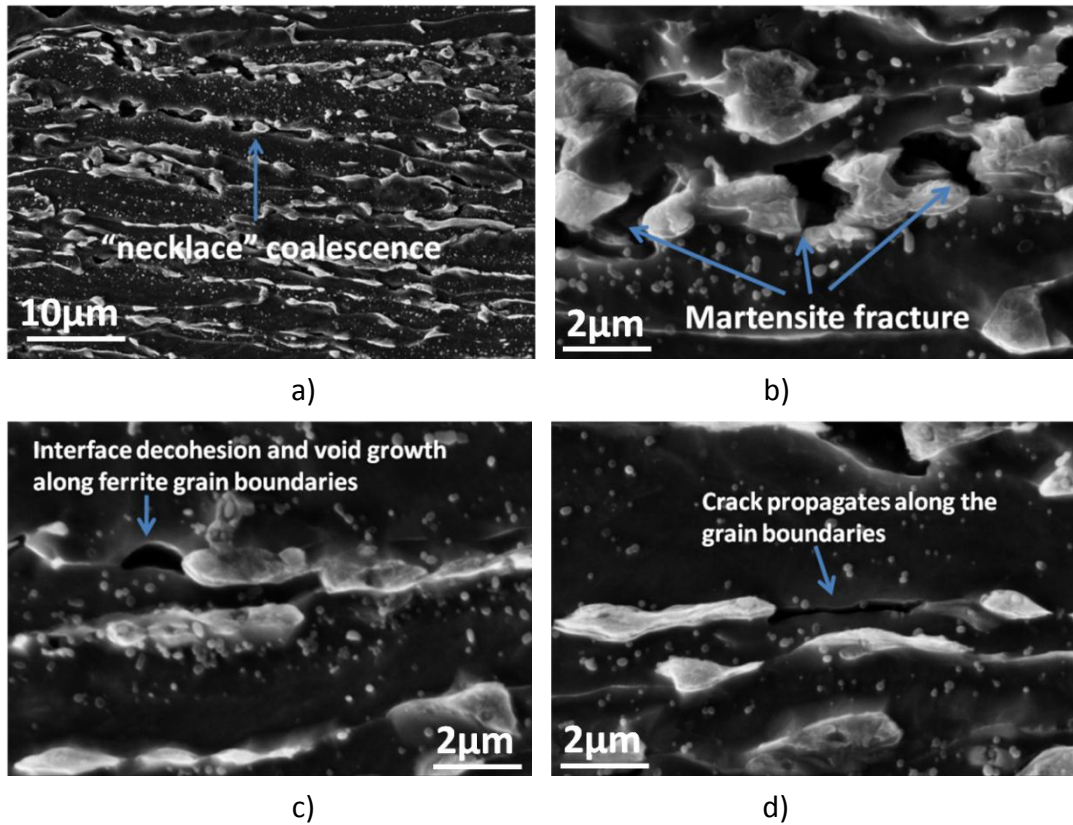


Figure 4.3. SEM micrographs showing damage mechanisms in QT-700-15%.

● **Damage mechanisms in QT-700-19%**

Figure 4.4a-d are SEM micrographs showing the damage characterization for QT-700-19% specimen. As V_m is increased, the distribution of martensite islands is becoming more banded (see chapter 3). Large voids are observed to locate inside martensite clusters or bands due to premature growth and coalescence while small voids are formed at the isolated martensite islands (Figure 4.4a).

Both martensite fracture (Figure 4.4b) and interface decohesion (Figure 4.4c and d) are observed as damage nucleation mechanisms for QT-700-19%. In Figure 4.4b, the void formed from martensite fracture has deviated significantly from a penny shape, indicating substantial growth has occurred. Several observations support the statement that interface decohesion is probably initiated at triple junction between ferrite grain boundary and martensite islands (Figure 4.4c and d).

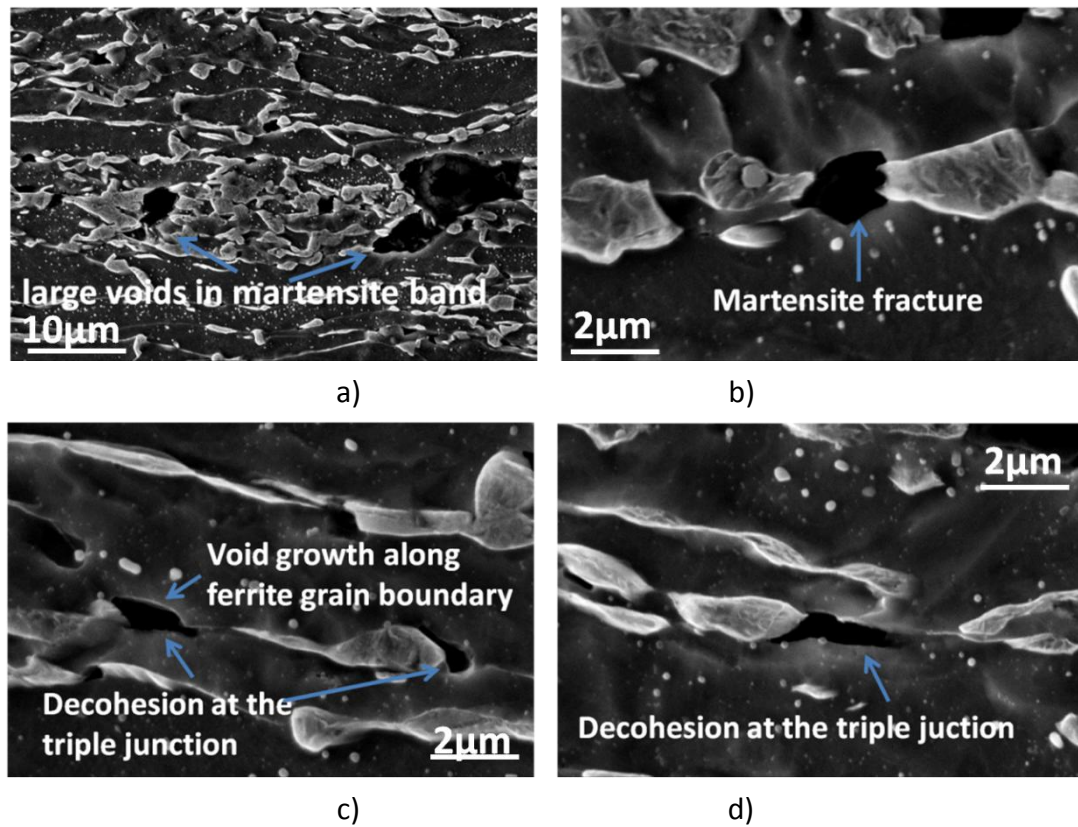


Figure 4.4. Damage mechanisms in QT-700-19%.

● **Damage mechanisms in QT-700-28%**

Figure 4.5a-d are SEM micrographs showing the damage mechanisms in QT-700-28%. The comparison with the observations in Figure 4.3 and Figure 4.4 should potentially reveal the effect of martensite volume fraction on damage behavior of dual-phase steels.

With this volume fraction of martensite, wide continuous martensite bands have formed and large voids are observed to locate inside the bands (Figure 4.5a). Cavities nucleate as penny-shape voids by martensite fracture (Figure 4.5b) and this local fracture seems to be initiated from the edge of the martensite phase (Figure 4.5c). The dominating damage nucleation mechanism for QT-700-28% is martensite fracture. But interface decohesion is still observed around small martensite islands and, again, is related to triple junctions (Figure 4.5d).

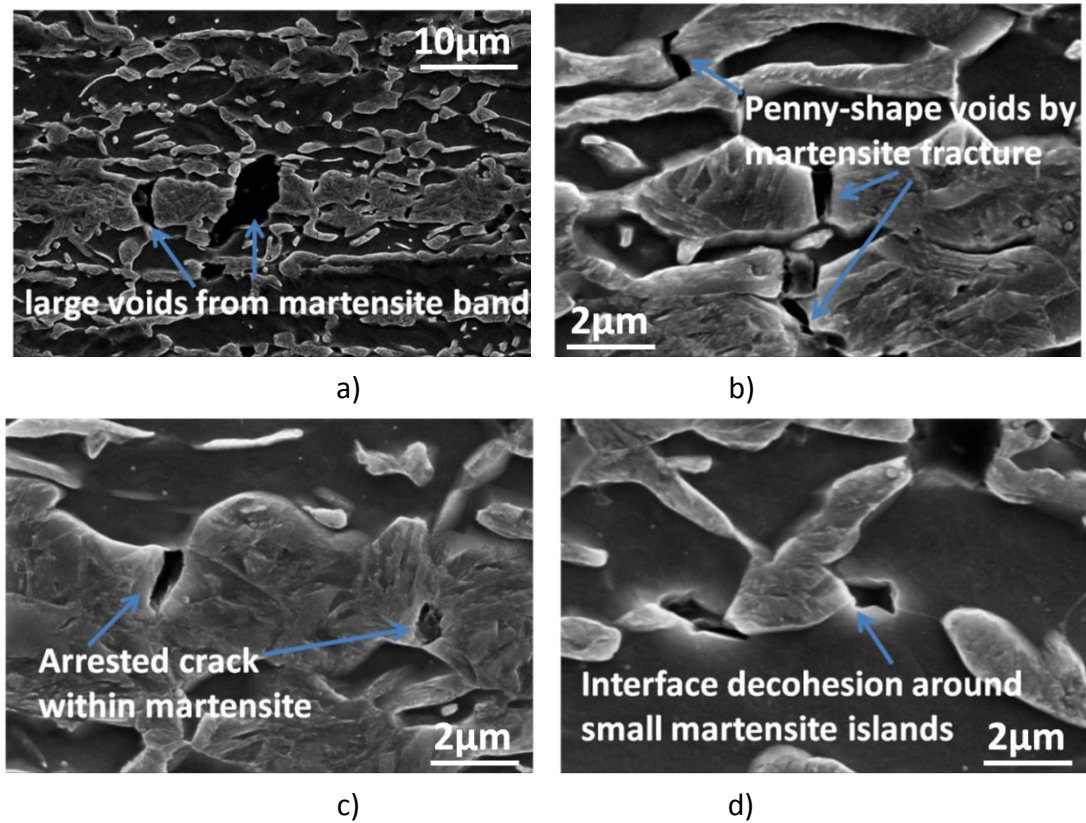


Figure 4.5. Damage mechanisms in QT-700-28%.

- **Damage mechanisms in QT-700-37%**

Figure 4.6a-d are SEM micrographs showing the damage mechanisms in QT-700-37%, which are supposed to be characteristic of the damage behavior of dual-phase steels involving large volume fraction of martensite.

Similar to QT-700-28%, large voids are located inside the wide continuous martensite bands (Figure 4.6a), and the coalescence between two adjacent large voids through martensite fracture is observed (Figure 4.6b). Penny-shape void can be formed by martensite fracture (Figure 4.6c), possibly along the block boundary as shown in Figure 4.6d.

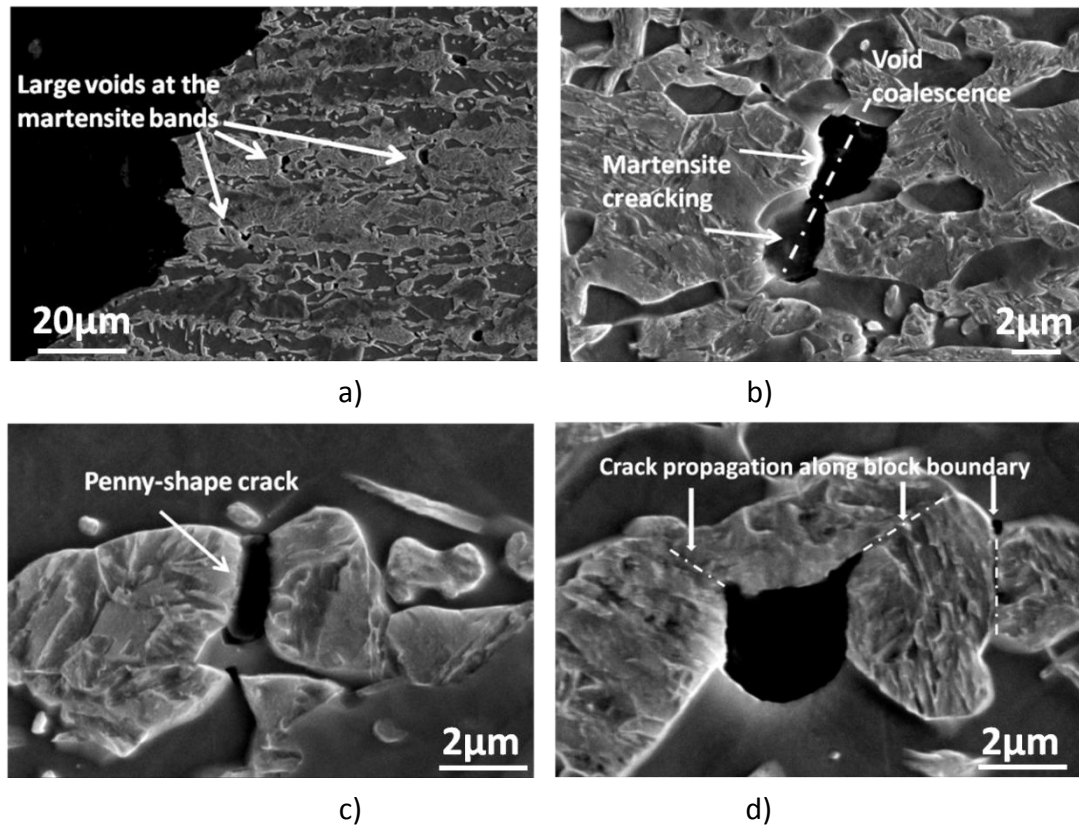


Figure 4.6. Damage mechanisms of QT-700-37%.

4.2.2 Effect of martensite volume fraction on fracture resistance

4.2.2.1 Evolution of fracture strain with martensite volume fraction

Figure 4.7a shows the effect of V_m on the fracture strain. The fracture strain decreases monotonically with increasing V_m . The scatter in the values of fracture strain is much less than the measurement of martensite volume fraction when V_m is larger than 28%. Since the tensile strength is increased with increasing V_m , the classical trade-off between tensile strength and fracture strain appears (Figure 4.7b).

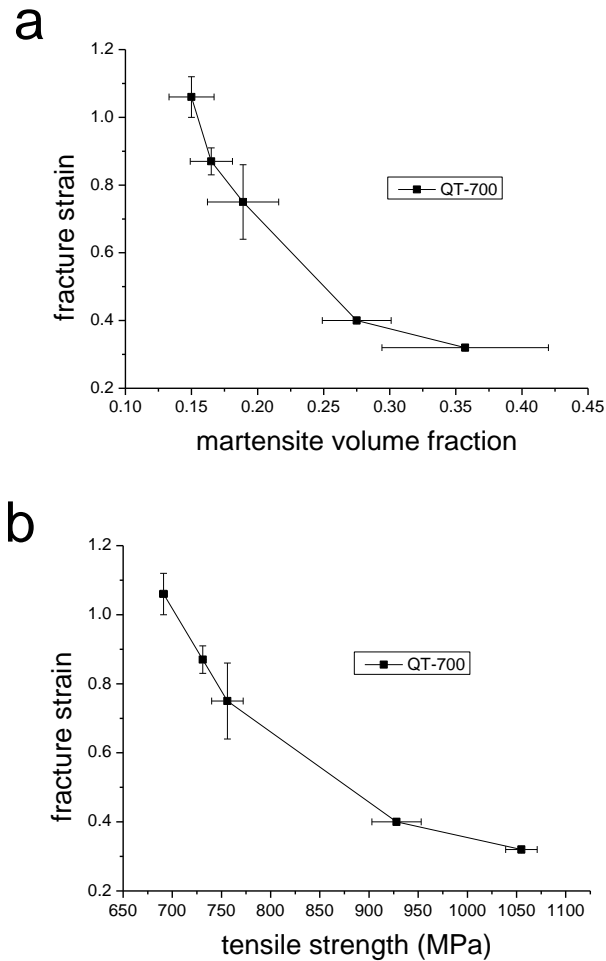
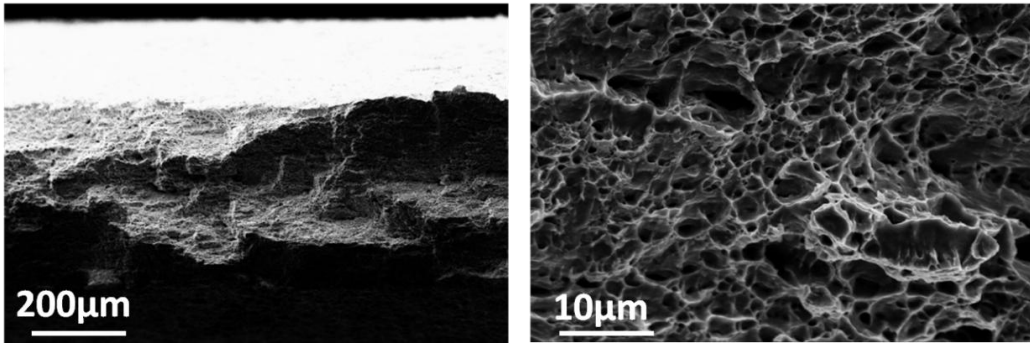


Figure 4.7. Evolution of fracture strain with martensite volume fraction (a) and fracture strain—tensile strength relationship (b) in QT-700.

4.2.2.2 Effect of martensite volume fraction on fracture behavior

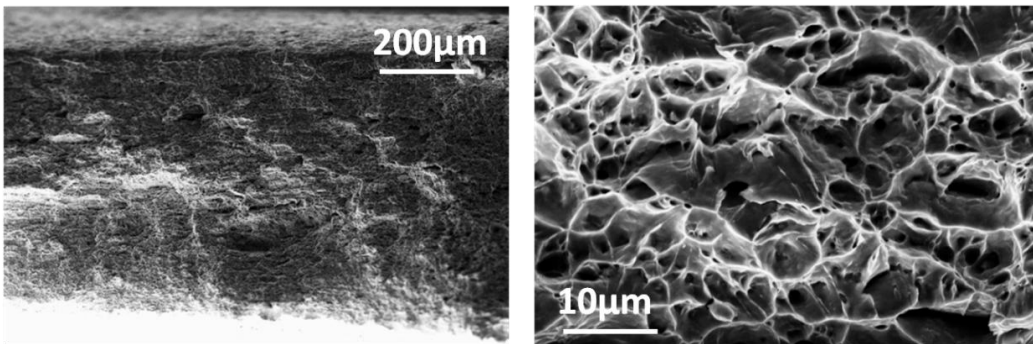
Within this range of martensite volume fraction (from 15% to 37%), the DP microstructures generally fail by ductile fracture (Figure 4.8-11). The mean distance between dimple centers in QT-700-15%, 19%, 28% and 37% is about $2.9 \pm 0.7 \mu\text{m}$, $3.0 \pm 0.3 \mu\text{m}$, $3.2 \pm 0.5 \mu\text{m}$ and $2.9 \pm 0.4 \mu\text{m}$, respectively. This value is not changed significantly even if V_m is increased a lot. In the case of high V_m , occurrence of cleavage is observed. As shown in Figure 4.10 and Figure 4.11, at the edge of the tensile specimens of QT-700-28% and QT-700-37%, the facet features are characteristics of cleavage cracking.



a)

b)

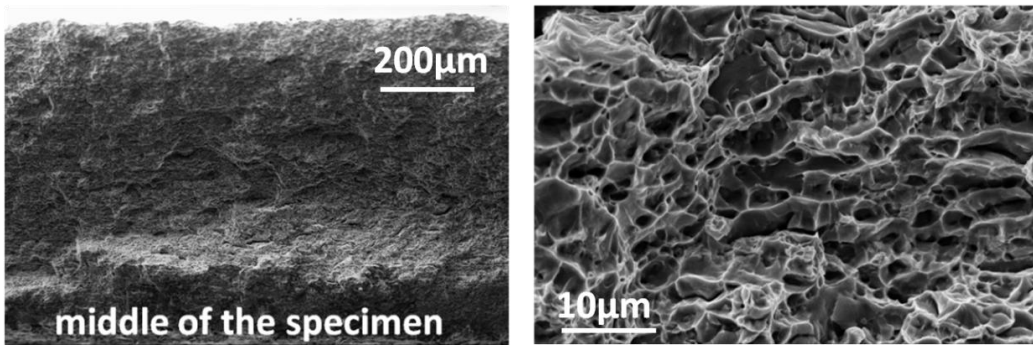
Figure 4.8. Fracture surface of QT-700-15%.



a)

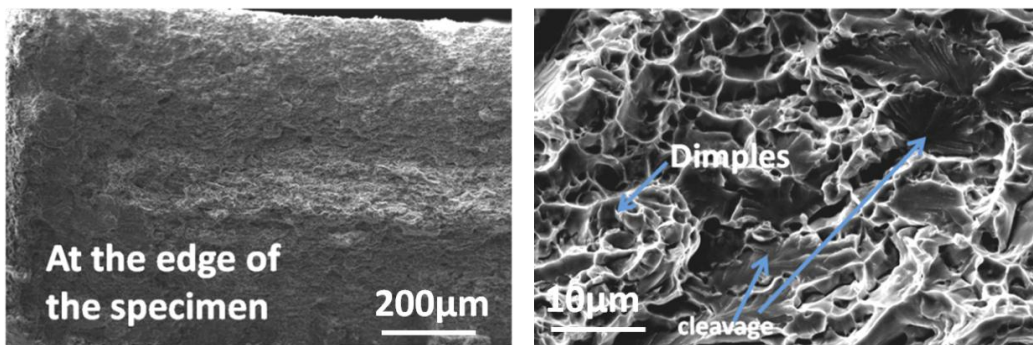
b)

Figure 4.9. Fracture surface of QT-700-19%.



a)

b)



c)

d)

Figure 4.10. Fracture surface of QT-700-28%. (a) and (b) are micrographs showing the

center of fracture surface, while (c) and (d) are showing the features at the edge.

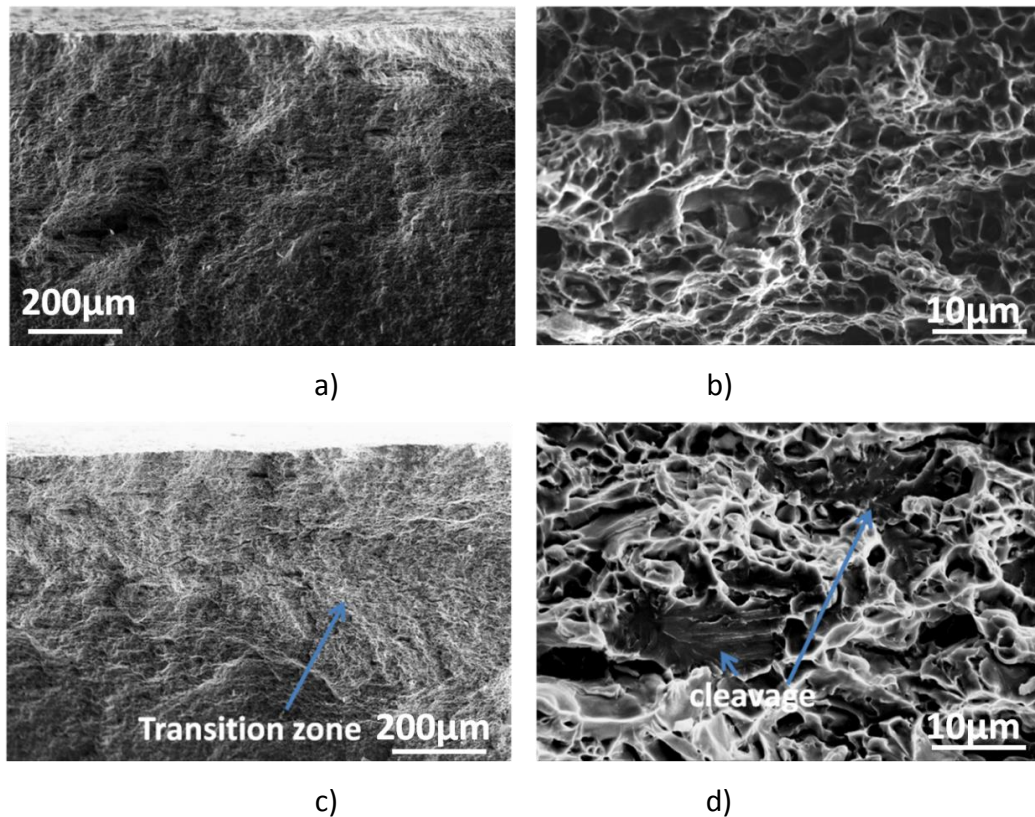


Figure 4.11. Fracture surface of QT-700-37%. (a) and (b) are micrographs showing the ductile fracture zone; while (c) and (d) are showing the transition zone with both dimples and cleavage facets.

4.2.3 Brief discussion

4.2.3.1 Martensite volume fraction and damage mechanism

As presented above, damage accumulation rate is enhanced with increasing amount of martensite (Figure 4.1). Both the increasing rates of the density and area fraction of voids are enhanced with increasing V_m , which agrees with the conclusions in [52, 59]. Furthermore, as V_m is increased, the population of voids of all sizes is increased accordingly (see the comparison between QT-700-19% and QT-700-37% in Figure 4.2). In another words, QT-700-37% has a larger number of both large and small voids.

Actually, the effect of V_m is multi-fold. Regarding the microstructure, as V_m is

increased, the average size of martensite islands is increased (Figure 2.23), and the banded distribution of martensite phase becomes significant until wide continuous bands are formed (Figure 3.1). An increase of island size leads to a higher probability of containing micro-defects, which tends to promote martensite fracture [99]. The martensite bands are figured out to be detrimental to damage resistance of dual-phase steels because of premature local fracture at these sites [98, 108]. It is observed that large voids are formed at the martensite bands (Figure 4.4-6) and they contribute of a large part to damage accumulation. Therefore, with an increased V_m , the damage accumulation is accelerated in that more large voids are formed at the large martensite phase. And there is a transition of dominating damage mechanisms that is schematically shown in Figure 4.12a and b, resulting from the increased martensite size and enhanced martensite connectivity.

Another consequence of higher V_m is that the flow stress is also increased. As a result of the higher connectivity and the efficient load transfer, the martensite phase bears higher stress, which leads to the earlier plastic deformation of the martensite (see the results in chapter 3). It is reasonable to assume that the small voids are formed at small martensite islands, and the small martensite islands are the less favorable sites for damage nucleation. However, the increasing stress in martensite by increasing volume fraction can promote the failure at such small martensite islands. This point can explain the results in Figure 4.2 that QT-700-37% has also higher density of small voids than QT-700-19%.

As a summary, increasing V_m can increase the void density by the mechanisms that more large voids are formed at the wide banded martensite phase and that failure at small martensite islands is also promoted.

4.2.3.2 Martensite volume fraction and fracture behavior

Cleavage in DP steels has been reported to correspond to the ferrite grains but not the martensite phase [63, 104, 105, 157, 158]. This is also observed in this work (see Figure 4.23). The brittle fracture of DP steels is attributed to the interconnected martensite [104, 105] and/or to a coarse microstructure [63, 157, 158]. Comparing with the isolated martensite islands, the interconnected martensite in DP steels constrains the plastic flow in the ferrite matrix by confining the slip system [104] and/or by imposing a high triaxiality state of stress. Once the martensite breaks, the cleavage crack in ferrite grain can be triggered due to the very large local stress

building up at the crack tip.

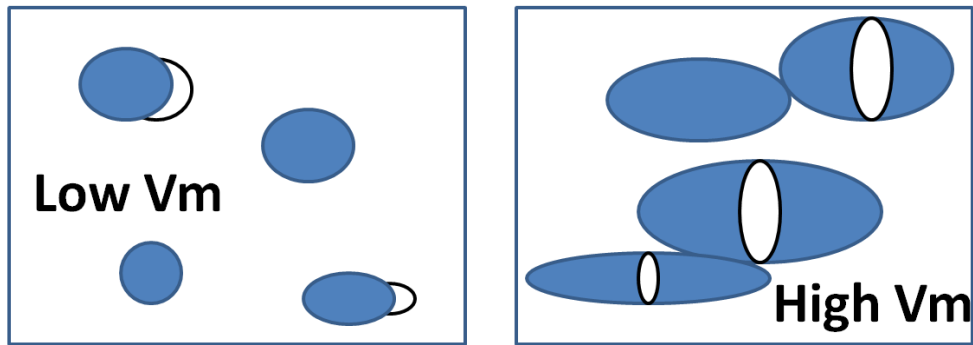
The scale of microstructure is also important to understand the fracture behavior, and a coarse DP microstructure favors cleavage. Firstly, the large ferrite grains can lower the fracture stress, corresponding to the onset of cleavage, by enhancing stress concentration through dislocations pile-up [99]. Secondly, the martensite phase is larger in a coarse microstructure, producing larger initial cracks in the brittle phase. A large initial crack results in high stress intensity over larger region in the ferrite adjacent to the crack tip [159], which also increases the tendency for cleavage.

The results in this section show that DP steels mainly fracture in a ductile manner but cleavage becomes operating with high V_m . This trend is shown schematically in Figure 4.12c. With the increase of V_m , the connectivity of martensite phase should be enhanced. Also, the size of the martensite phase is increased (Figure 2.23), and the continuous wide martensite bands are formed (Figure 3.1). As discussed above, for the DP microstructure with high martensite fraction, the microstructure features favors the occurrence of cleavage in ferrite, which rationalizes the trend in Figure 4.12c.

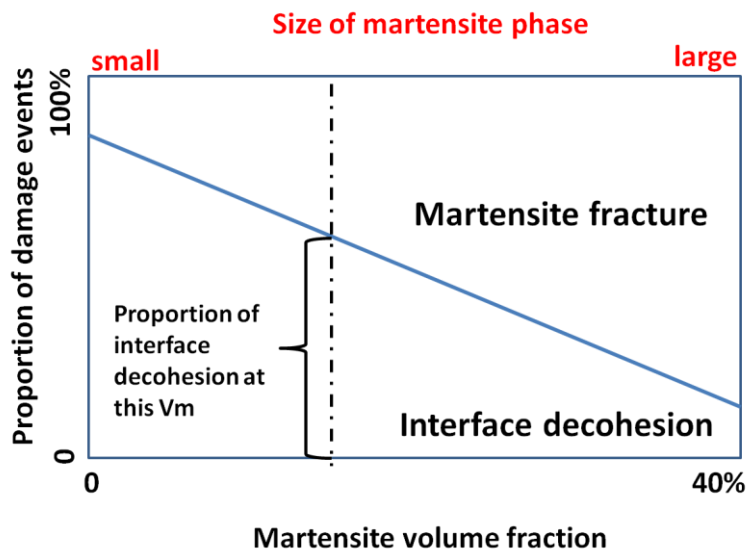
But these points are not sufficient to reveal the full physical conditions for brittle fracture observed in this study. With the highest V_m , dimples are covering the major part of the fracture surface of QT-700-37%. Additionally, cleavage is not mixing with dimples and uniformly distributing over the fracture surface, but is only located at the edge of the tensile specimen (Figure 4.10c and Figure 4.11c). These observations indicate that ductile fracture is the intrinsic or dominating mode of failure in uniaxial tensile test but the occurrence of brittle fracture is probably due to geometrical and dynamic effects. A large main crack can be formed during the failure of tensile specimen, as shown in Figure 4.13 [92]. And the consequential high stress intensity and stress triaxiality at the crack tip can result in unstable and fast crack propagation. Additionally, smaller load-bearing area remains after the formation of large crack, but the displacement speed is constant during tensile test. This leads to a high strain rate at the crack tip. The increased strain rate can increase the flow stress of ferrite [160], and an increased flow stress of ferrite favors the occurrence of cleavage [99].

As a summary, from the results in this section, the brittle fracture of DP steels can be triggered by martensite connectivity, size of martensite phase and also the geometrical and dynamic effects of crack propagation. However, since cleavage approximately occurs at the same stage as void coalescence, the fracture strain is still

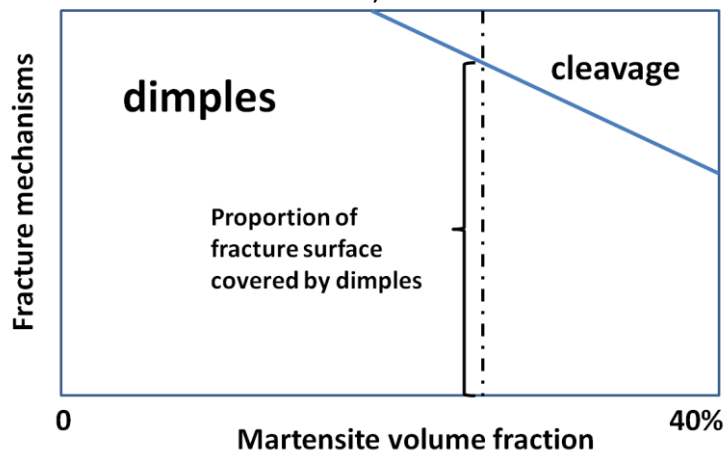
determined by the onset of void coalescence as for usual ductile fracture.



a)



b)



c)

Figure 4.12. Schematic representations of the evolution of damage initiation mechanisms (a), proportion of damage events (b), and fracture mechanisms (c) with martensite volume fraction. An associated increase of martensite size with increasing

V_m is also shown in (b).

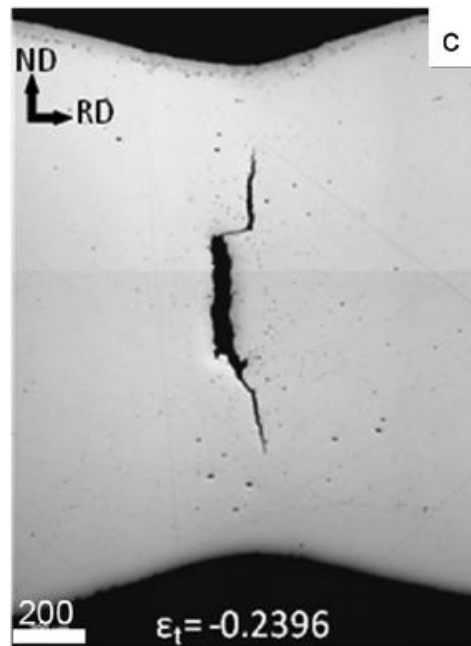


Figure 4.13. Formation of large crack in the tensile specimen before final fracture, which is observed in-situ in the SEM [92].

4.3 Influence of martensite composition on damage and fracture

4.3.1 Effect of martensite composition on fracture strain

Figure 4.14a shows the effect of martensite composition or hardness on fracture strain. The martensite hardness of QT-700 is higher than QT-740 (chapter 2). For the case of low V_m (less than 21%), both QT-700 and QT-740 share the same decreasing variation of fracture strain with increasing V_m . Notice that the nanohardness of martensite in QT-700-19% and QT-740-21% is about 9GPa and 7GPa, respectively. The fracture strain, in this case, is thus not sensitive to martensite hardness. When V_m is further increased, QT-740, which has lower martensite hardness, has higher fracture strain than QT-700.

Since the tensile strength is increased with increasing V_m , there is a trade-off between fracture strain and tensile strength, as shown in Figure 4.14b. Both QT-700 and QT-740 exhibit the same trade-off and thus the tensile strength—fracture strain

curve is not impacted by the martensite composition in the present situations.

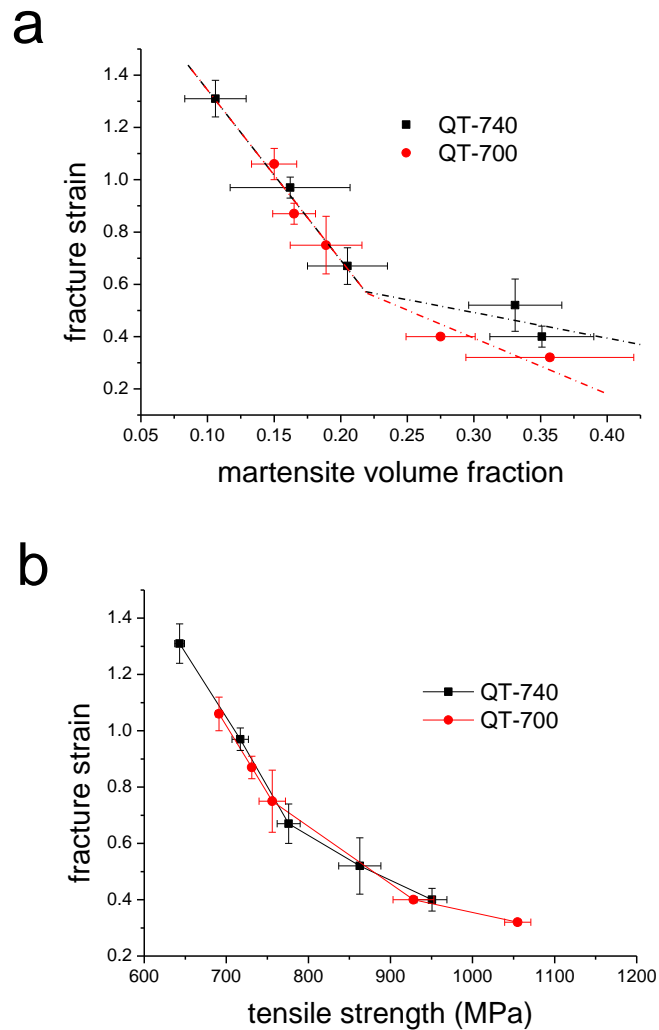


Figure 4.14. Variation of the fracture strain of QT-700 and QT-740 as a function of the martensite volume fraction (a) and fracture strain—tensile strength relationship (b).

4.3.2 Effect of martensite composition on damage accumulation

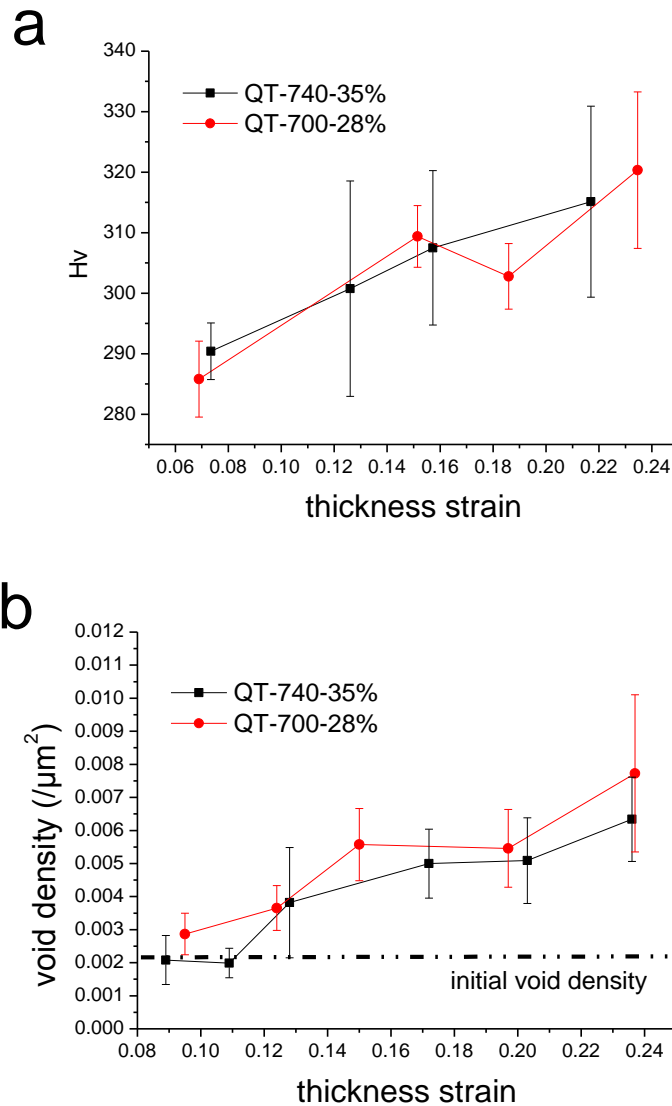
4.3.2.1 Comparison of damage accumulation in QT-700-28% and QT-740-35%

QT-700-28% and QT-740-35% have the same tensile strength and fracture strain,

Chapter 4 Damage and fracture of DP steels

although they involve different martensite volume fractions (Figure 4.13). In order to uncover the operating mechanisms, characterizations have been performed to probe the local state of hardening and damage accumulation.

Figure 4.15a shows that QT-700-28% and QT-740-35% exhibit similar flow stress evolution at large strain as indirectly measured by microhardness test. Regarding the damage accumulation, the increments of void density and area fraction of voids cannot be distinguished using this technique (Figure 4.15b and c), and they should be considered as similar. These results are in agreement with the equal fracture strain.



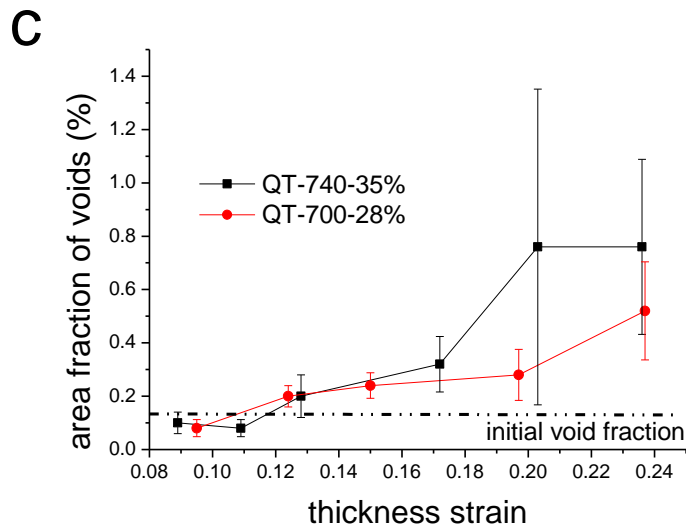


Figure 4.15. Variation of microhardness (a), void density (b) and area fraction of voids (c) of QT-740-35% and QT-700-28% as a function of thickness strain. Notice that only voids larger than $0.11\mu\text{m}^2$ are taken into account.

4.3.2.2 Comparison of damage accumulation in QT-700-37% and QT-740-35%

QT-700-37% and QT-740-35% involve almost the same V_m , but the fracture strain of QT-700-37% is lower. Figure 4.16a shows that QT-700-37% has a higher flow stress after necking. However, both the evolution of the density and area fraction of voids are very similar in terms of damage nucleation strain and damage nucleation rate (Figure 4.16b and c).

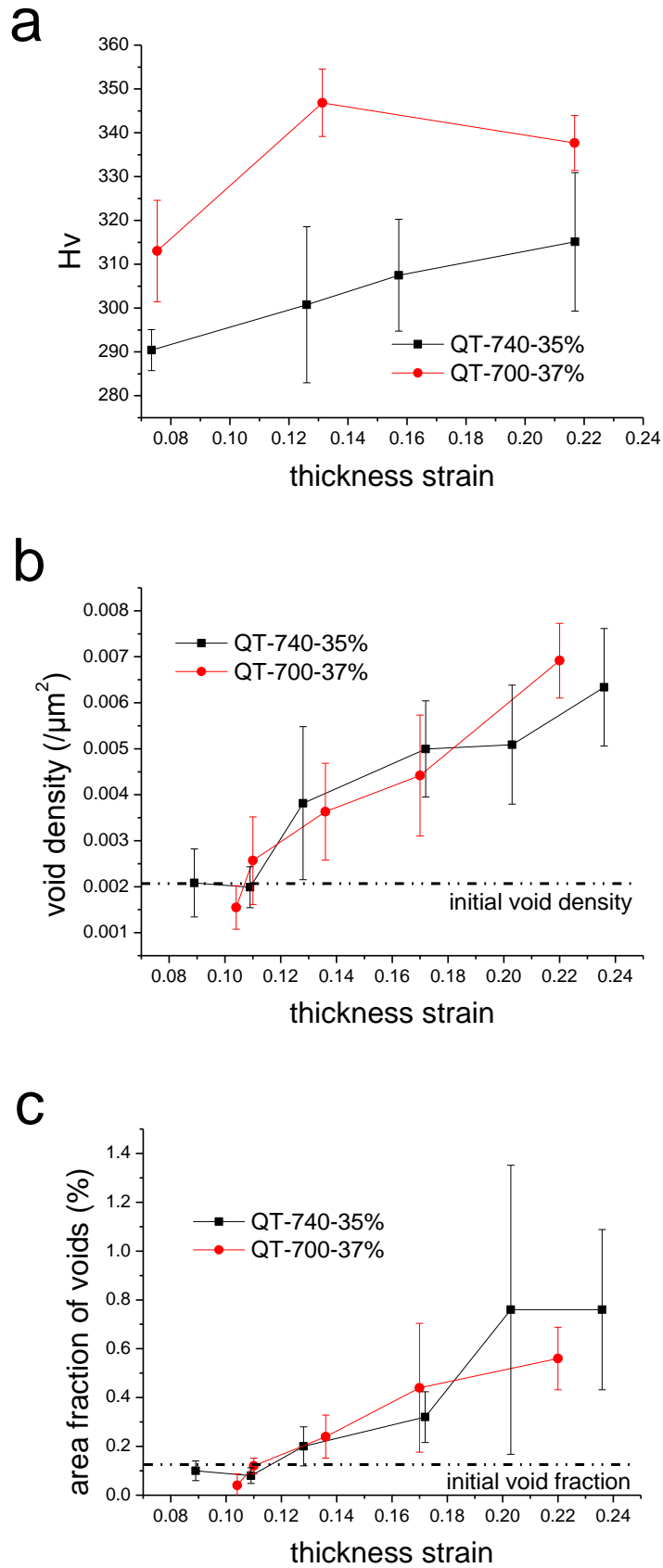


Figure 4.16. Variation of microhardness (a), void density (b) and area fraction of voids (c) of QT-740-35% and QT-700-37% as a function of thickness strain. Notice that only

voids larger than $0.11\mu\text{m}^2$ are taken into account.

4.3.3 Brief discussion

The martensite phase acts as a reinforcement in the composite dual-phase microstructure, bearing a significant fraction of load. The load transfer results in high stress in martensite and higher stress triaxiality in the ferrite matrix compared to the overall stress triaxiality [161]. High stress in martensite can lead to damage nucleation by martensite fracture; while high stress triaxiality in ferrite around martensite can lead to interface decohesion and faster void growth. The hardness contrast between ferrite and martensite, which determines the plastic incompatibility, is the origin of the load transfer. Therefore, the hardness of martensite should be an important factor in determining the damage resistance of DP steels.

However, the results in Figure 4.14a show the complexity of the effect of martensite hardness. That is, the fracture strain is only changed by the martensite composition with sufficiently high V_m . To clarify the physics behind, the discussion will be separated into two subsections. One is dedicated to the case of low V_m (<21%) and the other is for the case of high V_m (>21%).

4.3.3.1 Effect of martensite hardness: cases of low martensite volume fraction

It has been shown in chapter 3 that the plastic properties of DP steels are not sensitive to martensite composition when V_m is low (less than 21%). This is because the stress in the martensite does not reach the yield strength within both QT-700 and QT-740. The elastic properties of martensite are not significantly affected by a variation in composition. This point can explain that the fracture strain of QT-700 and QT-740 is the same when V_m is low (below 21%), since the martensite phase in QT-700 and QT-740 is deforming mainly elastically during damage accumulation and the dominating damage mechanism is interface decohesion but not martensite fracture (Figure 4.12b).

4.3.3.2 Effect of martensite hardness: cases of high martensite volume fraction

The difference in fracture strain can be observed when V_m is high enough (more than 21%), which is consistent with the trend of plastic properties (see chapter 3). QT-700 has higher hardness of martensite, and the fracture strain is lower.

The effect of martensite hardness is firstly attributed to the influence on damage nucleation. For the damage nucleation by interface decohesion, the increase of martensite hardness can increase the normal stress and also stress triaxiality at the ferrite/martensite interface [93], which can promote damage nucleation. But according to the damage observations in Figure 4.5 and Fig.4.6, interface decohesion is not the dominating damage mechanism when V_m is high. Thus, this effect should not significantly impact the fracture strain in this condition.

For the damage nucleation by martensite fracture, the effect of martensite hardness should be two-fold. Firstly, it is related to the plastic compatibility between ferrite and martensite. A hard martensite will favor load transfer and thus bears higher stress. This will increase the probability of martensite fracture. Secondly, the hardness of martensite is usually increased by carbon content. But an increase of carbon content can result in a more brittle martensite, the fracture strain of which is significantly decreased [39]. Therefore, a low martensite hardness or low martensite carbon content can improve the fracture strain of DP steels by enhancing the plasticity of martensite. In [57], it has been reported that a low carbon content in martensite (about 0.07wt%) can enhance the co-deformation between martensite and ferrite and the damage nucleation is significantly suppressed, resulting in an increased fracture strain. It should be emphasized that the martensite with 0.07wt% carbon, which is unusually low for commercial DP steels, must be very ductile and can undergo substantial plastic strain. A similar effect has been quantified by X-Ray micro-tomography in the comparison between 0.3wt% and 0.15wt% carbon content with 60% martensite volume fraction [59].

In this work, the effect of martensite hardness on fracture strain can be observed, but its effect on damage nucleation cannot be identified (Figure 4.15 and Figure 4.16). With the used metallographic technique, QT-700-37% and QT-740-35% have the same evolution of void density and area fraction of voids (Figure 4.16). This can be explained from the point of morphology when V_m is high. For a cold-rolled

dual-phase steel, the continuous wide martensite bands become significant, which can be observed in the microstructures analyzed in Figure 3.1. The continuous martensite bands are efficient in load-transfer but are also the highly preferential site of martensite fracture [98, 108]. Voids can easily form at the hard bands, which detrimentally influences the fracture resistance [108]. According to the damage characterization, large voids are formed dominantly at the wide continuous martensite bands in QT-700-28% (Figure 4.5) and QT-700-37% (Figure 4.6), and these large voids contribute significantly to damage accumulation by a large proportion of void area fraction (Figure 4.2c). Additionally, the martensite islands should become connected with each other when V_m is increasing. The joint part of the martensite islands also act as preferential site for martensite fracture [106]. Although the hardness of martensite in QT-740-35% has been decreased, it cannot efficiently postpone the damage nucleated at the martensite bands and connected martensite islands. As a result, a similar damage accumulation between QT-700-37% and QT-700-35% is observed.

Therefore, the improved fracture strain of QT-740-35%, comparing with QT-700-37%, cannot be explained by the damage accumulation measured by the metallographic method here. One of the limitations of these results is that the void density right before fracture cannot be sensitively probed. Another limitation is that the nano-voids or closed voids may not be detected by SEM [156]. Although the nano-voids are not important to the flow behavior of DP steels, it has been reported to influence the void coalescence through a local softening of the matrix in between the primary voids [99]. Considering the higher flow stress and higher martensite hardness in QT-700-37%, it is proposed that more damage can nucleate at the small martensite islands, resulting in larger population of small voids to promote void coalescence and thus a lower fracture strain.

4.4 Influence of microstructure refinement on damage and fracture

4.4.1 Effect of microstructure refinement on fracture strain

Figure 4.17a shows the comparison of fracture strain between CG- and UFG-DP. It is found that CG-DP-36% and UFG-DP-37%, which have practically the same V_m , have the same fracture strain. However, the fracture strain of UFG-DP-27% is equal to

Chapter 4 Damage and fracture of DP steels

CG-DP-21% that has even lower V_m .

As presented in chapter 3, microstructure refinement results in an increase of tensile strength. Therefore, the comparison between CG-DP-36% and UFG-DP-37% reveals that microstructure refinement can maintain fracture strain while increasing the strength. Furthermore, the results of UFG-DP-27% show a simultaneous increase of tensile strength and fracture strain. These results are summarized in Figure 4.17b.

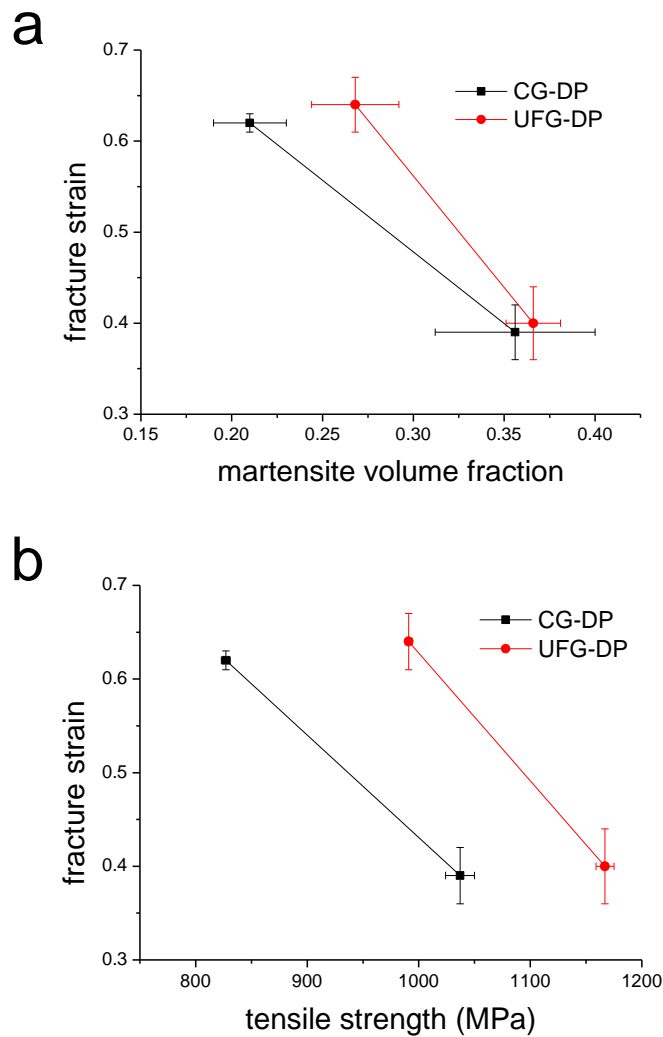


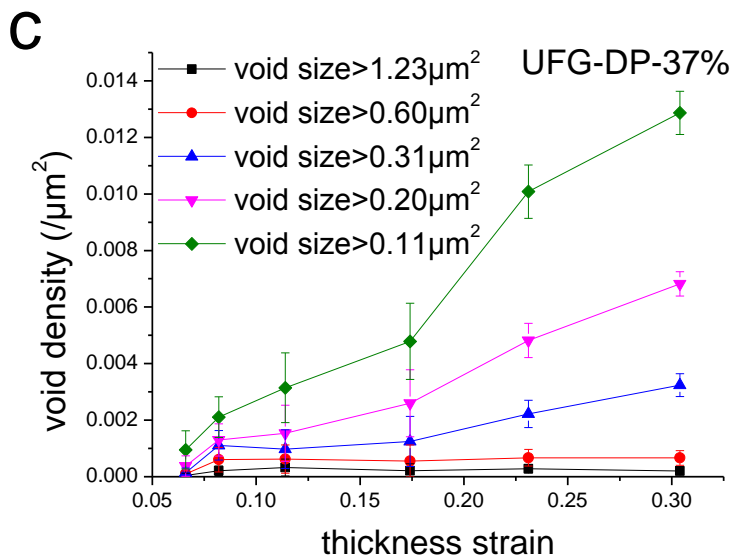
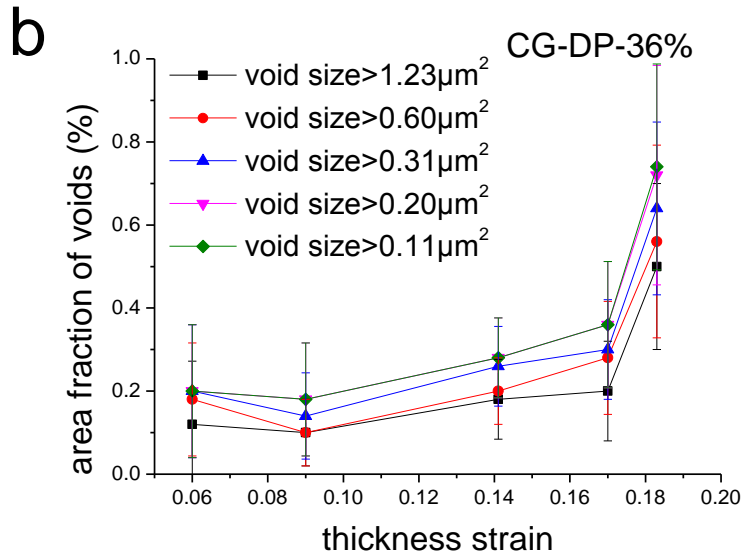
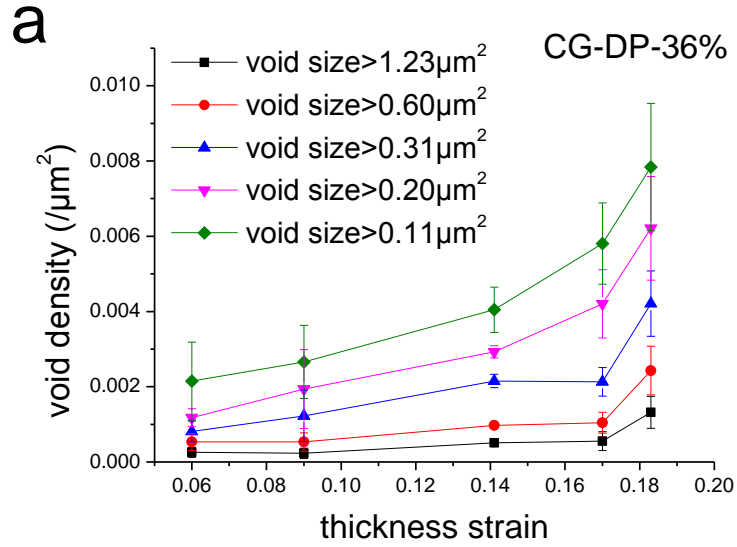
Figure 4.17. Variation of the fraction strain of CG- and UFG-DP with martensite volume fraction (a) and fracture strain—tensile strength relationship (b).

4.4.2 Effect of microstructure refinement on damage and fracture: CG-DP-36% VS UFG-DP-37%

4.4.2.1 Microstructure refinement and damage accumulation

Figure 4.18 shows the evolution of void size distribution with thickness strain in CG-DP-36% and UFG-DP-37%. For CG-DP-36%, there are a large proportion of small voids throughout the thickness strain and the density of large voids (larger than $1.23\mu\text{m}^2$) is limited (Figure 4.18a); but the large voids contribute to a large proportion of the total area fraction of voids (Figure 4.18b).

UFG-DP-37% presents very different damage accumulation evolution compared to CG-DP-36%. The population of voids in UFG-DP-37% mainly consist of small voids (with size from $0.31\mu\text{m}^2$ to $0.11\mu\text{m}^2$), and there is not an observable increase of the number of large voids (Figure 4.18c). Additionally, the area fraction of voids is mainly the result of the large proportion of small voids. Concerning the measurement scatter, the area fraction of large voids can be considered as unchanged with thickness strain (Figure 4.18d).



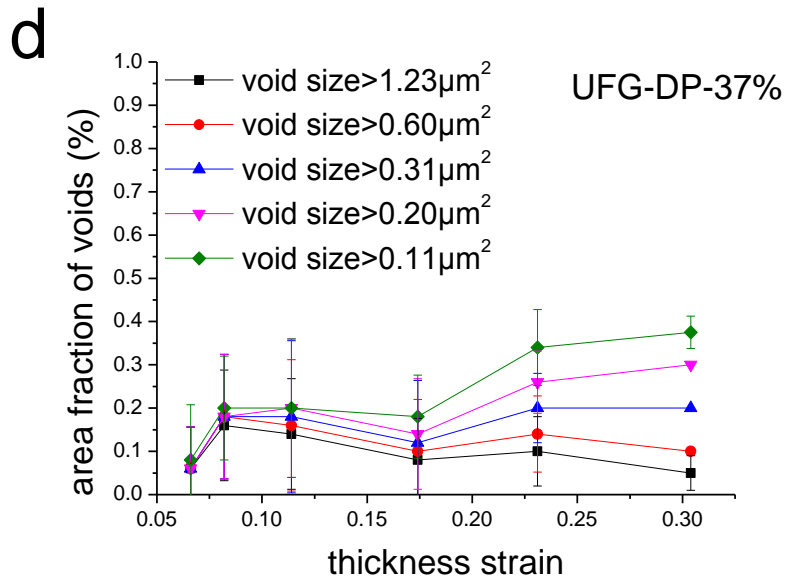


Figure 4.18. Evolution of damage with thickness strain for different ranges of void size in CG-DP-36% (a and b) and UFG-DP-37% (c and d).

The post-necking hardening and damage accumulation in CG-DP-36% and UFG-DP-37% are quantitatively compared in Figure 4.19. In accordance with higher tensile strength, UFG-DP-37% has also higher flow stress after necking (Figure 4.19a). However, the higher flow stress does not result in a more significant damage accumulation in UFG-DP-37%. The comparison of void density in Figure 4.19b shows that the void nucleation strain is very similar between CG-DP-36% and UFG-DP-37%. Additionally, the area fraction of voids in UFG-DP-37% is even smaller (Figure 4.19c).

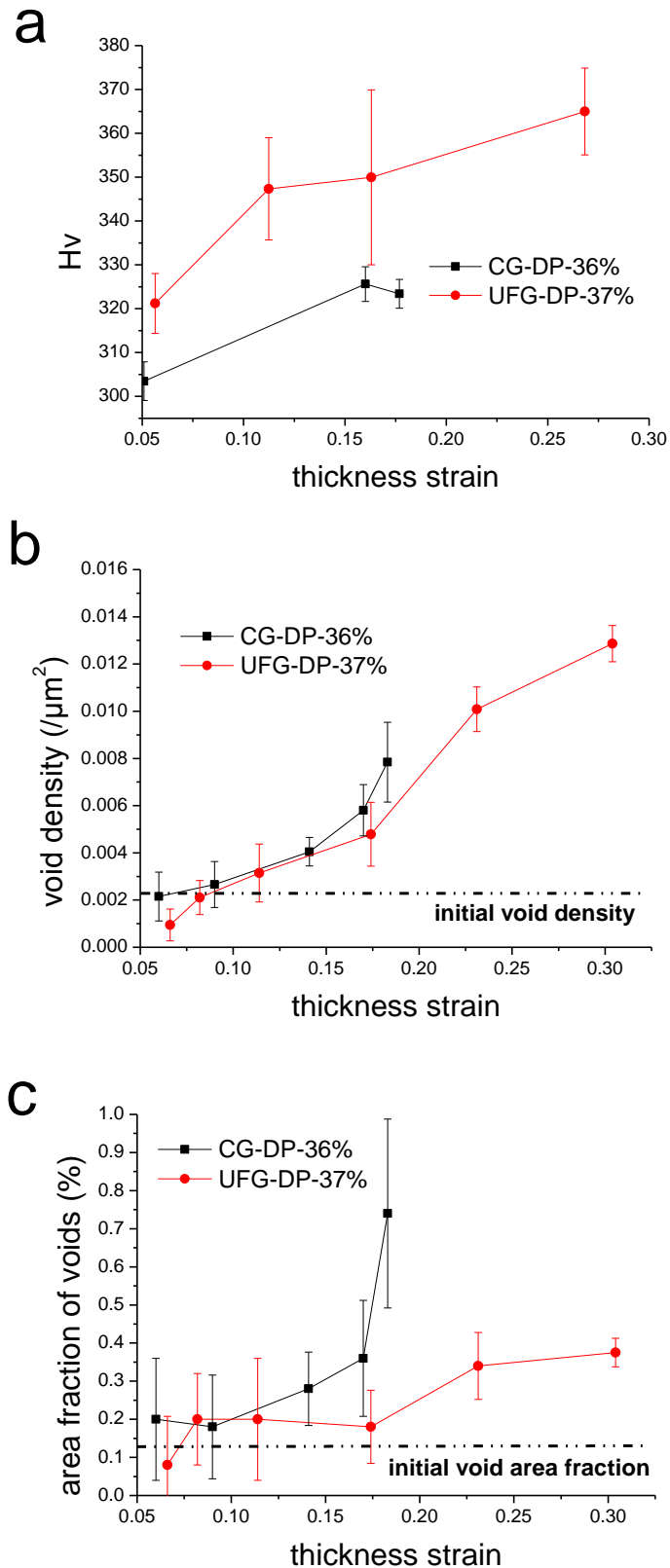


Figure 4.19. Variation of microhardness (a), void density (b) and area fraction of voids (c) of CG-DP-36% and UFG-DP-37% as a function of thickness strain. Notice that only voids larger than $0.11\mu\text{m}^2$ are taken into account.

4.4.2.2 Microstructure refinement and damage mechanisms

- **Damage mechanisms in UFG-DP-37%**

Figure 4.20 shows micrographs with damage occurrence in UFG-DP-37%. The tensile specimen was broken in a shear mode and there is no significant damage close to the fracture surface (Figure 4.20a and b). Comparing with the microstructure before deformation (Figure 2.28), both the martensite and ferrite grains are elongated, indicating substantial co-deformation between ferrite and martensite. Voids can be observed in the martensite cluster zone but there seems to be no significant growth (Figure 4.20b). Both interface decohesion (Figure 4.20c) and martensite fracture (Figure 4.20d) are operating in this refined microstructure.

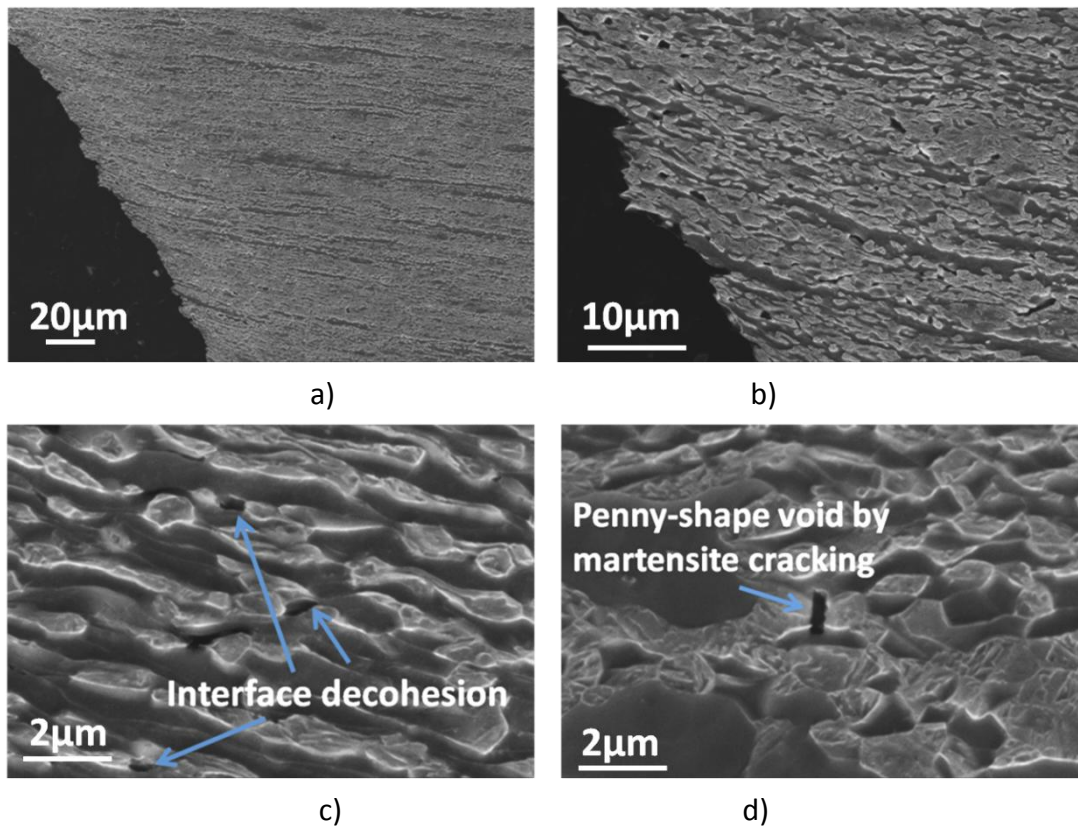


Figure 4.20. Micrographs showing damage mechanisms in UFG-DP-37%.

- **Damage mechanisms in CG-DP-36%**

Figure 4.21a-d are SEM micrographs showing damage mechanisms in CG-DP-36%. The comparison with Figure 4.20 reveals the consequences of microstructure refinement on damage behavior. The shape and distribution of martensite phase in

Chapter 4 Damage and fracture of DP steels

CG-DP-36% imply less co-deformation with ferrite (Figure 4.21a). Large voids are observed, formed by the fracture of the martensite bands (Figure 4.21b). The large voids grow by separating the broken martensite bands but do not grow into ferrite matrix. Smaller voids are formed at the martensite islands. Both martensite fracture (Figure 4.21c) and interface decohesion (Figure 4.21d) are operating damage nucleation mechanisms. But interface decohesion occurs only around small martensite islands and is playing a secondary role in the damage accumulation.

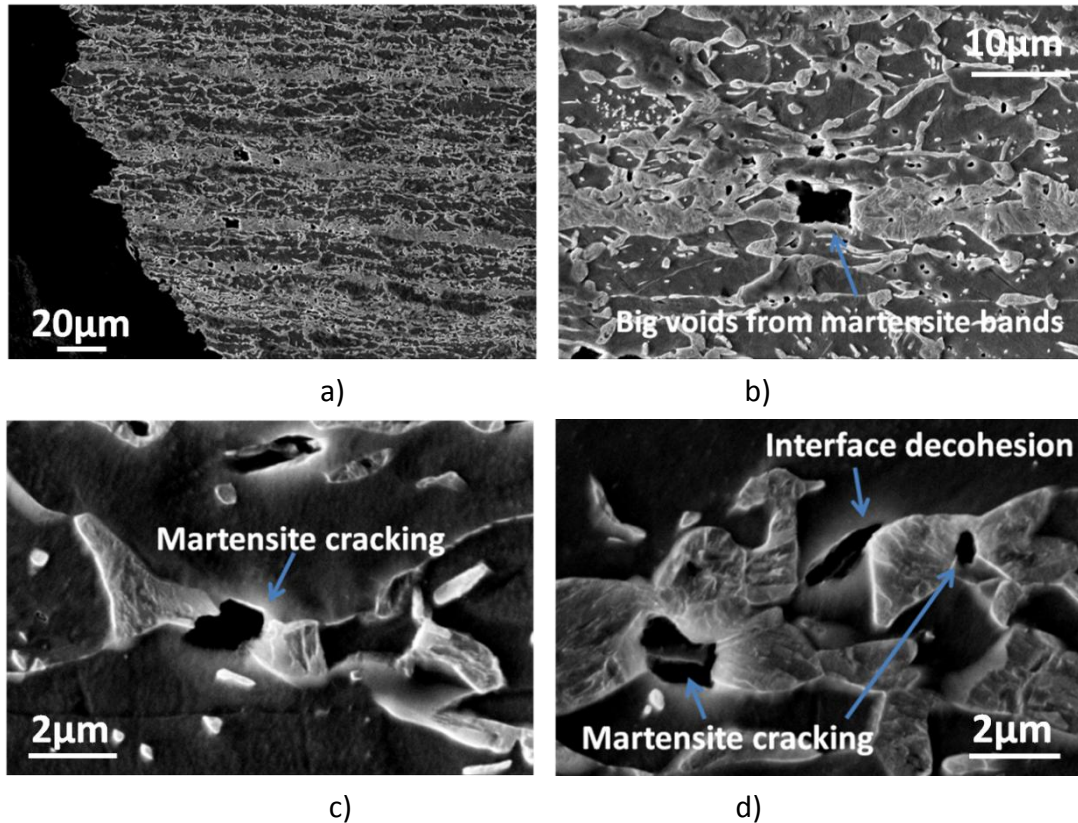


Figure 4.21. Micrographs showing damage mechanisms in CG-DP-36%.

4.4.2.3 Microstructure refinement and fracture behavior

- **Fracture mechanism in UFG-DP-37%**

UFG-DP-37% breaks in a ductile mode and the fracture surface is covered by dimples (Figure 4.22a and b). The dimples are small and shallow (Figure 4.22c and d). Some evidences of delamination can be observed in Figure 4.22c.

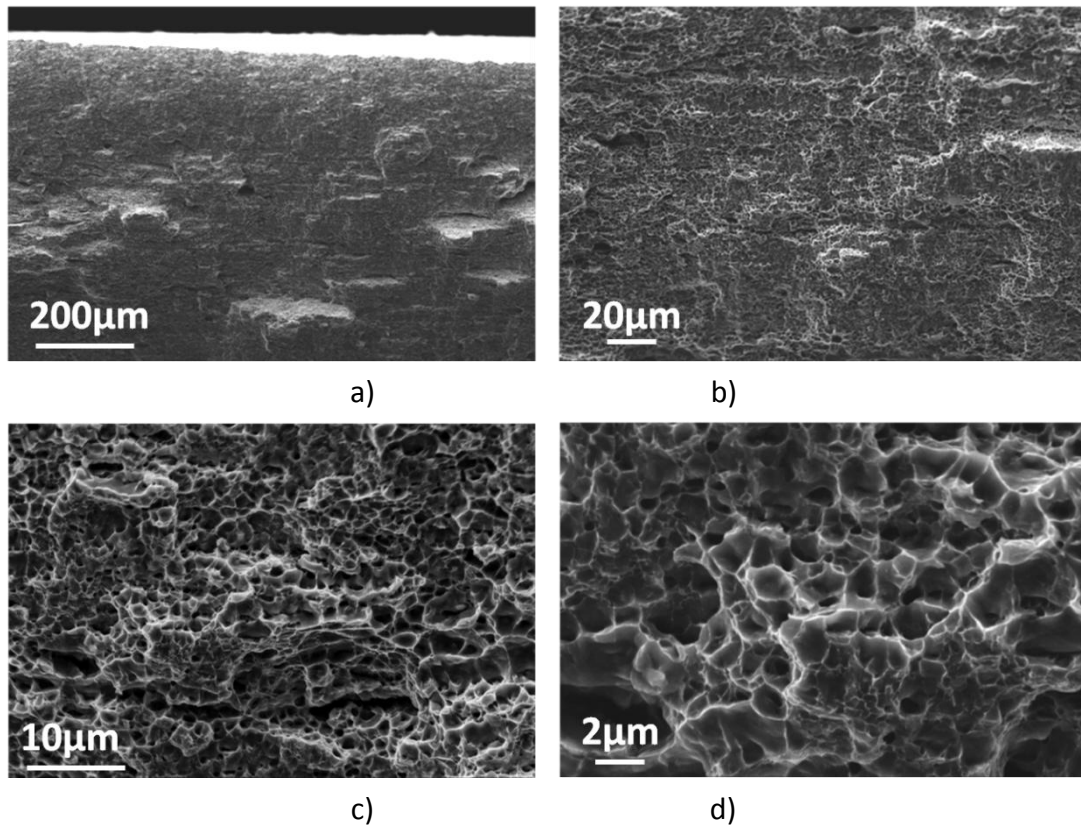


Figure 4.22. Fracture surface of UFG-DP-37%.

● **Fracture mechanism in CG-DP-36%**

Both the dimples and cleavage regions are observed on the fracture surface of CG-DP-36% (Figure 4.23a). The center of the fracture surface is covered with dimples (Figure 4.23b). The cleavage zone is located at the edge of tensile specimen, which is similar to the observations in Figure 4.10 and Figure 4.11. In the transition zone between ductile and brittle fracture, cleavage is observed to be surrounded by dimples (Figure 4.23c). In the zone mainly with brittle features, cleavage is dominating but a few dimples can still be observed (Figure 4.23d). The dimples of CG-DP-36% are larger than those of UFG-DP-37%. The mean distance between dimple centers (d_d) in CG-DP-36% and UFG-DP-37% are $3.5 \pm 0.7 \mu\text{m}$ and $1.6 \pm 0.3 \mu\text{m}$, respectively, and the ratio of $d_d^{\text{CG-DP-36\%}}/d_d^{\text{UFG-DP-37\%}}$ is about 2.2. According to the measurement in chapter 2, the mean distance between martensite (d_m) before deformation, which is the sum of mean free path of ferrite and mean linear size of martensite, of CG-DP-36% and UFG-DP-37% is $6.5 \mu\text{m}$ and $3.4 \mu\text{m}$, respectively, and the ratio of $d_m^{\text{CG-DP-36\%}}/d_m^{\text{UFG-DP-37\%}}$ is 1.9. The value of $d_d^{\text{CG-DP-36\%}}/d_d^{\text{UFG-DP-37\%}}$ is close to $d_m^{\text{CG-DP-36\%}}/d_m^{\text{UFG-DP-37\%}}$, indicating the similar probability of forming a void at every

Chapter 4 Damage and fracture of DP steels

martensite island between CG-DP-36% and UFG-DP-37% up to void coalescence.

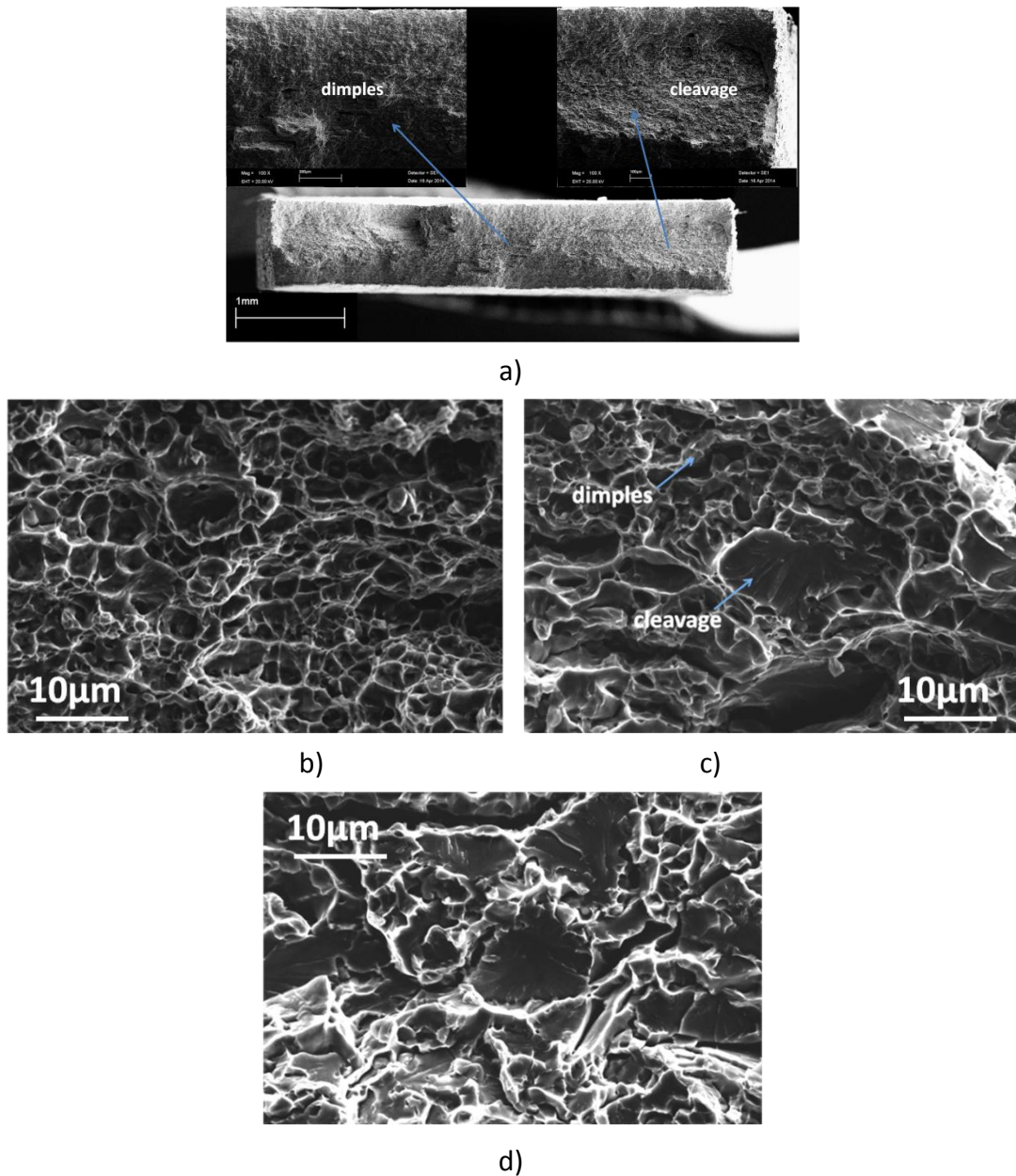


Figure 4.23. Fracture surface of CG-DP-36%.

Combining metallography and fractography observation can provide useful information regarding the cleavage areas. Cleavage patches are observed on the fracture surface perpendicular to the tensile axis (Figure 4.24a). Figure 4.24b and c clearly show that the cleavage patches correspond to the ferrite grains but not to the less ductile martensite phase. Arrested cracks within the ferrite matrix can be observed (Figure 4.24d and e) and the one in Figure 4.24e was arrested by the martensite islands at the ferrite grain boundary. Additionally, there are cracks propagating at the martensite clusters along the tensile axis (Figure 4.24f).

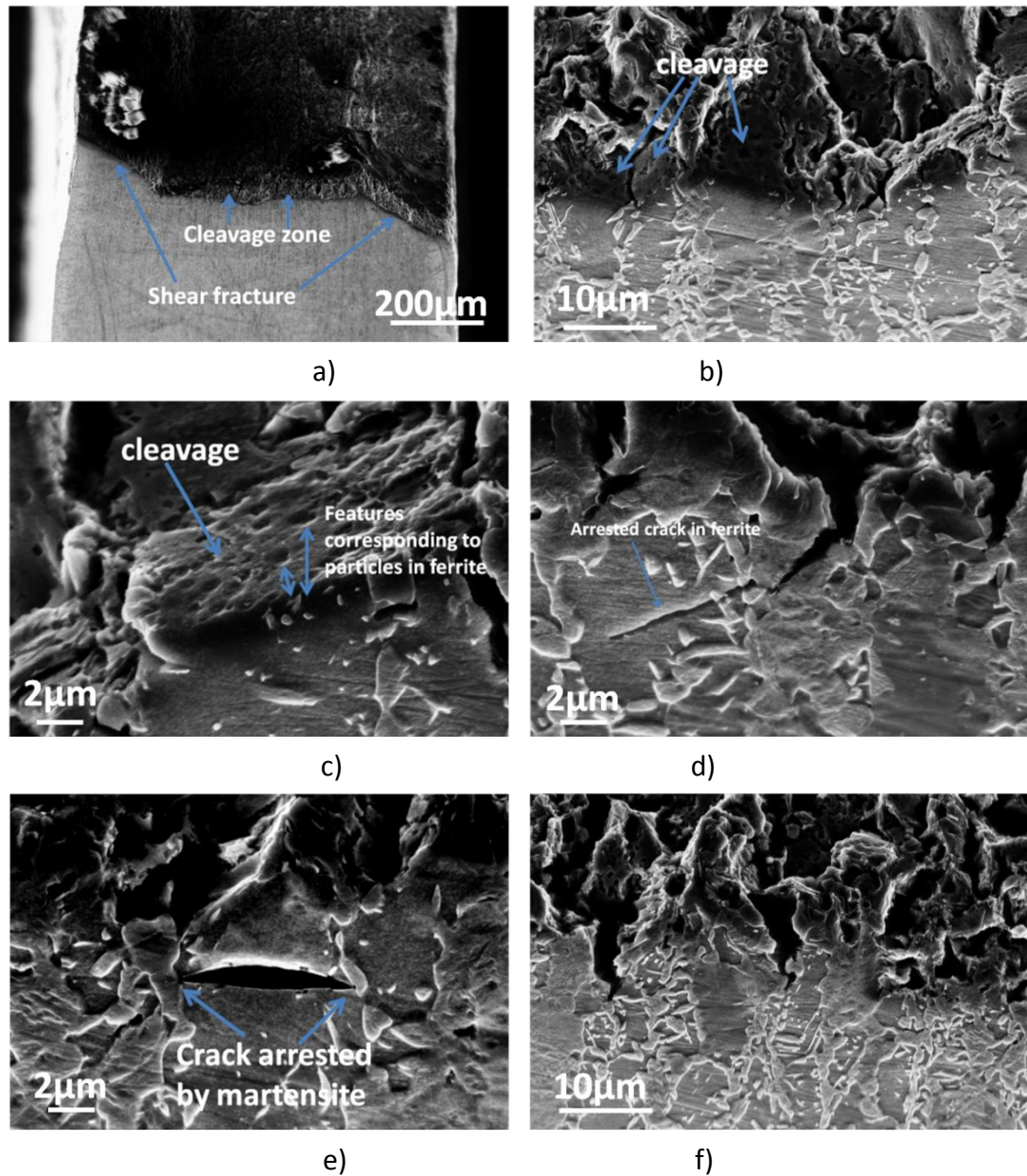


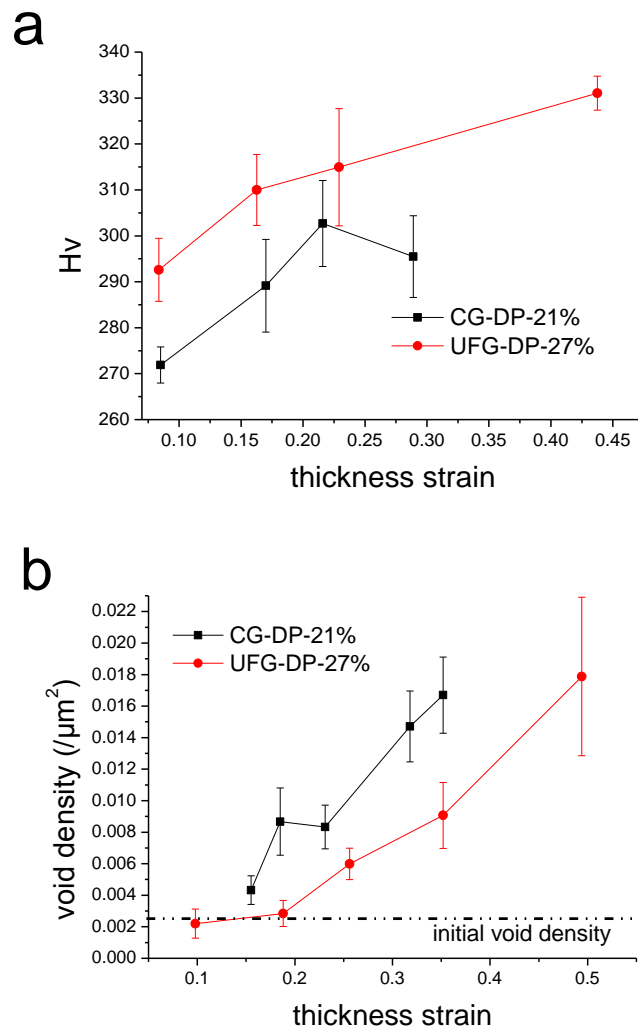
Figure 4.24. Metallography observation close to the fracture surface of CG-DP-36%.

4.4.3 Effect of microstructure refinement on damage and fracture: UFG-DP-27% VS CG-DP-21%

UFG-DP-27% presents excellent combination of strength and fracture strain. In this section, we uncover the possible factors that can explain why UFG-DP-27% and CG-DP-21% exhibit the same fracture strain even though the higher martensite volume fraction is involved in the refined microstructure.

4.4.3.1 Comparison of damage accumulation

Besides the higher tensile strength, UFG-DP-27% exhibits also a higher flow stress after necking, as shown in Figure 4.25a. However, damage formation in CG-DP-21% is accelerated in terms of void nucleation strain and nucleation rate (Figure 4.25b). With the same thickness strain, UFG-DP-27% has a lower density of voids than CG-DP-21%. Additionally, the area fraction of voids in CG-DP-21% is also larger than UFG-DP-27%. In these comparisons, damage accumulation in CG-DP-21% is more significant, even though it has lower martensite volume fraction.



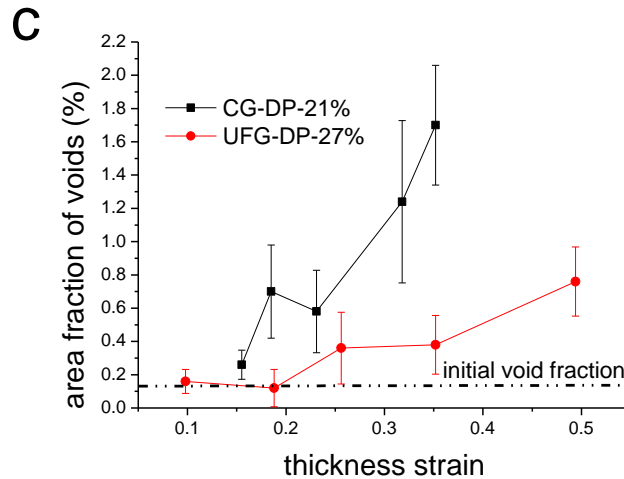


Figure 4.25. Comparing the evolution of microhardness (a), void density (b) and area fraction of voids (c) between CG-DP-21% and UFG-DP-27%. Notice that only voids larger than $0.11\mu\text{m}^2$ are taken into account.

4.4.3.2 Damage mechanisms of UFG-DP-27% and CG-DP-21%

Figure 4.26a-d are SEM micrographs showing the damage mechanisms in UFG-DP-27%. The tensile specimen breaks in a shear mode with more than one shear cracks are onset (Figure 4.26a). Voids can be observed but there is no large void even close to the fracture surface (Figure 4.26b). Both the martensite and ferrite phases have been elongated (Figure 4.26b), indicating a co-deformation similar to UFG-DP-37%. Both interface decohesion and martensite fracture are operating damage mechanisms (Figure 4.26c and d). The voids can grow into a considerably elongated shape, resulting in a large aspect ratio (Figure 4.26c).

Same as for UFG-DP-27%, CG-DP-21% also breaks by a shear mode (Figure 4.27a). Large voids can be observed adjacent to the fracture surface and they are located at the martensite bands (Figure 4.27a). The large voids can be formed by coalescence between adjacent voids in the martensite band (Figure 4.27b). Martensite fracture (Figure 4.27c) and interface decohesion (Figure 4.27d) are observed, but the later mechanism only occurs around the small martensite islands.

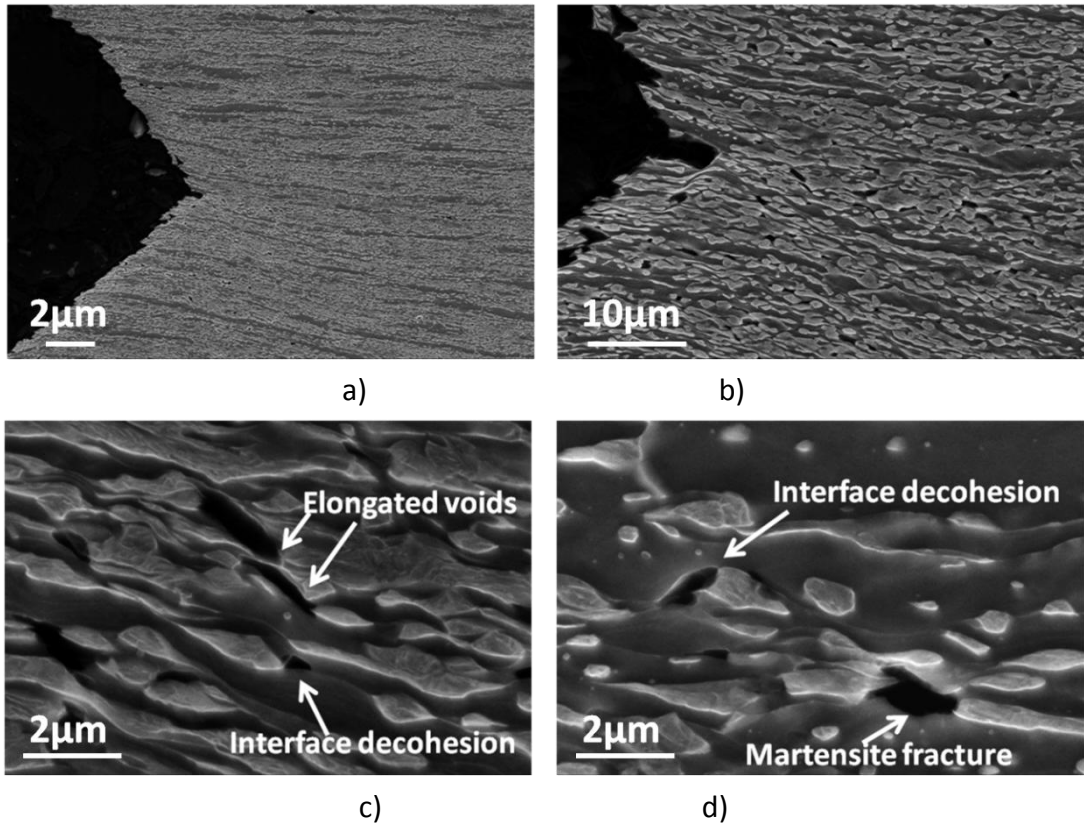


Figure 4.26. Damage mechanisms in UFG-DP-27%.

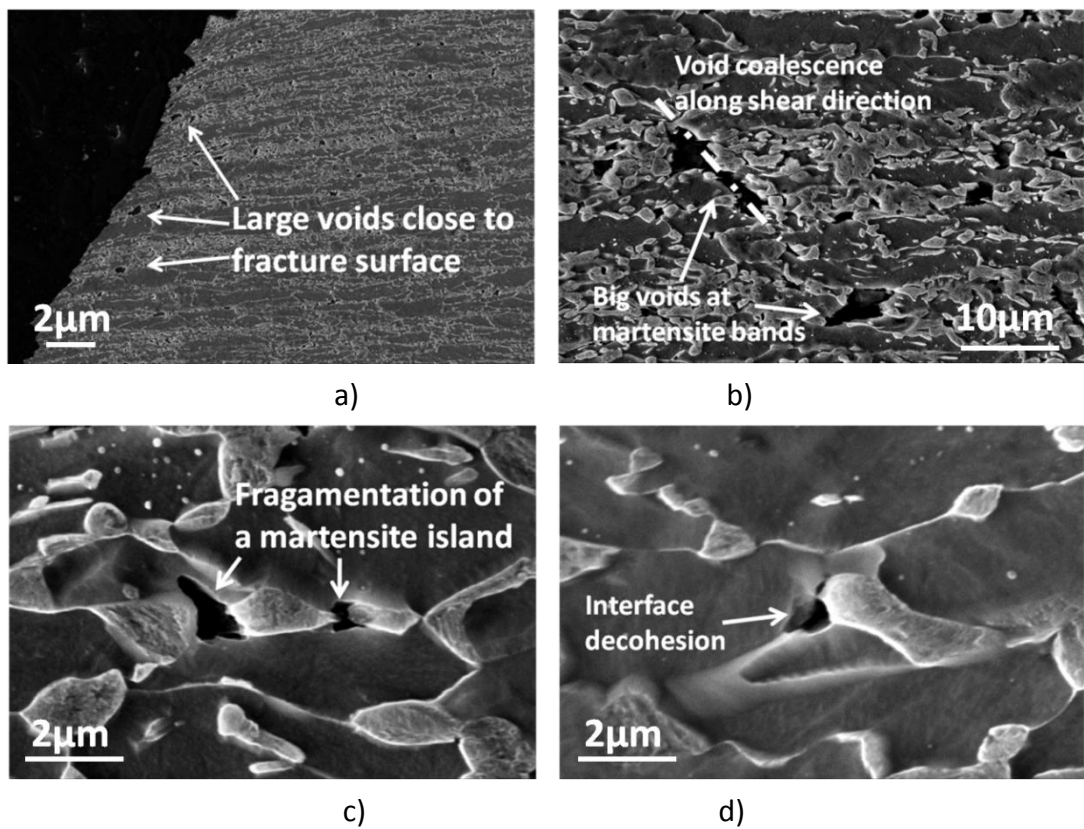


Figure 4.27. Damage mechanisms in CG-DP-21%.

4.4.3.3 Fracture mechanisms in UFG-DP-27% and CG-DP-21%

The fracture mechanism in UFG-DP-27% and CG-DP-21% is primarily ductile with fracture surfaces covered by dimples (Figure 4.28 and Figure 4.29). The dimples in UFG-DP-27% are smaller and the mean distance between dimple centers is about $1.7\mu\text{m}$; while that of CG-DP-21% is $2.7\mu\text{m}$. The ratio of $d_d^{\text{CG-DP-21\%}}/d_d^{\text{UFG-DP-27\%}}$ is about 1.6. According to the measurement in Figure 2.31, the ratio of $d_m^{\text{CG-DP-21\%}}/d_m^{\text{UFG-DP-27\%}}$ is about 2.2. The ratio of $d_d^{\text{CG-DP-21\%}}/d_d^{\text{UFG-DP-27\%}}$ is lower than the ratio of $d_m^{\text{CG-DP-21\%}}/d_m^{\text{UFG-DP-27\%}}$, indicating that the probability of forming a void at every martensite island is lower in UFG-DP-27% even though it has higher martensite volume fraction. Additionally, it should be noticed that the fracture surface of UFG-DP-27% shows obvious features of shear localization between dimples.

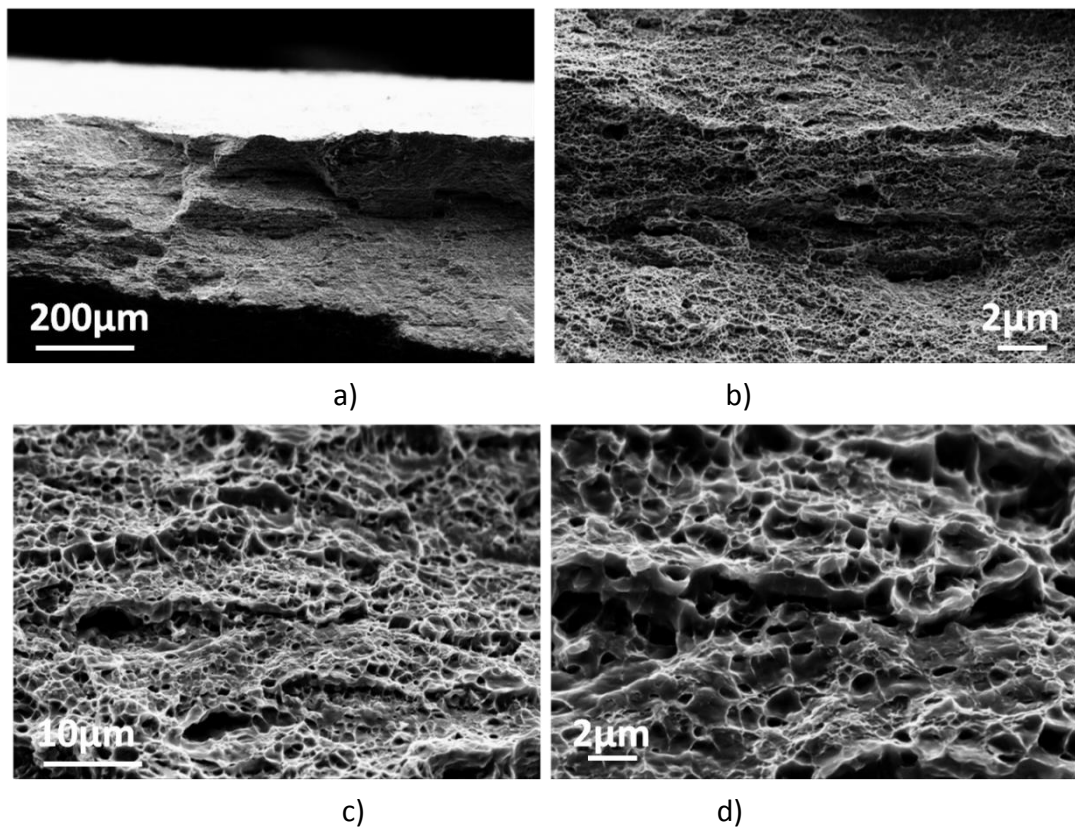


Figure 4.28. Fracture surface of UFG-DP-27%.

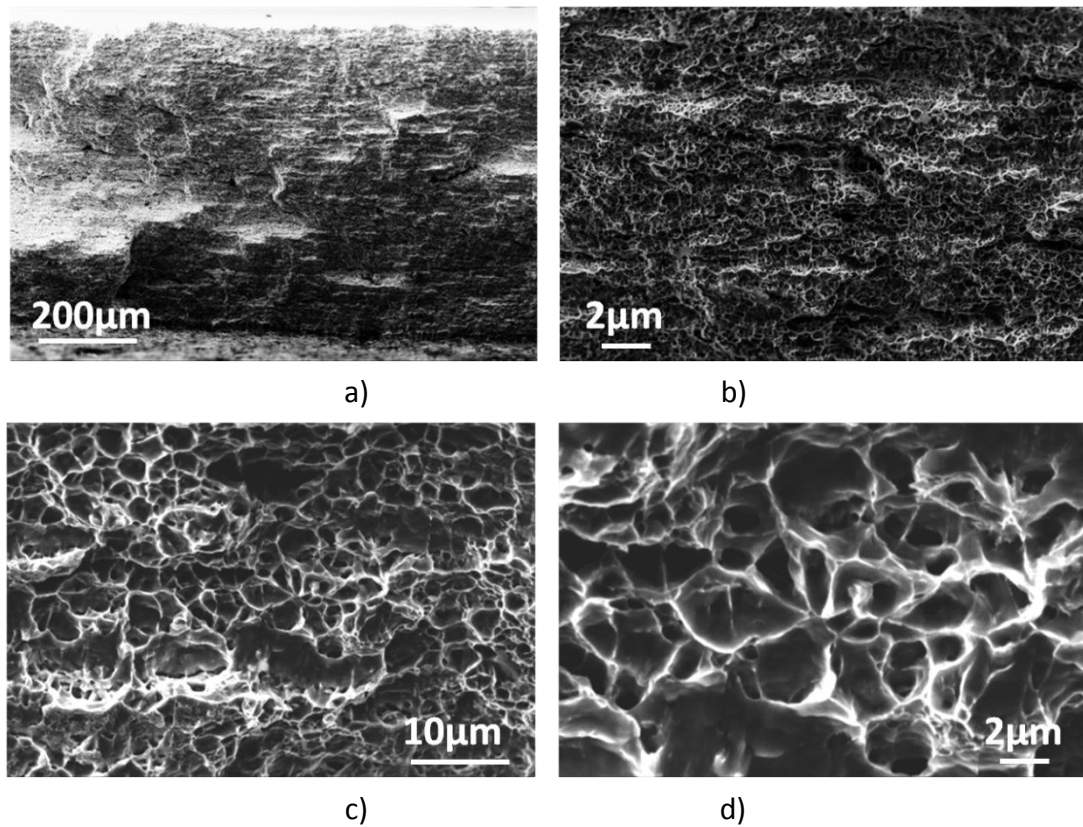


Figure 4.29. Fracture surface of CG-DP-21%.

4.4.4 Discussion

4.4.4.1 Effect of microstructure refinement and damage accumulation

Microstructure refinement results in a better combination of tensile strength and fracture strain (Figure 4.17b). But the origin of this good trade-off is difficult to understand. The fracture strain of CG-DP-36% and UFG-DP-37% is the same; while that of CG-DP-21% and UFG-DP-27% is the same even with different volume fractions of martensite. For the sake of simplicity, the discussion of damage will be separated into the cases of high and low martensite volume fractions in order to clarify the consequences of microstructure refinement to fracture strain.

- **Case of high martensite volume fraction**

- 1) **Damage nucleation**

Chapter 4 Damage and fracture of DP steels

The smaller ferrite grain size in UFG-DP reduces the hardness contrast between the two phases, promoting the co-deformation between matrix and reinforcement [63]. The comparison between Figure 4.20 and Figure 4.21 shows that the elongated martensite in UFG-DP-37% has undergone more deformation than in CG-DP-36%. Considering the low fracture strain of martensite with about 0.3wt% carbon [44], the presence of large deformation promotes void nucleation by martensite fracture, which is detrimental to damage resistance.

However, several counteracting factors are associated to microstructure refinement. The size of the martensite phase has been reduced to about 1 μ m in UFG-DP-37%. Only one variant of martensite laths is present in the small martensite islands [66]. This indicates the elimination of block boundaries. The block boundaries have high residual stress and involve a film of retained austenite [35], which can be the preferential site for martensite fracture. The observation in Figure 4.6 shows the relationship between block boundary and fracture initiation, supporting this argument. Therefore, reducing the size of martensite can decrease the amount of preferential sites for second phase fracture. Additionally, similar to the results reported in [63], the wide and continuous martensite bands have been fragmented by microstructure refinement, although the distribution of martensite islands is to some extent banded. Since premature failure can occur at the wide martensite bands at small strain [108], the elimination of these martensite bands can help to postpone damage nucleation. These two factors are related to the damage nucleation by martensite fracture, and they can be rationalized with the schematic graph in Figure 4.30a.

According to the results in Figure 4.19b, void nucleation is not suppressed by microstructure refinement. The evolution of void density is similar between CG-DP-36% and UFG-DP-37%. Considering the possible underestimation of void density by metallographic technique, the quantification of the dimple density can provide the void density at the moment of coalescence. This kind of comparison is sound only when the fracture strain is similar. The mean distance between dimple centers of CG-DP-36% and UFG-DP-37% are about 3.5 μ m and 1.6 μ m, respectively. Thus, the void density in UFG-DP-37% can even be higher, and the microstructure refinement does not necessarily lead to less damage nucleation events. However, since the ratio of $d_d^{CG-DP-36\%}/d_d^{UFG-DP-37\%}$ is similar to the ratio of $d_m^{CG-DP-36\%}/d_m^{UFG-DP-37\%}$, the probability of forming a void at every martensite island is roughly the same between CG-DP-36% and UFG-DP-37%.

2) Damage growth

Contrary to the void density, the area fraction of voids in UFG-DP-37% remains much lower than in CG-DP-36%. For UFG-DP-37%, the variation of void size distribution with thickness strain indicates the on-going growth process, but the density of voids larger than $0.6\mu\text{m}^2$ is not increasing with strain but keeps a very low level. However, the density of large voids in CG-DP-36% keeps increasing and the large voids contribute to a majority of area fraction of voids.

The observations in Figure 4.20 and Figure 4.21 agree with the quantitative comparison. Firstly, the large voids are mainly formed at the martensite bands and large martensite islands. The elimination of wide and continuous martensite bands and the size reduction of the martensite islands can also decrease the number of large voids. Secondly, as shown in Figure 4.20c, although the microstructure has been substantially deformed, the existing voids have not grown significantly in UFG-DP-37%. The growth of voids is constrained in the refined microstructure.

The growth of voids is controlled by plastic strain and stress triaxiality of ferrite [99]. Once the void is nucleated, it tends to grow into the ferrite matrix due to the larger strain and higher local stress triaxiality. After the microstructure refinement, the smaller ferrite grain size results in more difficult formation of dislocation pile-ups and the plasticity of ferrite becomes more restricted. This has been confirmed by the planar slip mode and only a few lattice rotations that are characterized with a UFG-DP as reported in [63]. Additionally, the reduced strength mismatch between phases in UFG-DP results in that the stress triaxiality in ferrite is not increasing a lot compared to the overall triaxiality. Therefore, the restricted plasticity and lower stress triaxiality of ferrite lead to confined void growth in UFG-DP, and then the damage accumulation is suppressed.

3) Damage coalescence and fracture strain

The area fraction of voids in UFG-DP-37% is lower than CG-DP-36%, but the fracture strain between them is the same. This indicates that the void coalescence cannot be simply predicted by the criterion of porosity only [99]. A recent work has shown that both the void coalescence at micro- and macro-scale can be predicted by a modified Thomason criterion [94]. In this criterion, the most important parameter is the relative void spacing. This parameter can be the same between microstructure that has large voids and large void spacing and that has small voids and small void spacing.

It has been measured that the mean distance between dimple centers in CG-DP-36% is more than twice than in UFG-DP-37%. Considering the void size in CG-DP-36% is obviously larger, it is suspected that the relative void spacing of CG-DP-36% and UFG-DP-37% might be similar, and their similar fracture strain can be predicted by the Thomason criterion.

➤ Case of low martensite volume fraction

It is found that UFG-DP-27% has achieved attractive combination of strength and fracture strain. Even with higher martensite volume fraction, UFG-DP-27 still has the same fracture strain with CG-DP-21%. Additionally, the damage accumulation in UFG-DP-27% is also suppressed (Figure 4.25), especially considering that the flow stress is higher and the carbon content in martensite is higher. The damage observations in Figure 4.26 and Figure 4.27 agree well with the quantified damage accumulation. There are no observable big voids in UFG-DP-27%; while big voids are observed at the martensite bands in CG-DP-21%. It is worth noting that TRIP effect should not contribute to damage because retained austenite has been consumed before necking.

UFG-DP-27% shows the potential of further improving the damage properties by microstructure refinement with lower martensite volume fraction. The quantitative metallography in chapter 2 has shown that UFG-DP-27% has similar mean free path of ferrite with UFG-DP-37%. That is, the area of ferrite grain boundaries should be similar between these microstructures. With lower martensite volume fraction, less ferrite grain boundary area is occupied by martensite phase in UFG-DP-27%, resulting in lower martensite connectivity and then less preferential damage sites. The ratio of $d_d^{CG-DP-21\%}/d_d^{UFG-DP-27\%}$ is lower than the ratio of $d_m^{CG-DP-21\%}/d_m^{UFG-DP-27\%}$, indicating the lower probability of forming a void at every martensite island in UFG-DP-27%, which supports this argument. Additionally, similar to the observation in [63], the martensite islands in UFG-DP are more spherical than in CG-DP. The less connectivity and lower aspect ratio of martensite phase should be the key factors in the delayed damage nucleation of UFG-DP-27%.

4.4.4.2 Effect of microstructure refinement and fracture mechanisms

Microstructure refinement can promote ductile fracture, which is schematically shown in Figure 4.30b. Dimples are covering the fracture surface of UFG-DP-37% while cleavage can be observed in the fracture surface of CG-DP-36%. Similar to QT-700-37%, the cleavage is observed only at the edge of the broken specimen and there is a transition from ductile manner to brittle manner.

In the results of section 4.2, the cleavage of ferrite is phenomenologically triggered by high martensite volume fraction. Here, the volume fraction of CG-DP-36% and UFG-DP-37% are the same. But the effect of microstructure refinement on suppressing brittle fracture might actually follow the same physics. As discussed before, the key issue of cleavage fracture is that the fracture stress of ferrite is reached. In the coarse microstructure, the martensite phase is larger and continuous big martensite bands are formed, resulting in big initial crack. Also, the larger ferrite grain size favors the pile-up of dislocations and results in higher stress concentration at the dislocation obstacles. The big initial crack and larger ferrite grain size can decrease the fracture stress of ferrite. Combining the previously-mentioned geometrical and dynamic effects of main crack propagation, brittle fracture occurs in CG-DP-36%. Microstructure refinement is counteracting the microstructure factors favoring cleavage, and thus promotes ductile fracture in DP steels.

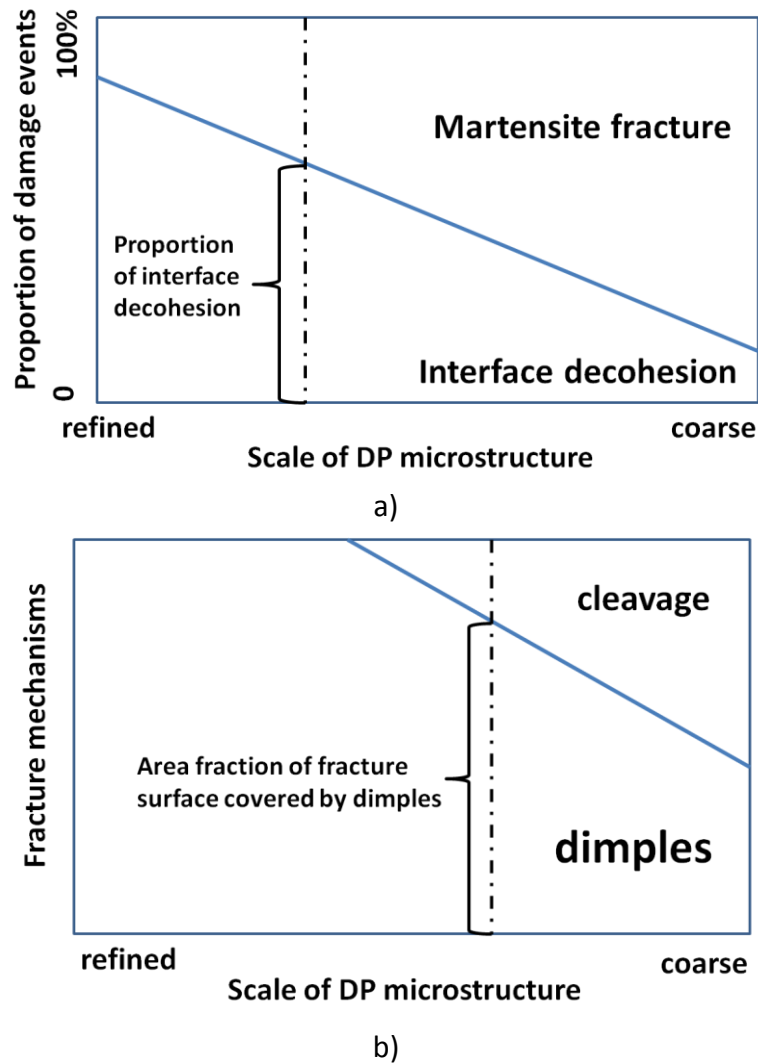


Figure 4.30. Microstructure refinement, the proportion of operating damage mechanisms (a) and fracture mechanisms (b). They are summarized from the observations.

4.5 Summary

With the microstructure developed in chapter 2, the influences of volume fraction and composition of martensite are decoupled, and the ultrafine-grained DP microstructures are achieved. The specific effects of microstructural features on damage and fracture properties are systematically studied. Additionally, detailed characterizations have been made to reveal the damage and fracture mechanisms of DP steels. The main conclusions are drawn as follows.

- 1) The damage accumulation, including both void density and area fraction of voids,

Chapter 4 Damage and fracture of DP steels

is promoted with increasing V_m . Both interface decohesion and martensite fracture are operating damage mechanisms, but the martensite fracture is becoming dominating when the martensite volume fraction is increased.

- 2) The fracture strain is decreased with increasing V_m . The DP steels mainly break in a ductile mode. But with high V_m , brittle fracture by cleavage can be observed, which is attributed to the geometric and dynamic effects.
- 3) The fracture strain is not sensitive to the martensite composition when V_m is low (below 20%). With high enough V_m , the fracture strain is increased with lower martensite hardness. However, the effect of martensite composition on damage accumulation cannot be observed with the microstructures in this study.
- 4) Microstructure refinement results in a better combination of tensile strength and fracture strain. With high V_m (about 37%), UFG-DP has higher tensile strength but the fracture strain is maintained. For the case of low V_m (27%), the tensile strength and fracture strain are simultaneously improved in UFG-DP.
- 5) Microstructure refinement can delay damage nucleation only when V_m is low. The void growth is suppressed in refined microstructures. Therefore, damage accumulation is less significant in UFG-DP steels.
- 6) UFG-DP steels all fracture in a ductile mode. But brittle fracture occurs in CG-DP steels when V_m is high.

Chapter 5 Micromechanical modeling of plasticity and fracture of DP steels

The experimental results in chapter 3 and 4 have shown the effects of various microstructural features on the plastic and fracture properties of DP steels. Qualitative discussions have been made on the deformation behavior and damage mechanisms of DP steels, in order to clarify the specific influences of martensite volume fraction and composition and the scale of microstructure. A micromechanical modeling approach is used to further analyze the results within a more quantitative framework. By systematic parametric studies, the specific influences of each microstructural parameter are studied one by one. The micromechanical modeling also provides a support for microstructure optimization of DP steels.

5.1 Micromechanical model

5.1.1 Constitutive laws of the phases

The constitutive law selected for each phase is the classical, rate-independent J_2 elastoplasticity theory with isotropic hardening. The Young's moduli of ferrite and martensite are presumed to be identical with $E=210\text{GPa}$ and the Poisson ratio $\nu=0.3$.

The plastic behavior of martensite was fitted based on the experimental curves of bulk martensitic samples [59] using the exponential law:

$$\sigma_{y,\alpha'} = \sigma_{y_0,\alpha'} + k_{\alpha'}(1 - \exp(-\varepsilon_p n_{\alpha'})) \quad (5.1)$$

where $\sigma_{y_0,\alpha'}$ is the current yield strength of martensite; ε_p is the accumulated plastic strain; $\sigma_{y_0,\alpha'}$, $k_{\alpha'}$ and $n_{\alpha'}$ are material parameters affected by martensite composition. For the sake of simplicity, only the effect of carbon content will be considered in this work. The influence of the carbon content on the flow behavior is accounted for in the following way. The initial yield stress $\sigma_{y_0,\alpha'}$ is given by:

$$\sigma_{y_0,\alpha'} = 300 + 1000C_{\alpha'}^{1/3} \quad (5.2)$$

where $C_{\alpha'}$ is the carbon content in martensite expressed in wt%. On the other hand, the hardening modulus $k_{\alpha'}$ increases with $C_{\alpha'}$ according to:

$$k_{\alpha'} = \frac{1}{n_{\alpha'}} \left[a + \frac{bC_{\alpha'}}{1 + \left(\frac{C_{\alpha'}}{C_0}\right)^q} \right] \quad (5.3)$$

with $a=33\text{GPa}$, $b=360\text{GPa}$, $C_0=0.7$ and $q=1.45$. The hardening exponent is set as $n_{\alpha'}=120$. The same values are also used in reference [59].

Ferrite is mainly hardened by dislocation storage and its work-hardening response is described by the exponential-type Voce law:

$$\sigma_{y,\alpha} = \sigma_{y_0,\alpha} + \frac{\theta_{\alpha}}{\beta}(1 - \exp(-\beta\varepsilon_p)) \quad (5.4)$$

where $\sigma_{y_0,\alpha}$ is the current yield strength of ferrite, θ_{α} is the initial work-hardening rate and β is the the dynamic recovery coefficient. These material parameters of

ferrite are a priori unknown as they depend on the details of the processing route. Hence, they are identified by fitting the model predictions with the mechanical response of the DP steels.

Only stage-III hardening is considered in the Voce law, with the flow stress saturating at large strain, which is experimentally not observed [147]. This discrepancy reveals that, no matter how efficient dynamic recovery is, there is always dislocation accumulation at large strain which leads to a strain hardening named “stage IV”. The stage-IV hardening is related to, for instance, the ferrite composition and grain size. A modified hardening law for ferrite is thus proposed, taking into account stage-IV hardening as shown below:

$$\sigma_{y,\alpha} = \sigma_{y_0,\alpha} + \frac{\theta_\alpha}{\beta} (1 - \exp(-\beta \varepsilon_p)) \quad \text{for } \sigma_{y,\alpha} \leq \sigma_y^{tr} \quad (5.5a)$$

$$\sigma_{y,\alpha} = \sigma_y^{tr} + \theta_{IV} (\varepsilon_p - \varepsilon_p^{tr}) \quad \text{for } \sigma_{y,\alpha} > \sigma_y^{tr} \quad (5.5b)$$

where σ_y^{tr} and ε_p^{tr} correspond, respectively, to the values of the flow stress and of the plastic strain at the transition point from stage-III to stage-IV hardening. The hardening rate θ_{IV} in stage IV is a constant, and σ_y^{tr} and ε_p^{tr} are given by:

$$\sigma_y^{tr} = \sigma_{y_0,\alpha} + \frac{\theta_\alpha - \theta_{IV}}{\beta} \quad (5.6)$$

and

$$\varepsilon_p^{tr} = \frac{1}{\beta} \ln\left(\frac{\theta_\alpha}{\theta_{IV}}\right). \quad (5.7)$$

5.1.2 Finite element unit cell model

Within the so-called unit cell approach, the behavior of complex microstructures is studied by numerical simulation of the behavior of a representative volume element of the microstructure. The main assumption is that the microstructure is considered as a periodic repeat of the volume under study, and that the aggregate is representative enough for the whole microstructure.

Chapter 5 Micromechanical modeling

The stacked hexagonal array (SHA) model has been proposed by Tvergaard [162] with the idealization shown in Figure 5.1 [79]. The microstructure consists of stacked hexagonal cylinders, each of which contains a single spherical particle. This kind of hexagonal cylinder is approximated as an axisymmetric cell, which is simulated using FEM calculation.

The simulations are performed using the FE commercial code ABAQUS [163]. The unit cell is shown in Figure 5.2. The elements are quadrangular axisymmetric with second-order interpolation function (CAX8R), and the mesh is fine enough (with about 4000 elements) for generating converged results independent of element size. The volume fraction of martensite (V_m) is given by $\frac{2d^3}{3L^3}$ where d is the radius of martensite inclusion and L is the radius of the axisymmetric cell. The boundary conditions applied to the unit cell model simulate the conditions of a uniaxial tensile test. Symmetry about the centerlines (S1 and S2 shown in Figure 5.2) is imposed. The side S3 is kept straight and parallel to S1. A uniform displacement boundary condition is imposed on side S4.

Volume averaging is employed to obtain the true stress—true strain graphs, and the true strain and true stress of the representative volume element (RVE) correspond to the average of these values at each integration point.

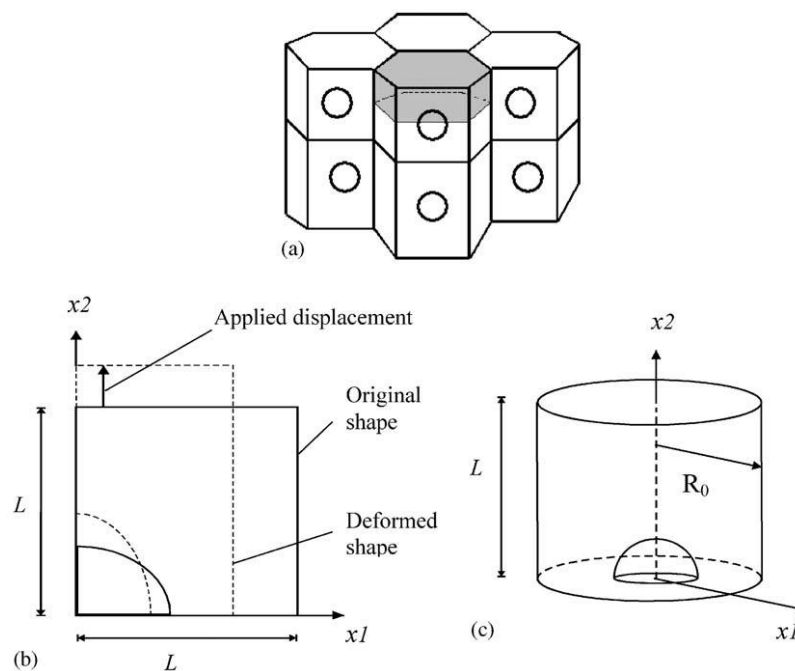


Figure 5.1. The SHA model: (a) three-dimensional array of stacked hexagonal

cylinders, each containing a spherical particle; (b) the deformed and undeformed shape of the RVE under axial loading; and (c) the SHA axisymmetric RVE cell [79].

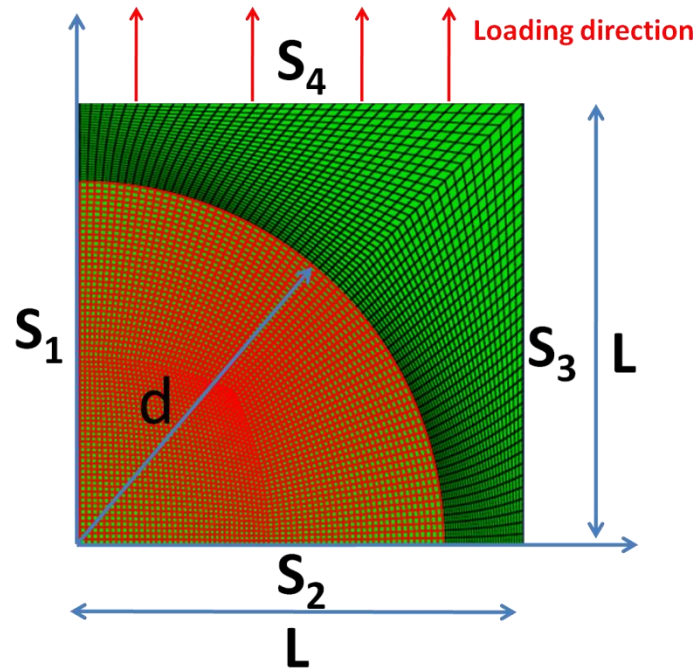


Figure 5.2. Configuration and dimensions of the axisymmetric unit cell.

5.2 Plastic properties of DP steels

The model described in section 5.1 offers a framework to study the effects of the microstructural parameters on the plastic properties of DP steels in order to rationalize the experimental results presented in chapter 3. The ferrite parameters are identified by simulating the experimental flow curves of QT-700 with 15%, 19%, 28% and 37% martensite, where the carbon content in martensite is assumed to be 0.3wt%. The influence of taking into account a stage-IV hardening in the ferrite response is analyzed by comparison with the results of the Voce law with stress saturation. Thereafter, a parametric study is performed to investigate the effect of martensite composition. Regarding the effect of microstructure refinement, a similar strategy is adopted, as presented later.

5.2.1 Effect of martensite volume fraction on strength and ductility of DP steels

The first problem to address is the effect of the martensite volume fraction. The distribution and properties of martensite are kept the same independent of V_m in the unit cell calculation. Indeed, according to the experiment design in chapter 2 and 3, starting from the same spheroidized microstructure, the DP steels have the same spatial distribution of martensite phase (mainly along the ferrite grain boundaries). Furthermore, the hardness of martensite is roughly the same at a fixed annealing temperature (Figure 2.25). Therefore, the simplified unit cell model can be considered as representative to the real microstructure in this sense, but, of course, the periodic distribution remains a strong assumption that will be discussed.

5.2.1.1 Simulation of the tensile curves and parameters identification

The flow behavior of QT-700 with various martensite volume fractions can be properly captured using the Voce law, as shown in Figure 5.3. All the curves are shown up to necking. For the case of low V_m values (such as 15% and 19%), a sharp elasto-plastic transition is shown in the simulated curves (Figure 5.3a and b). For the case of 37% of martensite, such transition is progressive, and the tensile curve shows high initial hardening rate (Figure 5.3d). However, except for the case of 15% martensite, necking as defined by the attainment of the Considere criterion occurs too early in the simulation curves, compared to the experimental curves.

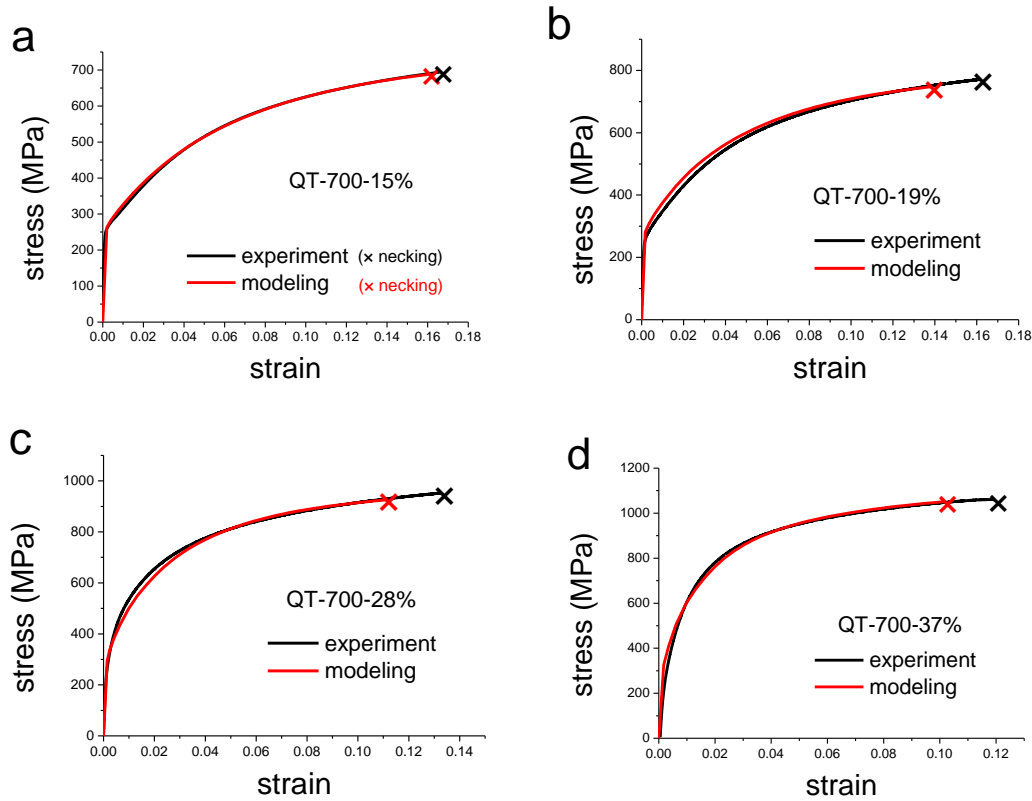


Figure 5.3. Comparison of experimental and simulated tensile curves for QT-700 with 15% (a), 19% (b), 28% (c) and 37% (d) of martensite. All the curves are shown up to necking.

The ferrite parameters are identified by fitting with experimental data, as shown in Figure 5.4. As V_m is increased, the mean free path of ferrite, which can be approximated as equal to the ferrite grain size, is decreased (see chapter 2). Therefore, the yield strength is increased accordingly (Figure 5.4a). The dislocation storage in the vicinity of the grain boundary will contribute both to forest hardening giving an isotropic hardening contribution [147] and to the building up of back stresses (giving a kinematic hardening contribution) [77, 164, 165]. As the grain size is refined, more grain boundaries are generated, and then the isotropic hardening is more efficient and the kinematic hardening becomes significant. These can explain higher θ_α value with finer grain sizes. Additionally, an increased β value can be explained by the enhanced dynamic recovery with more grain boundaries [166]. Therefore, the identified parameters from the experimental results are physically sound.

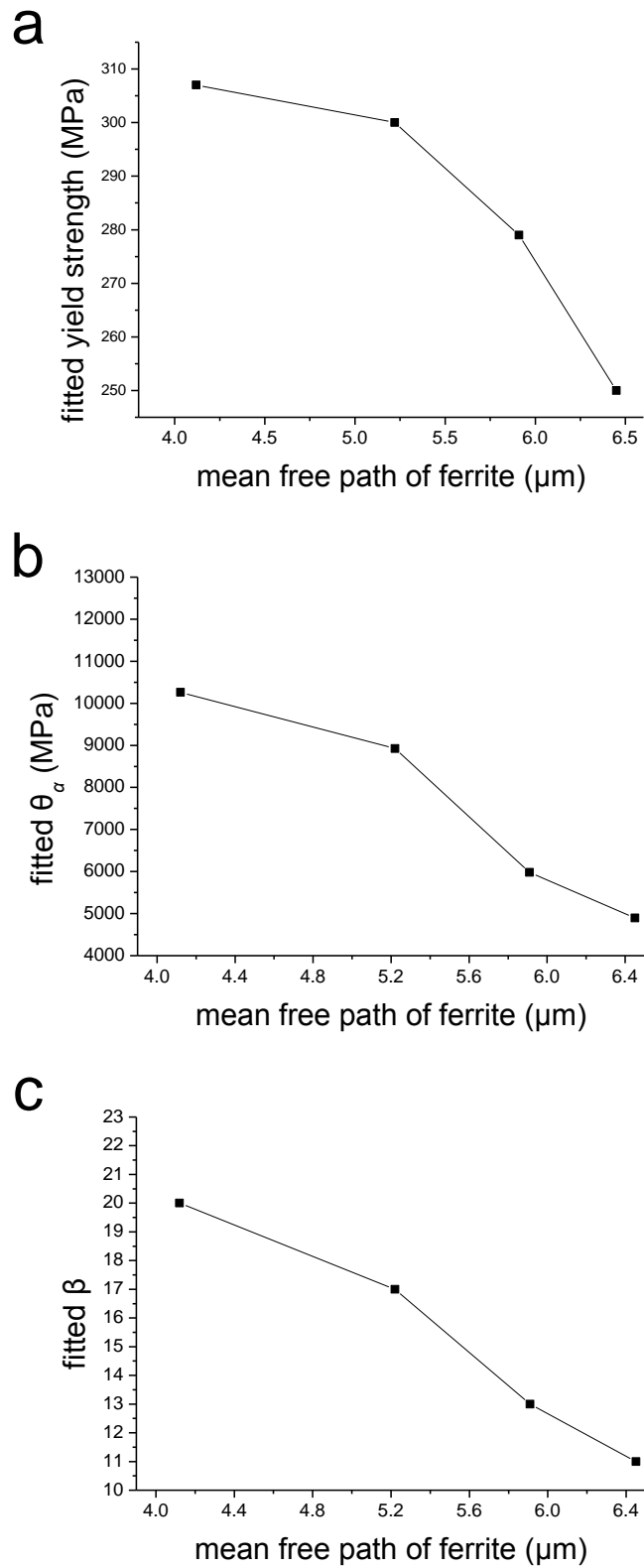


Figure 5.4. Identified ferrite parameters: evolution of (a) yield strength, (b) θ_α and (c) β with mean free path of ferrite. These parameters are identified by fitting with the experimental data.

5.2.1.2 Predictions of tensile strength and uniform elongation

As shown in Figure 5.3, the experimental tensile curves can be well simulated by the model, which provides the basis for the properties predictions. As shown in Figure 5.5a, the tensile strength as a function of martensite volume fraction is accurately described by the model. Both experimental and predicted tensile strengths have an approximately linear relationship with martensite volume fraction.

The predicted uniform elongation decreases with increasing V_m (Figure 5.5b), which also fits the experimental trend (Figure 3.3). However, necking starts earlier in the simulation (Figure 5.3) and the model underestimates the uniform elongation. Except for the cases of 15% and 19% martensite, the predicted uniform elongation is about 2% (in absolute terms) less than the experimental one. This reflects an underestimation of the work-hardening rate at a given flow stress.

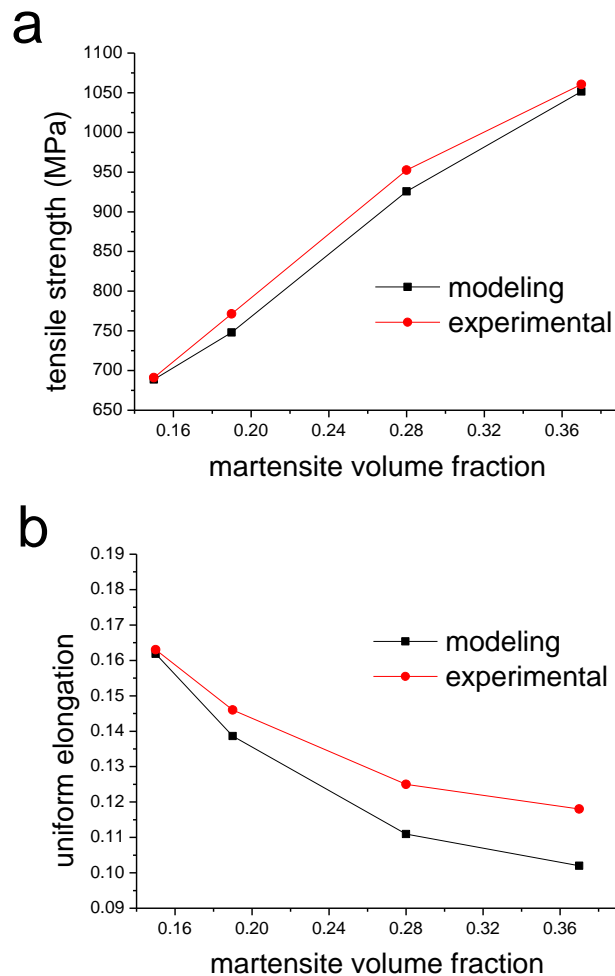


Figure 5.5. Predictions of tensile strength (a) and uniform elongation (b).

5.2.1.3 Improved predictions with stage-IV hardening of ferrite

This section will firstly analyze the origin of the deficiency of the cell calculation regarding the proper prediction of the hardening rate at large strain, and then propose to improve the prediction with a modified behavior law of ferrite (equation 5.5).

➤ **Strain concentration: the necessity of improving the hardening law at large strain**

Since martensite is much stronger than ferrite, strain is higher in the ferrite matrix with a heterogeneous distribution of plastic strain. As shown in Figure 5.6, the equivalent plastic strain (PEEQ) is strongly concentrated in the ferrite at the ferrite/martensite interface, and there is a tendency for strain localization. The plastic strain of the elements at the interface can be up to 5.

In stage III, the work-hardening rate of metals keeps decreasing during deformation, but this trend changes at large strain after entering stage IV and a constant work-hardening rate is reached [147]. This kind of linear hardening in the large strain regime has been observed in several engineering alloys [167] and the transition from stage-III to stage-IV occurs in polycrystals at strain typically between 0.15 and 0.6. Farrell et al. [167] found for a large variety of metallic alloys that the post-necking flow response is well represented by a linear hardening (with necking starting at strain between 0.15 and 0.4). Simar [168] found that the prediction of fracture strain, which depends on the behavior law at large strain, requires accounting for stage-IV hardening. Lecarme [169] also found that a linear hardening regime at large strain can influence the damage evolution.

Referring to the simulated tensile curves in Figure 5.3, the uniform elongation is underestimated by the model because the work-hardening rate is decreasing relatively fast. It is proposed that taking into account for stage-IV hardening of ferrite (equation 5.5) by a moderate constant hardening rate can improve the prediction of uniform elongation, counteracting also partly the tendency for strain localization in the ferrite in the unit cell. The hardening rate will be fitted with the experimental results of QT-700-37% and kept constant for all the martensite volume fractions.

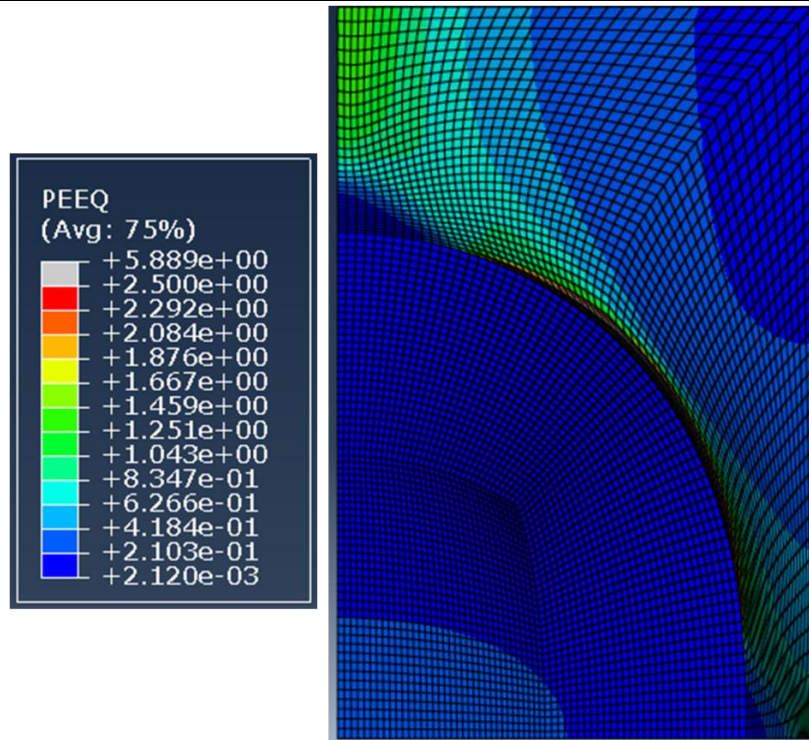


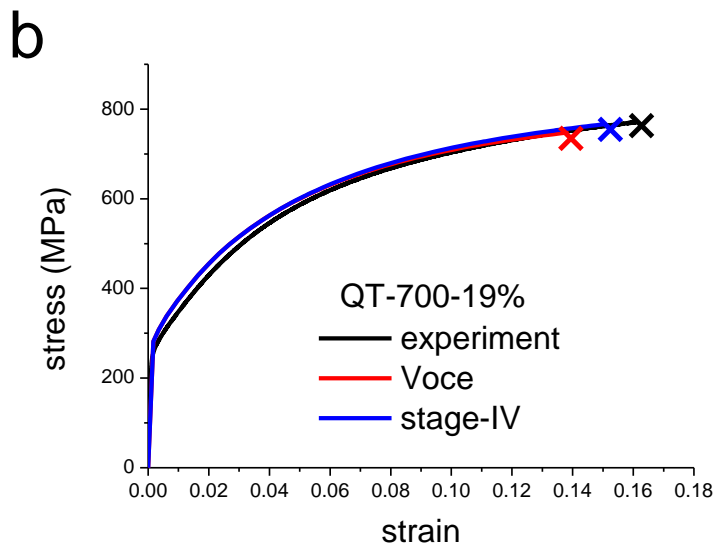
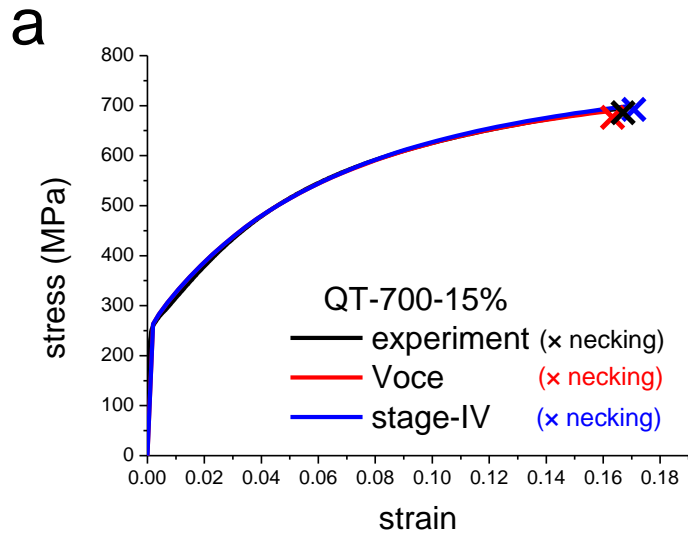
Figure 5.6. Equivalent plastic strain (PEEQ) distribution within the unit cell (QT-700-37%). The macroscopic strain is 0.3.

➤ **Tensile curves and work-hardening**

Figure 5.7 shows the comparison of the simulated tensile curves with and without stage-IV hardening of ferrite. The stage-IV hardening rate (θ_{IV}) is fitted to be 100MPa (about $\mu/800$, slightly higher than the values reported in [147]). The macroscopic response of the unit cell is changed, especially when V_m is large. With the modified law for ferrite, the initial deformation is not influenced and the tensile strength is not affected obviously. But the onset of necking is postponed due to the increased work-hardening rate at large strain. Figure 5.8 shows the effect of the modified law on the work-hardening of RVE at large strain. The work-hardening rate is the same until large strain, and the Voce law of ferrite results in a faster drop of the work-hardening rate. Although 100MPa is a small value comparing with the initial hardening rate, the modified behavior of the ferrite can lead to a higher work-hardening of the composite at large strain, which postpones the onset of necking and improves the prediction of uniform elongation.

For pure metals, the stage-IV hardening rate is very small [147]. As to engineering metals, values between 40 and 110 MPa were identified for aluminum alloys, and the heavily overaged materials were found to reach stage-IV even before the onset of

necking [168]. In this sense, 100 MPa in this work is a physically acceptable value. However, this value is actually empirical. It also accounts for other microstructural factors, such as morphological effects not properly taken into account and the inaccuracy of martensite behavior law.



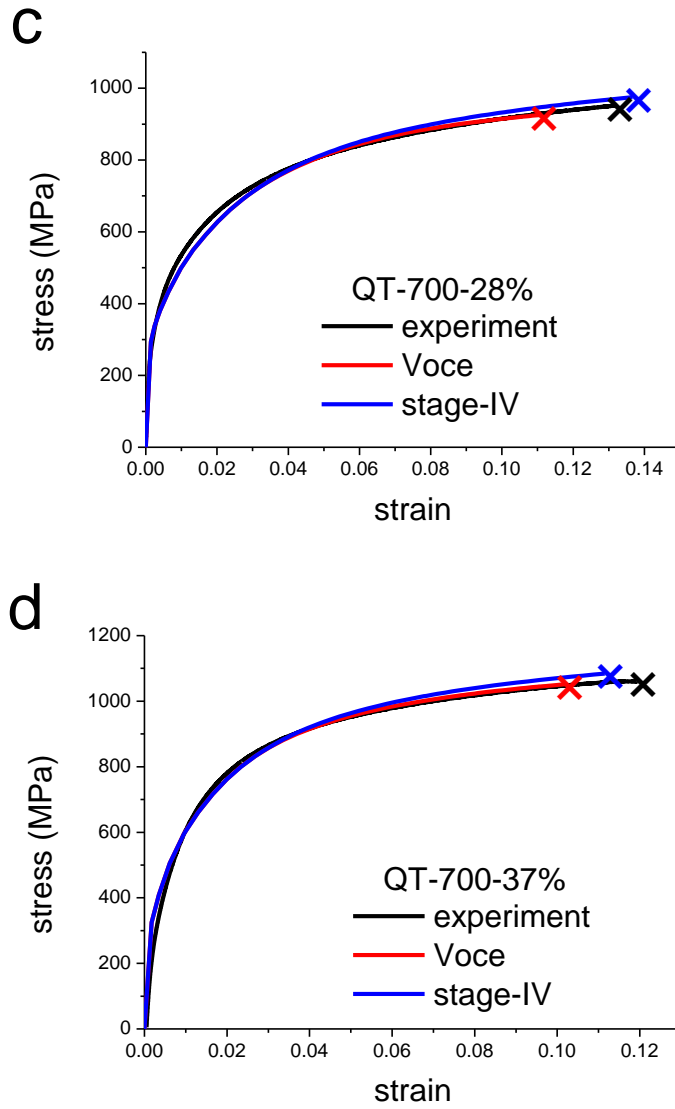


Figure 5.7. Comparison of the tensile curves with and without considering stage-IV hardening of ferrite for QT-700-15% (a), 19% (b), 28% (c) and 37% (d).

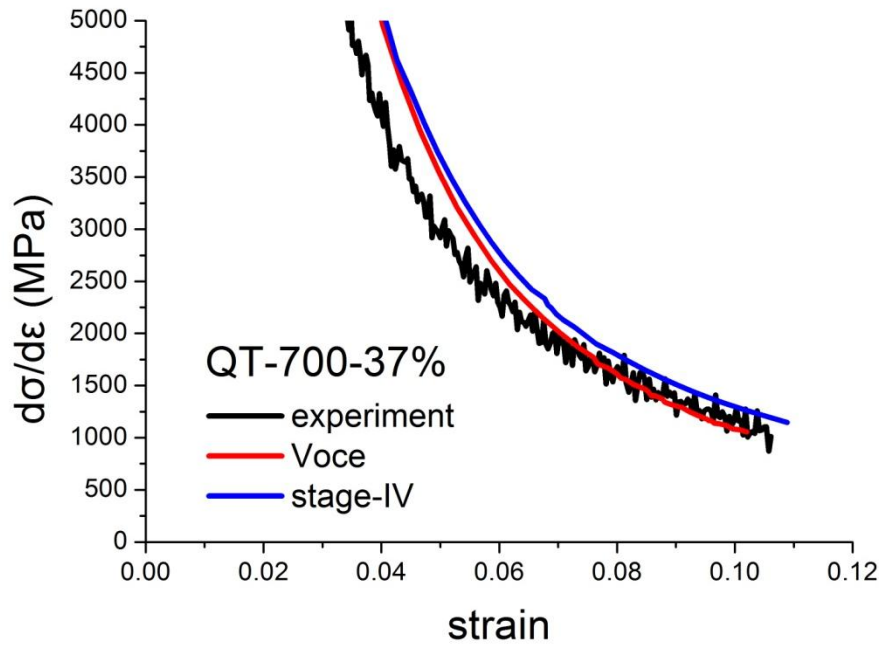


Figure 5.8. Effect of stage-IV hardening of ferrite on work-hardening of the unit cell.

➤ **Effect on properties prediction**

Figure 5.9 shows the experimental and predicted tensile strength and uniform elongation. The tensile strength is only slightly influenced by the stage-IV hardening of ferrite. But the uniform elongation can be better predicted after using the modified behavior law of ferrite.

The decrease in uniform elongation with increasing V_m has been reported [5, 52] and theoretically predicted by Delince [77], but the underlying physics must be discussed. If the martensite remains elastic, an increase in V_m can increase significantly the back stress [50], which tends to enhance work-hardening and to improve the uniform elongation. However, the co-deformation of martensite with ferrite is promoted when V_m is large [170]. This argument is supported by the calculated results shown in Figure 5.10 that the plastic strain in the martensite is larger for a higher martensite volume fraction. According to the tensile behavior of martensite, the work-hardening rate decreases dramatically with strain and the flow stress tends to become saturated at large strain [40]. Therefore, the reduced plastic incompatibility between martensite and ferrite counteracts the effect of increasing V_m , resulting in a rapid decrease of work-hardening rate (see chapter 3).

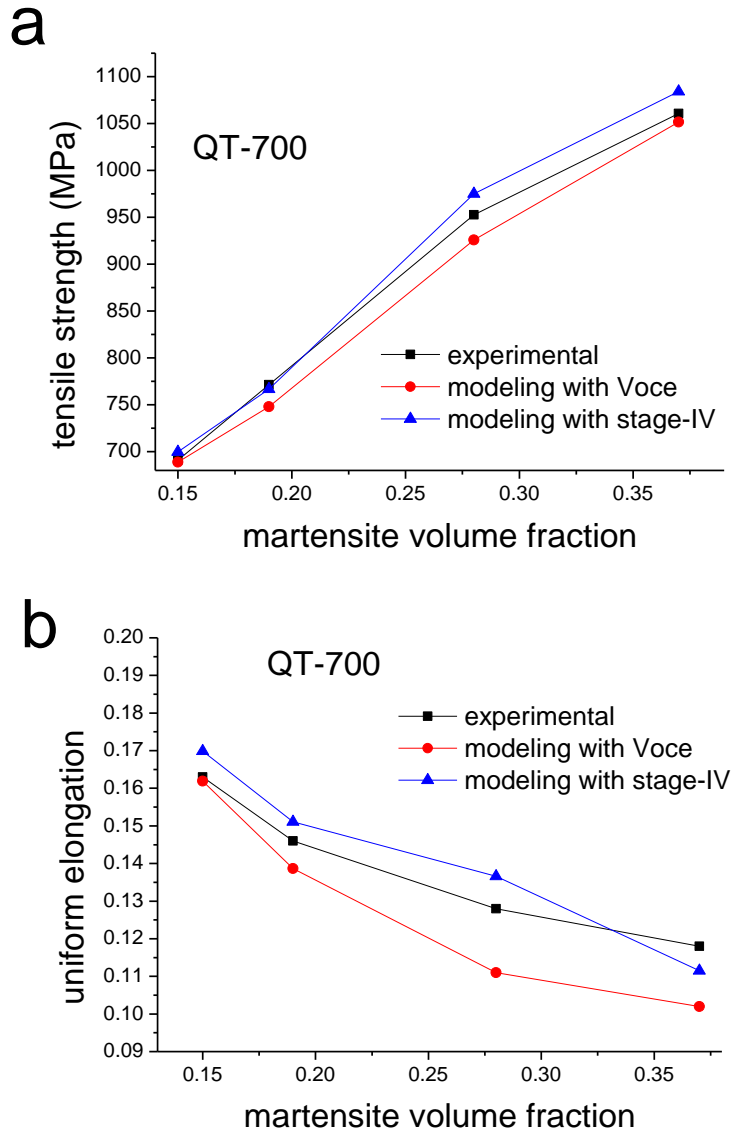


Figure 5.9. Prediction of the tensile strength (a) and uniform elongation (b) with and without accounting for the stage-IV hardening of ferrite.

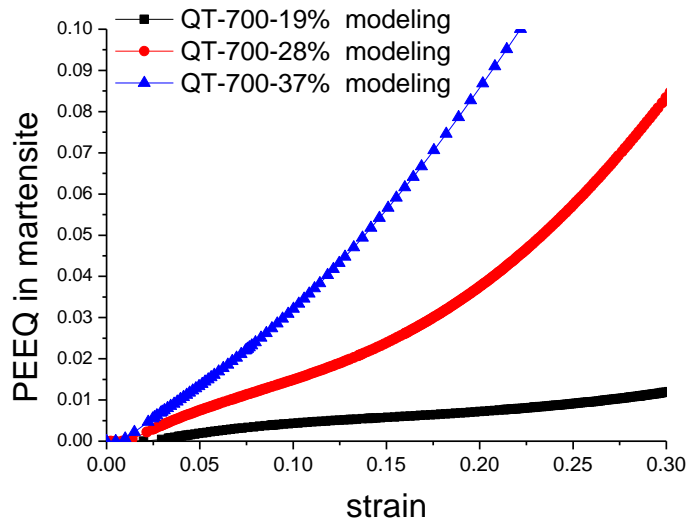


Figure 5.10. Evolutions of the average equivalent plastic strain in the martensite with the macroscopic strain as predicted by the unit cell calculations (with stage-IV hardening taken into account).

5.2.2 Effect of the martensite composition on the strength and ductility of DP steels: a parametric study

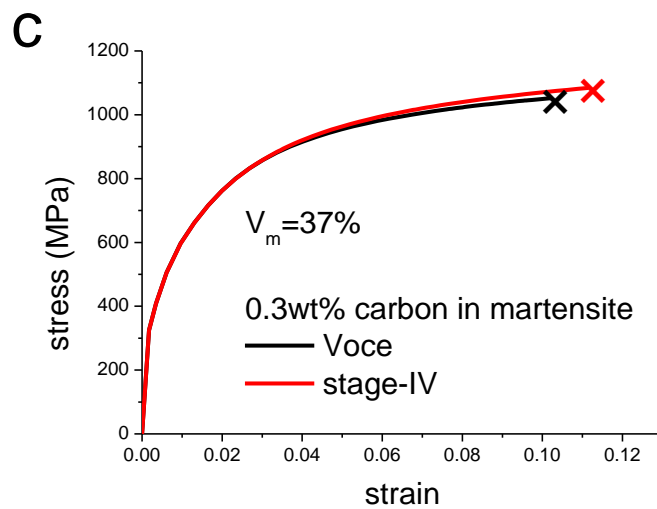
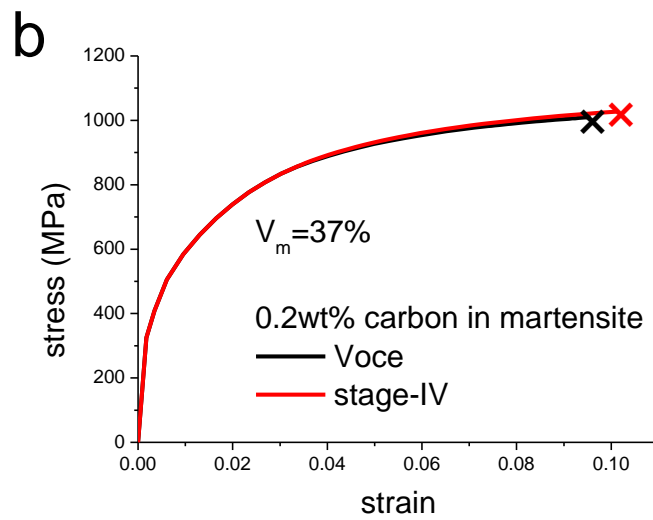
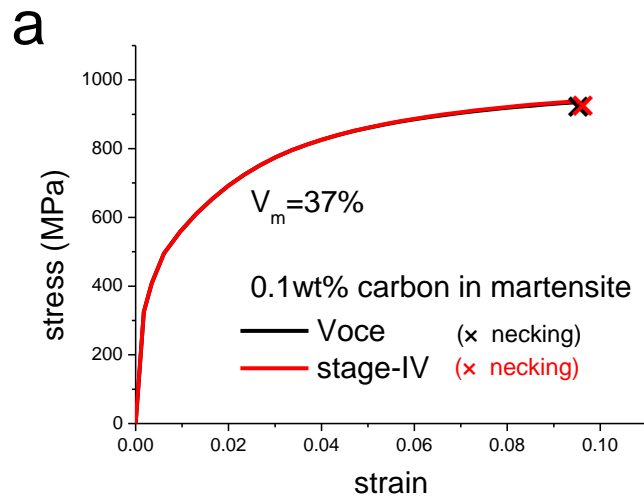
The effect of the martensite volume fraction has been investigated in section 5.2.1, in which the properties of martensite are assumed to be identical. Using the parameters identified earlier, it is possible to perform a systematic parametric study for the effect of martensite composition (mainly carbon content) on the plastic properties of DP steels.

5.2.2.1 Tensile curves and work-hardening

Figure 5.11 shows the effect of accounting for a stage-IV hardening of ferrite on the simulated tensile curves. When the carbon content in martensite is low (0.1wt%), the influence is negligible. But since the martensite becomes harder, the work-hardening at large strain is increased with a modified ferrite law, resulting in a postponed necking. This can be explained by the fact that a soft martensite can co-deform more with ferrite matrix than a hard martensite. More co-deformation decreases the strain partitioning and the strain concentration in the ferrite. Thus the stage-IV hardening of ferrite cannot make an observable difference in the case of 0.1wt% in martensite. Additionally, in the case of 0.3wt% and 0.5wt% carbon in martensite, the flow stress

Chapter 5 Micromechanical modeling

is also increased at large strain. The use of a hardening law with stage IV is thus important for high carbon content in martensite.



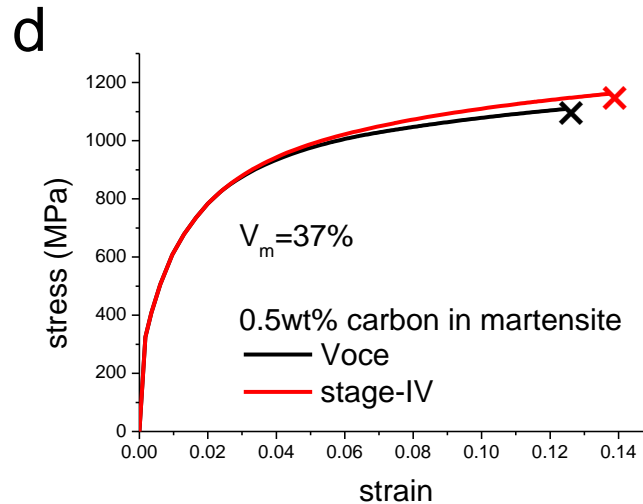


Figure 5.11. Effect of stage-IV hardening of ferrite on the tensile behavior when the martensite carbon content is 0.1wt% (a), 0.2wt% (b), 0.3wt% (c) and 0.5wt% (d).

5.2.2.2 Properties prediction

Figure 5.12 shows the effect of martensite carbon content on the plastic behavior of DP steels with various martensite volume fractions. Carbon content in martensite has negligible effect if V_m is small. When V_m is as high as 28%, the flow stress is lower when the martensite carbon content is 0.1wt% but the difference between 0.2wt%, 0.3wt% and 0.5wt% is small. In the case of 37% martensite, the effect of carbon content in martensite becomes significant. Although the yielding is nearly not influenced, the flow stress is increased by increasing martensite carbon content.

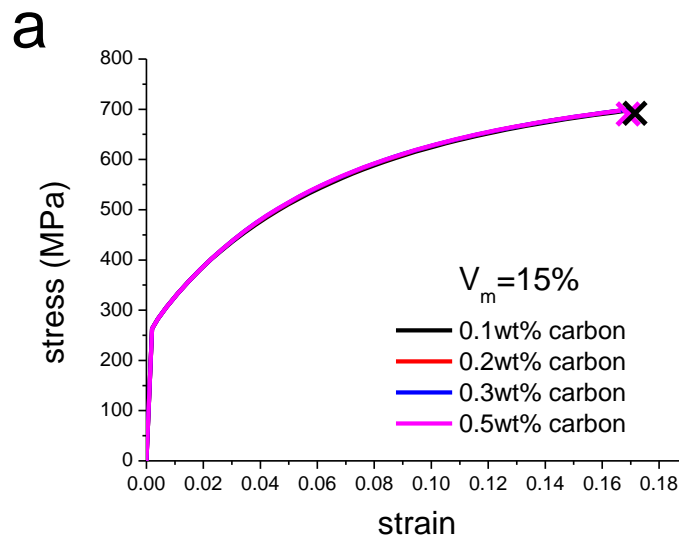
Figure 5.13 shows the predictions of the variations of the tensile strength and uniform elongation with V_m and martensite carbon content. In the case of 15% and 19% of martensite, the carbon content in martensite has very limited influence on the plastic properties, even if the composition is rather different (from 0.1wt% to 0.5wt%). However, the difference becomes more and more significant when V_m is further increased.

As shown in Figure 5.13a, the tensile strength can be increased with higher carbon content in martensite, and the linear tensile strength— V_m relationship can be maintained with a hard martensite only (carbon content $\geq 0.3\text{wt}\%$).

Besides the result of higher tensile strength, higher martensite carbon content can

also lead to slightly higher uniform elongation. As shown in Figure 5.13b, in the case of 28% and 37% of martensite, the uniform elongation increases as the martensite becomes harder, although it still decreases with increasing V_m . This is consistent with the analysis in reference [76, 77]. The work of Delince [77] shows that the uniform elongation is determined by the capacity or not for martensite to deform plastically. Once martensite deforms plastically, the uniform elongation drops. Pierman [76] performed systematic experimental and modeling work to show that a stronger martensite (with higher carbon content) leads to higher uniform elongation, except when high-carbon martensite prematurely breaks in the case of high V_m . The case of 0.5wt% carbon in martensite is interesting in that the uniform elongation is much less affected by V_m . This indicates a possibility that further increase of martensite hardness can result in an increased uniform elongation with increasing V_m .

As to the strength-ductility product (Figure 5.13c), the martensite carbon content has negligible effect when V_m is smaller than 19%. However, for higher V_m , the strength-ductility product increases with the martensite carbon content, and its evolution with V_m can be even changed. For the case of 0.1wt% carbon in martensite, the strength-ductility product decreases with increasing V_m ; while for the case of 0.5wt%, the strength-ductility product increases with increasing V_m .



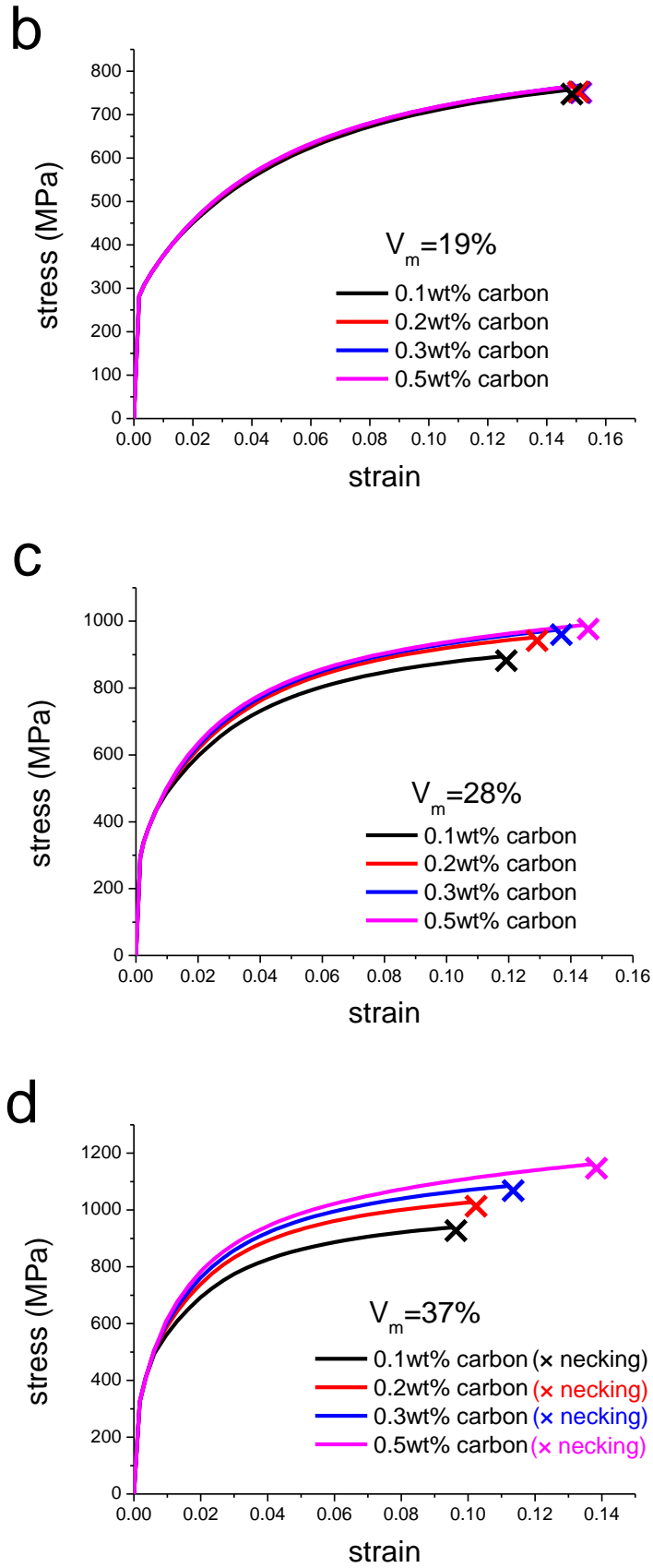


Figure 5.12. Effect of martensite carbon content for the martensite volume fractions of 15% (a), 19% (b), 28% (c) and 37% (d).

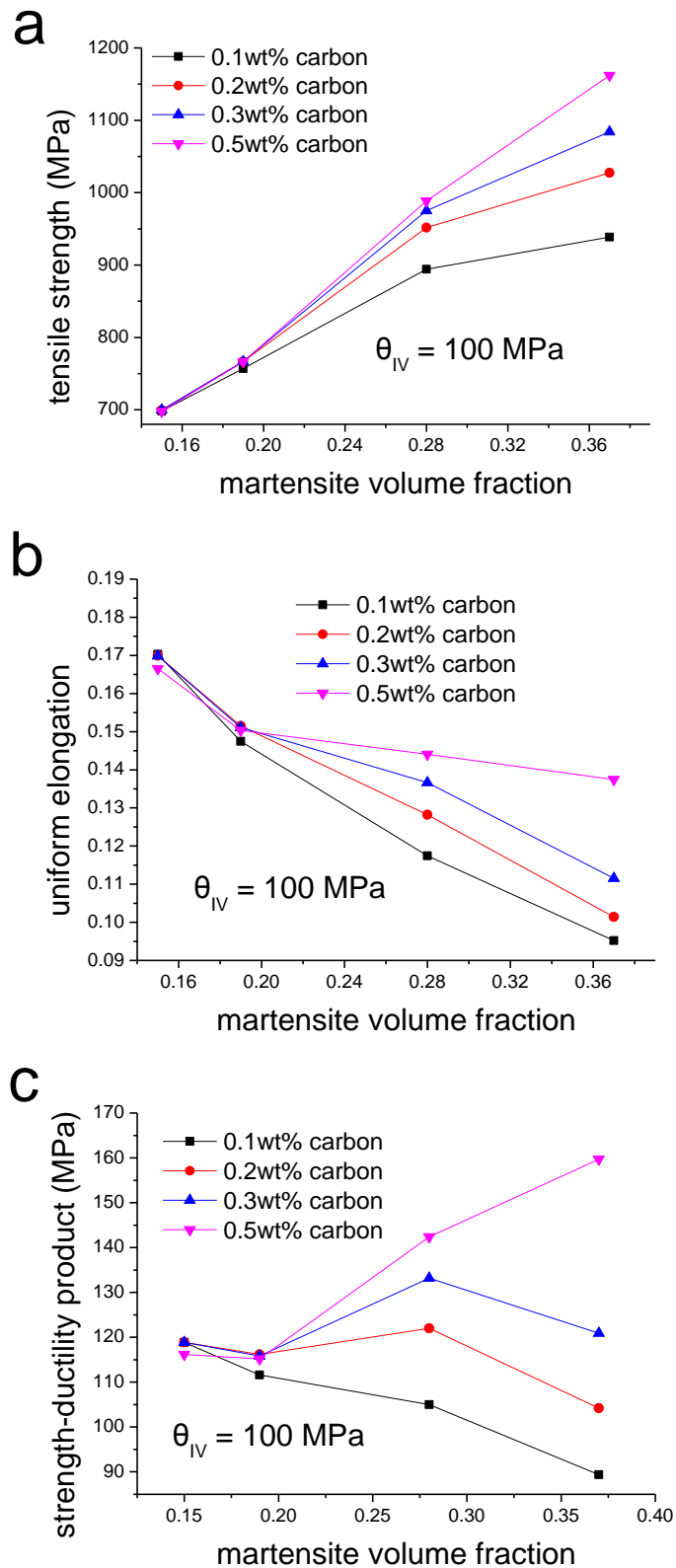
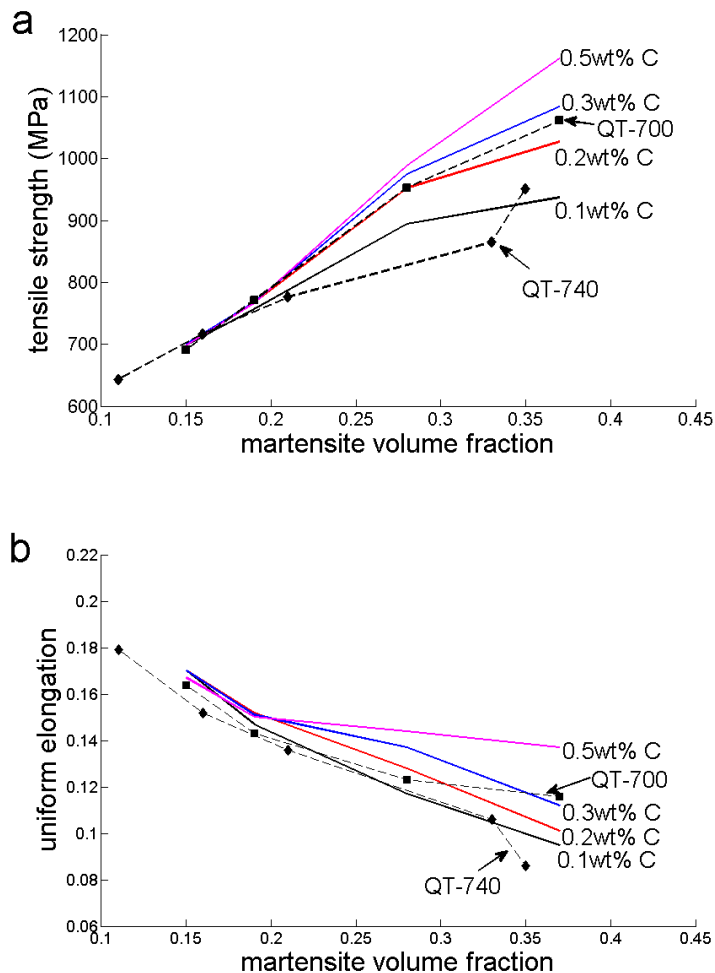


Figure 5.13. Prediction of tensile strength (a), uniform elongation (b) and strength-ductility product (c).

Chapter 5 Micromechanical modeling

The predictions shown in Figure 5.13 are used for comparison with the experimental results on QT-700 and QT-740, as shown in Figure 5.14. The experimental trends are well captured. Firstly, the carbon content in martensite can only affect the tensile strength and uniform elongation when V_m is high enough (20%). Secondly, a higher carbon content in martensite can increase the tensile strength and maintain a linear strength— V_m relationship. Last but not least, the strength-ductility product increases with increasing carbon content in martensite, and the difference is more significant with large martensite volume fraction.

According to the DICTRA calculations (Figure 2.17), the difference of martensite carbon content between QT-700 and QT-740 is about 0.05wt%. However, the results in Figure 5.14a show that the difference of tensile strength is similar to the change predicted by a variation of 0.2wt% in carbon content. Note that the martensite behavior law in this model considers the strengthening by carbon only. But the martensite hardness actually can be determined by a synergic effect of Mn and C [43] when the Mn content is high.



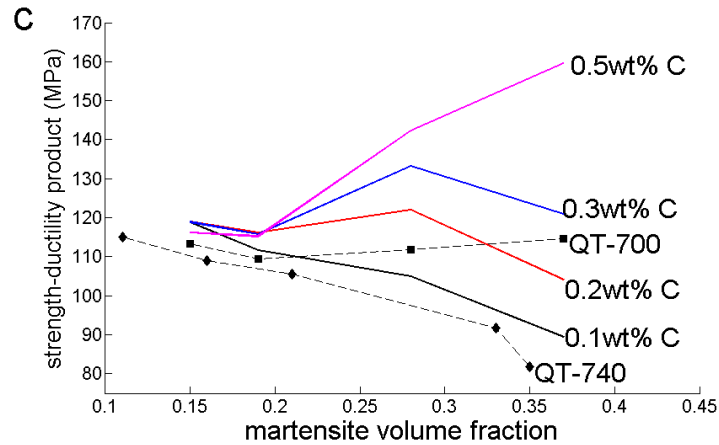


Figure 5.14. Comparison of predicted tensile strength (a), uniform elongation (b) and strength-ductility product (c) with the experimental results.

5.2.3 Effect of microstructure refinement on strength and ductility of DP steels

The results in chapter 3 show that microstructure refinement of DP steels can increase the strength with almost no change of ductility. Several microstructural features are modified by the refinement, including ferrite grain size, distribution and size of martensite islands. This modeling work assumes that the first-order effect is the refinement of ferrite grain size, and the axisymmetric FE cell model of section 5.2.1 and 5.2.2 is also used in this section. The effects of morphology and topology are thus not taken into account, and the only variables are the properties of constituent phases.

In this section, the experimental results of CG-DP-36% and UFG-DP-37% are rationalized by modeling. According to the analysis in chapter 2, the martensite carbon contents are not the same in these microstructures. It is about 0.19% in CG-DP-36% and 0.24wt% in UFG-DP-37%. Ferrite parameters are identified by fitting the experimental results. Then, a parametric study of the effect of martensite carbon content is performed.

5.2.3.1 Simulation of the tensile curves and parameter identification

Figure 5.15 shows the comparison between the experimental and the simulated tensile curves of UFG-DP-37% and CG-DP-36%. The model used the modified law for ferrite, taking the stage-IV hardening into account. For both microstructures, the flow behavior can be well simulated.

The parameters are identified by fitting the experimental curves, which are summarized in Table 5.1. The hardening laws for UFG- and CG- ferrite can be given as follows:

$$\sigma_{f,UFG} = 500 + \frac{8470}{19} [1 - \exp(-19\varepsilon_p)] \quad \text{for } \varepsilon_p^{tr} < 0.236, \quad (5.8a)$$

$$\sigma_{f,UFG} = 955 + 100(\varepsilon_p - 0.236) \quad \text{for } \varepsilon_p^{tr} \geq 0.236; \quad (5.8b)$$

$$\sigma_{f,CG} = 340 + \frac{8000}{16} [1 - \exp(-16\varepsilon_p)] \quad \text{for } \varepsilon_p^{tr} < 0.274, \quad (5.9a)$$

$$\sigma_{f,CG} = 834 + 100(\varepsilon_p - 0.274) \quad \text{for } \varepsilon_p^{tr} \geq 0.274. \quad (5.9b)$$

The identified flow curves of coarse- and ultrafine-grained ferrite are shown in Figure 5.16. The UFG-ferrite has a higher yield stress, a higher initial work-hardening rate and also a larger dynamic recovery coefficient, which is in agreement with the consequence of grain refinement (see the detailed review of [147]).

Parameter	UFG-ferrite	CG-ferrite
Grain size (μm)	2	3.8
Yield stress (MPa)	500	340
Initial work-hardening rate (MPa)	8470	8000
Dynamic recovery coefficient	19	16
ε_p^{tr}	0.236	0.274
σ_y^{tr}	955	834

Table 5.1. Identified parameters of ferrite.

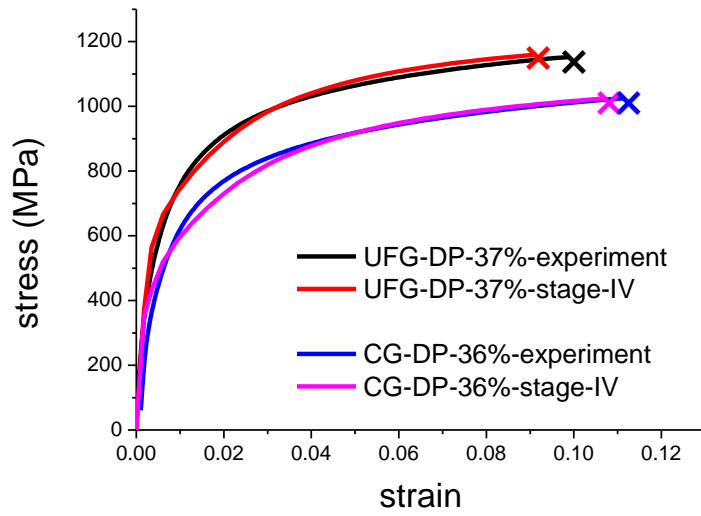


Figure 5.15. Comparison of experimental tensile curves with the simulation with and without stage-IV hardening of the ferrite.

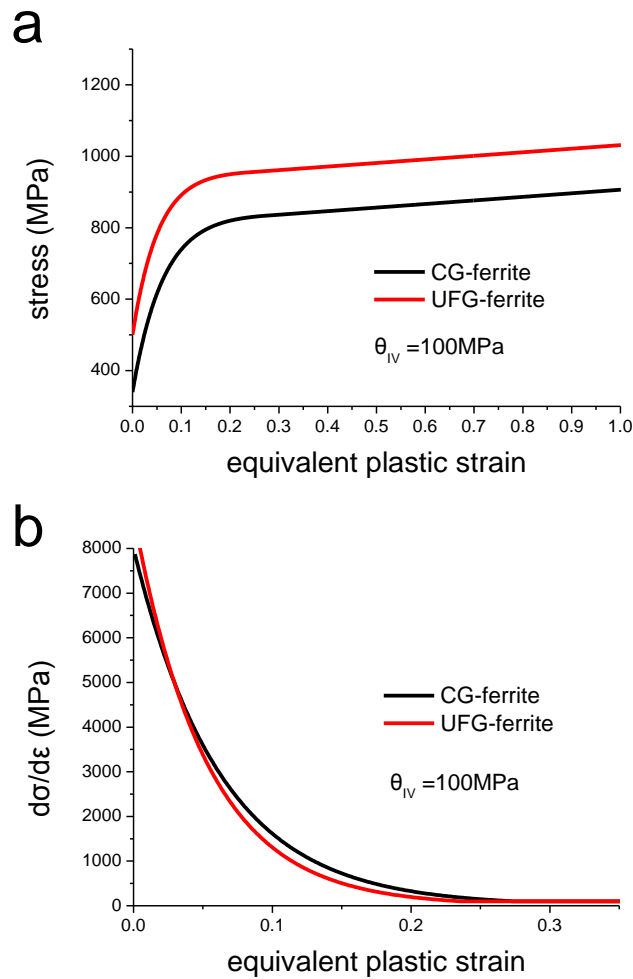
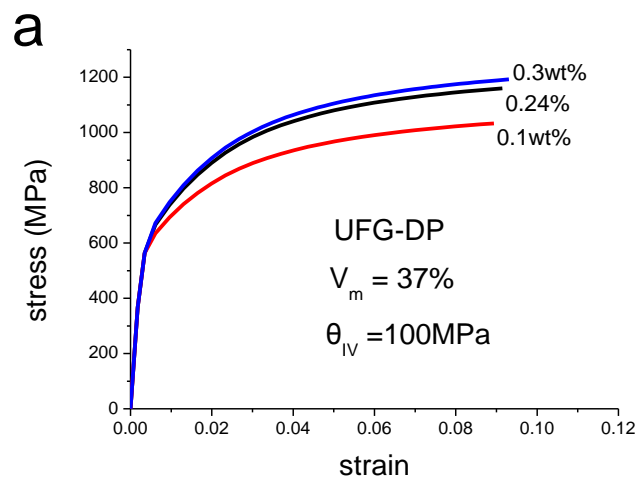


Figure 5.16. Identified tensile curves (a) and work-hardening (b) of CG- and

5.2.3.2 Effect of carbon content in martensite: a parametric study

The martensite composition of CG-DP-36% and UFG-DP-37% is not the same. Thus the comparison of plastic properties is not influenced by the ferrite grain size only. To better understand the consequences of microstructure refinement, it is necessary to compare the microstructures with the same martensite composition. This can be done by a parametric study based on the parameters identified before. The good agreement between the experimental and simulation results demonstrate the predictive character of the model.

In this parametric study, the constitutive law of ferrite and the volume fraction of martensite are kept unchanged for both CG-DP and UFG-DP. The martensite properties take into account a variation of carbon content (from 0.1wt% to 0.3wt%), according to equations 5.1-5.3. The predicted tensile curves are shown in Figure 5.17. For both UFG- and CG-DP steels, the increase of carbon content in martensite can simultaneously increase the tensile strength and uniform elongation. The comparison of work-hardening in Figure 5.18 also shows the effect of martensite carbon content on plastic behavior of DP steels. With lower carbon content, martensite deforms plastically at lower strain, resulting in a lower work-hardening rate due to reduced plastic incompatibility with ferrite. The trend is the same in CG- and UFG-DP.



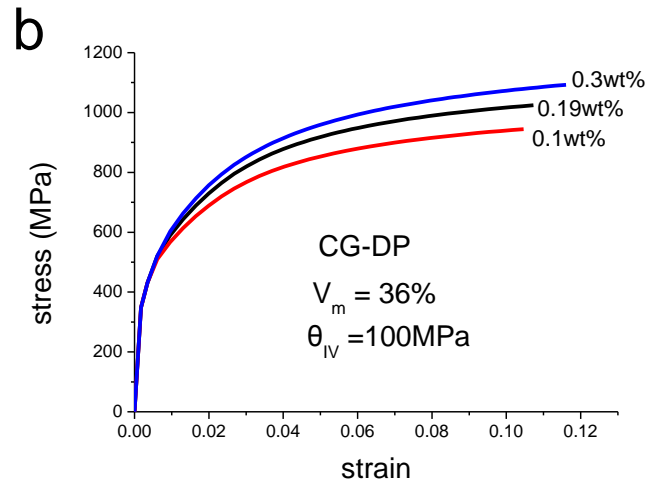


Figure 5.17. Effect of martensite carbon content on tensile behavior of UFG- (a) and CG-DP (b) predicted by the unit cell model.

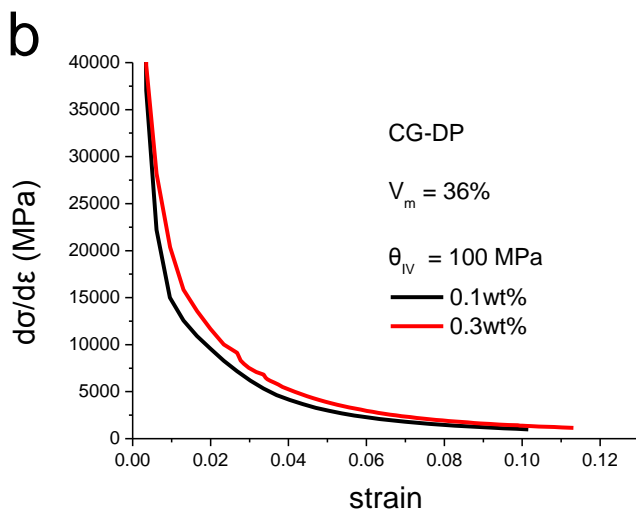
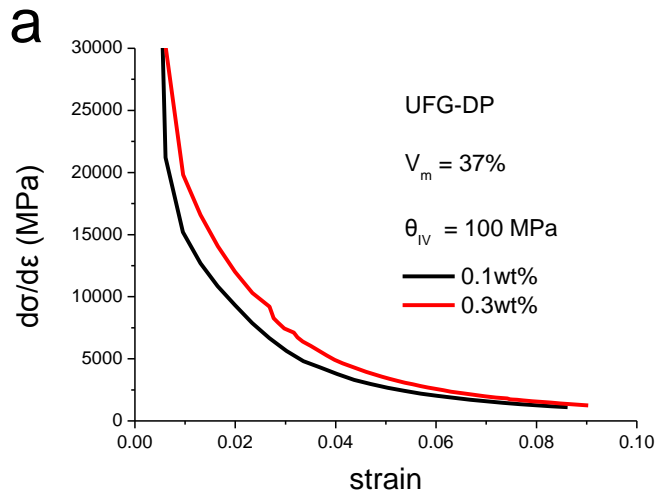


Figure 5.18. Effect of martensite carbon content on work-hardening of UFG- (a) and CG-DP (b) predicted by the unit cell model.

The predictions of the plastic properties are given in Figure 5.19. For all the martensite carbon contents, the tensile strength is increased by refinement of the microstructure and the increment is about 100MPa. According to parameters of UFG- and CG-ferrite identified in Table 5.1, the difference of ferrite tensile strength is 120MPa. The increased strength of UFG-DP results from the matrix strengthening.

As to the uniform elongation, within this range of martensite carbon content, CG-DP has slightly higher uniform elongation than UFG-DP, and the difference is between 0.015 and 0.025. This result agrees with the experimental results in chapter 3. The strengthening resulting from a hard martensite can increase the work-hardening, but the grain refinement tends to decrease the uniform elongation. However, the difference in uniform elongation is relatively small. Necking of CG-DP is slightly postponed with increasing martensite carbon content, but the ductility of UFG-DP is nearly unchanged.

The strength-ductility product is a quantity revealing the energy-absorption capability. A high strength-ductility product can result from the high strength or from the high ductility. UFG-DP has higher tensile strength than CG-DP, but the uniform elongation is smaller. As a result, the strength-ductility product of CG-DP is finally higher when the martensite carbon content is the same. In this sense, microstructure refinement is not necessarily improving the plastic properties of DP steels.

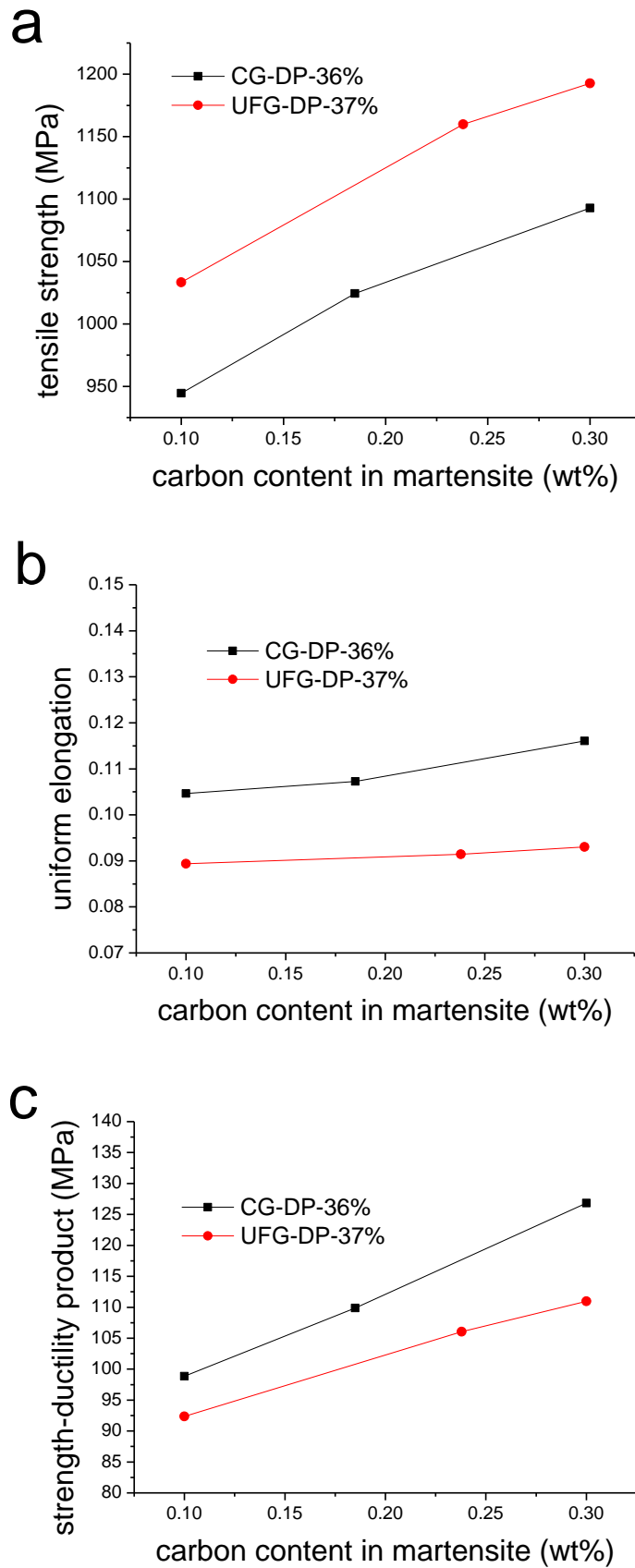


Figure 5.19. Prediction of tensile strength (a), uniform elongation (b) and strength—ductility product (c).

5.3 Fracture of DP steels

The plastic properties of DP steels in chapter 3 have been rationalized using the FE unit cell based micromechanical modeling. The behavior laws and parameters of ferrite and martensite have been identified and the predictive character of the model is justified.

DP steels failure is addressed using a ductile fracture model in this study. Ductile fracture proceeds by the nucleation, growth and coalescence of voids. Therefore, the phase responses extracted from FEM analysis, such as the variation of the maximum principal stress (MPS) in the martensite, can be used to rationalize the experimental damage analysis described in chapter 4. Additionally, these phase responses can be incorporated into a simple fracture model in order to predict the fracture strain. Systematic parametric studies will be performed to investigate the effects of microstructural features on the fracture properties of DP steels.

5.3.1 Description of fracture modeling

5.3.1.1 A closed-form estimation of fracture strain and strategy of modeling

A simple physically-based micromechanical model is developed to estimate the fracture strain. It uses the theories elaborated to describe the void nucleation, growth and coalescence [99, 171, 172]. The dominating damage mechanism is assumed to be martensite fracture. We assume that the voids nucleate when the MPS in martensite reaches a critical value. Voids then open and grow until coalescing with nearest neighbours. Only martensite volume fractions larger than 19% will be considered, because the interface decohesion becomes an important damage nucleation mechanism when V_m is small (as 15%).

The transverse growth of the void is assumed to follow the Rice and Tracey relationship [172]:

$$\frac{R_x}{R_{x0}} = \frac{1}{\beta_H \exp\left(\frac{3}{2}T_\alpha\right)} \left\{ \left[\beta_H \exp\left(\frac{3}{2}T_\alpha\right) - 1 \right] \exp \left[\beta_H \exp\left(\frac{3}{2}T_\alpha\right) (\varepsilon_\alpha - \varepsilon_{c,\alpha}) \right] + 1 \right\} \quad (5.10)$$

with R_x the radial radius of the void. The constant β_H has been calculated by Huang [173] who determined a value equal to 0.427. As observed in this study and reported in [174], voids grow essentially in the soft phase. Their size is a function of the average plastic strain ε_α and the stress triaxiality T_α in the ferrite. The evolution of void size with the macroscopic response σ_{macro} and ε_{macro} is calculated with the FEM unit cell model. $\varepsilon_{c,\alpha}$ is the plastic strain in ferrite when the maximum principal stress of the martensite reaches the fracture stress $\sigma_{c,\alpha}$.

Coalescence occurs when the Thomason criterion [99] is fulfilled:

$$\frac{\sigma_n}{\sigma_\alpha} = (1 - \chi^2) \left[\delta \left(\frac{1 - \chi}{\chi W} \right)^2 + 1.24 \sqrt{\frac{1}{\chi}} \right] \quad (5.11)$$

where σ_n is the stress normal to the ligament; δ is a parameter which is a function of the strain hardening exponent n : $\delta = 0.1 + 0.22n + 4.8n^2$ when a power law is used. Since an exponential law is used for ferrite in this study, the value of n is considered equal to the uniform elongation of ferrite. W is the void aspect ratio. The void aspect ratio in the case of penny-shaped voids is given by [171]:

$$W = \frac{R_z}{R_x} = \lambda_0 \frac{\exp(\varepsilon_\alpha - \varepsilon_{c,\alpha}) - 1}{\exp\left(\frac{\varepsilon_{c,\alpha} - \varepsilon_\alpha}{2}\right)} \quad (5.12)$$

where λ_0 is the initial particle distribution parameter fixed to 1; R_z is the void radius in the tensile (z) direction; χ is the relative void spacing defined by $\frac{R_x}{L_x}$ with L_x half the distance between voids. The relative void spacing is given by:

$$\chi = \frac{R_x}{L_x} = \chi_0 \frac{R_x}{R_{x0}} \exp\left(\frac{\varepsilon_{macro}}{2}\right) \quad (5.13)$$

with χ_0 the initial void spacing. The geometrical idealization of this fracture model is shown in Figure 5.20.

In this model, $\sigma_{c,\alpha}$ and χ_0 are the only fitting parameters. The experimental values of fracture strain and the calculated response of ferrite and martensite will be

incorporated into the model for parameter identification. Note that the identified value of χ_0 can be compared to the realistic values coming from the microstructure and fracture surface to justify whether they are physically acceptable.

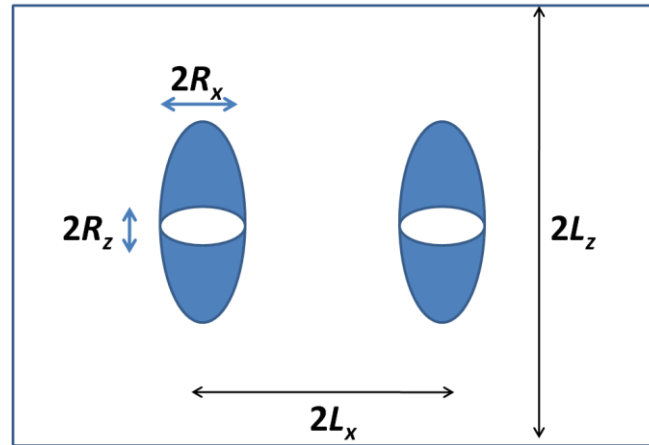


Figure 5.20. Geometrical idealization of the fracture model.

5.3.1.2 On the stress triaxiality

The Rice-Tracey model of void growth (equation 5.10) requires the input of stress triaxiality. Since the voids grow essentially in the ferrite matrix, the local stress triaxiality on the ferrite is required in the model. However, the problem of estimating the stress state in the composite during a tensile test is rather complicated. Firstly, necking will occur in the tensile specimen, resulting in a macroscale stress triaxiality change. The stress triaxiality is evolving, departing from $1/3$ after onset of necking, and depends on the geometry of the tensile specimens. Secondly, the plastic incompatibility between ferrite and martensite results in the microscale stress triaxiality. The real stress state in the ferrite matrix should be the superposition of these two and is spatially heterogeneous.

In this work, we use a simple description of the stress triaxiality evolution, so that semi-quantitative parametric studies can be performed for the effects of microstructural features. Pardoen [175] has calculated the evolution of the stress triaxiality in the center of the minimum cross-section area of tensile specimens by FEM analysis, which is approximated as:

$$T = \frac{1}{3}, \quad \varepsilon < \varepsilon_n \quad (5.14a)$$

$$T = \frac{1}{3} + 0.37(\varepsilon - \varepsilon_n), \varepsilon \geq \varepsilon_n \quad (5.14b)$$

with T the stress triaxiality and ε_n the strain at necking (uniform elongation). This evolution of stress triaxiality is an input to equation 5.10.

5.3.2 Effect of martensite volume fraction on fracture strain

5.3.2.1 Determination of damage parameters for fracture strain estimation

In the model described in section 5.3.1, there are only two fitting parameters $\sigma_{c,\alpha'}$ and χ_0 . Assuming that the martensite breaks through a brittle mode (cleavage), the fracture stress should be insensitive to carbon content because it is determined by the characteristics of atomic bonding, which is negligibly influenced by the carbon content. Although the fracture mechanism of martensite is influenced by the carbon content, this strong assumption is acceptable for a parametric study. The fracture stress of martensite is chosen to be 1200MPa, which is close to the value used in [59]. Therefore, the initial void spacing χ_0 can be fitted in order to reproduce the experimental fracture strain of QT-700-19%, 28% and 37%, see Table 5.2. In principal, if every martensite island gives rise to a void, the initial void spacing should be proportional to $V_m^{1/3}$ [99]. As shown in Table 5.2, this initial void spacing generally increases with increasing V_m and the ratio of $\chi_0/V_m^{1/3}$ is relatively constant, indicating these parameters are physically sound [99]. The values of χ_0 for QT-700-28% and 37% are rather close, implying a similar void density. Actually, the damage characterization in chapter 4 supports this point.

Additionally, assuming $\chi_0 = \frac{R_x}{L_x} \approx \frac{R_{\alpha'}}{L_{\alpha'}}$, the martensite volume fraction is given as:

$$V_m = \frac{\frac{4}{3}\pi R_{\alpha'}^3}{L_{\alpha'}^3} \approx \frac{4R_{\alpha'}^3}{L_{\alpha'}^3} = 4\chi_0^3 \quad (5.15)$$

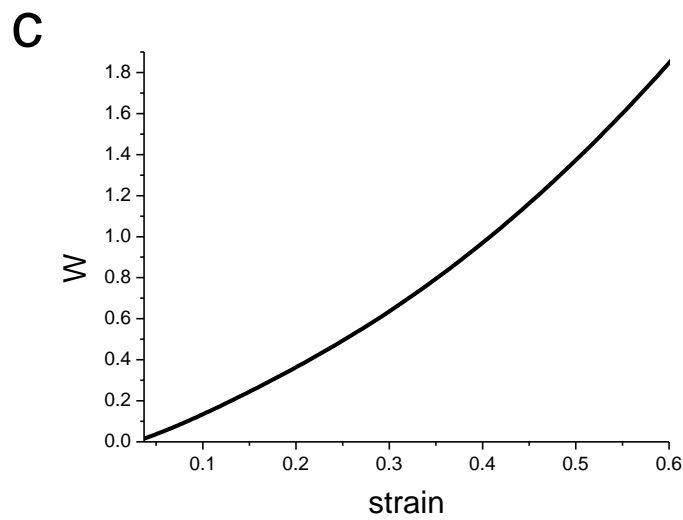
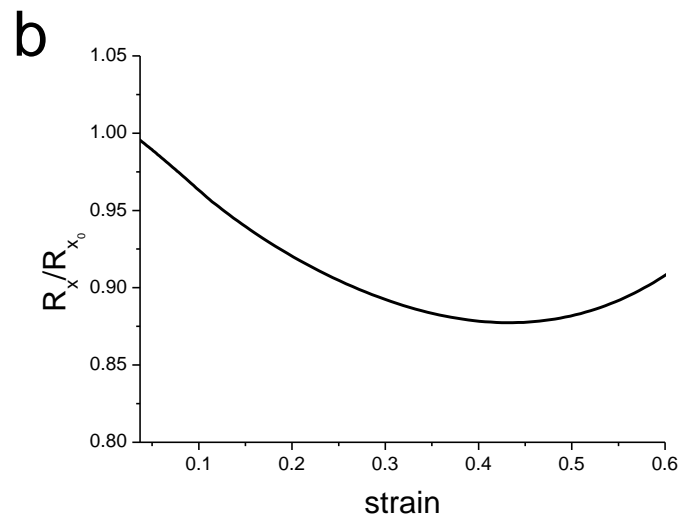
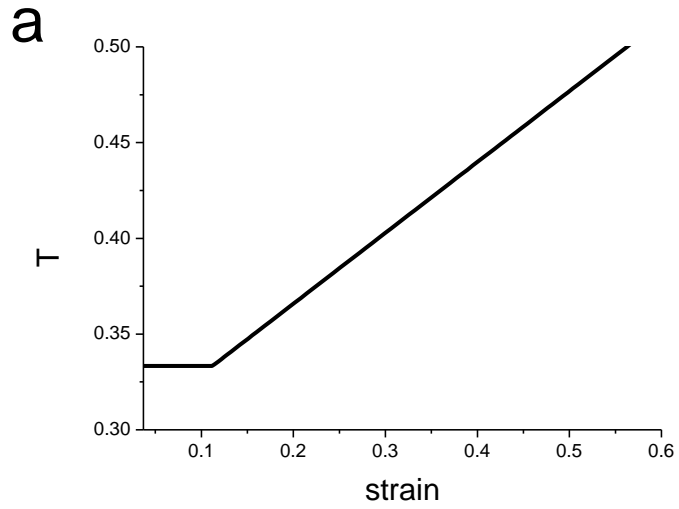
where R_{α} is the average radius of martensite islands and L_{α} is the half spacing between martensite islands. Therefore, the initial relative void spacing for QT-700-19%, 28% and 37% can be estimated as 0.36, 0.41 and 0.45, respectively. These values agree well with the fitted values in Table 5.2.

Martensite volume fraction	χ_0	$\frac{\chi_0}{V_m^{1/3}}$
19%	0.378	0.142
28%	0.510	0.168
37%	0.512	0.154

Table 5.2. Optimum initial void spacing.

5.3.2.2 Evolution of void characteristics

Figure 5.21 shows the variation of the stress triaxiality and of the void characteristics with macroscopic strain. The stress triaxiality starts to increase linearly after necking according to equation 5.14 (Figure 5.21a). The void size in the transverse direction first decreases with strain but then increases at large strain due to increasing stress triaxiality (Figure 5.21b). The void growth along the tension direction results in an increasing aspect ratio W (Figure 5.21c) and the voids should become elongated. As to the relative void spacing, it is a representation of the interaction between specimen shrinkage in the transverse direction and the evolution of void size. During tensile deformation, the cross-section of the specimen is decreasing and this causes a decreasing L_x ; while the void size R_x is evolving as shown in Figure 5.21b. These result in an increasing relatively void spacing, as shown in Figure 5.21d.



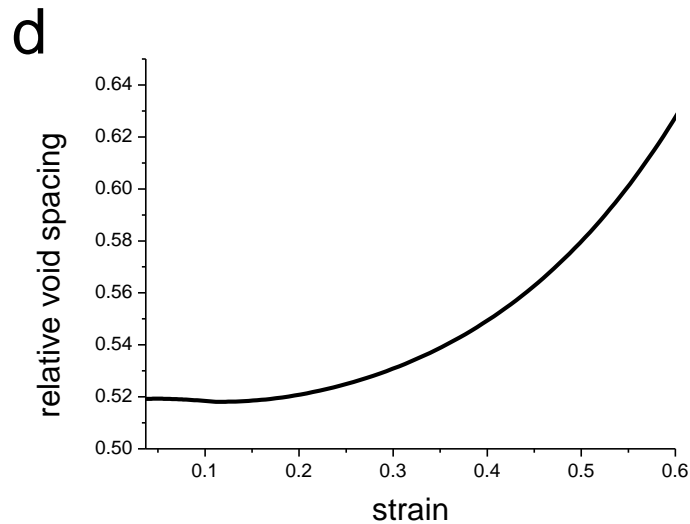


Figure 5.21. Predicted evolution of the stress triaxiality (a), void size (b), aspect ratio (c) and relative void spacing (d) with macroscopic strain in QT-700-37%.

5.3.2.3 Comparison of maximum principal stress in martensite and damage nucleation

The results in chapter 4 show that the damage nucleation is promoted with increasing martensite volume fraction. In the qualitative discussion given there, this is attributed to a higher stress level in the martensite when V_m is larger and also to the increased martensite connectivity. The unit cell model cannot capture the change of martensite connectivity, but it can reveal the evolution of stress level in martensite with V_m , partly explaining the damage characterizations in chapter 4.

Figure 5.22 shows the evolution of MPS in martensite for V_m equaling to 19%, 28% and 37%. It is clear that MPS increases most dramatically when V_m is large. Once it reaches the critical value for cleavage nucleation, then martensite can fail. An increase of maximum principal stress implies an increased possibility of martensite fracture, which can explain why QT-700-37% has the highest void density and void nucleation rate (Figure 4.1).

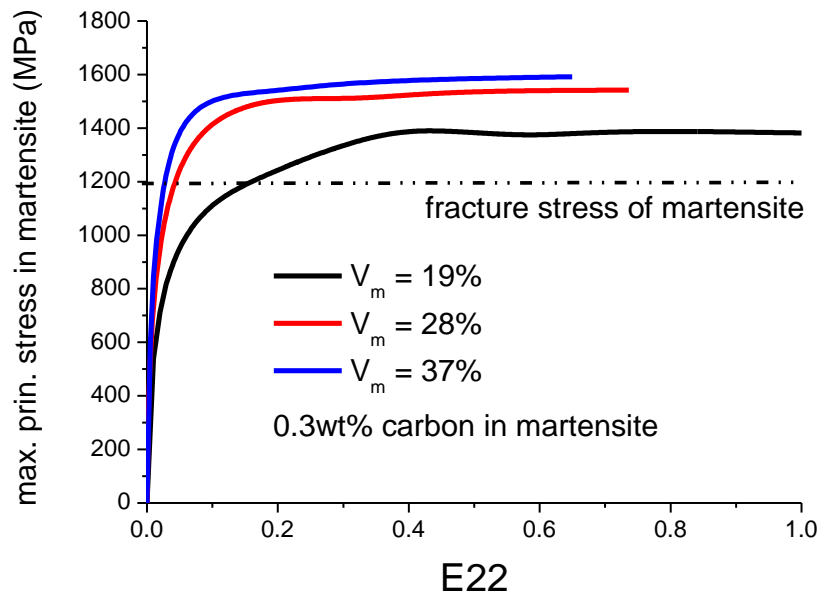


Figure 5.22. Comparison of average maximum principal stress in martensite with different martensite volume fractions.

5.3.3 Effect of martensite composition on fracture strain: a parametric study

Using the model described in section 5.3.1 and the parameters identified in section 5.3.2, a parametric study is performed for the effect of martensite carbon content on fracture strain.

5.3.3.1 Comparison of maximum principal stress in martensite and damage nucleation

Figure 5.23 shows the evolution of MPS in martensite in the cases of different carbon contents. Generally speaking, the probability of martensite failure is increased with increasing carbon content in the martensite. In the case of 0.1wt%, the fracture stress of martensite is reached at the macroscopic strain of 0.37 only, which is much delayed comparing with other cases. For the carbon content between 0.2wt% and 0.5wt%, the macroscopic strain corresponding to the fulfilling of martensite failure

criterion (or damage nucleation strain) is between 0.04 and 0.03. In the ideal microstructure with uniform martensite size and spatial distribution, the void nucleation should be very similar between the cases of 0.2wt% and 0.5wt% carbon in martensite and the difference only becomes significant at large strain. But in the real microstructure where the martensite islands are interconnected and the size of the islands is not uniform, this model cannot cover all the factors. For example, the joint part of the martensite islands is the preferential site for damage occurrence [106] but the martensite in the unit cell is isolated. Additionally, it has been reported that the smaller martensite islands have lower stress level and undergo smaller strain [81], and thus the probability of failure is lower.

QT-700 and QT-740 share the same microstructure features, and the comparison in Figure 5.23 can reveal the effect of martensite carbon content on damage nucleation in an average sense. The small difference in damage nucleation strain between the case of 0.2wt% and 0.5wt% can rationalize the results in chapter 4 that the void density of QT-700-37% and QT-740-35% is very similar.

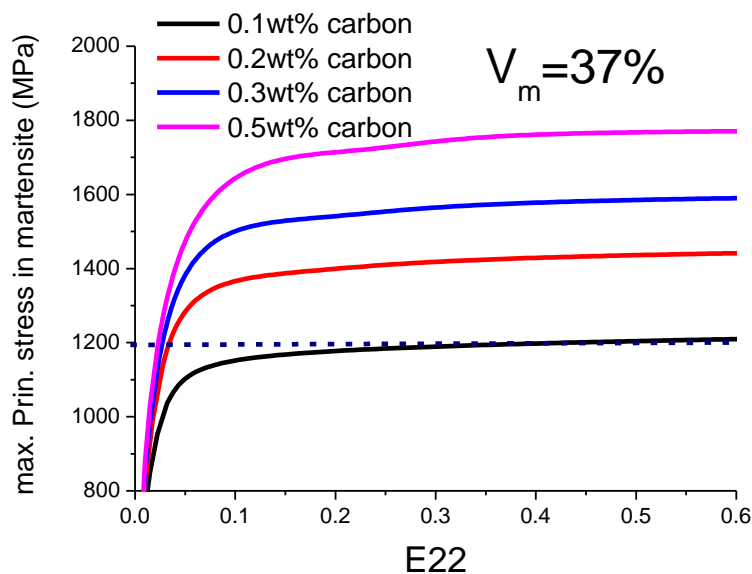


Figure 5.23. Comparison of average maximum principal stress in martensite with different martensite carbon contents.

5.3.3.2 Estimation of fracture strain

The prediction of fracture strain is shown in Figure 5.24. The difference of fracture

strain is marginal between the cases of 0.2wt% and 0.5wt% carbon in martensite, especially when $V_m=19\%$. But a significant improvement of fracture strain can be observed when the martensite carbon content is decreased down to 0.1wt%. For the case with 0.1wt% carbon and $V_m=19\%$, the fracture stress of martensite cannot be reached and the fracture strain cannot be estimated with this model.

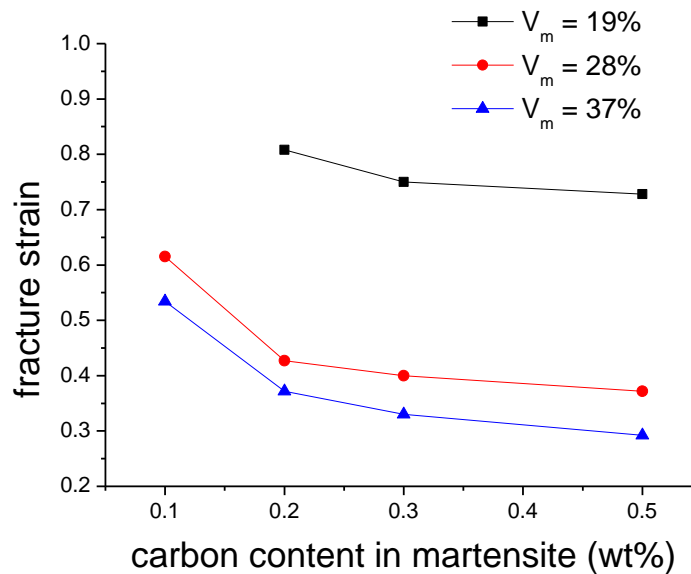


Figure 5.24. Effect of carbon content in martensite on fracture strain of DP steels.

5.3.3.3 Effect of behavior law of ferrite

The void growth and coalescence usually occur at large strain. The proper modeling relies on the accuracy of the behavior law of materials. It has been reported that taking into account of stage-IV hardening improves the model prediction [168]. The work in [169] shows that the stage-IV hardening can have a profound effect on delaying void coalescence and increasing ductility.

In this work, the effect of stage-IV hardening of ferrite on plasticity has been shown in the previous section. It can delay the onset of necking to some extent but the tensile strength is less affected. However, with the value used in this study, it has negligible effect on the fracture strain, as shown in Table 5.3.

Carbon content in martensite	Fracture strain	
	With stage-IV hardening of ferrite	Without stage-IV hardening of ferrite
0.1wt%	0.534	0.624
0.2wt%	0.372	0.370
0.3wt% (fitting)	0.33	0.33
0.5wt%	0.292	0.290

Table 5.3. Influence of stage-IV hardening of ferrite on fracture strain.

5.3.4 Effect of microstructure refinement on fracture strain

The micromechanical model in this work properly captures the consequence of microstructure refinement on plastic properties of DP steels. Incorporating the data of FEM analysis into the fracture model, the results obtained for the damage and fracture can be rationalized in order to understand the fracture behavior of CG- and UFG-DP.

5.3.4.1 Determination of damage parameters for fracture strain estimation

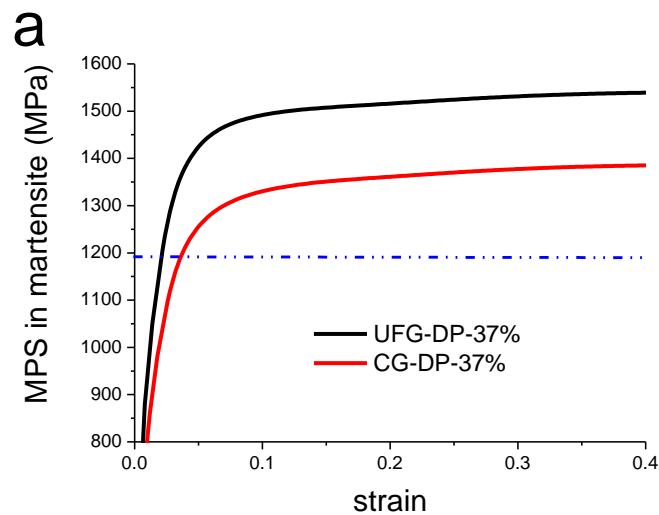
The parameter identification follows the same route as in section 5.3.2.1. The fracture stress of martensite is also assumed to be 1200MPa, and the initial relative void spacing χ_0 is fitted on the experimental fracture strain. The values of χ_0 of UFG-DP-37% and CG-DP-36% are equal to 0.506 and 0.511, respectively. Since they have practically the same V_m , these similar χ_0 values indicate that the parameters are physically sound [99]. They also agree with the values found in section 5.3.2 which were justified already as being realistic.

5.3.4.2 Comparison of maximum principal stress in martensite and the evolution of void characteristics

The calculated microscopic responses are shown in Figure 5.25, including the MPS in

martensite, the evolution of R_x , W and χ . As shown in Figure 5.25a, MPS in martensite is higher in UFG-DP-37%, indicating that the damage nucleation rate should be higher in it. Although the damage characterization in chapter 4 can, to some extent, support this calculation, the real situation is much more complicated. Firstly, the small martensite islands in UFG-DP can undergo substantial plastic strain and they did not fracture in a brittle mode. Secondly, after microstructure refinement, the proportion of damage by interface decohesion is increased, which is not taken into account in this model. Therefore, a more sophisticated model has to be developed to capture the effect of microstructure refinement on damage nucleation of DP steels.

The results in Figure 5.25b and c show that the characteristics of the voids are quite similar between CG-DP-36% and UFG-DP-37%. The relative void spacing of CG-DP is slightly larger (Figure 5.25d), which can explain why the fracture strain of CG-DP-36% is the same as for UFG-DP-37% although the stress level is lower. However, the experimental characterization in chapter 4 shows that the void growth is suppressed in UFG-DP. The micromechanical model oversimplifies the morphology and the statistics of damage occurrence, limiting the capability of capturing void growth behavior in UFG-DP.



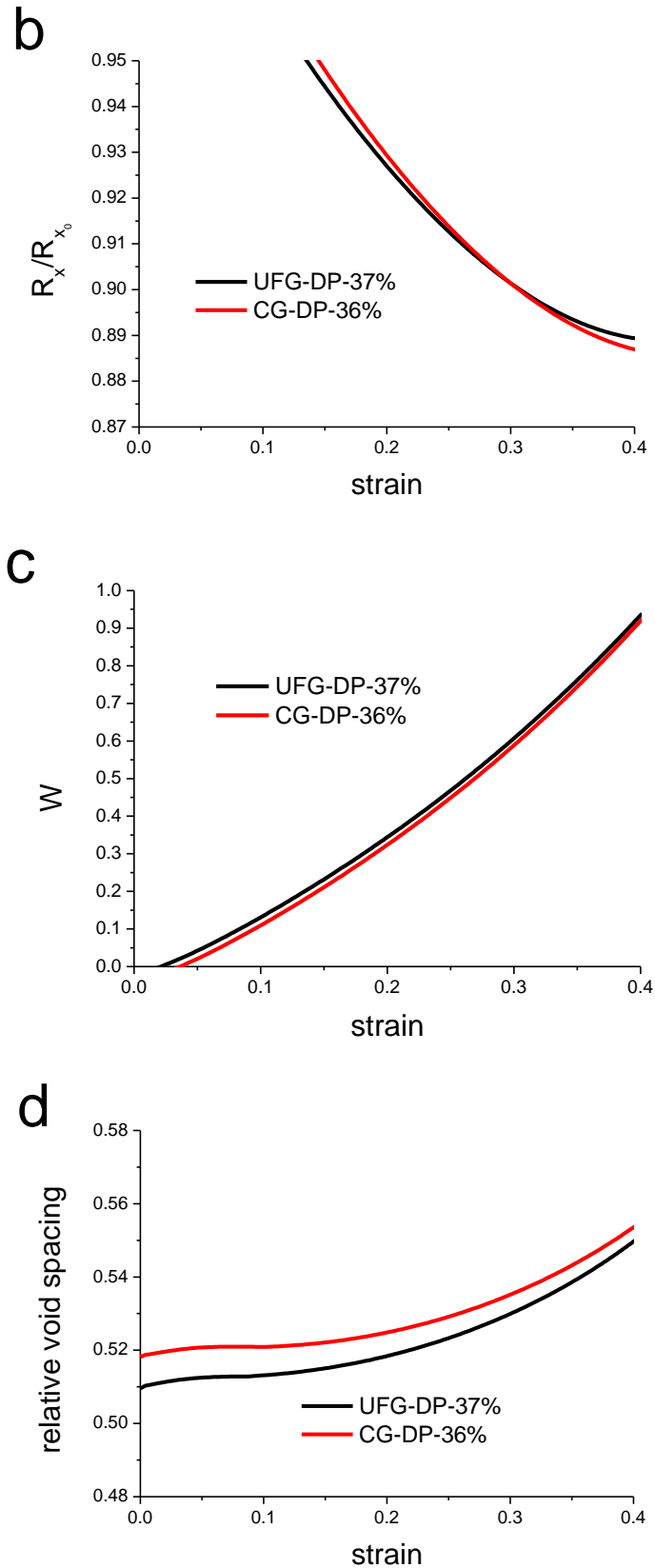


Figure 5.25. Predicted evolution of stress triaxiality (a), void size (b), void aspect ratio (c) and relative spacing of voids (d) with macroscopic strain.

5.3.4.3 Effect of carbon content in martensite: a parametric study

UFG-DP-37% and CG-DP-36% have different carbon contents in martensite, thus the analysis of the effect of microstructure refinement is not straightforward. A parametric study is performed for the effect of martensite carbon content on the fracture strain, in order that the consequence of microstructure refinement can be directly analyzed.

Figure 5.26 shows that the fracture strain can be improved by decreasing the martensite carbon content for both the UFG- and CG-DP steels. With martensite carbon content higher than 0.15wt%, UFG-DP should have higher fracture resistance than CG-DP. However, the comparison is reversed at low carbon content (0.1wt%) that CG-DP has higher fracture strain. This reversion can be explained by the difference in damage nucleation strain. As shown in Figure 5.27, with 0.1wt% carbon in martensite, the maximum principal stress in martensite is higher in UFG-DP. The damage nucleation strain is 0.09 and 0.41 for UFG- and CG-DP, respectively, corresponding to the fracture stress of martensite of 1200MPa. The accelerated void nucleation results in a lower fracture strain in UFG-DP with a soft martensite.

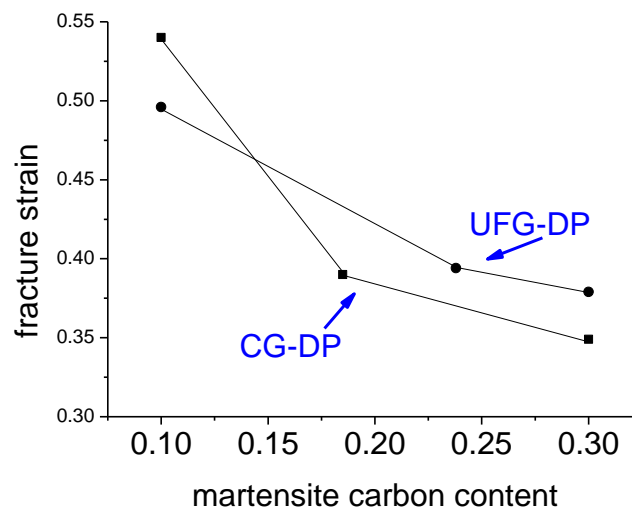


Figure 5.26. Predicted effect of martensite carbon content on the fracture strain of CG- and UFG-DP.

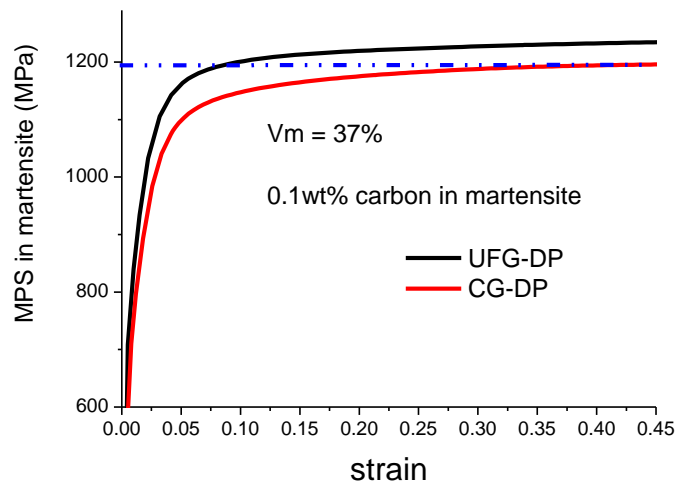


Figure 5.27. Comparison of MPS in martensite of UFG-DP and CG-DP with 0.1wt% carbon in martensite.

5.4 Summary

Micromechanical modeling has been performed in order to rationalize the experimental results described in chapter 3 and 4. The axisymmetric RVE cell model works reasonably well for simulating the deformation behavior of DP steels. A modified law for ferrite, taking into account of the stage-IV hardening, can improve the predictions of mechanical properties, especially the strain for the onset of necking. These results support the semi-quantitative validity of the parametric study performed to guide microstructure optimization.

The mechanical properties have been quantitatively discussed, and the deformation and damage mechanism of DP steels can be better understood. The main conclusions from the modeling analysis are drawn as follows:

On the volume fraction of martensite

- 1) With an increased volume fraction, martensite undergoes more plastic strain, which results in a lower plastic incompatibility among the phases. Thus the uniform elongation decreases with martensite volume fraction.
- 2) The maximum principle stress in martensite increases with the volume fraction, which leads to an increase of the void nucleation rate.

On the martensite composition

Chapter 5 Micromechanical modeling

- 1) Higher carbon content in martensite promotes elastic deformation and results in a better combination of tensile strength and uniform elongation.
- 2) The maximum principal stress in martensite is increased with martensite carbon content, promoting void nucleation and resulting in a smaller fracture strain.

On microstructure refinement

- 1) Microstructure refinement of DP steels increases the tensile strength but decreases the uniform elongation and the strength-ductility product.
- 2) Microstructure refinement tends to increase the maximum principal stress in martensite and promote the void nucleation by martensite fracture. But it is predicted that UFG-DP can have higher fracture strain than CG-DP except when the martensite carbon content is low.

Chapter 6 Microstructure optimization

The systematic analysis in chapter 3 and 4 has discussed the effects of microstructural features on plastic and fracture properties of DP steels, which are validated by the micromechanical modeling in chapter 5. The previous efforts have provided a framework for parametric study, so that the DP microstructure can be optimized for improved properties, adopting the so-called materials-by-design approach.

Additionally, with FEM analysis, a concept of DP steel with graded martensite islands is discussed, which is a possible way of improving the balance of strength and formability.

6.1 Microstructure optimization for the balance between strength and formability

The formability is characterized by either uniform strain or fracture strain, depending on the processing routes. Therefore, the balance between strength and formability should be specified by the trade-off between strength and uniform elongation or fracture strain. Microstructure-properties relationship can be built using the framework in chapter 5, so that the optimized conditions are identified. The logic is shown in Figure 6.1.

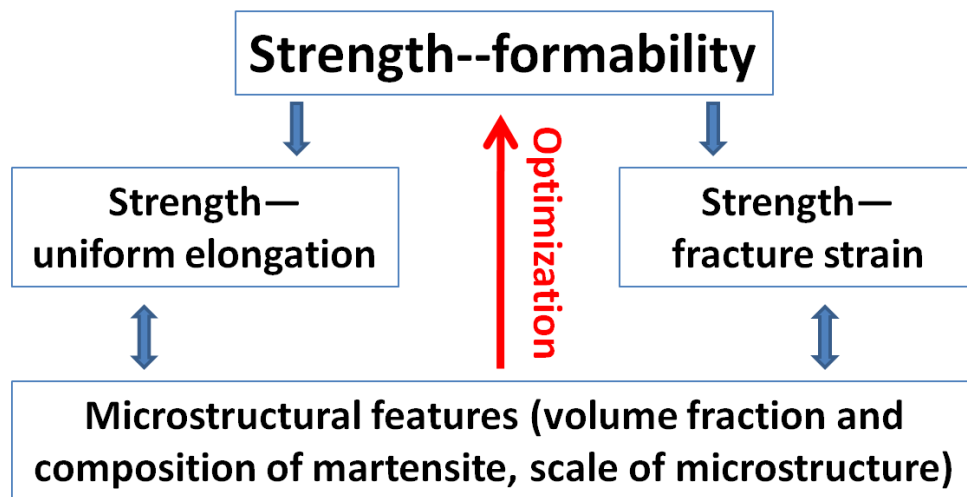


Figure 6.1. Logic of optimizing DP steels for the balance between strength and formability.

6.1.1 Predictions of mechanical properties

Using the same behavior law of CG- and UFG-ferrite in chapter 5 and the damage parameters in Table 6.1, a systematic parametric study is performed and the predicted mechanical properties are shown in Figure 6.2. The tensile strength is increased by increasing martensite volume fraction, martensite carbon content, and microstructure refinement (Figure 6.2a). Therefore, UFG-DP-37% with 0.3wt% carbon in martensite has the best performance of crash worthiness.

Chapter 6 Microstructure optimization

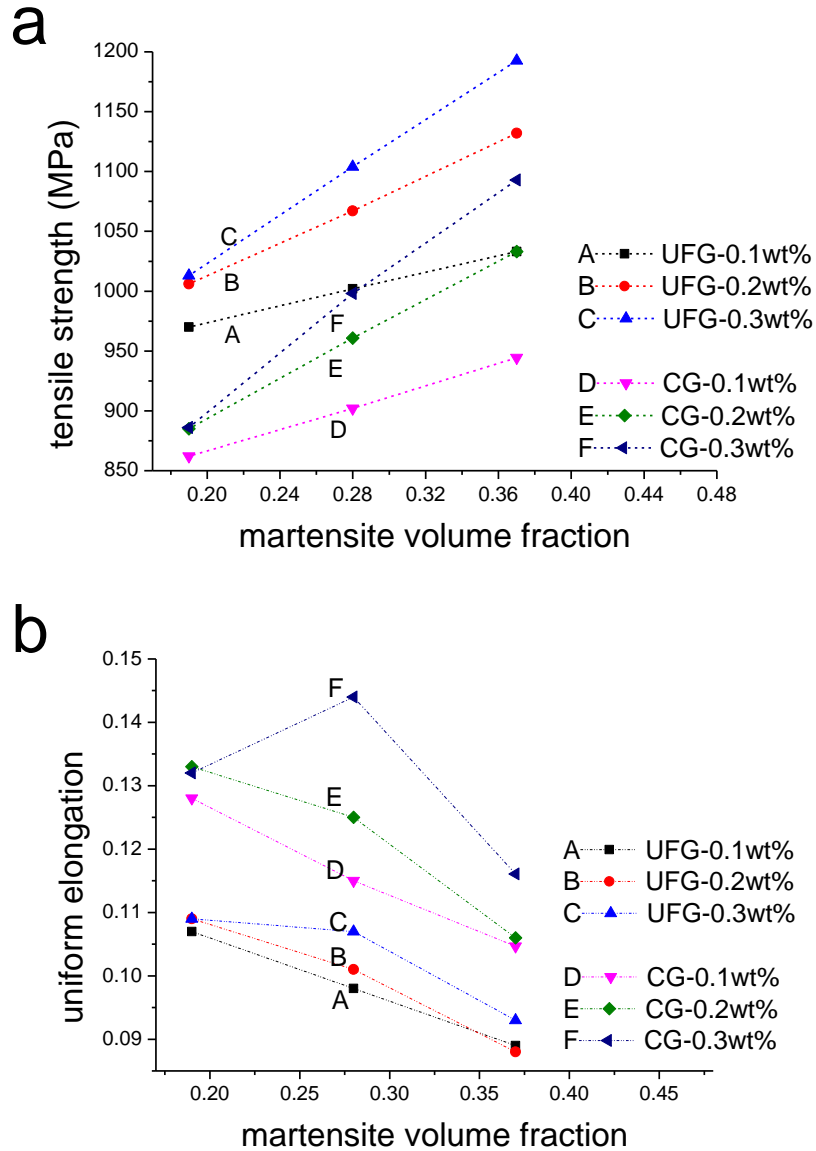
	V_m	Martensite carbon content	ε_n	$\sigma_{c,\alpha'}$	δ	χ_0	$\frac{\chi_0}{V_m^{1/3}}$
UFG-DP	19%	0.1wt%	--	--	--	--	
		0.2wt%	0.109	1190MPa	0.194	0.406	0.152
		0.3wt%	0.109	1190MPa	0.194	0.406	0.152
	28%	0.1wt%	0.098	1190MPa	0.194	0.412	0.152
		0.2wt%	0.101	1190MPa	0.194	0.412	0.152
		0.3wt%	0.107	1190MPa	0.194	0.412	0.152
	37%	0.1wt%	0.089	1190MPa	0.194	0.506	0.152
		0.2wt%	0.088	1190MPa	0.194	0.506	0.152
		0.3wt%	0.087	1190MPa	0.194	0.506	0.152
CG-DP	19%	0.1wt%	--	--	--	--	
		0.2wt%	0.133	1190MPa	0.233	0.406	0.152
		0.3wt%	0.132	1190MPa	0.233	0.406	0.152
	28%	0.1wt%	0.115	1190MPa	0.233	0.412	0.152
		0.2wt%	0.125	1190MPa	0.233	0.412	0.152
		0.3wt%	0.144	1190MPa	0.233	0.412	0.152
	37%	0.1wt%	0.105	1190MPa	0.233	0.506	0.152
		0.2wt%	0.106	1190MPa	0.233	0.506	0.152
		0.3wt%	0.116	1190MPa	0.233	0.506	0.152

Table 6.1. Parameters as inputs in the fracture model.

However, the microstructure refinement of DP steels results in a reduced uniform elongation. As shown in Figure 6.2b, the group of UFG-DP steels locates below the CG-DP steels within these ranges of martensite volume fraction and composition, although the difference in uniform elongation is not large. The better uniform elongation of CG-DP also leads to higher strength-ductility product (Figure 6.2.c). In the case of CG-DP with 0.3wt% carbon in martensite, the uniform elongation is not monotonically decreased with increasing martensite volume fraction, which is not the situation in the corresponding UFG-DP. The strong martensite provides the back stress to enhance work-hardening. This effect is increased with increasing V_m . However, an increase of V_m promotes the co-deformation of martensite and ferrite, reducing plastic incompatibility and back stress. Therefore, theoretically speaking, a maximum uniform elongation can be obtained with a relatively high V_m where the martensite almost remains elastic. CG-DP-28% with 0.3wt% carbon in martensite is such a case. In the corresponding UFG-DP-28% with 0.3wt% carbon in martensite, the martensite undergoes more plastic strain due to stronger ferrite matrix, and a maximum uniform elongation cannot be observed.

Chapter 6 Microstructure optimization

For both UFG- and CG-DP, the fracture strain can be increased with decreasing carbon content in martensite (Figure 6.2d). But microstructure refinement is not necessarily resulting in an increased fracture strain, especially with low martensite volume fraction and low martensite carbon content.



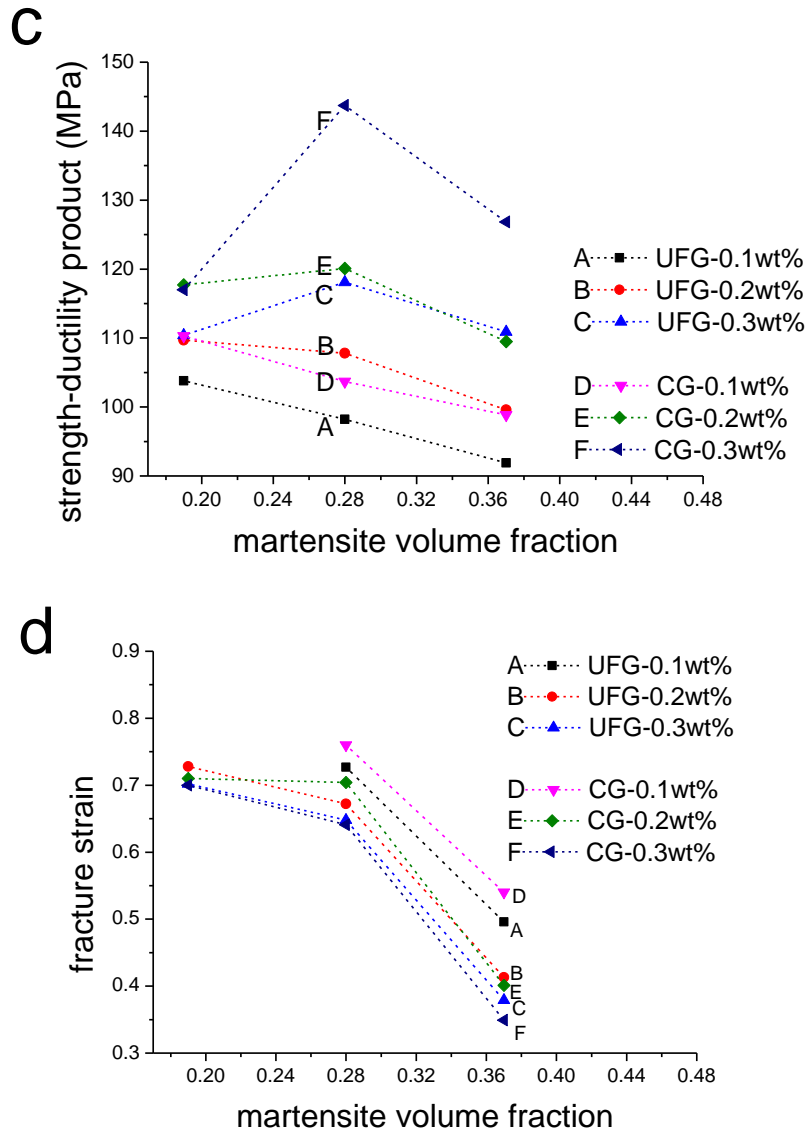


Figure 6.2. Predicted evolution of tensile strength (a), uniform elongation (b), strength-ductility product (c) and fracture strain (d) with martensite volume fraction for different martensite carbon contents and microstructure scale.

6.1.2 Microstructure optimization of DP steels

With the predictions in Figure 6.2, it is possible to optimize the properties of DP steels with the considerations of martensite volume fraction and composition and scale of microstructure. For both UFG-DP (Figure 6.3a) and CG-DP (Figure 6.3b), the combination of tensile strength and uniform elongation can be improved with higher carbon content in martensite. A comparison in Figure 6.3c shows that CG-DP has a better tensile strength—uniform elongation trade-off. In this sense, for the forming

Chapter 6 Microstructure optimization

operation limited by strain hardening, DP steels with coarse microstructure and high carbon content in martensite should be chosen.

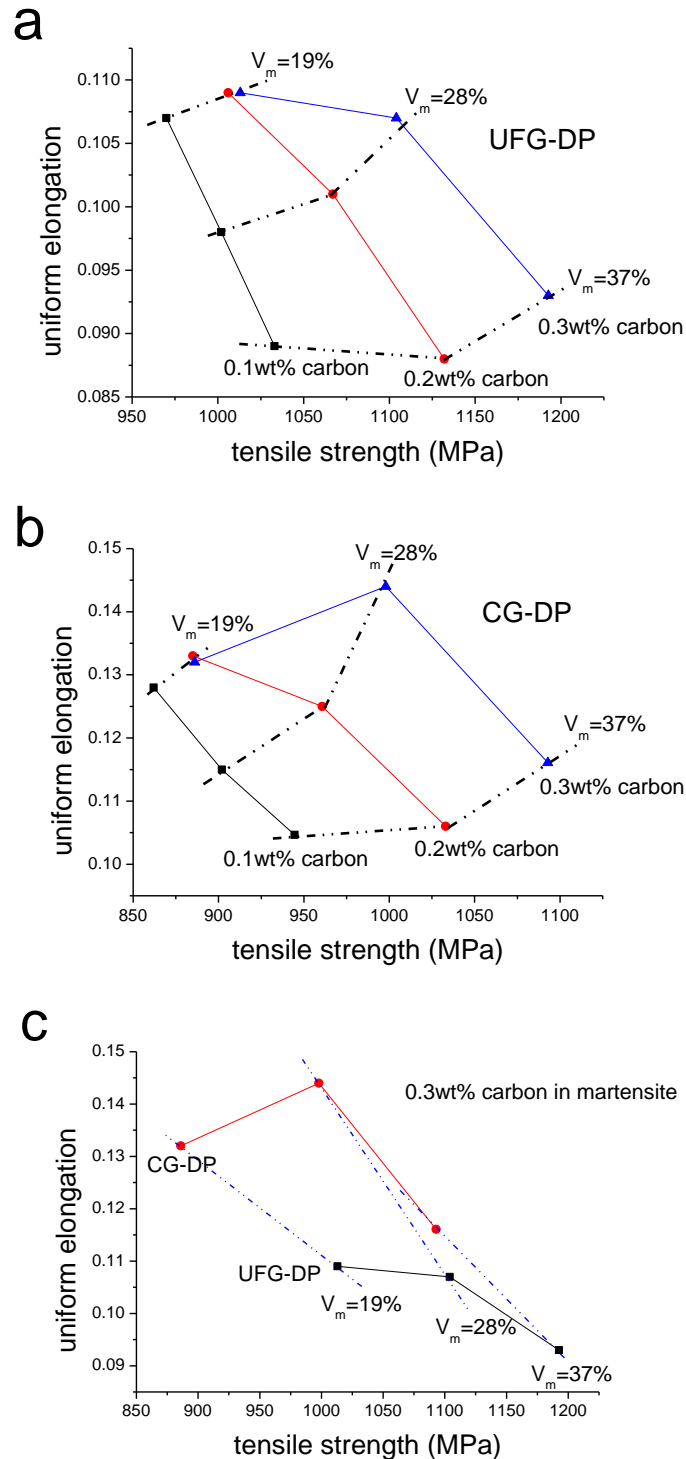


Figure 6.3. Identifying the optimized situation in UFG-DP (a) and CG-DP (b) for the trade-off between strength and uniform elongation, and the effect of microstructure refinement (c).

For the forming operation controlled by fracture, the trade-off between tensile

Chapter 6 Microstructure optimization

strength and fracture strain has to be considered, and the comparison is shown in Figure 6.4. Microstructure refinement increases the tensile strength significantly but the fracture strain is much less affected. Therefore, for the martensite carbon content from 0.1wt% to 0.3wt%, UFG-DP has better combination of tensile strength and fracture strain. In other words, for a chosen steel grade, the trade-off between tensile strength and fracture strain can be improved by microstructure refinement.

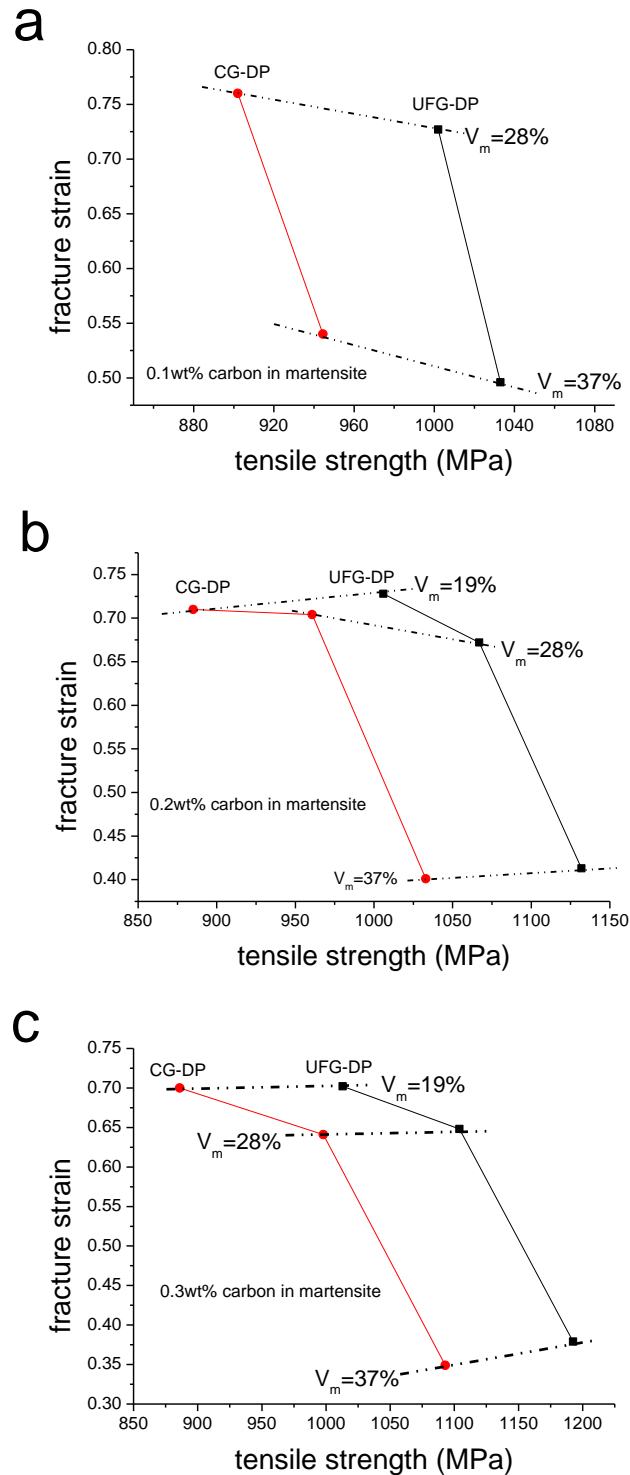


Figure 6.4. The comparison of tensile strength—fracture strain relationship between

UFG- and CG-DP steels with 0.1wt% (a), 0.2wt% (b) and 0.3wt% (c) carbon in martensite.

6.2 On the concept of graded martensite islands

In section 6.1, we have implicitly assumed that the carbon distribution in martensite is uniform, and thus the DP microstructure is optimized by choosing the right martensite volume fraction, martensite carbon content and the scale of microstructure. An alternative way to design DP steels is to introduce a distribution of carbon in order to attain graded martensite, which might improve the mechanical properties.

As discussed in chapter 2, the austenite growth in this steel grade is controlled by Mn partitioning, and the carbon distribution is relatively uniform. To achieve a significant carbon gradient within martensite, the austenite growth must be controlled by carbon diffusion in austenite, and the necessary condition for this is low Mn content in carbide. In addition, the austenite growth controlled by carbon diffusion is rather fast and can be finished in a few seconds (Figure 2.13). Therefore, the DP microstructure with graded martensite islands is not experimentally achieved in this study, and the consequences of graded microstructure are only discussed theoretically.

In this section, the concept of graded martensite island is tested with FEM analysis. A soft martensite layer with 0.1wt% carbon is designed at the matrix/inclusion interface while the average carbon content of the whole inclusion is kept as 0.3wt%. The volume fractions of the layer and the core are the same. Thus, the carbon content in the core is balanced to be 0.5wt%.

The distribution of equivalent plastic strain and maximum principal stress (MPS) in the unit cell are shown in Figure 6.5. The plastic strain is concentrated at the ferrite/martensite interface and also at the interface between the soft layer and the hard core of the inclusion (Figure 6.5a). The maximum principal stress is concentrated in several regions, including the center of the core and the interface between the soft layer and the hard core, indicating the preferential sites of failure.

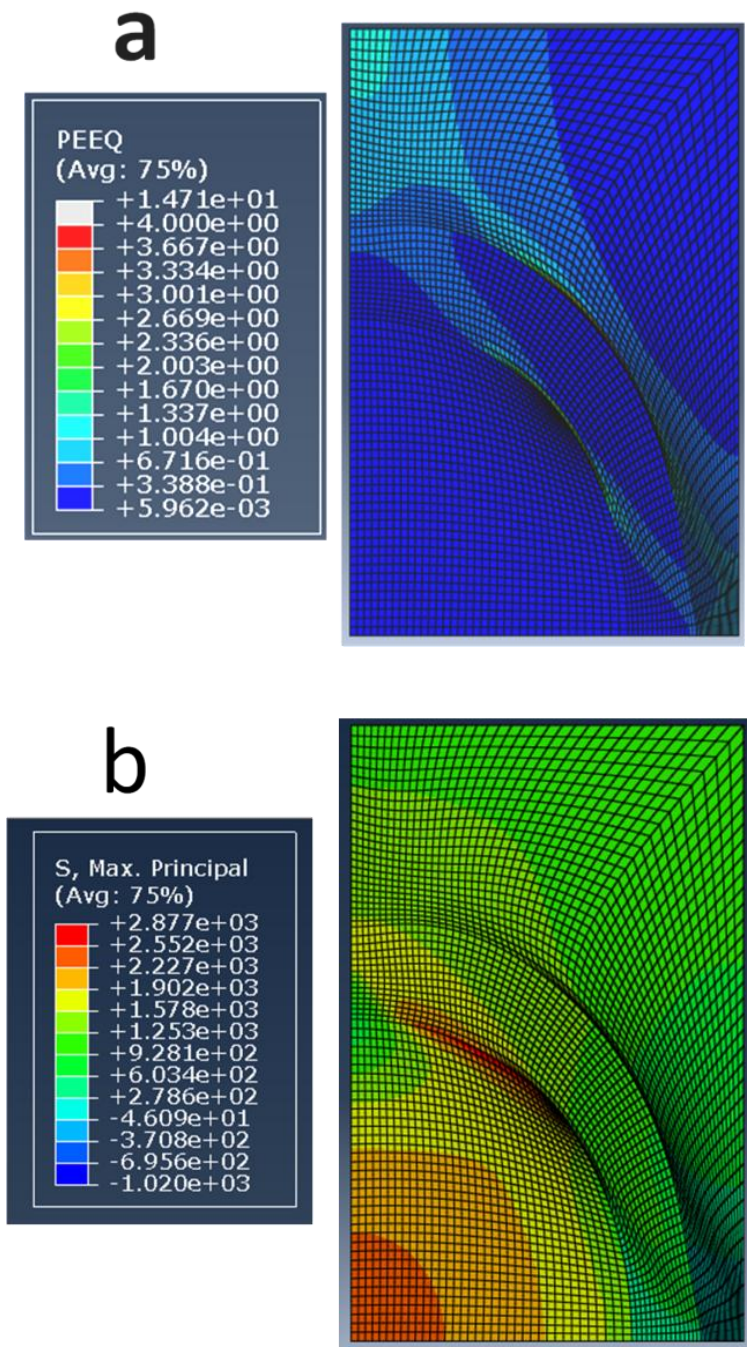
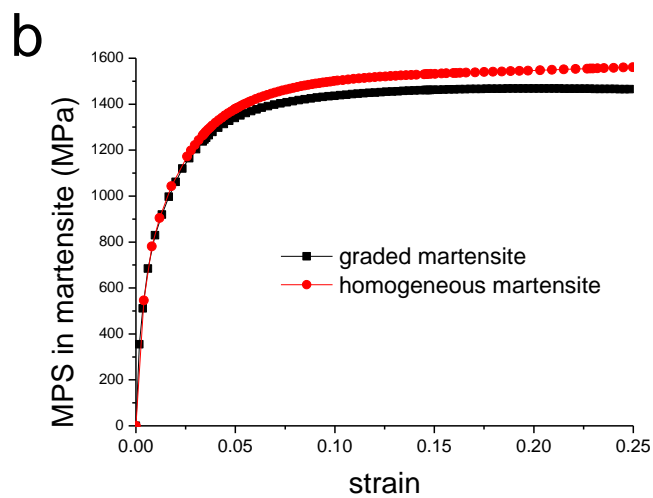
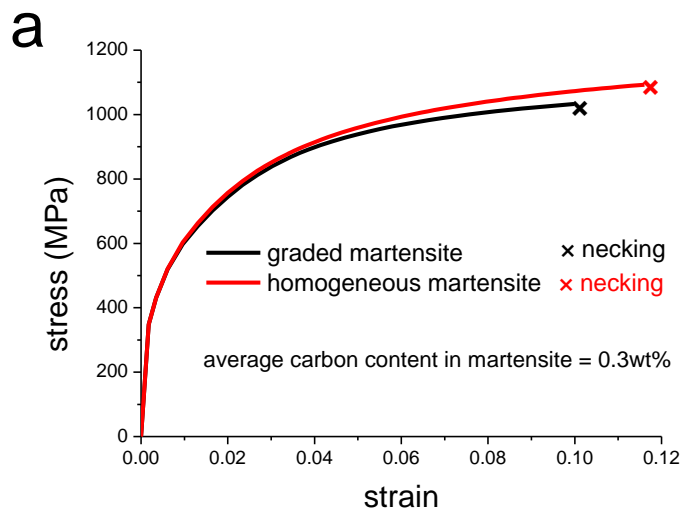


Figure 6.5. The distribution of equivalent plastic strain (a) and maximum principal stress (b) in the graded composite. The macroscopic strain is about 0.3.

The tensile curves of the unit cells with graded and homogeneous martensite are compared in Figure 6.6a. The curves are shown up to necking. The initial deformation is not influenced by the soft layer, but the work hardening at large strain is decreasing faster with the graded martensite. The unit cell with homogeneous martensite has both higher tensile strength and uniform elongation.

However, the average maximum principal stress in martensite is decreased if the soft layer is designed in the inclusion (Figure 6.6b), even if the average carbon content in the inclusion is the same. A lower MPS indicates a lower probability of martensite fracture and then a lower damage nucleation rate. Additionally, the strain partitioning to ferrite is decreased with graded martensite (Figure 6.6c), indicating the less tendency of strain localization and shear band formation in ferrite matrix. According to this primary study, the design of graded martensite in DP steels is not resulting in an improved combination of strength and uniform elongation. But the damage nucleation and strain localization are possible to be delayed. Additionally, the effect of the soft layer at the interface can be significant when the deformation mode of the real martensite islands is considered. As reported in [92], the martensite islands can be deformed in a bending mode, and thus a soft layer at the interface should be efficient in delaying cracking initiation in martensite.



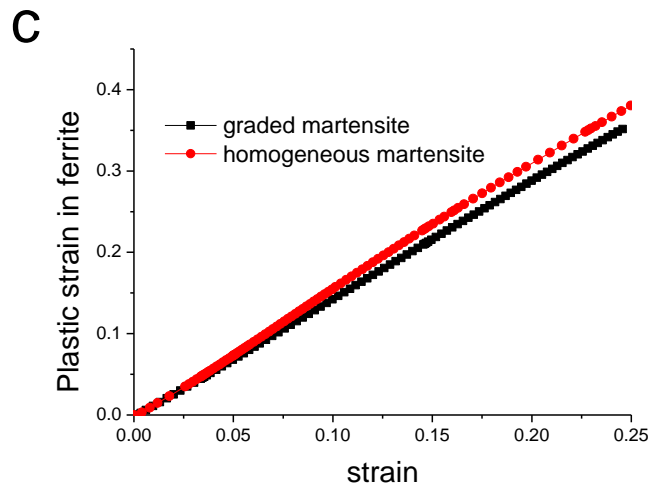


Figure 6.6. Comparison of the tensile curves (a), the evolution of average MPS in martensite (b) and plastic strain in ferrite (c) with macroscopic strain.

6.3 Summary

In this chapter, systematic parametric study is performed to identify the optimum microstructural features so that the improved balance between strength and formability can be achieved. For the forming operation determined by uniform strain, a high carbon content in martensite is favored, as well as the moderately coarse microstructure. For the forming operation controlled by material fracture, refined DP microstructure should be required.

A concept of DP steels with graded martensite is also discussed. A graded martensite island with a soft layer at the interface would result in a decrease of tensile strength and uniform elongation, but the failure by martensite fracture or strain localization is possible to be delayed.

Conclusions and perspectives

Ferrite-martensite dual-phase steels are characterized by a low yield/tensile strength ratio, high initial strain hardening and a good combination of strength and ductility. This steel grade has been widely used in automotive industry, but the trade-off between strength and formability is still the main limitation for a more extensive use of this class of alloys. In order to fully exploit the potential of this composite material, it is of primary importance to clarify the effect of individual microstructural feature on the mechanical properties, such as tensile strength, uniform elongation and fracture strain. After nesting a comprehensive understanding of the microstructure—properties relationship, it is possible to design DP steels with improved mechanical properties, fulfilling the list of requirements for specific applications.

From the literature review, the volume fraction and composition of martensite and the scale of microstructure were highlighted as the key factors in determining the plastic and fracture properties of DP steels.

The re-austenitization from spheroidized microstructure has been studied. The austenite islands nucleate preferentially at the carbides located at ferrite grain boundaries. The kinetics of austenite formation is first controlled by Mn partitioning from ferrite and later approaching to final equilibrium by Mn diffusion within austenite. Although there are significant carbon and Mn gradients in the small volume of the core, carbon and Mn can be approximated as uniformly distributed within the austenite. The expected distribution of carbon is supported by the qualitative carbon mapping by NanoSIMS, and is rationalized using DICTRA calculation.

The re-austenitization from cold-rolled martensite has also been studied. The refined initial microstructure, high stored energy, and low intercritical temperature due to relatively high Mn content result in significant interaction between ferrite recrystallization and austenite formation. Ultrafine-grained dual-phase microstructure can be attained with conventional heating rate.

Based on the control of the phase transformations, microstructures have been developed to decouple the effects of martensite volume fraction and martensite

Conclusions and perspectives

composition. UFG-DP steels were also processed so that the consequences of microstructure refinement could be studied.

The effects of martensite volume fraction, martensite composition and scale of microstructure on the plastic properties of DP steels are investigated experimentally. The main conclusions and highlights are summarized as follows:

- 1) DP steels start to yield at a lower stress than ferrite or than a spheroidized microstructure. But the presence of martensite phase eliminates the yield point phenomenon and dramatically increases the work-hardening rate, this effect being more pronounced with increasing martensite volume fraction.
- 2) The yield strength and the tensile strength are both increased with martensite volume fraction, but the uniform elongation shows an opposite trend. This is related to the onset of plastic deformation in the martensite, which results in a reduction of the kinematic hardening contribution.
- 3) The martensite composition has limited influence on the yield strength of DP steels. And its effect on the tensile strength is only significant when the martensite volume fraction is large. With V_m larger than 21%, a DP steel with higher martensite hardness has higher tensile strength.
- 4) The uniform elongation is less affected by martensite composition except for large martensite volume fraction.
- 5) Microstructure refinement of DP steels increases the yield strength and tensile strength, but the uniform elongation is slightly decreased. As a consequence, the strength-ductility product is not significantly influenced by microstructure refinement.
- 6) A TRIP effect is observed after annealing at low temperature (680°C). The TRIP effect increases the work-hardening rate and then the ductility of UFG-DP.

The specific effects of the microstructure on fracture properties are also systematically studied. The main conclusions are drawn as follows.

- 1) The damage accumulation, including both nucleation and growth of voids, is promoted with increasing V_m . Both interface decohesion and martensite fracture

Conclusions and perspectives

are operating damage mechanisms, but the martensite fracture is becoming dominant when the martensite volume fraction is increased.

- 2) The fracture strain decreases with increasing V_m . Brittle fracture by cleavage can be observed in DP steels with high volume fraction of martensite.
- 3) The fracture strain is not sensitive to the martensite composition when V_m is low (below 20%). With high enough V_m , the fracture strain increases with lower martensite hardness.
- 4) Microstructure refinement can result in a better combination of tensile strength and fracture strain.
- 5) Microstructure refinement can delay damage nucleation only when V_m is low. Void growth is suppressed in refined microstructures. Therefore, damage accumulation is less significant in UFG-DP steels.
- 6) UFG-DP steels always fracture in a ductile mode. But brittle fracture occurs in CG-DP steels when V_m is high.

These experimental findings were analyzed with a micromechanical model based on the axisymmetric RVE cell model, and the model works reasonably well in simulating the deformation behavior of DP steels. A modified law for ferrite, taking into account of the stage-IV hardening, improves the predictions of mechanical properties. These results support the semi-quantitative validity of the parametric study performed to guide microstructure optimization.

A systematic parametric study is performed to identify the optimum microstructural features in order to reach the best possible strength/formability balance. For the forming operation determined by uniform strain, a high carbon content in the martensite is needed, as well as a coarse microstructure. For the forming operation controlled by material fracture, a refined DP microstructure should be required.

A concept of DP steels with graded martensite is also discussed. A graded martensite island with a soft layer at the interface results in a decrease of the tensile strength and uniform elongation, but the failure by martensite fracture or strain localization in ferrite can possibly be delayed.

● Perspectives

A comprehensive study has been performed on the microstructure development and mechanical properties of a model steel grade. The results are interesting for the fundamental understanding of the mechanical behavior of DP steels and also are helpful in developing the guideline for alloy design. This work opens numerous perspectives:

- 1) The connectivity of martensite islands and the damage accumulation in CG- and UFG-DP could be characterized by X-ray microtomography so that the effects of microstructure refinement on damage and fracture can be further clarified. Three points are to be addressed. The first is the evolution of martensite connectivity with martensite volume fraction and scale of microstructure, and the relationship with void nucleation. The second is suppressed growth of voids in UFG-DP. The third is the void coalescence process with and without substantial void growth in CG- and UFG-DP, respectively.
- 2) The fracture behavior of DP steels is changed when V_m is increased or the scale of microstructure is modified. The fracture toughness, which is the resistance to cracking from pre-existing defect, of DP steels is to be investigated, concerning the effects of microstructural features.
- 3) The advantages of UFG-DP in terms of formability are to be exploited. For example, since the wide continuous martensite bands are fragmented in UFG-DP, the premature void formation during bending, which is due to martensite bands, can be delayed, resulting in improved bendability.
- 4) The formation of ultrafine DP microstructure can be achieved in the steel grade with 3.5wt% Mn. In addition, a low annealing temperature (680°C) can introduce TRIP effect due to high carbon content in austenite. The TRIP effect is essential in the excellent mechanical properties of UFG-DP. In principle, further decreasing annealing temperature can increase the stability of the austenite so that the TRIP effect can be more pronounced. But the consequential low martensite volume fraction makes the microstructure refinement difficult for the steel grade 0.1C3.5Mn used in this thesis. It is proposed to increase the carbon content (to 0.15wt% or 0.2wt%) so that the low annealing temperature, for instance 660°C, is possible for achieving UFG-DP and the stability of austenite can be improved.

Conclusions and perspectives

- 5) The UFG-DP microstructure is stable after annealing for 1 hour. This refined microstructure and the relatively high stability indicate the possible superplasticity at intercritical temperature, extending the application of UFG-DP.

- 6) The modification of fully martensitic microstructure into a ferrite-martensite dual-phase microstructure results in dramatic change of mechanical properties, and the combination of strength and formability is significantly improved. Similar strategy can surely be applied to the maraging steels, which have very high strength but the formability is poor. The success of this idea strongly relies on the knowledges of phase transformation, especially the kinetics of austenite formation and the partitioning of alloying elements that involve in intermetallic compound formation.

References

- [1] **Bleck W.** Cold-rolled, high-strength sheet steels for auto applications. *JOM-Journal of the Minerals Metals & Materials Society* 1996;48:26.
- [2] **Bouaziz O, Zurob H, Huang MX.** Driving Force and Logic of Development of Advanced High Strength Steels for Automotive Applications. *Steel Research International* 2013;84:937.
- [3] **Rashid MS.** Dual Phase Steels. *Annual Review of Materials Science* 1981;11:245.
- [4] **Speich GR.** Physical Metallurgy of Dual-Phase Steels. In *Fundamental of Dual-Phase Steels*, The Metallurgical Society, 1981, p.1-45.
- [5] **Davies RG.** Influence of martensite composition and content on properties of dual phase steels. *Metallurgical Transactions A-Physical Metallurgy and Materials Science* 1978;9:671.
- [6] **Davies RG, Magee CL.** Physical metallurgy of automotive high strength steels. In *Structure and Properties of Dual-Phase Steels*, AIME, 1979, p.1-19.
- [7] **Thomas G, Koo JY.** Developments in Strong, Ductile Duplex Ferrite-Martensitic Steels. In *Structure and Properties of Dual-Phase Steels*, AIME, 1979: 183-201.
- [8] **Jacques P, Cornet X, Harlet P, Ladriere J, Delannay F.** Enhancement of the mechanical properties of a low-carbon, low-silicon steel by formation of a multiphased microstructure containing retained austenite. *Metallurgical and Materials Transactions A-Physical Metallurgy and Materials Science* 1998;29:2383.
- [9] **Jacques PJ.** Transformation-induced plasticity for high strength formable steels. *Current Opinion in Solid State & Materials Science* 2004;8:259.
- [10] **Bouaziz O, Allain S, Scott CP, Cugy P, Barbier D.** High manganese austenitic twinning induced plasticity steels: A review of the microstructure properties relationships. *Current Opinion in Solid State & Materials Science* 2011;15:141.
- [11] **Speer JG, Edmonds DV, Rizzo FC, Matlock DK.** Partitioning of carbon from supersaturated plates of ferrite, with application to steel processing and fundamentals of the bainite transformation. *Current Opinion in Solid State & Materials Science* 2004;8:219.
- [12] **Furukawa T.** Dependence of strength ductility characteristics on thermal history in low-carbon, 5wt-percent-Mn Steels. *Materials Science and Technology* 1989;5:465.
- [13] **Luo HW, Shi J, Wang C, Cao WQ, Sun XJ, Dong H.** Experimental and numerical analysis on formation of stable austenite during the intercritical annealing of 5Mn steel. *Acta Materialia* 2011;59:4002.
- [14] **Niikura M, Morris JW.** Thermal processing of ferritic 5Mn Steel for toughness at cryogenic temperatures. *Metallurgical Transactions A-Physical Metallurgy and Materials Science* 1980;11:1531.
- [15] **Landron C.** Ductile damage characterization in Dual-Phase steels using X-ray tomography. PhD thesis, INSA Lyon, 2011.

References

-
- [16] **Granbom Y.** Structure and Mechanical Properties of Dual-Phase Steels: An Experimental and Theoretical Analysis. PhD thesis, KTH, 2010.
- [17] **Yi JJ, Kim IS, Choi HS.** Austenitization during intercritical annealing of an Fe-C-Si-Mn dual-phase Steels. *Metallurgical Transactions A-Physical Metallurgy and Materials Science* 1985;16:1237.
- [18] **Goune M, Maugis P, Drillet J.** A Criterion for the Change from Fast to Slow Regime of Cementite Dissolution in Fe-C-Mn Steels. *Journal of Materials Science & Technology* 2012;28:728.
- [19] **Savran VI, Van Leeuwen Y, Hanlon DN, Kwakernaak C, Sloof WG, Sietsma J.** Microstructural features of austenite formation in C35 and C45 alloys. *Metallurgical and Materials Transactions A-Physical Metallurgy and Materials Science* 2007;38A:946.
- [20] **Shtansky DV, Nakai K, Ohmori Y.** Pearlite to austenite transformation in an Fe-2.6Cr-1C alloy. *Acta Materialia* 1999;47:2619.
- [21] **Azizi-Alizamini H, Militzer M, Poole WJ.** Austenite Formation in Plain Low-Carbon Steels. *Metallurgical and Materials Transactions A-Physical Metallurgy and Materials Science* 2011;42A:1544.
- [22] **Yang DZ, Brown EL, Matlock DK, Krauss G.** The formation of austenite at low intercritical annealing temperatures in a normalized 0.08C-1.45Mn-0.21Si steel. *Metallurgical Transactions A-Physical Metallurgy and Materials Science* 1985;16:1523.
- [23] **Garcia CI, Deardo AJ.** Formation of austenite in 1.5 pct Mn steels. *Metallurgical Transactions A-Physical Metallurgy and Materials Science* 1981;12:521.
- [24] **Garcia CI, Cho KG, Redkin K, Deardo AJ, Tan SS, Somani M, Karjalainen LP.** Influence of Critical Carbide Dissolution Temperature during Intercritical Annealing on Hardenability of Austenite and Mechanical Properties of DP-980 Steels. *ISIJ International* 2011;51:969.
- [25] **Kulakov M, Poole WJ, Militzer M.** The Effect of the Initial Microstructure on Recrystallization and Austenite Formation in a DP600 Steel. *Metallurgical and Materials Transactions A-Physical Metallurgy and Materials Science* 2013;44A:3564.
- [26] **Speich GR, Demarest VA, Miller RL.** Formation of austenite during intercritical annealing of dual-phase steels. *Metallurgical Transactions A-Physical Metallurgy and Materials Science* 1981;12:1419.
- [27] **Wycliffe P, Purdy GR, Embury JD.** Austenite growth in the intercritical annealing of ternary and quaternary dual-phase steels. In *Fundamentals of Dual-Phase Steels*, The Metallurgical Society, 1981, p.59-83.
- [28] **Huang J, Poole WJ, Militzer M.** Austenite formation during intercritical annealing. *Metallurgical and Materials Transactions A-Physical Metallurgy and Materials Science* 2004;35A:3363.
- [29] **Peranio N, Li YJ, Roters F, Raabe D.** Microstructure and texture evolution in dual-phase steels: Competition between recovery, recrystallization, and phase transformation. *Materials Science and Engineering A-Structural Materials Properties Microstructure and Processing* 2010;527:4161.

References

-
- [30] **Mohanty RR, Girina OA, Fonstein NM.** Effect of Heating Rate on the Austenite Formation in Low-Carbon High-Strength Steels Annealed in the Intercritical Region. *Metallurgical and Materials Transactions A-Physical Metallurgy and Materials Science* 2011;42A:3680.
- [31] **Yang DZ, Brown EL, Matlock DK, Krauss G.** Ferrite recrystallization and austenite formation in cold-rolled intercritically annealed steel. *Metallurgical Transactions A-Physical Metallurgy and Materials Science* 1985;16:1385.
- [32] **Andrade-Carozzo V, Jacques PJ.** Interactions between recrystallisation and phase transformations during annealing of cold rolled Nb-added TRIP-aided steels. *Materials Science Forum* 2007; 539-543: 4649-4654.
- [33] **Zheng CW, Raabe D.** Interaction between recrystallization and phase transformation during intercritical annealing in a cold-rolled dual-phase steel: A cellular automaton model. *Acta Materialia* 2014;61:5504.
- [34] **Chbihi A, Barbier D, Germain L, Hazotte A, Goune M.** Interactions between ferrite recrystallization and austenite formation in high-strength steels. *Journal of Materials Science* 2014;49:3608.
- [35] **Bhadeshia HKDH.** *Steels: Microstructure and properties*: Elsevier, 2006.
- [36] **Nakada N, Arakawa Y, Park KS, Tsuchiyama T, Takaki S.** Dual phase structure formed by partial reversion of cold-deformed martensite. *Materials Science and Engineering A-Structural Materials Properties Microstructure and Processing* 2012;553:128.
- [37] **Huppi GS, Matlock DK, Krauss G.** An evaluation of the importance of epitaxial ferrite in dual-phase steel microstructures. *Scripta Metallurgica* 1980;14:1239.
- [38] **Nakada N, Mizutani K, Tsuchiyama T, Takaki S.** Difference in transformation behavior between ferrite and austenite formations in medium manganese steel. *Acta Materialia* 2014;65:251.
- [39] **Krauss G.** Martensite in steel: strength and structure. *Materials Science and Engineering A-Structural Materials Properties Microstructure and Processing* 1999;273:40.
- [40] **Allain S, Bouaziz O, Takahashi M.** Toward a new interpretation of the mechanical behaviour of as-quenched low alloyed martensitic steels. *ISIJ International* 2012;52:717.
- [41] **Hutchinson B, Hagstrom J, Karlsson O, Lindell D, Tornberg M, Lindberg F, Thuvander M.** Microstructures and hardness of as-quenched martensites (0.1-0.5%C). *Acta Materialia* 2011;59:5845.
- [42] **Grange RA, Hribal CR, Porter LF.** Hardness of tempered martensite in carbon and low-alloy steels. *Metallurgical Transactions A-Physical Metallurgy and Materials Science* 1977;8:1775.
- [43] **Arlazarov A, Bouaziz O, Hazotte A, Goune M, Allain S.** Characterization and modeling of manganese effect on strength and strain hardening of martensitic carbon steels. *ISIJ International* 2013;53:1076.
- [44] **Roumina R, Embury JD, Bouaziz O, Zurob HS.** Mechanical behavior of a compositionally graded 300M steel. *Materials Science and Engineering A-Structural Materials Properties Microstructure and Processing* 2013;578:140.

References

-
- [45] **Korzekwa DA, Matlock DK, Krauss G.** Dislocation substructure as a function of strain in a dual-phase steel. *Metallurgical Transactions A-Physical Metallurgy and Materials Science* 1984;15:1221.
- [46] **Kadkhodapour J, Schmauder S, Raabe D, Ziaei-Rad S, Weber U, Calcagnotto M.** Experimental and numerical study on geometrically necessary dislocations and non-homogeneous mechanical properties of the ferrite phase in dual phase steels. *Acta Materialia* 2011;59:4387.
- [47] **Sakaki T, Sugimoto K, Fukuzato T.** Role of internal stress for continuous yielding of dual-phase steels. *Acta Metallurgica* 1983;31:1737.
- [48] **Gerbase J, Embury JD, Hobbs RM.** The mechanical behavior of some dual phase steels-with emphasis on the initial work hardening rate. In *Structure and Properties of Dual-Phase Steels*, The Metallurgical Society of AIME, 1979, p.118-144.
- [49] **Sarosiek AM, Owen WS.** The work-hardening of dual-phase steels at small plastic strains. *Materials Science and Engineering* 1984;66:13.
- [50] **Brown LM, Clarke DR.** Work-hardening due to internal stresses in composite materials. *Acta Metallurgica* 1975;23:821.
- [51] **Movahed P, Kolahgar S, Marashi SPH, Pournavari M, Parvin N.** The effect of intercritical heat treatment temperature on the tensile properties and work hardening behavior of ferrite-martensite dual phase steel sheets. *Materials Science and Engineering A-Structural Materials Properties Microstructure and Processing* 2009;518:1.
- [52] **Speich GR, Miller RL.** Mechanical properties of ferrite-martensite steels. In *Structure and Properties of Dual Phase Steels*, The Metallurgical Society of AIME, 1979: 145-182.
- [53] **Ramos L, Matlock D, Krauss G.** On the deformation behavior of dual-phase steels. *Metallurgical Transactions A* 1979;10:259.
- [54] **Marder AR.** Deformation characteristics of dual-phase steels. *Metallurgical Transactions A-Physical Metallurgy and Materials Science* 1982;13:85.
- [55] **Kumar A, Singh SB, Ray KK.** Influence of bainite/martensite content on the tensile properties of low carbon dual-phase steels. *Materials Science and Engineering A-Structural Materials Properties Microstructure and Processing* 2008;474:270.
- [56] **Chang PH, Preban AG.** The effect of ferrite grain size and martensite volume fraction on the tensile properties of dual phase steel. *Acta Metallurgica* 1985;33:897.
- [57] **Mazinani M, Poole WJ.** Effect of martensite plasticity on the deformation behavior of a low-carbon dual-phase steel. *Metallurgical and Materials Transactions A-Physical Metallurgy and Materials Science* 2007;38A:328.
- [58] **Koo JY, Young MJ, Thomas G.** On the law of mixtures in dual-phase steels. *Metallurgical Transactions A-Physical Metallurgy and Materials Science* 1980;11:852.
- [59] **Pierman AP.** Micromechanical study of the influence of the microstructure and composition on the plastic flow and damage properties of Dual-Phase steels. PhD thesis, Universite catholique de Louvain, 2013.
- [60] **Jiang ZH, Guan ZZ, Lian JS.** Effects of microstructural variables on the deformation behavior of dual-phase steel. *Materials Science and Engineering A-Structural*

References

-
- Materials Properties Microstructure and Processing 1995;190:55.
- [61] **Azevedo G, Barbosa R, Pereloma EV, Santos DB.** Development of an ultrafine grained ferrite in a low C-Mn and Nb-Ti microalloyed steels after warm torsion and intercritical annealing. *Materials Science and Engineering A-Structural Materials Properties Microstructure and Processing* 2005;402:98.
- [62] **Son YI, Lee YK, Park KT, Lee CS, Shin DH.** Ultrafine grained ferrite-martensite dual phase steels fabricated via equal channel angular pressing: Microstructure and tensile properties. *Acta Materialia* 2005;53:3125.
- [63] **Calcagnotto M, Adachi Y, Ponge D, Raabe D.** Deformation and fracture mechanisms in fine- and ultrafine-grained ferrite/martensite dual-phase steels and the effect of aging. *Acta Materialia* 2011;59:658.
- [64] **Azizi-Alizamini H, Militzer M, Poole WJ.** Formation of ultrafine grained dual phase steels through rapid heating. *ISIJ International* 2011;51:958.
- [65] **Calcagnotto M, Ponge D, Raabe D.** Effect of grain refinement to 1 μm on strength and toughness of dual-phase steels. *Materials Science and Engineering A-Structural Materials Properties Microstructure and Processing* 2010;527:7832.
- [66] **Chehab B, Wang X, Masse JP, Bouaziz O, Zurob H, Embury D.** Bulk nanoscale materials in steel products. *Journal of Physics: Conference Series* 2010;240:012135.
- [67] **Bag A, Ray KK, Dwarakadasa ES.** Influence of martensite content and morphology on tensile and impact properties of high-martensite dual-phase steels. *Metallurgical and Materials Transactions A-Physical Metallurgy and Materials Science* 1999;30:1193.
- [68] **Sun SJ, Pugh M.** Properties of thermomechanically processed dual-phase steels containing fibrous martensite. *Materials Science and Engineering A-Structural Materials Properties Microstructure and Processing* 2002;335:298.
- [69] **Sarwar M, Priestner R.** Influence of ferrite-martensite microstructural morphology on tensile properties of dual-phase steel. *Journal of Materials Science* 1996;31:2091.
- [70] **Paul SK, Mukherjee M.** Determination of bulk flow properties of a material from the flow properties of its constituent phases. *Computational Materials Science* 2014;84:1.
- [71] **Huper T, Endo S, Ishikawa N, Osawa K.** Effect of volume fraction of constituent phases on the stress-strain relationship of dual phase steels. *ISIJ International* 1999;39:288.
- [72] **Tomota Y, Tamura I.** Mechanical behavior of steels consisting of 2 ductile phases. *Transactions of the Iron and Steel Institute of Japan* 1982;22:665.
- [73] **Bouaziz O, Jung T, Kandel M, Lecomte C.** Physical modelling of microstructure and mechanical properties of dual-phase steel. *Journal De Physique Iv* 2001;11:223.
- [74] **Jiang ZG, Liu JK, Lian JH.** A new relationship between the flow stress and the microstructural parameters for dual phase steel. *Acta Metall. Mater.* 1992;40:1587.
- [75] **Kim CM.** Modeling tensile deformation of dual-phase steel. *Metallurgical Transactions A-Physical Metallurgy and Materials Science* 1988;19:1263.
- [76] **Pierman AP, Bouaziz O, Pardoën T, Jacques PJ, Brassart L.** The influence of microstructure and composition on the plastic behaviour of dual-phase steels. *Acta Materialia* 2014;73:298.

References

-
- [77] **Delincé M, Brechet Y, Embury JD, Geers MGD, Jacques PJ, Pardoën T.** Structure-property optimization of ultrafine-grained dual-phase steels using a micro structure-based strain hardening model. *Acta Materialia* 2007;55:2337.
- [78] **Karlsson B, Sundström BO.** Inhomogeneity in plastic deformation of two-phase steels. *Materials Science and Engineering* 1974;16:161.
- [79] **Al-Abbasi FM, Nemes JA.** Micromechanical modeling of dual phase steels. *International Journal of Mechanical Sciences* 2003;45:1449.
- [80] **Lani F, Furnemont Q, Van Rompaey T, Delannay F, Jacques PJ, Pardoën T.** Multiscale mechanics of TRIP-assisted multiphase steels: II. Micromechanical modelling. *Acta Materialia* 2007;55:3695.
- [81] **Al-Abbasi FM, Nemes JA.** Characterizing DP-steels using micromechanical modeling of cells. *Computational Materials Science* 2007;39:402.
- [82] **Liedl U, Traint S, Werner EA.** An unexpected feature of the stress-strain diagram of dual-phase steel. *Computational Materials Science* 2002;25:122.
- [83] **Ramazani A, Mukherjee K, Quade H, Prah U, Bleck W.** Correlation between 2D and 3D flow curve modelling of DP steels using a microstructure-based RVE approach. *Materials Science and Engineering A-Structural Materials Properties Microstructure and Processing* 2013;560:129.
- [84] **Paul SK, Kumar A.** Micromechanics based modeling to predict flow behavior and plastic strain localization of dual phase steels. *Computational Materials Science* 2012;63:66.
- [85] **Landron C, Maire E, Bouaziz O, Adrien J, Lecarme L, Bareggi A.** Validation of void growth models using X-ray microtomography characterization of damage in dual phase steels. *Acta Materialia* 2011;59:7564.
- [86] **Szewczyk AF, Gurland J.** A study of the deformation and fracture of a dual-phase steel. *Metallurgical Transactions A-Physical Metallurgy and Materials Science* 1982;13:1821.
- [87] **Ghadbeigi H, Pinna C, Celotto S, Yates JR.** Local plastic strain evolution in a high strength dual-phase steel. *Materials Science and Engineering A-Structural Materials Properties Microstructure and Processing* 2010;527:5026.
- [88] **Steinbrunner DL, Matlock DK, Krauss G.** Void formation during tensile testing of dual phase steels. *Metallurgical Transactions A-Physical Metallurgy and Materials Science* 1988;19:579.
- [89] **Han SK, Margolin H.** Void formation, void growth and tensile fracture of plain carbon steel and a dual-phase steel. *Materials Science and Engineering A-Structural Materials Properties Microstructure and Processing* 1989;112:133.
- [90] **Avramovic-Cingara G, Saleh CAR, Jain MK, Wilkinson DS.** Void Nucleation and Growth in Dual-Phase Steel 600 during Uniaxial Tensile Testing. *Metallurgical and Materials Transactions A-Physical Metallurgy and Materials Science* 2009;40A:3117.
- [91] **Kadkhodapour J, Butz A, Rad SZ.** Mechanisms of void formation during tensile testing in a commercial, dual-phase steel. *Acta Materialia* 2011;59:2575.
- [92] **Ghadbeigi H, Pinna C, Celotto S.** Failure mechanisms in DP600 steel: Initiation, evolution and fracture. *Materials Science and Engineering A-Structural Materials*

References

- Properties Microstructure and Processing 2011;588:420.
- [93] **Landron C, Bouaziz O, Maire E, Adrien J.** Characterization and modeling of void nucleation by interface decohesion in dual phase steels. *Scripta Materialia* 2010;63:973.
- [94] **Landron C, Bouaziz O, Maire E, Adrien J.** Experimental investigation of void coalescence in a dual phase steel using X-ray tomography. *Acta Materialia* 2013;61:6821.
- [95] **Maire E, Bouaziz O, Di Michiel M, Verdu C.** Initiation and growth of damage in a dual-phase steel observed by X-ray microtomography. *Acta Materialia* 2008;56:4954.
- [96] **Bareggi A, Maire E, Bouaziz O, Di Michiel M.** Damage in dual phase steels and its constituents studied by X-ray tomography. *International Journal of Fracture* 2012;174:217.
- [97] **Landron C, Maire E, Adrien J, Bouaziz O, Di Michiel M, Cloetens P, Suhonen H.** Resolution effect on the study of ductile damage using synchrotron X-ray tomography. *Nucl. Instrum. Methods Phys. Res. Sect. B-Beam Interact. Mater. Atoms* 2012;284:15.
- [98] **Avramovic-Cingara G, Ososkov Y, Jain MK, Wilkinson DS.** Effect of martensite distribution on damage behaviour in DP600 dual phase steels. *Materials Science and Engineering A-Structural Materials Properties Microstructure and Processing* 2009;516:7.
- [99] **Pineau A, Pardoën T.** Failure of Metals. In *Comprehensive Structural Integrity*. Pergamon, 2007.
- [100] **Requena G, Maire E, Leguen C, Thuillier S.** Separation of nucleation and growth of voids during tensile deformation of a dual phase steel using synchrotron microtomography. *Materials Science and Engineering A-Structural Materials Properties Microstructure and Processing* 2014;589:242.
- [101] **Davis CL, King JE.** Cleavage initiation in the intercritically reheated coarse-grained heat-affected zone: 1 fractographic evidence. *Metallurgical and Materials Transactions A-Physical Metallurgy and Materials Science* 1994;25:563.
- [102] **Tomota Y, Yoshino H, Kuroki K.** Effect of ductility of 2nd phase on ductile fracture. *Scripta Metallurgica* 1977;11:853.
- [103] **Azuma M, Goutianos S, Hansen N, Winther G, Huang X.** Effect of hardness of martensite and ferrite on void formation in dual phase steel. *Materials Science and Technology* 2012;28:1092.
- [104] **Kunio T, Shimizu M, Yamada K, Suzuki H.** An effect of the second phase morphology on the tensile fracture characteristics of carbon steels. *Engineering Fracture Mechanics* 1975;7:411.
- [105] **Uggowitzer P, Stuwe HP.** The tensile fracture of ferritic-martensitic carbon steels. *Materials Science and Engineering* 1982;55:181.
- [106] **Park K, Nishiyama M, Nakada N, Tsuchiyama T, Takaki S.** Effect of the martensite distribution on the strain hardening and ductile fracture behaviors in dual-phase steel. *Materials Science and Engineering A-Structural Materials Properties Microstructure and Processing* 2014;604:135.

References

-
- [107] **Ramazani A, Ebrahimi Z, Prah U.** Study the effect of martensite banding on the failure initiation in dual-phase steel. *Comput. Mater. Sci.* 2014;87:241.
- [108] **Tasan CC, Hoefnagels JPM, Geers MGD.** Microstructural banding effects clarified through micrographic digital image correlation. *Scripta Materialia* 2010;62:835.
- [109] **Sun X, Choi KS, Soulami A, Liu WN, Khaleel MA.** On key factors influencing ductile fractures of dual phase (DP) steels. *Materials Science and Engineering A-Structural Materials Properties Microstructure and Processing* 2009;526:140.
- [110] **Sun X, Choi KS, Liu WN, Khaleel MA.** Predicting failure modes and ductility of dual phase steels using plastic strain localization. *International Journal of Plasticity* 2009;25:1888.
- [111] **Choi KS, Liu WN, Sun X, Khaleel MA.** Influence of martensite mechanical properties on failure mode and ductility of dual-phase steels. *Metallurgical and Materials Transactions A-Physical Metallurgy and Materials Science* 2009;40A:796.
- [112] **Kadkhodapour J, Butz A, Ziaei-Rad S, Schmauder S.** A micro mechanical study on failure initiation of dual phase steels under tension using single crystal plasticity model. *International Journal of Plasticity* 2011;27:1103.
- [113] **Vajragupta N, Uthaisangsuk V, Schmaling B, Munstermann S, Hartmaier A, Bleck W.** A micromechanical damage simulation of dual phase steels using XFEM. *Computational Materials Science* 2012;54:271.
- [114] **LeRoy G, Embury JD, Edward G, Ashby MF.** A model of ductile fracture based on the nucleation and growth of voids. *Acta Metallurgica* 1981;29:1509.
- [115] **Rauch EF, Veron M.** Coupled microstructural observations and local texture measurements with an automated crystallographic orientation mapping tool attached to a TEM. *Materialwissenschaft Und Werkstofftechnik* 2005;36:552.
- [116] <http://www.nanomegas.com/>.
- [117] **Slodzian G, Hillion F, Stadermann FJ, Horreard F.** Oxygen isotopic measurements on the Cameca Nanosims 50. *Applied Surface Science* 2003;203:798.
- [118] **Hoppe P.** NanoSIMS: A new tool in cosmochemistry. *Applied Surface Science* 2006;252:7102.
- [119] **Drillet J, Valle N, Iung T.** Nanometric scale investigation of phase transformations in advanced steels for automotive application. *Metallurgical and Materials Transactions A-Physical Metallurgy and Materials Science* 2012;43A:4947.
- [120] **Valle N, Drillet J, Bouaziz O, Migeon HN.** Study of the carbon distribution in multi-phase steels using the NanoSIMS 50. *Applied Surface Science* 2006;252:7051.
- [121] **Exner HE.** Qualitative and quantitative surface microscopy. In *Physical Metallurgy*, 5th edition: Elsevier, 1996.
- [122] <http://imagej.nih.gov/ij/>.
- [123] <http://www.thermocalc.com/products-services/software/>.
- [124] **Wei R, Enomoto M, Radian R, Zurob HS, Purdy GR.** Growth of austenite from as-quenched martensite during intercritical annealing in an Fe-0.1C-3Mn-1.5Si alloy. *Acta Materialia* 2013;61:697.
- [125] **Garcia CI, DeArdo AJ.** The Formation of Austenite in Low-Alloy Steels. In *Structure and Properties of Dual-Phase Steels*, AIME, 1979, p.40-61.

References

-
- [126] **Porter DA, Easterling KE.** Phase Transformation in Metals and Alloys: Chapman & Hall, 1992.
- [127] **Huang X, Morito S, Hansen N, Maki T.** Ultrafine Structure and High Strength in Cold-Rolled Martensite. *Metallurgical and Materials Transactions A-Physical Metallurgy and Materials Science* 2012;43A:3517.
- [128] **Hu H, Goodman SR.** Effect of manganese on the annealing texture and strain ratio of low-carbon steels. *Metallurgical Transactions* 1970;1:3057.
- [129] **Li XD, Bhushan B.** A review of nanoindentation continuous stiffness measurement technique and its applications. *Materials Characterization* 2002;48:11.
- [130] **Oliver WC, Pharr GM.** Measurement of hardness and elastic modulus by instrumented indentation: Advances in understanding and refinements to methodology. *Journal of Materials Research* 2004;19:3.
- [131] **Nix WD, Gao HJ.** Indentation size effects in crystalline materials: A law for strain gradient plasticity. *Journal of the Mechanics and Physics of Solids* 1998;46:411.
- [132] **Furnemont Q, Kempf M, Jacques PJ, Goken M, Delannay F.** On the measurement of the nanohardness of the constitutive phases of TRIP-assisted multiphase steels. *Materials Science and Engineering A-Structural Materials Properties Microstructure and Processing* 2002;328:26.
- [133] **Delince M, Jacques PJ, Pardoën T.** Separation of size-dependent strengthening contributions in fine-grained Dual Phase steels by nanoindentation. *Acta Materialia* 2006;54:3395.
- [134] **Ghassemi-Armaki H, Maass R, Bhat SP, Sriram S, Greer JR, Kumar KS.** Deformation response of ferrite and martensite in a dual-phase steel. *Acta Materialia* 2014;62:197.
- [135] **Durst K, Goken M, Vehoff H.** Finite element study for nanoindentation measurements on two-phase materials. *Journal of Materials Research* 2004;19:85.
- [136] **Ohmura T, Tsuzaki K, Matsuoka S.** Nanohardness measurement of high-purity Fe-C martensite. *Scripta Materialia* 2001;45:889.
- [137] **Su YL, Gurland J.** Strain partition, uniform elongation and fracture strain in dual-phase steels. *Materials Science and Engineering* 1987;95:151.
- [138] **Kang JD, Ososkov Y, Embury JD, Wilkinson DS.** Digital image correlation studies for microscopic strain distribution and damage in dual phase steels. *Scripta Materialia* 2007;56:999.
- [139] **Marteau J, Haddadi H, Bouvier S.** Investigation of Strain Heterogeneities Between Grains in Ferritic and Ferritic-Martensitic Steels. *Experimental Mechanics* 2013;53:427.
- [140] **Joo SH, Lee JK, Koo JM, Lee S, Suh DW, Kim HS.** Method for measuring nanoscale local strain in a dual phase steel using digital image correlation with nanodot patterns. *Scripta Materialia* 2013;68:245.
- [141] **Pussegoda N, Tyson WR, Wycliffe P, Purdy GR.** Segregation of manganese during intercritical annealing of dual phase steels. *Metallurgical Transactions A-Physical Metallurgy and Materials Science* 1984;15:1499.
- [142] **Moyer JM, Ansell GS.** Volume expansion accompanying martensite transformation in

References

- iron-carbon alloys. *Metallurgical Transactions A-Physical Metallurgy and Materials Science* 1975;6:1785.
- [143] **Jacques PJ, Ladriere J, Delannay F.** On the influence of interactions between phases on the mechanical stability of retained austenite in transformation-induced plasticity multiphase steels. *Metallurgical and Materials Transactions A-Physical Metallurgy and Materials Science* 2001;32:2759.
- [144] **Sachdev AK.** Effect of retained austenite on the yielding and deformation behavior of a dual phase steel. *Acta Metallurgica* 1983;31:2037.
- [145] **Jacques PJ, Furnemont Q, Lani F, Pardoën T, Delannay F.** Multiscale mechanics of TRIP-assisted multiphase steels: I. Characterization and mechanical testing. *Acta Materialia* 2007;55:3681.
- [146] **Tsuji N, Kamikawa N, Ueji R, Takata N, Koyama H, Terada D.** Managing both strength and ductility in ultrafine grained steels. *ISIJ International* 2008;48:1114.
- [147] **Kocks UF, Mecking H.** Physics and phenomenology of strain hardening: the FCC case. *Progress in Materials Science* 2003;48:171.
- [148] **De Cooman BC, Gibbs P, Lee S, Matlock DK.** Transmission Electron Microscopy Analysis of Yielding in Ultrafine-Grained Medium Mn Transformation-Induced Plasticity Steel. *Metallurgical and Materials Transactions A-Physical Metallurgy and Materials Science* 2013;44A:2563.
- [149] **Ryu JH, Kim JI, Kim HS, Oh CS, Bhadeshia HKDH, Suh DW.** Austenite stability and heterogeneous deformation in fine-grained transformation-induced plasticity-assisted steel. *Scripta Materialia* 2013;68:933.
- [150] **Lee S, Lee SJ, De Cooman BC.** Austenite stability of ultrafine-grained transformation-induced plasticity steel with Mn partitioning. *Scripta Materialia* 2011;65:225.
- [151] **Furukawa T, Huang H, Matsumura O.** Effects of carbon content on mechanical-properties of 5-percent-Mn steels exhibiting transformation-induced plasticity. *Materials Science and Technology* 1994;10:964.
- [152] **Tomita Y, Okabayashi K.** Tensile stress-strain analysis of cold-worked metals and steels and dual-phase steels. *Metallurgical Transactions A-Physical Metallurgy and Materials Science* 1985;16:865.
- [153] **Huang H, Matsumura O, Furukawa T.** Retained austenite in low-carbon, manganese steel after intercritical heat-treatment. *Materials Science and Technology* 1994;10:621.
- [154] **Breedis JF.** Influence of dislocation substructure on the martensitic transformation in stainless steel. *Acta Metallurgica* 1965;13:239.
- [155] **Yang HS, Bhadeshia H.** Austenite grain size and the martensite-start temperature. *Scripta Materialia* 2009;60:493.
- [156] **Tasan CC, Hoefnagels JPM, Geers MGD.** Identification of the continuum damage parameter: An experimental challenge in modeling damage evolution. *Acta Materialia* 2012;60:3581.
- [157] **Kim NJ, Thomas G.** Effects of morphology on the mechanical-behavior of a dual phase Fe-2Si-0.1C steel. *Metallurgical Transactions A-Physical Metallurgy and*

References

- Materials Science 1981;12:483.
- [158] **Cai XL, Feng J, Owen WS.** The dependence of some tensile and fatigue properties of a dual-phase steel on its microstructure. *Metallurgical Transactions A-Physical Metallurgy and Materials Science* 1985;16:1405.
- [159] **Meyers M, Chawla K.** *Mechanical behavior of Materials*: Cambridge University Press, 2008.
- [160] **Shi MF, Meuleman DJ.** On certain aspects of strain-rate sensitivity of sheet metals. *Journal of Materials Engineering and Performance* 1995;4:321.
- [161] **Yerra SK, Martin G, Veron M, Brechet Y, Mithieux JD, Delannay L, Pardoën T.** Ductile fracture initiated by interface nucleation in two-phase elastoplastic systems. *Eng. Fract. Mech.* 2013;102:77.
- [162] **Tvergaard V.** Influence of voids on shear band instabilities under plane-strain conditions. *International Journal of Fracture* 1981;17:389.
- [163] ABAQUS. *Analysis User's Manual*, Version 6.8, 2008.
- [164] **Bouaziz O, Aouafi A, Allain S.** Effect of grain refinement on the mechanical behaviour of ferritic steels: Evolution of isotropic hardening and kinematic hardening. *Materials Science Forum* 2008;584-586:605-609.
- [165] **Sinclair CW, Poole WJ, Brechet Y.** A model for the grain size dependent work hardening of copper. *Scripta Materialia* 2006;55:739.
- [166] **Verdier M, Brechet Y, Guyot P.** Recovery of AlMg alloys: Flow stress and strain-hardening properties. *Acta Materialia* 1998;47:127.
- [167] **Byun TS, Farrell K, Li MM.** Deformation in metals after low-temperature irradiation: Part I - Mapping macroscopic deformation modes on true stress-dose plane. *Acta Materialia* 2008;56:1044.
- [168] **Simar A, Nielsen KL, de Meester B, Tvergaard V, Pardoën T.** Micro-mechanical modelling of ductile failure in 6005A aluminium using a physics based strain hardening law including stage IV. *Engineering Fracture Mechanics* 2010;77:2491.
- [169] **Lecarme L, Tekoglu C, Pardoën T.** Void growth and coalescence in ductile solids with stage III and stage IV strain hardening. *International Journal of Plasticity* 2011;27:1203.
- [170] **Shen HP, Lei TC, Liu JZ.** Microscopic deformation-behavior of martensitic ferritic dual-phase steels. *Materials Science and Technology* 1986;2:28.
- [171] **Lassance D, Scheyvaerts F, Pardoën T.** Growth and coalescence of penny-shaped voids in metallic alloys. *Engineering Fracture Mechanics* 2006;73:1009.
- [172] **Rice JR, Tracey DM.** On the ductile enlargement of voids in triaxial stress fields. *Journal of the Mechanics and Physics of Solids* 1969;17:201.
- [173] **Huang Y.** Accurate dilatation rates for spherical voids in triaxial stress-fields. *Journal of Applied Mechanics-Transactions of the ASME* 1991;58:1084.
- [174] **Martin G, Yerra SK, Brechet Y, Veron M, Mithieux JD, Chehab B, Delannay L, Pardoën T.** A macro- and micromechanics investigation of hot cracking in duplex steels. *Acta Materialia* 2012;60:4646.
- [175] **Pardoën T.** Numerical simulation of low stress triaxiality ductile fracture. *Computers & Structures* 2006;84:1641.

References

Appendix A: Pre-existing defects of cold-rolled martensite

For ferrite + pearlite mixture, defects are usually not formed during cold-rolled processing. However, defects are observed in cold-rolled martensite (Figure A.1), probably due to the higher flow stress. Most of the defects are elongated along the rolling direction.

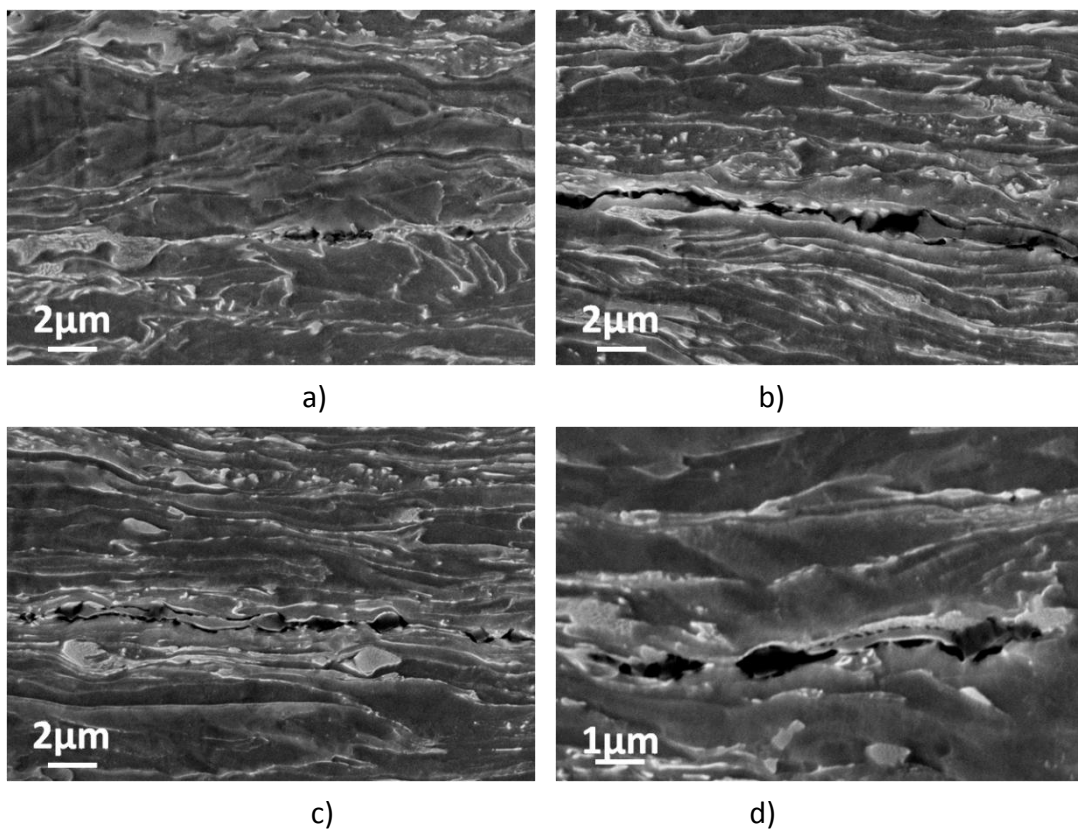


Figure A.1. Micrographs showing the pre-existing defects in cold-rolled martensite.

Résumé étendu

1. Introduction et revue bibliographique

Les aciers Dual Phase (DP) ferrite-martensite sont largement utilisés dans l'industrie automobile pour leurs excellentes propriétés mécaniques. Mais l'étendue limitée des compromis entre résistance mécanique et aptitude à la mise en forme actuellement offerte par ce type d'aciers reste le principal frein à une utilisation plus large de cette gamme d'alliages. Afin de pouvoir exploiter au mieux le potentiel des aciers DP, les effets individuels des caractéristiques microstructurales doivent être précisés.

Nous avons réalisé une revue bibliographique détaillée portant sur l'évolution de la microstructure et des propriétés mécaniques des aciers DP. Nous y résumons les propositions majeures pour le contrôle de la microstructure des aciers DP et nous y mettons en évidence les paramètres déterminants pour les propriétés de déformation plastique et de rupture, tels que la fraction volumique et la composition de la martensite ainsi que l'effet de taille de la microstructure.

2. Transformation de phases

La ré-austénitisation depuis une microstructure sphéroïdale a été étudiée et les mécanismes de croissance austénitique ont été modélisés à l'aide du logiciel DICTRA. Comme le montre la Figure I a, la cinétique de la croissance austénitique peut être reproduite par simulation. Cette concordance nous permet d'analyser avec confiance les mécanismes de croissance austénitique et le profil de composition de la phase austénitique. Pour une température de recuit de 740°C, la cinétique de transformation est rapide. Cependant, la croissance austénitique est dans ce cas contrôlée par la répartition du Mn (Figure I b) et la distribution du carbone dans l'austénite peut alors être considérée comme uniforme, comme cela a été confirmé par une cartographie NanoSIMS.

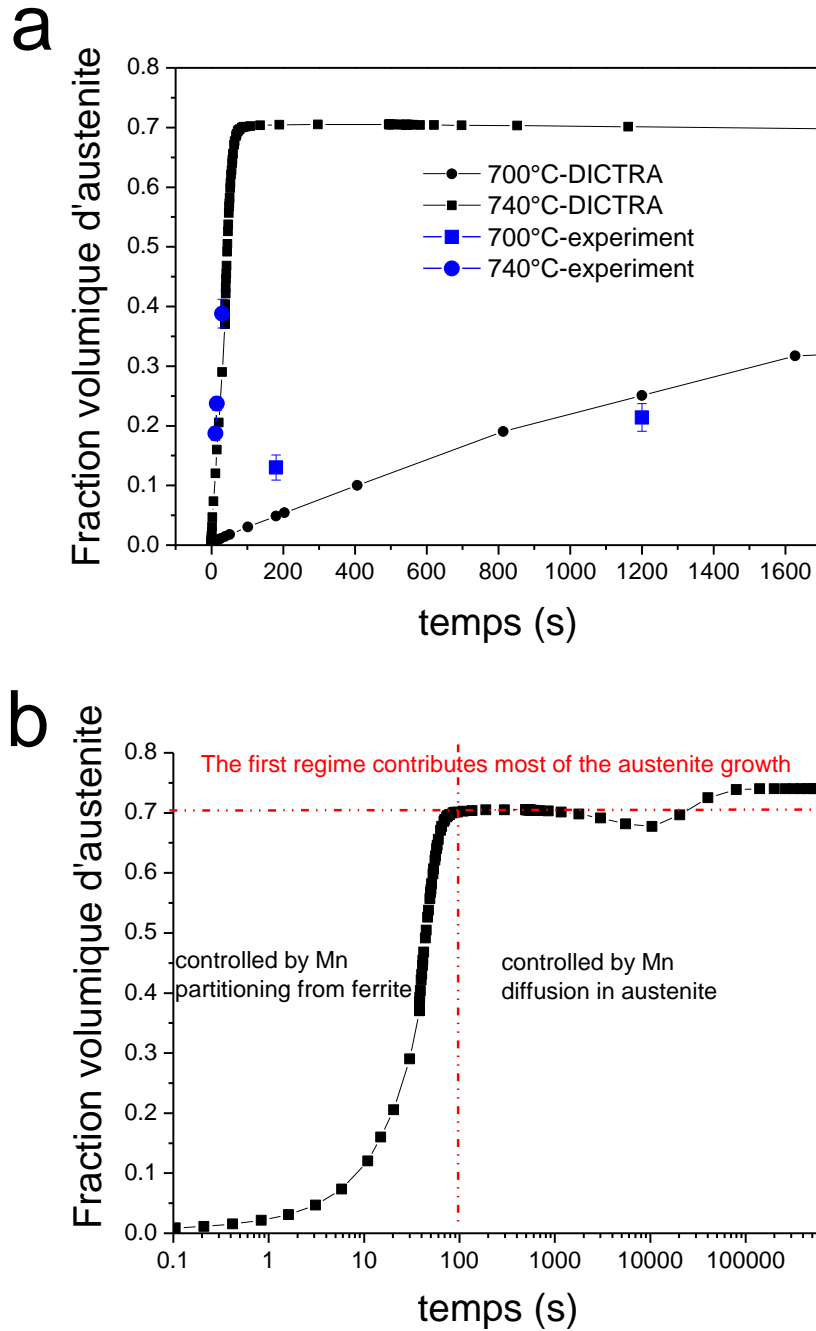


Figure I . Valeurs expérimentales et simulation de la cinétique de ré-austénitisation (a). Mécanismes de formation de l'austénite à 740°C (b).

En jouant sur les paramètres de traitement thermique, différentes microstructures ont été obtenues afin d'étudier les propriétés mécaniques des aciers DP. Nous nous sommes en premiers lieux intéressés à découpler l'influence de la fraction volumique de martensite et de sa composition. A cette fin nous avons effectué des recuits à différentes températures de la microstructure sphéroïdale. Ainsi, les aciers DP obtenus possèdent les mêmes caractéristiques microstructurales et en particulier

Résumé étendu

la répartition spatiale de la martensite. Les évolutions de la distance caractéristique dans la ferrite et de la longueur moyenne de la martensite en fonction de la fraction volumique de cette dernière V_m sont représentées sur la Figure II. Les différentes températures de recuit influant sur la partition des éléments d'alliage permettent d'obtenir différentes compositions martensitiques. Il en résulte une évolution de la nanodureté montrée en Figure III. Nous observons que la nanodureté de la martensite est relativement constante pour une température de recuit fixée.

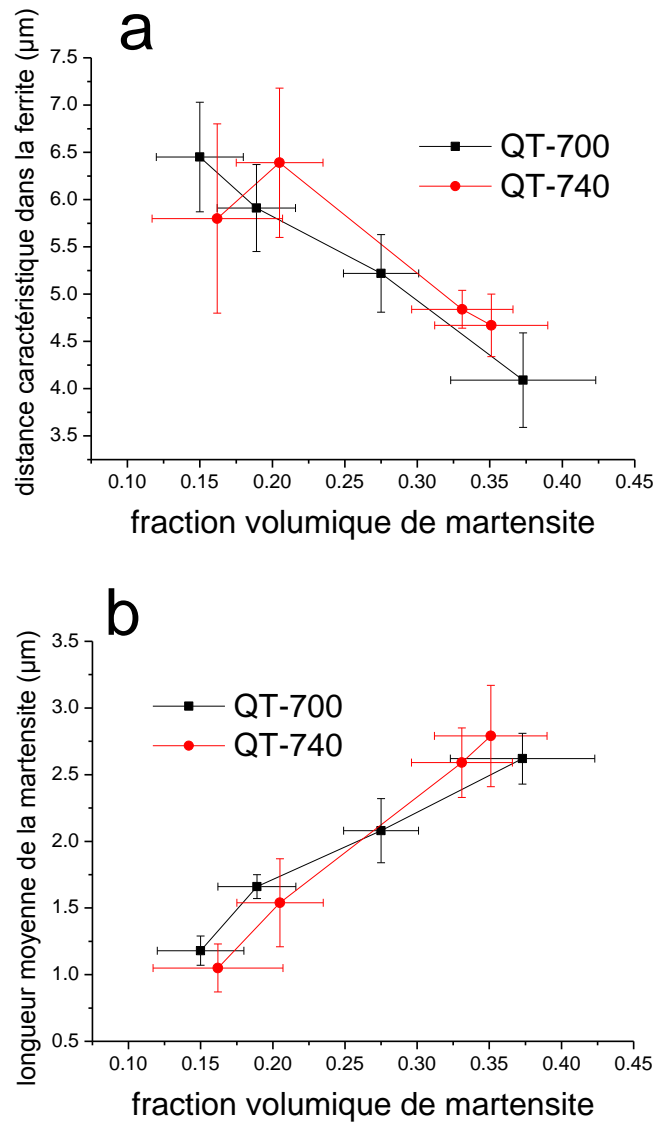


Figure II. Evolution de la distance caractéristique dans la ferrite (a) et de la longueur moyenne de la martensite (b) en fonction de la fraction volumique de martensite après recuit à 700°C et 740°C.

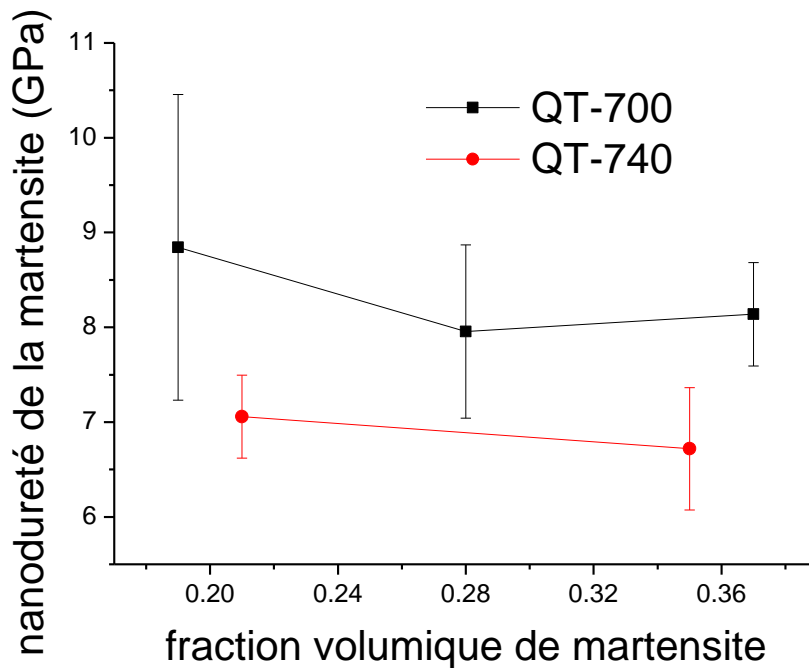


Figure III. Evolution de la nanodureté de la martensite après recuit à 700°C et 740°C en fonction de la fraction volumique de martensite.

Nous nous sommes également intéressés aux effets du raffinement de la microstructure des aciers DP (réduction simultanée de la taille de grain de la ferrite (Figure V a) et des îlots de martensite (Figure V b)). La concentration en manganèse de 3,5pds % permet d'abaisser significativement la température de formation de l'austénite en martensite et le revenu d'une martensite laminée à froid donne lieu à une plus forte interaction entre la recristallisation de la ferrite et la transformation en austénite. Une microstructure à grain ultra-fins d'acier DP (UFG-DP, Figure IV) est obtenue avec une vitesse de montée en température de 10°C/sec.

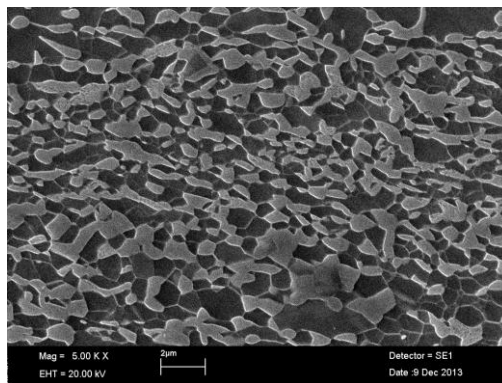


Figure IV. Microstructure à grains ultra-fins d'acier DP observée en microscopie

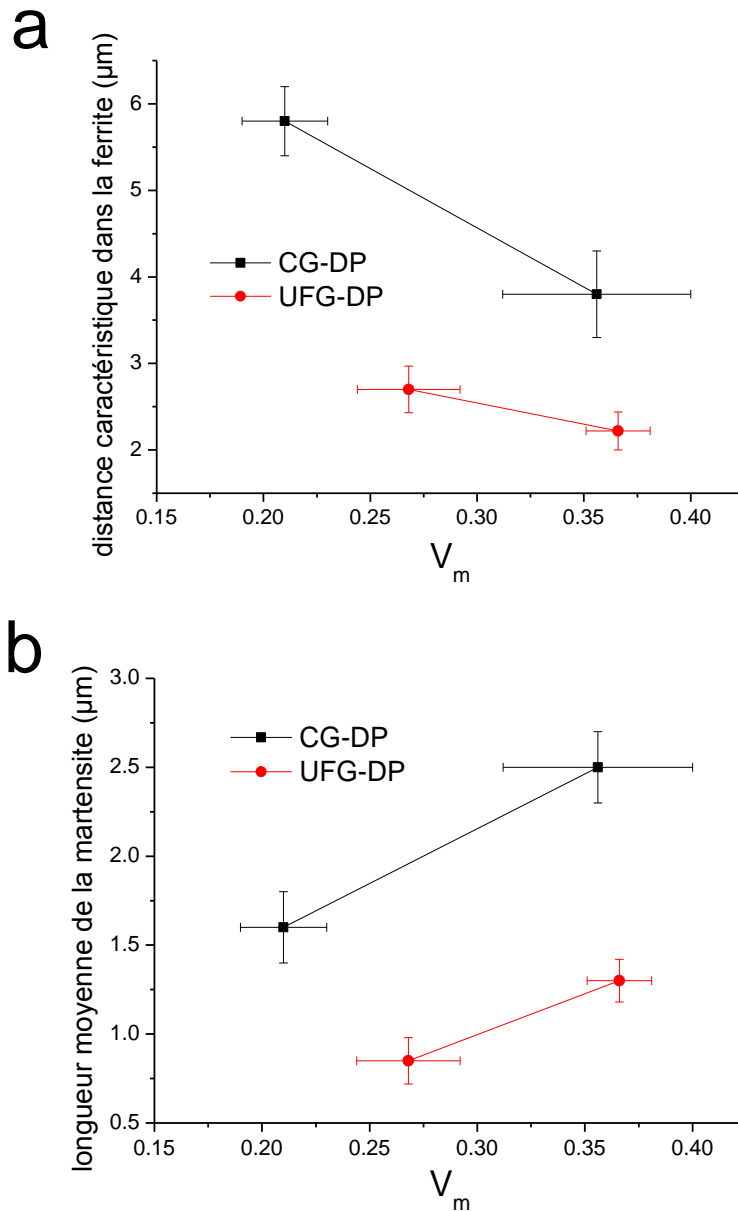


Figure V. Mesures de la distance caractéristique dans la ferrite (a) et de la longueur moyenne de la martensite (b) pour une microstructure à gros grains (CG) ou à grains ultra-fins (UFG-DP)

3. Propriétés de déformation plastique des aciers DP

Les propriétés de déformation plastique correspondant aux différentes microstructures précédemment décrites ont été systématiquement déterminées. Nous avons observé que la limite élastique (Figure VIa) ainsi que la résistance à la traction (Figure VIb) augmentent avec la fraction volumique de martensite V_m , alors

Résumé étendu

que l'allongement uniforme diminue (Figure VIc). Une relation quasi linéaire est observée dans le cas du revenu à 700°C.

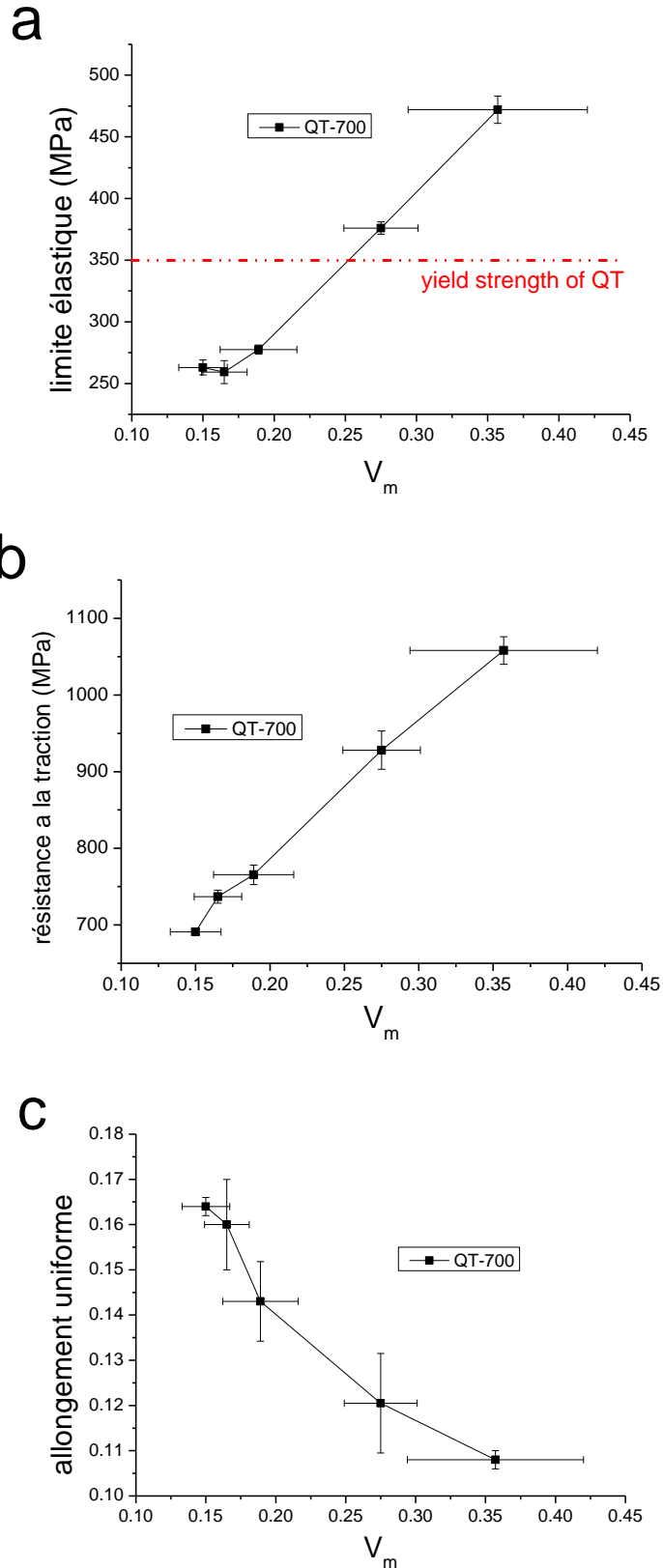
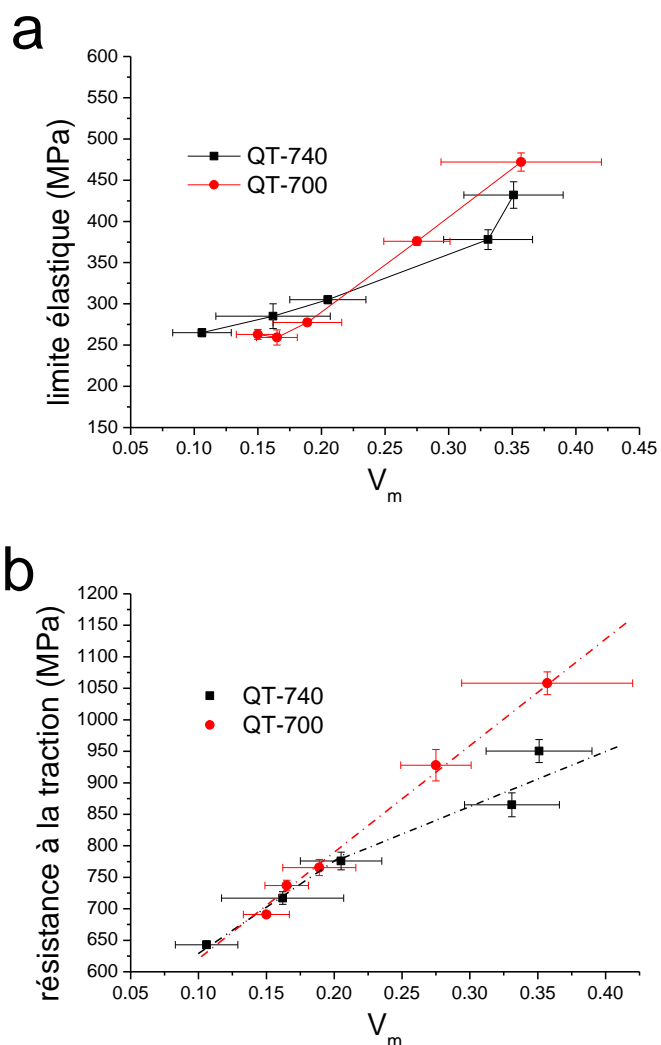


Figure VI. Evolutions de la limite élastique (a), de la résistance à la traction (b) et de

Résumé étendu

l'allongement uniforme (c) avec la fraction volumique de martensite.

Les effets de la composition/dureté de la martensite sur les propriétés de déformation plastique des aciers DP sont présentés en Figure VII. La dureté de la martensite, plus importante après un revenu à 700°C qu'après un revenu à 740°C, n'a que très peu d'influence sur la limite d'élasticité et l'allongement uniforme comme on peut le constater en Figure VIIa et Figure VIIc respectivement. La résistance à la traction peut quant à elle évoluer selon la composition de la martensite, mais seulement lorsque sa fraction volumique est supérieure à 20%. La relation linéaire entre la résistance à la traction et fraction volumique de martensite peut être maintenue dans le cas du traitement à 700°C (Figure VIIb). Le traitement à 700°C aboutissant à une martensite de forte dureté permet d'atteindre un meilleur compromis entre résistance et ductilité que dans le cas d'un revenu à 740°C (Figure VII d).



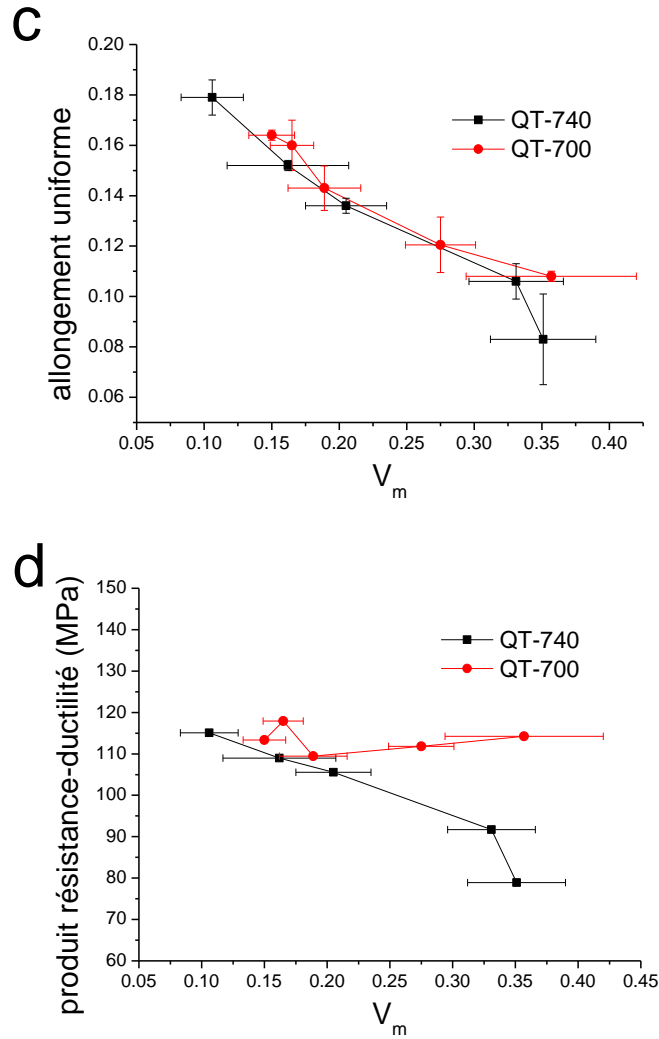


Figure VII. Comparaison de l'évolution pour les revenus à 700°C et 740°C de la limite d'élasticité (a), de la résistance à la traction (b), de l'allongement uniforme (c) et du produit résistance-ductilité (d) en fonction de la fraction volumique de martensite.

La Figure VIII présente les effets sur les propriétés mécaniques des aciers DP du raffinement de leur microstructure. L'analyse est d'autant plus complexe qu'il faut prendre en compte l'effet TRIP dans les UFG-DP recuit à 680°C. Cet effet est dû au taux relativement élevé de manganèse. En comparaison, sans l'effet TRIP, un UFG-DP possède une résistance à la traction plus élevée (Figure VIIIa) mais un allongement uniforme un peu plus faible (Figure VIIIb). Ainsi, un UFG-DP et un CG-DP possèdent approximativement le même produit résistance-ductilité (Figure VIIIc). Cependant, l'effet TRIP permet d'augmenter simultanément la résistance à la traction, l'allongement uniforme et donc ainsi le produit résistance-ductilité.

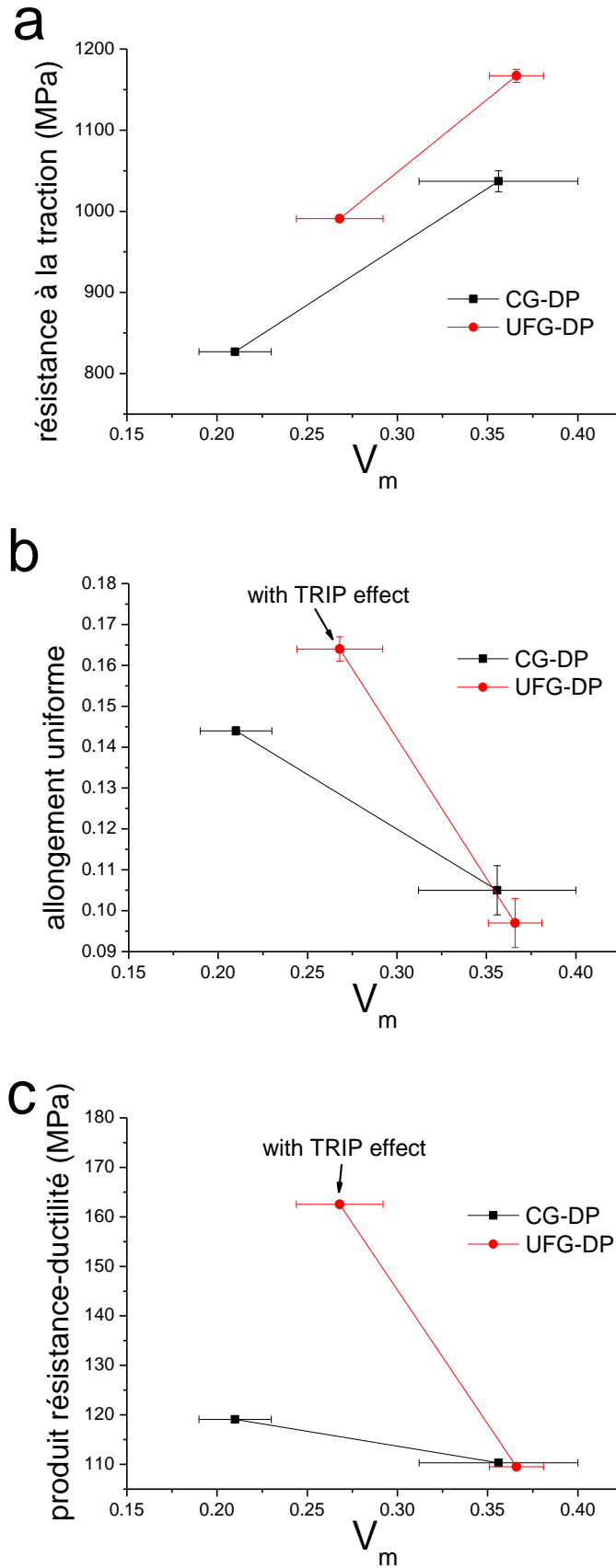


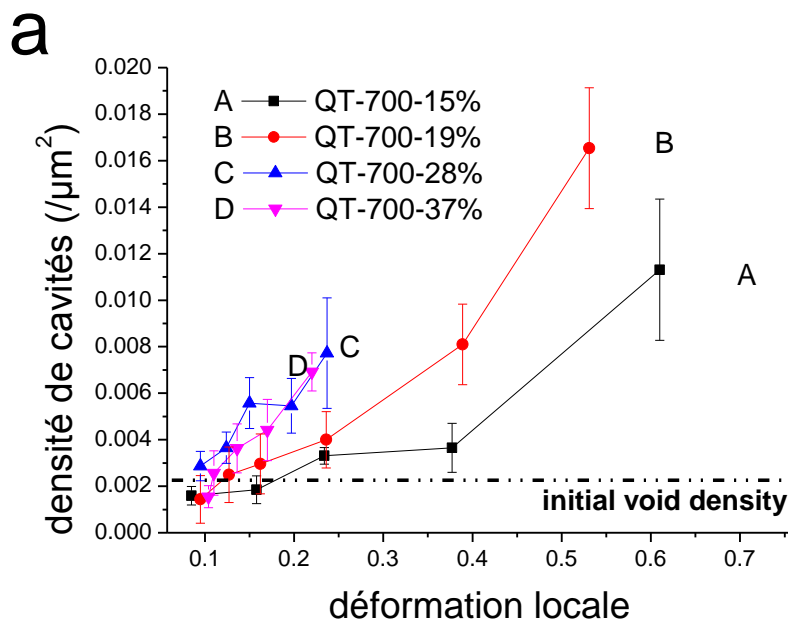
Figure VIII. Comparaison de l'évolution de la résistance à la traction (a), de l'allongement uniforme (b) et du produit résistance-ductilité (c) avec la fraction

4. Endommagement et rupture des aciers DP

Grâce aux différentes microstructures élaborées, les effets de la microstructure sur les propriétés de rupture des aciers DP sont étudiées expérimentalement. Une caractérisation détaillée est effectuée afin de comprendre les mécanismes de rupture.

L'influence de la fraction volumique sur l'endommagement est présentée en figure IX. Une augmentation de V_m permet l'accumulation d'endommagement, que ce soit en termes de germination de cavités (Figure IXa) ou de fraction surfacique de ces cavités (Figure IXb). Ainsi, la déformation à rupture décroît de manière monotone avec l'augmentation de la fraction volumique de martensite comme nous pouvons le constater sur la Figure X.

La déformation à rupture ne dépend pas de la composition de la martensite tant que sa fraction volumique est faible (inférieure à 21%). Pour des fractions volumiques de martensite supérieures à 21%, la déformation à rupture est plus importante dans le cas du revenu à 740°C conduisant à une martensite plus douce.



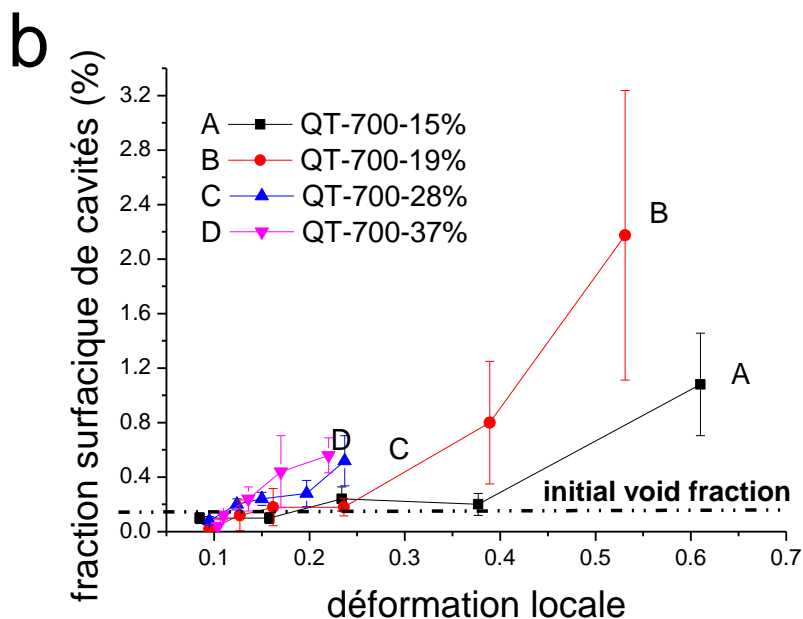


Figure IX. Evolutions de la densité de cavités (a) et de leur fraction surfacique (b) en fonction de la déformation locale. Seules les cavités dont la surface est supérieure à $0.11 \mu\text{m}^2$ ont été prises en compte.

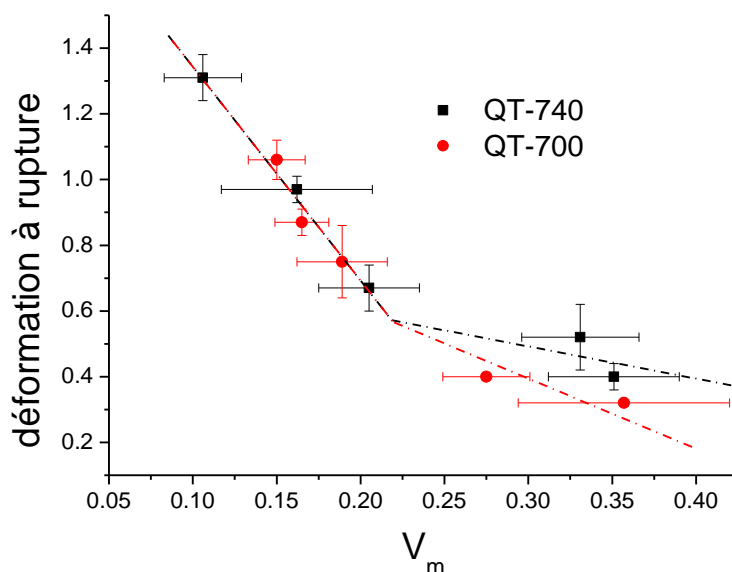


Figure X. Evolution de la déformation à rupture pour les revenus à 700°C et 740°C en fonction de la fraction volumique de martensite

Comme on peut le voir en Figure XI, le raffinement de la microstructure ainsi que la fraction volumique de martensite influent tous deux sur la déformation à rupture de l'alliage. Dans le cas des fortes fractions volumiques de martensite le raffinement de la microstructure n'a quasi pas d'effet sur la déformation à rupture, alors que pour

Résumé étendu

les faibles fractions une microstructure plus fine permet d'atteindre de plus hautes déformations à rupture (Figure XIa). Le raffinement de la microstructure est donc un moyen d'atteindre un meilleur compromis entre résistance à la traction et déformation à la rupture comme illustré en Figure XIb.

Les images obtenues par microscopie électronique à balayage présentées en Figure XII. Nous renseignent sur les mécanismes d'endommagement et de rupture des aciers UFG-DP et CG-DP. Les cavités que l'on peut observer dans l'alliage UFG-DP (Figure XIIa) sont très petites en comparaison de celles présentes dans l'alliage CG-DP (Figure XIIb), ce qui nous indique que le raffinement de la microstructure limite grandement la croissance des cavités. Les fractographies constituant les Figures XIIc et XII d nous apprennent que l'acier UFG-DP rompt de manière ductile (présence de cupules en Figure XIIc) alors que l'acier CG-DP rompt de manière fragile (présence de surfaces de clivage en Figure XII d).

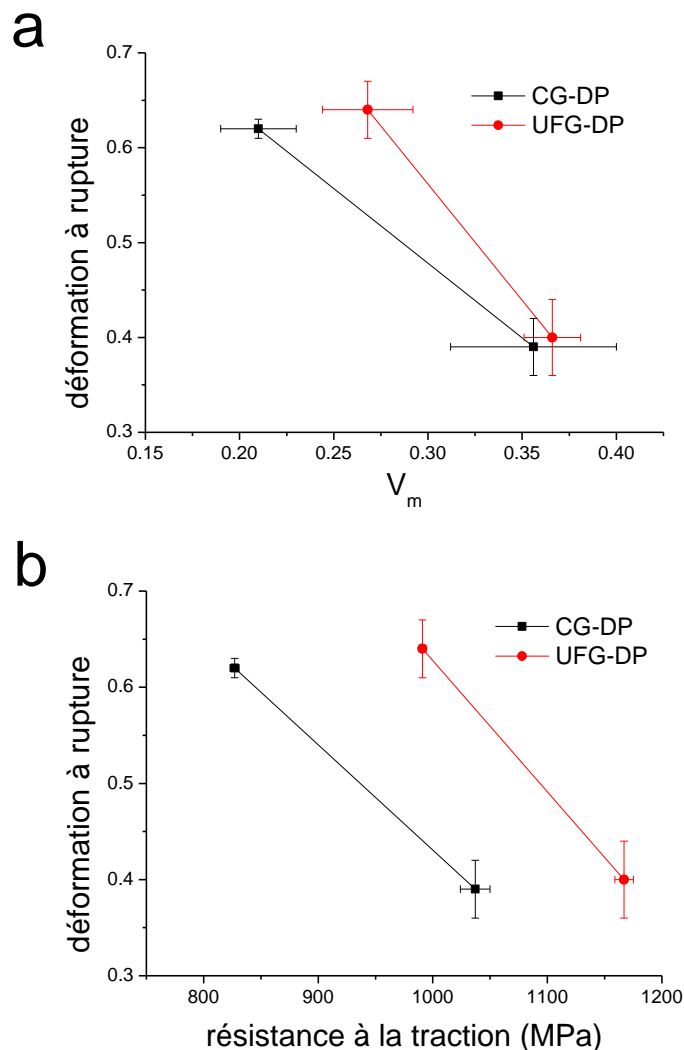


Figure XI. Effets du raffinement de la microstructure des aciers DP sur les propriétés

mécaniques : déformation à rupture en fonction de la fraction volumique de martensite (a) et de la résistance à la traction (b).

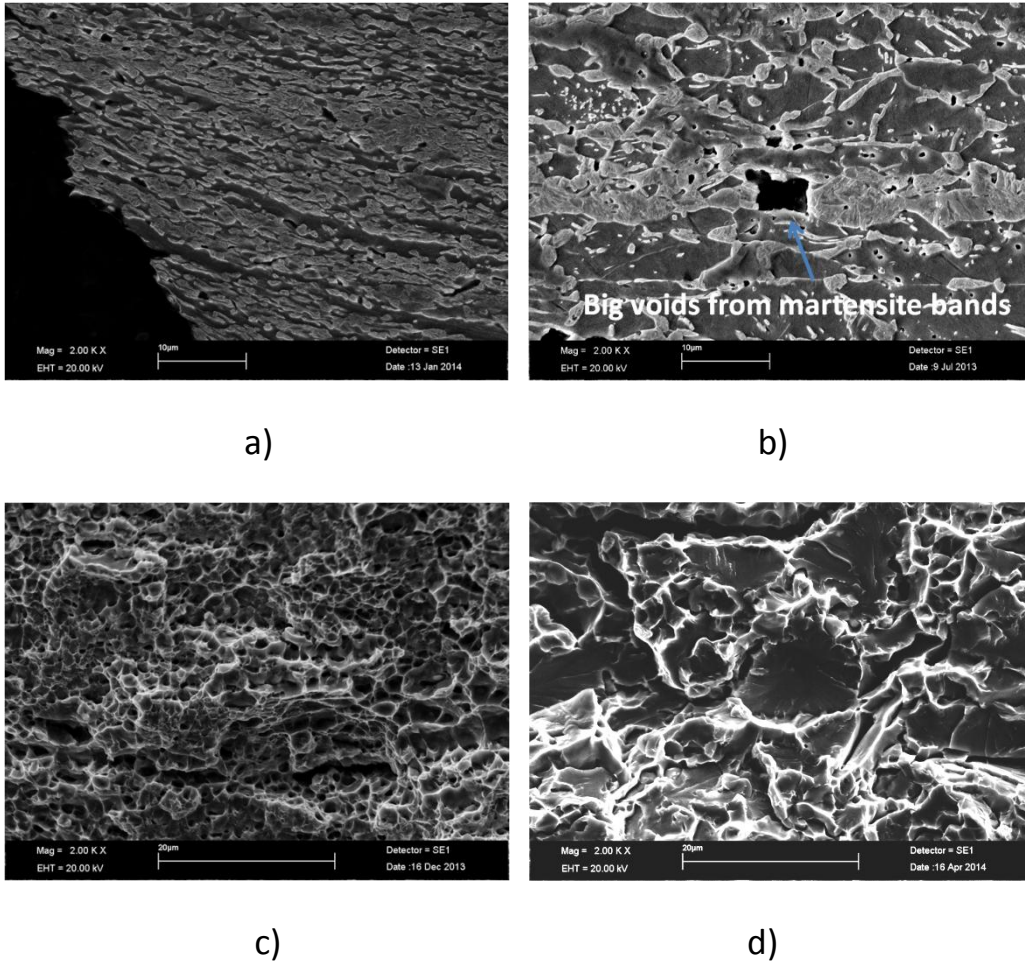


Figure XII. Images MEBde l'endommagement et des surfaces de rupture deséchantillons UFG-DP (a et c respectivement) et CG-DP (b et d respectivement).

5. Modélisation micromécanique

Afin de poursuivre l'analyse du comportement mécanique des aciers DP d'une manière plus quantitative, nous avons utilisé une modélisation micromécanique par éléments finis (Figure XIII). L'intégration à la modélisation d'une loi modifiée pour le comportement de la ferrite, prenant en compte le stade IV d'écrouissage, permet d'améliorer la prédiction des propriétés mécaniques.

Comme nous pouvons le constater en Figure XIVa, nous sommes en mesure de prédire la résistance à la traction reproduisant ainsi la relation linéaire existant entre

Résumé étendu

cette propriété et la fraction volumique de martensite pour le cas du revenu à 700°C. Le stade IV de la ferrite a un effet limité sur la prévision de la résistance à la traction. Cependant, cette prévision peut tout de même être améliorée en considérant la loi de comportement modifiée de la ferrite, alors qu'une simple loi de Voce pour la ferrite aboutit à une sous-estimation de la déformation uniforme (Figure X IVb).

Ce modèle permet également d'appréhender les effets de la dureté de la martensite (liée à sa composition) sur les propriétés de déformation plastique. Comme nous pouvons le constater sur la Figure X V a, la résistance à la traction augmente avec la teneur en carbone de la martensite. Cet effet est d'autant plus important que la fraction volumique de martensite est élevée, en accord avec ce que nous avons observé expérimentalement. La composition de la martensite n'a que peu d'effet sur la déformation uniforme (Figure X V b), bien que théoriquement l'apparition de la striction puisse être retardée dans le case d'une martensite plus dure. De plus, nous prévoyons que le produit résistance-ductilité augmente avec la dureté de la martensite (Figure X V c), ce que nous avons également déjà établi expérimentalement.

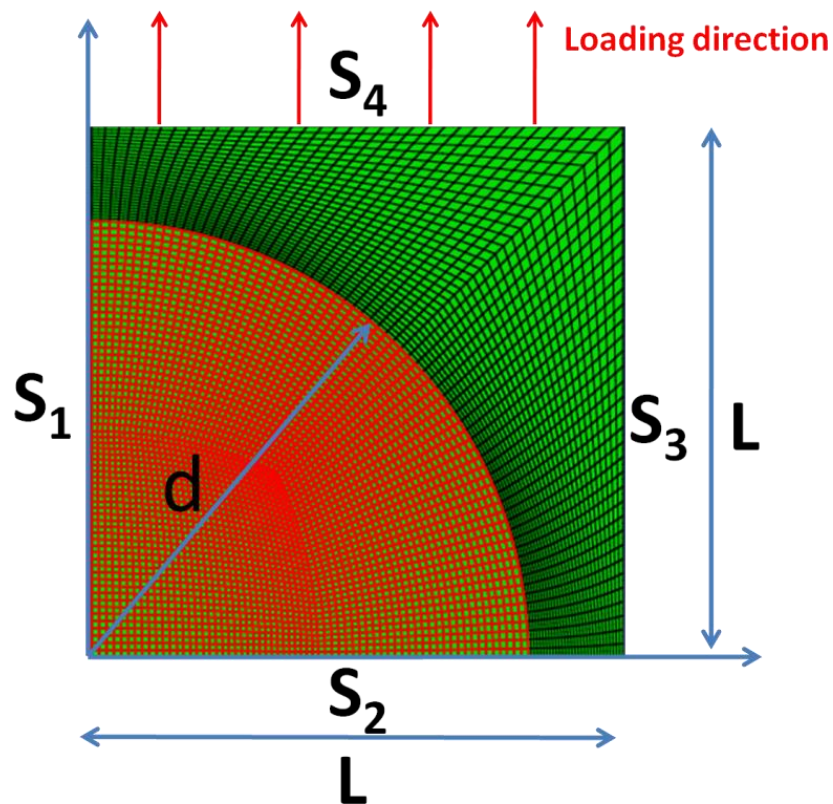


Figure X III. Présentation de la cellule axisymétrique unitaire utilisée.

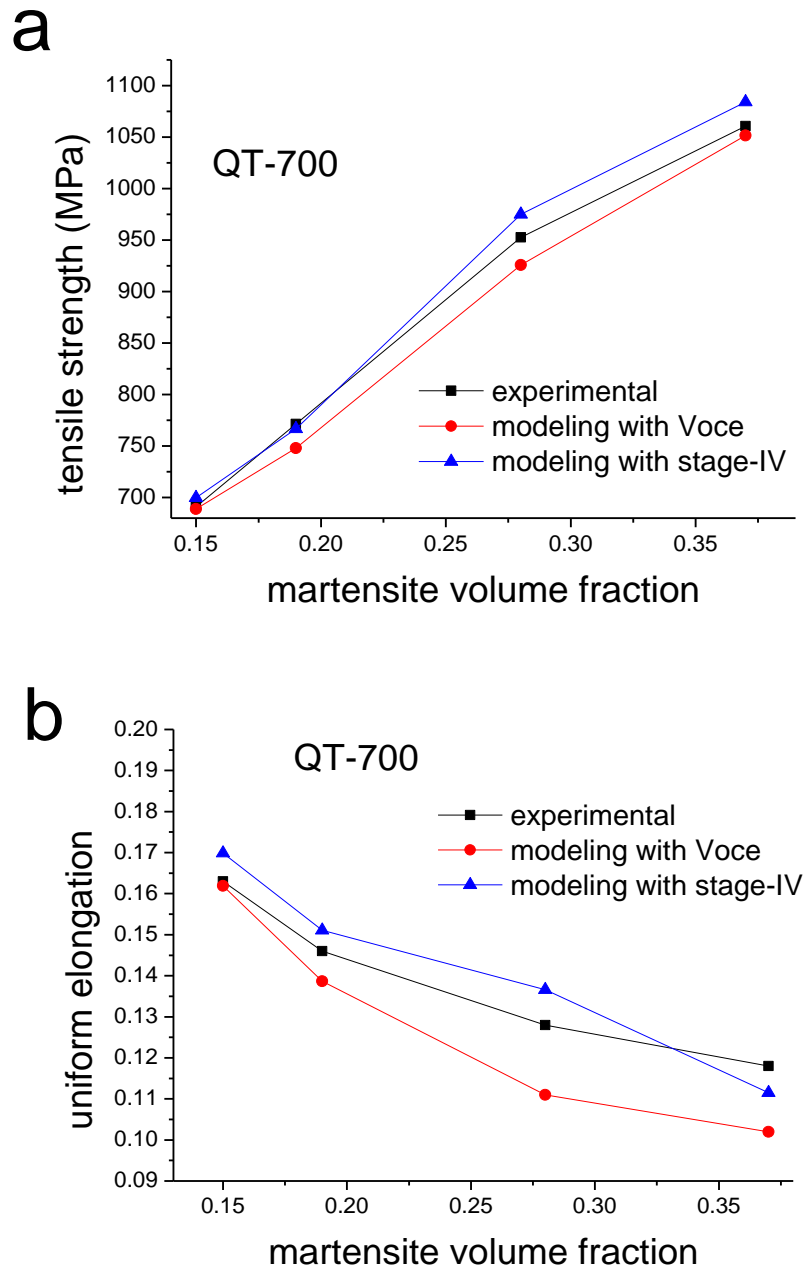


Figure X IV. Prévisions de la résistance à la traction (a) et de l'allongement uniforme (b) avec et sans prise en compte du stade IV d'écroissage pour la ferrite.

Résumé étendu

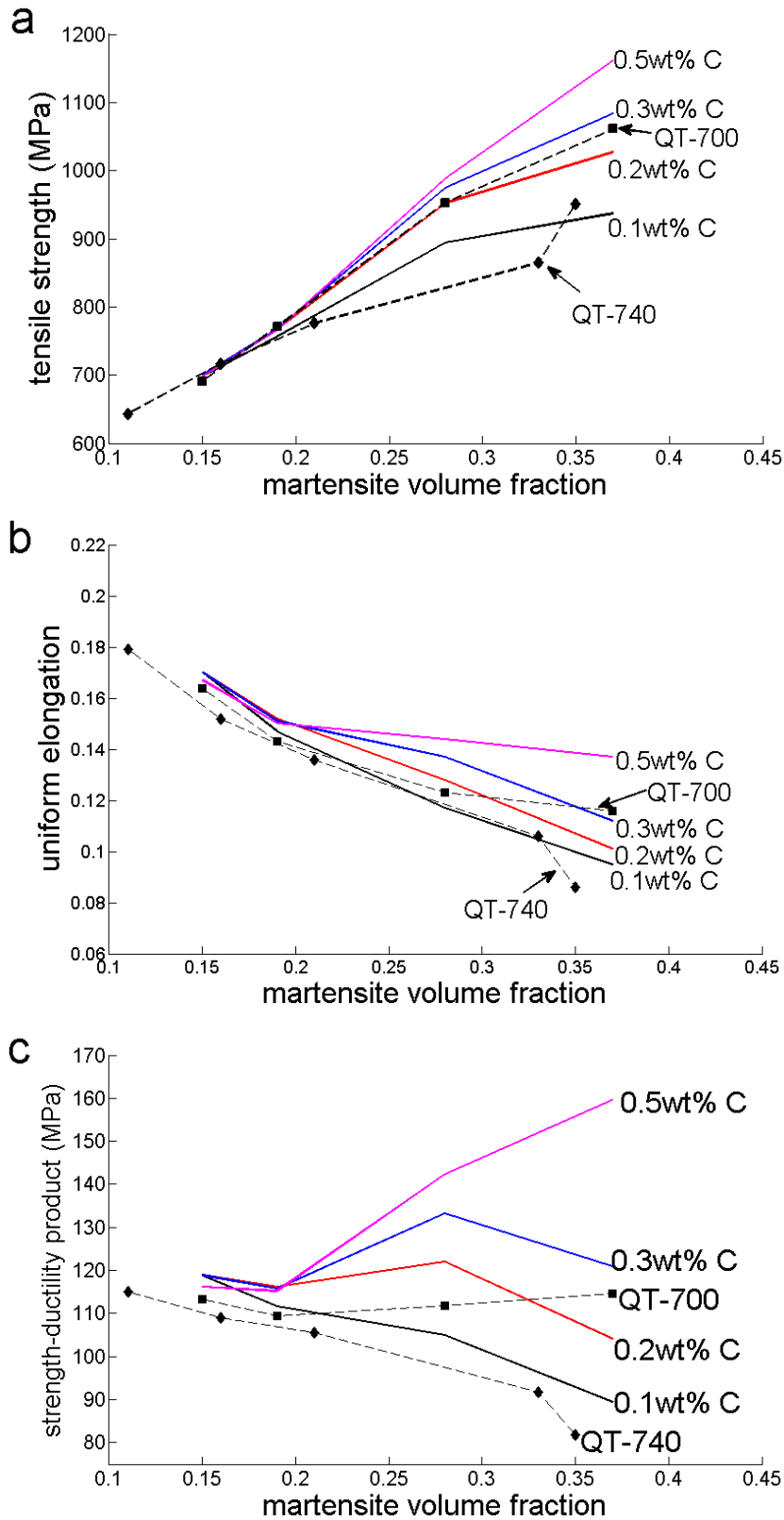
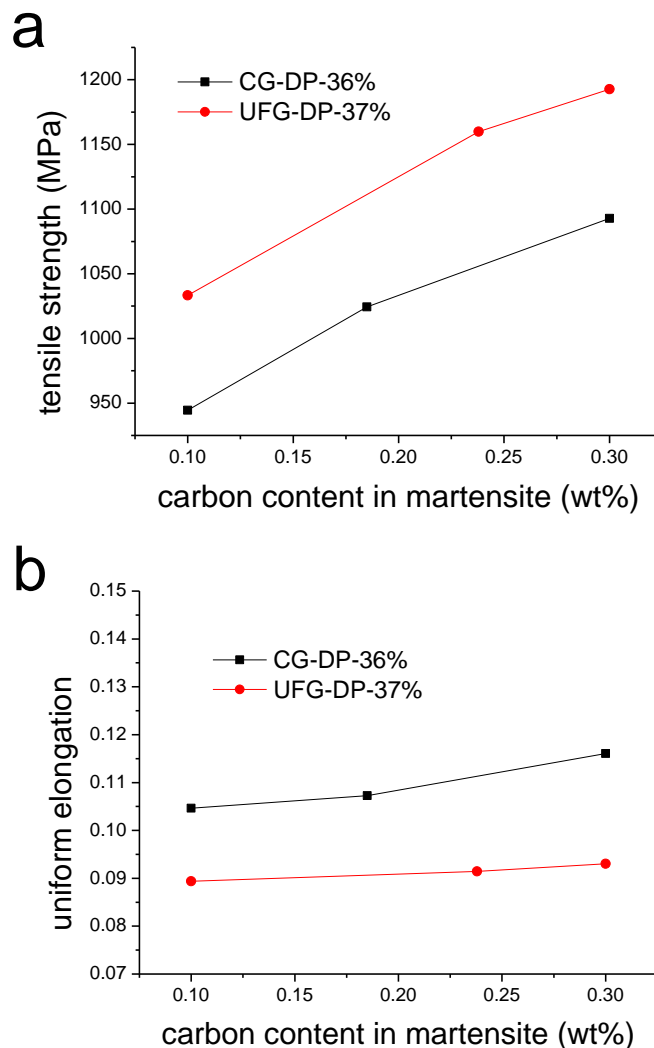


Figure X V. Comparaisons de la résistance à la traction (a), de l'allongement uniforme (b) et du produit résistance-ductilité (c) prévus par la modélisation avec les valeurs expérimentales.

Résumé étendu

Les effets du raffinement de la microstructure sur les propriétés de déformation plastique des aciers DP sont également discutés sur la base du modèle par éléments finis. Une étude paramétrique a été menée afin de comparer les propriétés de déformation plastique des alliages UFG-DP et CG-DP obtenues pour différentes teneurs en carbone de la martensite. Nous pouvons constater en Figure XVIa que la résistance à la traction est plus importante pour les alliages UFG-DP tandis que leur allongement uniforme est plus faible (Figure XVIb). Cela résulte en un produit résistance-ductilité légèrement inférieur pour les alliages UFG-DP. Ainsi, le raffinement de la microstructure ne conduit pas à une amélioration des propriétés de déformation plastique des aciers DP.



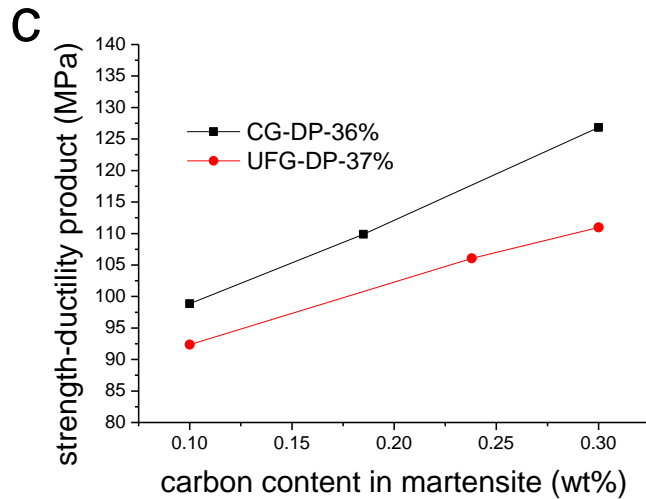


Figure X VI. Prévisions de la résistance à la traction (a), de l'allongement uniforme (b) et du produit résistance-ductilité.

L'analyse par éléments finis permet d'obtenir à la fois les réponses à l'échelle macroscopique et microscopique de la cellule unitaire, qui constituent des paramètres d'entrée importants du modèle de rupture. L'utilisation d'un simple de la déformation à rupture permet de déterminer les effets de la fraction volumique de martensite, de sa composition et de l'échelle de la microstructure sur la déformation à rupture des aciers DP par une étude paramétrique.

Comme le montre la Figure X VII, la fraction volumique de martensite a un effet de premier ordre sur la déformation à rupture dans le cas d'une martensite riche en carbone. Pour des teneurs en carbone de la martensite comprises entre 0,2pds% et 0,5pds% l'effet est minime ; la déformation à rupture n'est fortement augmentée que pour des teneurs en carbone inférieures ou égales à 0,1pds%.

La Figure X VIII nous montre l'effet du raffinement de la microstructure pour une fraction volumique de martensite fixe égale à 37%. L'alliage UFG-DP présente une déformation à rupture supérieure à celle de l'alliage CG-DP lorsque la teneur en carbone de la martensite est supérieure à 0,15pds%. Cependant, dans le cas d'une martensite plus douce, nous obtenons l'inverse. L'alliage CG-DP peut alors avoir une déformation à rupture plus importante car la rupture de la martensite est favorisée par le renforcement de la matrice dans l'alliage UFG-DP.

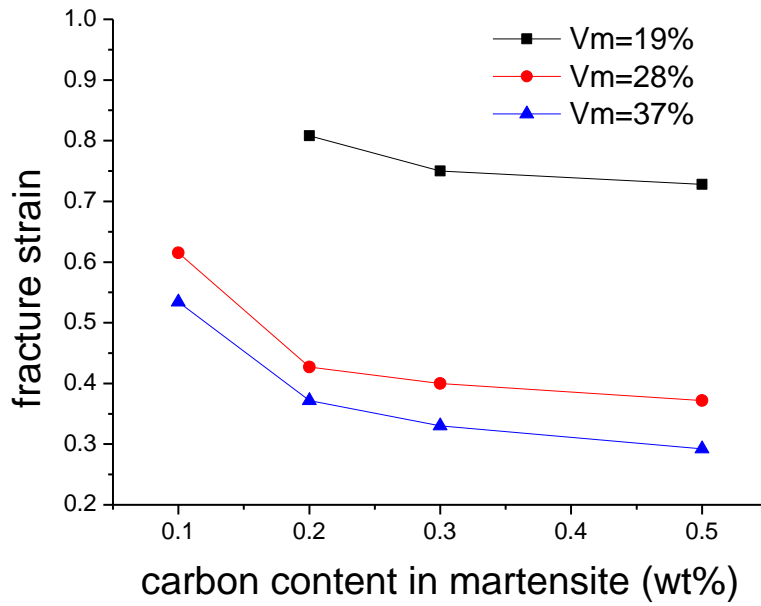


Figure X VII. Illustration de l'effet de la teneur en carbone de la martensite sur la déformation à rupture des aciers DP pour différentes valeurs de la fraction volumique de martensite.

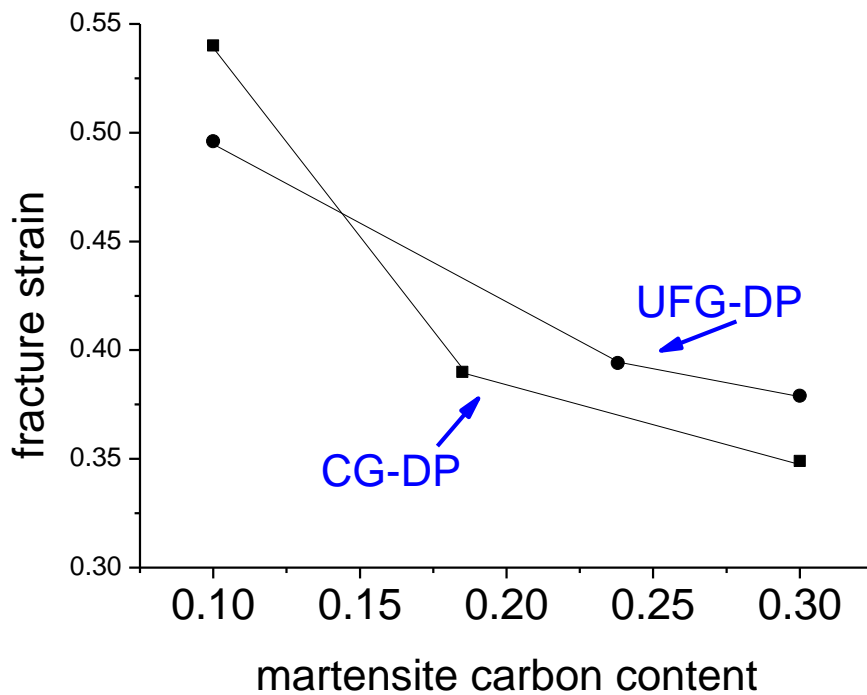


Figure X VIII. Illustration de l'effet de la teneur en carbone de la martensite sur la déformation à rupture des aciers DP pour différentes échelles de la microstructure.

6. Optimisation de la microstructure

Dans le cadre du modèle présenté précédemment, la microstructure des aciers DP peut être optimisée dans le but d'atteindre de meilleures propriétés mécaniques par des études paramétriques systématiques. Ainsi la voie à suivre pour obtenir des aciers DP sur mesures a été mise en évidence : pour les procédés de mise en forme pour lesquels la déformation uniforme joue un rôle majeur, une forte teneur en carbone de la martensite est préférable de même qu'une microstructure pas trop fine et pour ceux où ce sont les propriétés de rupture du matériau qui sont déterminantes, il est utile de diminuer l'échelle de la microstructure.

Le concept d'un alliage DP possédant une martensite à gradient est également discuté. Des îlots de martensite à gradient avec une couche moins dure à l'interface conduiraient à une diminution de la résistance à la traction et de l'allongement à rupture mais permettraient de retarder la rupture causée par une rupture initiée dans la martensite ou par striction.

7. Conclusions

La recherche de bons compromis entre les propriétés mécaniques en traction et celles de formabilité nécessite une optimisation des paramètres microstructuraux, ce qui a guidé les travaux effectués au cours de cette thèse. Nous proposons un travail expérimental original permettant de mieux comprendre la formation des microstructures des aciers DP et de découpler l'effet de certains paramètres microstructuraux sur les propriétés de ces aciers. De plus, un travail sur la modélisation micromécanique permet de compléter et d'interpréter la synthèse de ces données expérimentales. Ce travail ouvre des voies intéressantes de « design » des microstructures des aciers DP en vue de développer de nouvelles générations de ce type d'alliages possédant des propriétés de tenue mécanique et de formabilité sur mesures.